

**Spectroscopic Studies On The Medicinally
Important Molecules With Various Nanoparticles
And Their Interaction With Different Cell Lines**

THESIS

**SUBMITTED FOR THE DEGREE OF
DOCTOR OF PHILOSOPHY (SCIENCE)**

BY

SIDDHI CHAUDHURI

**DEPARTMENT OF BIOCHEMISTRY
UNIVERSITY OF CALCUTTA**

2016

*Dedicated To My Parents
and Sister*

Acknowledgements

It gives me the greatest pleasure to acknowledge my debt to those who have contributed to this dissertation. I would like to extend my thanks to all of them. First and foremost, I owe my deepest gratitude to Professor Samir Kumar Pal, my enthusiastic research supervisor. I thank Sir wholeheartedly for accepting me as his research student and giving me the opportunity to work on this wonderful research area of "Drug Sensitization with Nanoparticles.". He has been actively interested in my work and has always been available to clarify my doubts despite his busy schedule. I am very grateful for his constant patience, motivation, immense knowledge in multidisciplinary field of science, commitment to the highest scientific standards, unconditional support during crisis that, taken together, make him an exemplary mentor. As my supervisor, he has constantly forced me to remain focused on achieving my goal. His observations and comments helped me to establish the overall direction of the research and to move forward with investigation in depth. I am amazingly fortunate to have an advisor who has left no stone unturned so that I could complete my Ph.D. in such restricted time span. I thank him for providing me with the opportunity to work with a talented team of researchers and an excellent research environment.

The members of my thesis committee and all the teaching and non-teaching staff of S. N. Bose National Centre for Basic Sciences have been very kind enough to extend their help at various phases of this research; and I express my gratitude to all of them.

I would also like to thank Prof. Peter Lemmens of Braunschweig University of Technology (Germany), Dr. Achintya Singha of Bose Institute (Kolkata), and Prof. Partha Saha of Saha Institute of Nuclear Physics (Kolkata) for fruitful collaboration. Shib Shankar, Dr. Anup Maiti and Dr. Sushanta Debnath helped in conducting some experiments.

I gratefully acknowledge the Council of Scientific & Industrial Research of India for providing me a fellowship. My work was also supported by the Department of Science and Technology (DST).

I'd like to express my sincere thanks to all my seniors and colleagues for providing a stimulating and enriching environment. Special thanks to Dr. Soma Banerjee and Dr. Nirmal Goswami for their significant contribution in my research work. I am also thankful to Soma for her warmth and care when I was a fresher in the lab. I thank Dr. Subrata Batabyal and Dr. Anupam Giri for their assistance in some research areas. I am grateful to Samim for helping me in a substantial portion of my research work. He was always willing to give his best suggestions and never denied whenever I asked for any help related to research. I express my gratitude to Nabarun and Susobhan who helped me out from many technical difficulties. I acknowledge Damayanti and Dr. Shreyasi Dutta for working with me in the field of 'Nano-Bio'. My sincere appreciation goes to Prasenjit, Priya, Aniruddha, Tuhin, Jayita, Probir, Ramesh and Soumendhra da for providing a homely and a cheerful environment; and also for assisting me in research. Special thanks to Samim, Aniruddha, Susobhan and Damayanti for their assistance in formatting and proof-reading my thesis.

I pay tribute to all the faculty members of Biochemistry Department (Calcutta University) who taught me in my post-graduation and motivated me into research. I also acknowledge all my teachers from school and college.

I value the friendship of all my friends from school (especially Debanwita and Soma), college (especially Soma), university (especially Jayeeta), IIT KGP (especially Kacoli) and SNBNCBS (especially Urmi and Poulami). I sincerely thank Sayan Mukherjee for extending me academic help during my graduation days.

Finally, I am indebted to my family for their love, patience, and understanding. My beloved parents (Mr. Tarun Kumar Chaudhuri and Ms. Sukti Chaudhuri) have always been unbelievably supportive and encouraging in my pursuits. Their sacrifices and prayer for me have made me sustain thus far. I feel myself very fortunate to have Riddhi as my younger sister. I would like to pay high regards to my paternal grandmother and all my relatives (A long list! You know who you are!) for their blessings and good wishes. Special mention goes to my aunts (Baro mashi and Mukti mashi) for their keen interest in my studies. I cherish childhood memories with my cousins Lopamudra, Arka and Shubham. I hereby acknowledge all those who directly or indirectly helped me in this mesmerizing venture and I apologize for not being able to mention personally everybody.

Dated:

Department of Chemical, Biological and Macromolecular Sciences,

S. N. Bose National Centre for Basic Sciences,

Salt Lake, Kolkata 700098,

India.

(Siddhi Chaudhuri)

Table of Contents

	Page
Chapter 1: Introduction	
1.1. Background	1
1.2. Understanding the Nanoparticles	1
1.3. Photophysics Involved in Drug Sensitization by Nanoparticles	4
1.4. Interaction of Nanoparticles with Cells	5
1.5. Scope of the Spectroscopic Studies on the Medicinally Important Molecules with Various Nanoparticles and Their Interaction with Different Cell Lines	7
1.6. Objective	10
1.7. Summary of the Work Done	15
I. Photo-Sensitization of Medicinally Important Drugs	15
A. Vitamin B ₂ in Nanoscopic Environments under Visible Light: Photosensitized Antioxidant or Phototoxic Drug?	15
II. Sensitization of Medicinally Important Drugs with Inorganic Nanoparticles	16
A. Sensitization of an Endogenous Photosensitizer: Electronic Spectroscopy of Riboflavin in the Proximity of Semiconductor, Insulator and Metal Nanoparticles	16
III. Surface Modification of Nanoparticles using Medicinally Important Ligands	18
A. Surface Engineering for Controlled Nanocatalysis: Key Dynamical Events from Ultrafast Electronic Spectroscopy	18

	Page	
IV.	Mechanism of Photo-sensitized Carcinogenic Cell Damage by a Food Carcinogen in Various Cell Lines and Protective Role of a Medicinally Important Molecule	19
A.	Ultrafast Spectroscopic Study on Caffeine Mediated Dissociation of Mutagenic Ethidium from Synthetic DNA and Various Cell Nuclei	19
V.	Nanoparticle-sensitization of Photodynamic Drugs for Cancer Therapy	20
A.	Photoinduced Dynamics and Toxicity of a Cancer Drug in Proximity of Inorganic Nanoparticles under Visible Light	20
1.4.	Plan of Thesis	21
	References	23

Chapter 2: An Overview of Steady-State, Dynamical, Theoretical Tools and Systems

2.1.	Steady-State and Dynamical Tools	28
2.1.1.	Förster Resonance Energy Transfer (FRET)	28
2.1.2.	Nanosurface Energy Transfer (NSET)	32
2.1.3.	Data Analysis of Time-Resolved Fluorescence Transients	33
2.1.3.1.	Distance Distribution in Donor-Acceptor Systems	33
2.1.4.	Photoinduced Electron Transfer	35
2.2.	Systems	35
2.2.1.	Organized Assemblies (Biomimetics)	36
A.	Micelle	36
B.	Reverse Micelle (RM)	38

	Page
2.2.2. Deoxyribonucleic Acids (DNAs)	40
2.2.3. Molecular Probes	40
2.2.3.1. Riboflavin (Rf)	42
2.2.3.2. Methylene Blue (MB)	43
2.2.3.3. Bilirubin (BR)	43
2.2.3.4. Benzo[a]pyrene (BP)	43
2.2.3.5. Rose Bengal (RB)	44
2.2.3.6. 4',6-Diamidino-2-phenylindole (DAPI)	46
2.2.3.7. p-Benzoquinone (BQ)	46
References	47

Chapter 3: Instrumentation and Sample Preparation

3.1. Instrumental Setups	54
3.1.1. Steady-State UV-Vis Absorption and Emission Measurement	54
3.1.2. Time Correlated Single Photon Counting (TCSPC) Technique	55
3.1.3. Transmission Electron Microscopy (TEM)	57
3.1.4. Fourier Transform Infrared (FTIR) Measurement	58
3.1.5. Laser Raman Spectroscopy	59
3.1.6. Thermogravimetric-Differential Thermal Analyzer (TG-DTA) Setup	62
3.1.8. Viscosity Measurement	63
3.1.9. Refractive Indices Measurement	64
3.2. Sample Preparation	61
3.2.1. Chemicals Used	65
3.2.2. Preparation of Micellar Solution	65
3.2.3. Preparation of Reverse Micellar Solution	65
3.2.4. Synthesis of 5 nm ZnO NPs	66
3.2.5. Synthesis of Riboflavin Nanohybrids with ZnO NPs, TiO ₂ NPs and Al ₂ O ₃ NPs	66
3.2.6. Synthesis of Riboflavin-Gold Nanohybrids	66

	Page
3.2.7. Synthesis of Citrate-capped Gold Nanoparticles	67
3.2.8. Synthesis of Rose Bengal Nanohybrids with ZnO NPs	67
3.2.9. Preparation of DNA Fragment	67
3.2.10. Preparation of Dye-DNA Complex	68
3.2.11. Preparation of Dichlorofluorescein and ROS Measurements	68
3.2.12. Cells and Cell Culture Conditions	68
3.2.13. Bacterial Strain and Culture Conditions	68
3.2.14. Fungal Strain and Culture Conditions	69
3.2.15. 3-(4,5-dimethylthiazol-2-yl)-2,5- diphenyltetrazolium bromide (MTT) Assay	69
3.2.16. Fluorescence Microscopy Studies	70
3.2.17. Quantum Yield (QD) Calculation	70
References	71

Chapter 4: Photo-Sensitization of Medicinally Important Drugs

4.1. Introduction	73
4.2. Results and Discussion	75
4.2.1. Vitamin B ₂ in Nanoscopic Environments under Visible Light: Photosensitized Antioxidant or Phototoxic Drug?	75
4.3. Conclusion	88
References	89

Chapter 5: Sensitization of Medicinally Important Drugs with Inorganic Nanoparticles

5.1. Introduction	94
5.2. Results and Discussion	96

	Page
5.2.1. Sensitization of an Endogenous Photosensitizer: Electronic Spectroscopy of Riboflavin in the Proximity of Semiconductor, Insulator and Metal Nanoparticles	96
5.3. Conclusion	106
References	108

Chapter 6: Surface Modification of Nanoparticles Using Medicinally Important Ligands

6.1. Introduction	111
6.2. Results and Discussion	115
6.2.1. Surface Engineering for Controlled Nanocatalysis: Key Dynamical Events from Ultrafast Electronic Spectroscopy	115
6.2.1.1. TEM and HRTEM Studies	115
6.2.1.2. UV-Visible, Luminescence and FTIR Studies	117
6.2.1.3. Photocatalysis	120
6.2.1.3.1. Photodegradation of Methylene Blue	120
6.2.1.3.2. Controlled Photodegradation of Bilirubin	124
6.3. Conclusion	128
References	129

Chapter 7: Mechanism of Photo-Sensitized Carcinogenic Cell Damage by a Food Carcinogen and Protective Role of a Medicinally Important Molecule

7.1. Introduction	133
7.2. Results and Discussion	136
7.2.1. Ultrafast Spectroscopic Study on	

	Page
Caffeine Mediated Dissociation of Mutagenic Ethidium from Synthetic DNA and Various Cell Nuclei	136
7.2.1.1. Caffeine-BP Complexation in Aqueous Medium: Structural Characterization	136
7.2.1.2. Effect of Caffeine on Electron Transfer (ET) Reaction from BP to DNA under UVA Radiation	139
7.2.1.3. Role of Caffeine in the Prevention of BP and UVA Induced DNA Damage	142
7.2.1.4. Caffeine Mediated Exclusion of BP from Various Cell Lines: Cellular Studies under Ex vivo Condition	147
7.3. Conclusion	153
References	154
Chapter 8: Nanoparticle-sensitization of Photodynamic Drugs for Cancer Therapy	
8.1. Introduction	158
8.2. Results and Discussion	161
8.2.1. Photoinduced Dynamics and Toxicity of a Cancer Drug in Proximity of Inorganic Nanoparticles under Visible Light	161
8.3. Conclusion	173
References	175
List of Publications	180

Chapter 1

Introduction

1.1. Background:

‘Medicine’ is the expertise and practice of maintaining and restoring health. Its Greek etymon is ‘medome’ which means ‘to care for’. The word also means ‘to think deeply and to execute artfully’ in both English and Greek. This indicates that medicine has deep roots in craft or technology. ‘Nano’ is a term which is used as a prefix in International System of Units (SI) for one-billionth of a meter i.e. 10^{-9} m. ‘Nano’ is the Greek word for ‘dwarf’ which means ‘very small’ and Spanish word for ‘young child’. In 1974, Professor N. Taniguchi defined *nanotechnology* as “the processing of separation, consolidation and deformation of materials by one atom or one molecule.” It is the utilization of nanoscience for practical purposes in order to benefit society. Eric Drexler, Christine Peterson and Gayle Pergamit coined the term ‘*nanomedicine*’ in the context of application of nanoscience for therapeutic purpose in, *Unbounding the Future (1991)*. Nanomedicine is interpreted as an application of nanotechnology to medicine and it is the revolutionary interdisciplinary of nanotechnology, nanobiotechnology and nanobiomimetics.

1.2. Understanding the Nanoparticles:

Richard Feynman’s “plenty of room at the bottom” vision influenced the synthesis and manipulation of nanoscale materials to attain exclusive physical, chemical and electronic properties for a wide range of applications. There are four correlative

definitions of nanoparticles. As defined by Kohler and Fritzsche (2004), “nanostructures or nanoparticles are defined according to their geometric dimensions induced by external forming processes, so that the forming, orientation and positioning are achieved in relation to an external reference system, such as the geometry of a substrate. Nanostructures must have at least one dimension of less than 100 nanometers and may have two or three”. The ISO (2004), states that a nanoparticle is a “particle with a small enough diameter for the physical and chemical properties to differ measurably from those of bulk materials. The rated maximum but non-exclusive diameter is 40 nm”. These definitions go along with the one approved by the US National Nanotechnology Initiative (2004), viz. that nanotechnology represents research and technology development at the atomic, molecular and macromolecular levels in the length scale of approximately 1 to 100 nanometers; the creation or use of structures, devices or systems that have novel properties and functions because of their size; the capacity to control and manipulate at the atomic scale. In conclusion, the definition of the Royal Society and the Royal Academy of Engineering (2004) is plausibly the one that perfectly compiles the attributes and unique facets of nanomaterials. It maintains that nanoscience is the study of phenomena and the manipulation of materials at the atomic, molecular and macromolecular scales, where the properties differ significantly from those on a larger scale. Thus, the properties of nanostructures are more directly related to those of individual molecules than to those of bulk material. This results in the development of very distinct and novel properties of nanoparticles. The very principles of chemistry and classical solid state physics must be replaced by quantal approaches based on the probabilities where each atom and each molecule can play an important role and where the interactions among them have a major impact on the holistic behavior. Thus, the classical mechanical parameters of

solids no longer predominate, but the individual molecular and atomic dimensions and the interactions determine the arrangement, stability, flexibility and function of nanostructures. Two main factors may be responsible for the changes of properties observed in nanoparticles: a much greater relative surface area per unit of mass and a prevalence of quantal effects. The first of these factors is responsible for the changes in reactivity, which can increase considerably as particles decrease in size [1, 2]. The second factor which has been observed is that minuscule particles (of size of few nm), induce modifications in terms of optical, electrical, mechanical and magnetic properties [3]. As commercial materials claimed higher performance and need of the hour was to exhibit multiple functions simultaneously, material research moved its target from singular nanomaterials (NMs) to hierarchical ensembles. Such nanoscale conjugates are commonly termed nanohybrids (NHs), which bring together divergent combinations of metals, metalloids and carbon-only nanostructures with unique soft and hard external coatings.

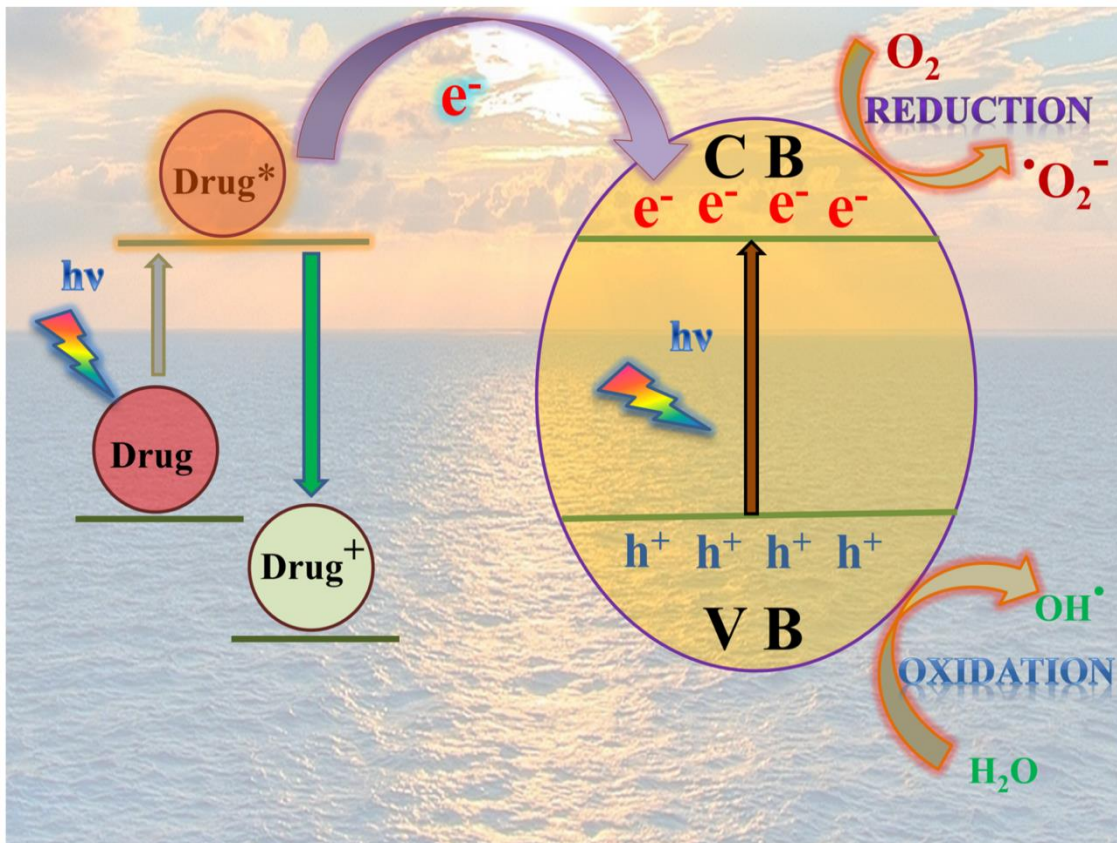
In brief, nanomaterials can be classified in terms of dimensioning of the nanostructures involved. Therefore, quantum dots or nanocrystals, fullerenes, particles, precipitates, colloids and catalysts are restricted to the three-dimensional nanometric domain. Nanotubes, dendrimers, nanowires, fibers and fibrils have two nanometric dimensions, whereas surface coatings, thin films and interfaces have only one nanometric dimension [4].

There are different approaches of synthesis of nanoparticles. Production of nanoparticles can be generally classified into the bottom-up and top-down methods. In the bottom-up approach, construction of nanoparticles occurs by atom by atom or molecule by molecule. The strategies which are employed to produce such materials are namely chemical synthesis, self-assembly and positioning of individual

nanoparticles. Chemical synthesis is well known and allows production of nanoparticles in huge quantities, while positioning of individual nanoparticles requires microscopy methodologies that are very unproductive. Self-assembly attributes to production techniques in which atoms or molecules organize themselves to form an orderly structure on the nanometric scale. In the top-down approach, a large structure is progressively scaled down until nanometric dimensions are reached. The common processes are etching, precision engineering, lithography and grinding approaches. Several of these techniques are routinely used in the electronics industry white rooms, where production and occupational health and safety conditions normally are strictly controlled.

1.3. Photophysics Involved in Drug Sensitization by Nanoparticles:

Semiconductors (e.g., ZnO, TiO₂) can act as sensitizers and can assist in light-induced redox processes due to their electronic structure, which is characterized by a filled valence band and an empty conduction band [5, 6]. As shown in Scheme 1.1, a drug in the proximity of a semiconductor does not undergo the recombination process upon excitation with light. The photoexcited drug (Drug*) transfers the electrons to the conduction band (CB) of the semiconductor. This leads to the creation of photogenerated pair (e⁻/h⁺) in the semiconductor [7, 8]. Excited state conduction-band electrons (e⁻_{CB}) can react with triplet oxygen from the dissolved medium producing reactive oxygen species (ROS). Thus upon light irradiation, the drug molecules attached to the nanoparticle surface can generate more ROS compared to that of the free drug molecules. The enhancement in the ROS generation can essentially increase the overall activity of a drug, thereby reducing the concentration of the essential drug molecules.



Scheme 1.1. Drug Sensitization with Semiconductor Nanoparticles.

1.4. Interaction of Nanoparticles with Cells:

Cell-nanoparticle interactions are often restricted by the low concentration of cells and the lower diffusion kinetics of nanoparticles [9]. However, uptake by white blood cells in the circulation and by resident macrophages in the liver and spleen can effectively remove nanoparticles that have been opsonized, exhibiting epitopes that are recognized by the cells as markers for clearance. The cell surface is rich with proteins and is marginally negative in charge. Like proteins, charged particles associate with cells more rapidly than neutral particles with cationic ones adhering strongly to the anionic

cell membranes [10]. Nanoparticles with higher hydrophobic character also demonstrate faster uptake and association with cells due to the interaction with lipophilic domains of the plasma membrane. In addition, zwitterionic and neutral coatings and hydrophilic flexible polymers minimize the nonspecific associations with cells. Cellular binding and uptake of nanoparticles are highly dependent on whether the nanoparticles have already been fouled by proteins. In fact, this characteristic is abstruse to study as it is unclear whether the binding event is mediated by the targeting protein attached to the nanoparticle or by fouling proteins bound to the nanoparticle and/or targeting ligand. Even for studies in which cell cultures are prepared with media free from exogenous proteins, cells continually secrete their own proteins, which can adsorb to the nanoparticle surface locally at the plasma membrane to facilitate adhesion and uptake. Although nanoparticles that are nearly neutral and resistant to protein fouling usually have upgraded cellular association once they become fouled, it has been observed that charged and/or hydrophobic nanoparticles will exhibit lower cellular association once they are fouled with a protein corona. This lowering of adhesion rates may arise from an electrostatic charge reduction and masking of hydrophobic domains by steric repulsion provided by the proteins. Once fouled, particles may associate with cells through interactions that are more specific, involving epitope binding of the adsorbed protein to its corresponding receptor on the cell membrane. Recent work by Walkey et al. has identified protein corona fingerprints, suggesting that hyaluronan receptors are the major mediators of nanoparticle-cell interactions [10]. Besides cellular targeting, the fate of the nanoparticles within the cells is crucial for drug delivery. Particles generally end intracellularly in endosomes or lysosomes prior to degradation. Chemical characteristics such as surface charge determine the fate of the nanoparticles.

For instance, surface functionalization of gold nanoparticles with PEG results in efficient internalization in endosomes and cytosol, localized in nuclear region [11].

1.5. Scope of the Spectroscopic Studies on the Medicinally Important Molecules with Various Nanoparticles and their Interaction with Different Cell Lines:

Over the past few decades, nanotechnology research has focused on understanding the correlation between the optical, electrical, and magnetic properties of nanomaterials with respect to their size, shape, and surface chemistry [12]. These studies have provided a concrete foundation for engineering nanotechnology-based electronics, computer, and biomedical devices [13]. With the advent of nanotechnology, a cutting-edge research field which studies the interactions of nanomaterials with biological systems, known as nano-bio interactions, has gained importance. Research on the modulated physicochemical properties of medicinally important organic molecules (drugs) has attracted attention in the scientific community as they have wide therapeutic applications to combat various diseases [14-16].

Bioavailabilities of traditional drugs, which are in a class of medicinally significant organic molecules, are found to be a very crucial parameter for their efficacy as medicines. Bioavailability can be broadly defined as the dynamic manner in which a drug and/or its metabolites enter the body to reach the systemic circulation, the site(s) of action, or become released at preabsorption sites into the body [17]. In case of organic molecules, the bioavailability is considerably reduced due to their poor intrinsic permeability across cell membrane. Therapeutic efficacy of such restricted drug dosage is further diminished by factors such as poor pharmacokinetics of the drugs, including limited systemic circulation lifetime, undesirable bio-distribution, non-specific cellular

uptake and poor tumor vascularity that limit drug accession to tumor tissues [15, 18]. In order to improve bioavailability, the physicochemical properties of the drug should be manipulated or innovative drug delivery carrier system should be used [19, 20]. Specifically, the biological activity of redox active drugs relies on two key parameters, namely redox potential/ability of electron transfer and their trans-cellular bioavailability or effective concentration of the drugs in biological cells. Both the parameters are expected to be influenced upon conjugation (sensitization) of the drugs with inorganic and non-toxic nanometer sized particles (nanoparticle). As multiple drug molecules bind to a single nanoparticle, the bioavailability is expected to increase in the cells. Besides, the proximity of the drug to the nanoparticle of various electronic bands would change the electron transfer properties (redox activity) of the drug. There is an efficient transfer of photoexcited electrons from the LUMO of the dye to the conduction band (CB) of the semiconductor which results in generation of augmented reactive oxygen species (ROS). This leads to an increase in antioxidant activity of the drug as well. Hence, these drug nanoformulations (nanohybrid) are superior to conventional medicine with respect to control release, targeted delivery and therapeutic effect [21]. In this respect, the mechanism of drug action and their enhancement upon conjugation with different nanoparticles is within the purview of our studies. Hence, ultrafast spectroscopic technique has been employed which is an ideal tool to address the type of conjugation (covalent/non-covalent), charge transfer, surface coverage and toxicity of the nanocomposites. Consequently, a principal understanding of the mechanisms and dynamics of these ultrafast charge transfer processes is crucial from the viewpoint of developing effective nanomedicine.

The key focus of this thesis is to prepare detailed spectroscopic and microscopic characterizations of various nanohybrids of medicinally important organic molecules

with different inorganic nanoparticles [22]. Within the scope of the thesis, we have also investigated the medicinal activity of the nanohybrids *in vitro*. In one of our studies, we have explored the photoinduced antioxidant activity of a well-known vitamin (B₂) in drug delivery systems like micelles [Sodium dodecyl sulphate (SDS), TritonX-100 (TX-100), Cetyl trimethyl ammonium bromide (CTAB)] and AOT-reverse micelles. Micelles, including polymeric micelle, represent another favorable type of pharmaceutical carrier [23]. They are colloidal dispersions and their particle size ranges within 5 to 50–100 nm. An important property of micelles is their ability to increase the solubility and bioavailability of poorly soluble drugs [13]. In another study, we have synthesized nanohybrids of this vitamin with various nanoparticles such as semiconductor (TiO₂ and ZnO), insulator (Al₂O₃) and metal (Au) nanoparticles through electronic coupling. Interestingly, we observed that the drug conjugated to semiconductor nanoparticles facilitate charge separation which results in enhanced antioxidant activity of the drug. Moreover, the surface modification of nanoparticles has profound effect on the interaction of these particles in cellular milieu as it reduces the toxicity of the nanomaterials. In this regard, in one of our studies, we investigated the efficient reusable photocatalytic activities of tartrate functionalized nanoparticles (T-Fe₃O₄ NPs) which were completely absent in parent nanoparticles with methylene blue (MB). In addition, T-Fe₃O₄ NPs also proved to assist in photodegradation of bilirubin (BR), physiologically important disease marker. We have also attempted to understand the role of a medicinally important drug (caffeine) in prevention of electron transfer from a carcinogen (benzopyrene) in various cell lines. Furthermore, in one of our previous reports, we have explored the photoinduced ultrafast dynamics in a well-known cancer drug, protoporphyrin IX (PP) sensitized with ZnO NPs (PP–ZnO). We successfully confirmed that the PP–ZnO nanohybrid exhibits enhanced activity in

photodynamic therapy (PDT) compared to that of only PP [24]. In the present study, we have synthesized and characterized nanohybrids of another notable cancer drug (Rose Bengal) with zinc oxide nanoparticles which act as efficient drug delivery vehicle. By using a picosecond-resolved Förster resonance energy transfer (FRET) technique, we have demonstrated the role of photoinduced charge transfer from the excited drug to the semiconductor nanoparticles. The characterized nanohybrid upon photo-irradiation has proved to possess antimicrobial as well as cytotoxicity in cancer cells. It is our conviction that, the studies provide potentiality for further research in the development of new generation nanomedicine.

The experimental tools used for studying the dynamical processes involve picosecond -resolved carrier relaxation dynamics, such as, PET (Photoinduced Electron Transfer) and FRET (Föster's Resonance Energy Transfer) or NSET (Nanosurface Energy Transfer). The different experimental techniques employed for the structural and functional characterization of the drugs and their nanoconjugates include steady-state UV-Vis absorption and fluorescence, thermogravimetric analysis (TGA), picosecond-resolved fluorescence spectroscopy, Fourier transform infrared spectroscopy (FTIR), Raman scattering, high-resolution transmission electron microscopy (HRTEM) and fluorescence microscopy. Furthermore, bacterial, fungal and HeLa cell culture techniques are also used to study the biological activities.

1.6. Objective:

Recent years have witnessed innovative growth in the application of the use of nanotechnology in medicine [25, 26]. Nanoparticles sustain interest for medical purposes due to their larger surface to mass ratio than other particles, their quantum properties and their capability of adsorbing and carrying other compounds such as

drugs, probes and proteins [27]. Hence, 'nanomedicine' is synthesized by conjugating many medicinally important drug molecules with a biocompatible nanoparticle which acts as a 'carrier'. These drug-loaded nanoparticles are expected to have improved drug targeting and delivery, better insight on the pathophysiological conditions of a disease, yield more sophisticated diagnostic opportunities and hence crop upgraded therapies.

There are earlier studies which report increased photocatalytic activity in dye due to charge separation upon conjugation with semiconductor nanomaterials [6]. In this regard, the drug activity needs to be explored when it is bound to nanomaterials. Therefore, the key objective of the thesis is to sensitize drug molecules with different nanomaterials, characterize the nanohybrids employing various spectroscopic techniques and to investigate the modified physiochemical properties of the drug. There are some medicinally important organic drugs which are well-known as photosensitizers. Beneficial as well as adverse effects of light have been known since aeon, and visible-light has always been used for many therapeutic purposes. However, the transference of basic comprehension into mechanism and dynamics of drug sensitization would be imperative for the practical utilization of designing photodynamic therapeutic agents, which will be one of the motives of this thesis. In one of our studies, we have sensitized vitamin B₂ (common name: riboflavin) with 'photons' and demonstrated the photoinduced antioxidant activity [23]. This water-soluble vitamin is an endogenous photosensitizer which is found in food of both vegetable and animal origin [28-30]. It is the prosthetic group in the many flavine oxidoreductase enzymes which is vital for cellular metabolism in human beings [31-33]. It has a dual nature of being a well-known antioxidant as well as generating several toxic products upon light-exposure [34-37]. Although the antioxidant property of this vitamin is well recognized in dark, to the best of our knowledge, no effort has been

made to detect the antioxidant activity under visible light irradiation. We have investigated antioxidant activity of this drug in various physiologically relevant environments such as micelles and reverse micelles. In this regard, small biomimetic systems including nanoscopic micelles could serve as a suitable mimic for the biological membranes, macromolecules and are also useful in organizing the reactants at a molecular level [38].

Diet derived antioxidants are essential for our health and well-being due to inadequacy of autogenously present antioxidant defenses (such as superoxide dismutases, H₂O₂-removing enzymes and metal binding proteins). The basic *in vivo* role of an antioxidant is to scavenge reactive oxygen species (ROS) and reactive nitrogen species (RNS) which cause damage to DNA, lipids, proteins, and other biomolecules [39]. Hence, enhancing the antioxidant property of a drug can help to overcome many challenges in treatment of various diseases. In another study, we have sensitized this vitamin with various nanoparticles such as metal, semiconductor and insulator [22]. Fascinatingly, we observed a dramatic increase in the antioxidant activity of the semiconductor nanohybrids, no change in case of insulator and decreased activity in gold nanohybrids. The study will provide a mechanistic explanation for the ultrafast excited state electron migration as well as deactivation considering every single aspect of the quenching mechanisms, namely PET, FRET and NSET from the host vitamin to the nanoparticles. Based on these techniques, the donor-acceptor distance for gold nanoparticles has been reported and the phenomenon of NSET predominates over FRET. In this regard, spectroscopy has emerged as a useful tool for nanohybrid characterization and exploration of ultrafast charge or energy transfer processes.

Magnetic nanoparticles, as crucial division of nanomaterials, are accelerating exciting advancement in various fields especially in biomedical engineering. For instance, magnetic nanoparticles are used as negative contrast agents for MR imaging and their heat effect was utilized in cancerous hyperthermia. The unique sizes of nanoparticles are amenable to surface functionalization or modification in order to achieve required traits [21]. The stability and monodispersity of the nanoparticles need to be improved for applications in biological systems. Surface modification becomes necessary when hydrophobic surface capping agents are used in the synthesis of particles. It is desirable that the functionalized particles retain their electrical, optical and magnetic properties while having improved stability, potential for further conjugation to achieve required hydrophilicity for solvent compatibility. The general strategy for modification or functionalization of nanoparticles depends on the specific atomic structures of the surfaces and their interactions with ligands. Nanoparticles with capped groups on their surfaces can be modified with organic or inorganic molecules, regardless of whether they are synthesized in aqueous or non-hydrolytic solutions. The hydroxyl group is one of the commonly used functional groups for capping as it can react with carboxyl groups via its oxygen atom or with various silane groups through -O-Si bond [40]. In one of our works, we have used top-down fabrication methodology to modify a model ferrofluid with parent NPs of ~23 nm size, using tartrate as a functionalizing ligand as well as solubilizing agent [41]. The size was reduced to 5 nm by the process of 'core etching'. This tartrate functionalized Fe₃O₄ NPs (T-Fe₃O₄) proved to be fluorescent and possess reusable photocatalytic activities with methylene blue which is a model cationic dye. Moreover, photodegradation of bilirubin (BR), a bio-medically important jaundice marker, was also observed with these particles.

Since time immemorial, natural products have played a very significant role in health care and prevention of diseases. Nevertheless, it was not until the nineteenth century that scientists isolated active components from various plants in order to screen them for medicinal purposes. Among various plant alkaloids, caffeine is the most commonly consumed drugs in the world which has drawn attention in the field of modern research [42, 43]. There are previous studies on interaction of this xanthine alkaloid with several DNA intercalating and cancer inducing agents such as doxorubicin (DOX), ethidium bromide (EtBr), acridine orange (AO) [43-45]. Caffeine also solubilizes benzo[a]pyrene (BP) which a class of polycyclic aromatic hydrocarbons (PAHs), in aqueous phase. BP is a potent carcinogen as it induces DNA damage by producing double strand breaks in DNA involving electron transfer (ET) mechanism under UV-irradiation [45]. In one of our investigations, we emphasized the caffeine-mediated inhibition of ET from BP to DNA under UVA radiation employing picosecond resolved emission spectroscopic studies [46]. These findings suggest that caffeine plays a pivotal role in removal of carcinogens and has possibility of cancer prevention.

Photodynamic therapy (PDT) is now a well prominent technique for clinical treatment in various diseases, including cancer and especially for the treatment of superficial tumours (e.g. in oesophagus, bladder, melanoma) [47]. This treatment involves the localized administration of a photosensitizer. After a predefined time-interval to allow the photosensitizer to accumulate in the tumour tissue, the irradiation of the tumour site with non-thermal light leads to the formation of an excited photosensitizer. The concerted action of the excited triplet photosensitizer and molecular oxygen results in the evolution of singlet oxygen (1O_2), which is thought to be the main mediator of cellular death induced by PDT. Cytotoxicity is generated due

to overproduction of ROS in cells which results in inducing oxidative stress and so normal physiological redox-regulated functions are impaired [48]. Among the semiconductor nanoparticles, ZnO nanoparticles (ZnO NPs) perform better in biomedical applications as competent drug delivery vehicle due to their low-cost and minimal toxicity. The nanocomposites can be prepared either by ZnO NPs loaded with drugs or ZnO hollow spheres containing drugs as they are capable of penetrating cancer cells through specific ligand–receptor recognition or nonspecific binding forces based on hydrophobic or coulombic interactions [49]. In one of our studies, we have illustrated an enhanced photodynamic therapeutic activity of Rose Bengal (RB) upon conjugation with ZnO NPs. RB is a potent photosensitizer and there are substantial studies which report the cytotoxicity of this drug when irradiated with green light [50-52]. However, we have demonstrated the increased production of ROS with RB-ZnO nanohybrids. We have validated the *in vitro* toxicity results in various cell lines. The result of these studies of drug sensitized nanoparticles could be incorporated in designing more effective photodynamic therapeutic agents to benefit human health. The studies are important in the context that the interaction of NPs with medically important molecules has emerged as a key parameter in nanomedicine and the present work may find its application in nanotoxicology.

1.7. Summary of the Work Done:

I. Photo-Sensitization of Medically Important Drugs:

A. Vitamin B₂ in Nanoscopic Environments under Visible Light: Photosensitized Antioxidant or Phototoxic Drug? [23]:

Vitamin B₂ is a conventional antioxidant (in dark) since its discovery in 1926. Effect of visible light on vitamin B₂-containing food has a long history of scientific investigation.

While photodegradation of the vitamin producing several photoproducts is evident in certain experimental conditions, phototoxicity revealing an additional oxidative stress in the medium is also clear from some reports. Here we report photosensitized antioxidant effect of the vitamin, which is found to be more than two orders of magnitude efficient than that in dark condition. The photoinduced antioxidant property is apparently paradoxical compared to the reported phototoxic effect of the vitamin. Our present study unravels a unified picture underlying in the difference in character of vitamin B₂ under visible light irradiation. UV-Vis absorption and fluorescence studies in a number of physiologically relevant nanoscopic environments (micelles and reverse micelles) reveal the antioxidant activity of a well-known oxidative stress marker 2,2-diphenyl-1-picrylhydrazyl (DPPH) as well as phototoxicity effect resulting in self-degradation of the vitamin. Picosecond-resolved Förster Resonance Energy Transfer (FRET) from the vitamin to the marker DPPH in the biomimetic environments clearly reveals the role of proximity of an oxidizing agent in the photoinduced effect of the vitamin. Our systematic and detailed studies unravel a simple picture of the mechanistic pathway of the photosensitized vitamin in the physiologically important environments leading to antioxidant/ phototoxicity effect of the vitamin. The excited vitamin transfers its electron to the oxidizing agent in proximity for the antioxidant effect, otherwise it employs oxygen to generate reactive oxygen species (ROS) resulting in phototoxicity/self-degradation.

II. Sensitization of Medicinally Important Drugs with Inorganic Nanoparticles:

A. Sensitization of an Endogenous Photosensitizer: Electronic Spectroscopy of Riboflavin in the Proximity of Semiconductor, Insulator and Metal Nanoparticles [22]:

In this study, we have synthesized nanohybrids of Riboflavin (Rf) with a number of inorganic nanoparticles (NPs); namely zinc oxide (ZnO), titanium dioxide (TiO₂), aluminium oxide (Al₂O₃) and gold NPs of similar sizes. While high resolution transmission electron microscopy (HRTEM) confirms integrity and sizes of the NPs, intactness of the molecular structure of the drug Rf is revealed from absorption and steady-state emission spectra of the drug in the nanohybrid. Raman spectroscopy on the nanohybrids shows the nature of molecular complexation of the drug with the inorganic NPs. For the semiconductor and insulator NPs, the complexation is found to be non-covalent, however, a covalent attachment of the drug with the dangling bonds of metal atoms at the surface is observed. In order to investigate antioxidant activity of the nanohybrids, we have performed 2, 2-diphenyl-1-picrylhydrazyl (DPPH) assay of the nanohybrids in dark as well as under blue light irradiation. Whereas change of the antioxidant activity of the nanohybrids with respect to free riboflavin in the absence of light is observed to be insignificant, a drastic change in the activity in the case of TiO₂ and ZnO in presence of light is evident. No change in the case of Al₂O₃ and a significant decrease in the antioxidant activity for gold nanohybrids are also remarkable. Picosecond-resolved fluorescence studies on the nanohybrids reveal a molecular picture of the differential antioxidant activities. An ultrafast photoinduced electron transfer from Rf to ZnO and TiO₂ are clearly evident from the corresponding fluorescence transients. We have compared the picosecond-resolved transients with that of Rf in presence of a well-known electron acceptor benzoquinone (BQ) and found similar time scales. No temporal change in the fluorescence transient of riboflavin in Al₂O₃ nanohybrids compared to that of free Rf is observed indicating uneventful excited state relaxation of the nanohybrids. Nanosurface energy transfer (NSET) over Förster resonance energy transfer (FRET) is found to be the prevailing de-excitation

mechanism in the case of gold nanohybrids, because of the strong spectral overlap between Rf emission and surface plasmon absorption of the gold NPs. Different excited state mechanisms as revealed from our studies are expected to be useful for the design of NP-sensitized drugs, which are reported sparsely in the literature.

III. Surface Modification of Nanoparticles using Medicinally Important Ligands:

A. Surface Engineering for Controlled Nanocatalysis: Key Dynamical Events from Ultrafast Electronic Spectroscopy [41]:

Surface engineering of various nanoparticles (NPs) is of growing interest and an important step to induce/control optical and/or catalytic activities. Although a wide variety of biomedical applications of magnetic Fe₃O₄ NPs in diagnostics as well as therapeutics are well documented, the optical properties of the NPs still remain less well studied. Here we report a top-down fabrication methodology to modify a model ferrofluid with parent NPs sizes ~23 nm, using tartrate as a functionalizing ligand as well as solubilizing agent. The surface engineering involves ‘ligand exchange’, and simultaneous ‘phase transfer’ of Fe₃O₄ NPs (size ~23 nm) from chloroform to water along with subsequent ‘core etching’, resulting in a reduction of particle diameter to ~5 nm. We demonstrate that tartrate functionalized Fe₃O₄ NPs (T-Fe₃O₄) exhibit ligand to metal charge transfer transition in the UV spectral region, excellent blue luminescence and efficient reusable photocatalytic activities which are completely absent in the parent NPs. We have used the functionalized NPs for the photodegradation of biomedically important jaundice marker bilirubin in aqueous solution. The surface adsorption of Mn ions on the surface of the T-Fe₃O₄ NPs enables to control the degradation under UV light illumination. While the Mn-adsorbed T-Fe₃O₄ NPs can efficiently degrade bilirubin in dark condition, the activity is significantly reduced

under UV light. Finally, the detailed photocatalytic mechanism associated with ultrafast charge and energy transfer process has been discussed. We believe that bilirubin degradation rate can be controlled under UV light by varying Mn-ion concentration on the surface of NPs which can be a significant advancement for bilirubin degradation study. Overall, the results represent a promising route for the fabrication of Fe₃O₄ NPs adaptable to diverse applications.

IV. Mechanism of Photo-sensitized Carcinogenic Cell Damage by a Food Carcinogen in Various Cell Lines and Protective Role of a Medicinally Important Molecule:

A. Ultrafast Spectroscopic Study on Caffeine Mediated Dissociation of Mutagenic Ethidium from Synthetic DNA and Various Cell Nuclei [46]:

Electron transfer (ET) reactions are important for their implications in both oxidative and reductive DNA damages. The current contribution investigates the efficacy of caffeine, a xanthine alkaloid in preventing UVA radiation induced ET from a carcinogen, benzo[a]pyrene (BP) to DNA by forming stable caffeine-BP complexes. While steady-state emission and absorption results emphasize the role of caffeine in hosting BP in aqueous medium, the molecular modeling studies propose the energetically favorable structure of caffeine-BP complex. The picosecond resolved emission spectroscopic studies precisely explore the caffeine-mediated inhibition of ET from BP to DNA under UVA radiation. The potential therapeutic activity of caffeine in preventing DNA damage has been ensured by agarose gel electrophoresis. Furthermore, time gated fluorescence microscopy has been used to monitor caffeine mediated exclusion of BP from various cell lines including squamous epithelial cells, WI-38 (fibroblast), MCF-7 (breast cancer) and HeLa (cervical cancer) cells. Our *in*

vitro as well as *ex vivo* experimental results provide imperative evidences about the role of caffeine in modified biomolecular recognition of a model carcinogen BP by DNA resulting dissociation of the carcinogen from various cell lines, implicating its potential medicinal applications in the prevention of other toxic organic molecule induced cellular damages.

V. Nanoparticle-sensitization of Photodynamic Drugs for Cancer Therapy:

A. Photoinduced Dynamics and Toxicity of a Cancer Drug in Proximity of Inorganic Nanoparticles under Visible Light [53]:

Drug sensitization with various inorganic nanoparticles (NPs) has proved to be a promising and an emergent concept in the field of nanomedicine. Rose Bengal (RB), a notable photosensitizer, triggers the formation of ROS under green light irradiation and consequently it induces cytotoxicity and cell death. In the present study, the effect of photoinduced dynamics of RB upon complexation with semiconductor zinc oxide NPs. has been explored. To accomplish this, we have successfully synthesized nanohybrids of RB with ZnO NPs of particle size of 24 nm and optically characterized them. The uniform size and integrity of the particles were confirmed by high resolution transmission electron microscopy (HRTEM). UV-Vis absorption and steady-state fluorescence studies reveal the formation of the nanohybrid. Ultrafast picosecond-resolved fluorescence studies of RB–ZnO nanohybrids demonstrate an efficient electron transfer from the photoexcited drug to the semiconductor NPs. Picosecond-resolved Förster Resonance Energy Transfer (FRET) from ZnO NPs to RB unravel the proximity of the drug to the semiconductor at the molecular level. The photoinduced ROS formation has been monitored using Dichlorofluorescein (DCFH) oxidation assay, which is a conventional oxidative stress indicator. It is observed that the ROS

generation under green light illumination is greater in low concentration of RB-ZnO nano hybrids compared to free RB. Substantial photodynamic activity of the nano hybrid in bacterial and fungal cell lines validated the *in vitro* toxicity results. Furthermore, the cytotoxic effect of the nano hybrids in HeLa cells which was monitored by MTT assay is also noteworthy.

1.8. Plan of Thesis:

The plan of the thesis is as follows:

Chapter 1: This chapter gives a brief introduction to the scope and motivation behind the thesis work. A brief summary of the work done is also included in this chapter.

Chapter 2: This chapter provides an overview of the dynamical and steady-state tools, the structural aspects of biologically important systems (micelles, reverse micelles, DNAs) and probes used in the research.

Chapter 3: Details of instrumentation, data analysis and experimental procedures have been discussed in this chapter.

Chapter 4: In this chapter, photoinduced antioxidant activities of Vitamin B₂ in various nanoscopic environments were reported. A new mechanistic pathway was suggested where the excited vitamin quenches the free radical DPPH without being facilitated by the reactive oxygen species prior to electron transfer.

Chapter 5: In this chapter, we report synthesis and characterization of nano hybrids of Vitamin B₂. Antioxidant activities of semiconductor nano hybrids increase over control under light irradiation. The phenomenon of ultrafast photoinduced electron transfer occurs from photoexcited Rf to ZnO and TiO₂ whereas NSET predominates over FRET in case of Rf-AuNPs.

Chapter 6: In this chapter, surface modification by top-down fabrication methodology of a model ferrofluid with of ~23 nm sizes is discussed. Here, tartrate is used as a

functionalizing ligand as well as solubilizing agent. Tartrate functionalized Fe_3O_4 nanoparticles (T- Fe_3O_4 NPs) exhibit ligand to metal charge transfer transition in the UV spectral region, excellent blue luminescence and efficient reusable photocatalytic activities, which are completely absent in the parent nanoparticles.

Chapter 7: In this chapter, the role of caffeine in the prevention of UVA radiation induced ET from a carcinogen; benzo[a]pyrene (BP) to DNA by forming stable caffeine-BP complexes is elucidated. It has a role in modified biomolecular recognition of BP by DNA resulting in the dissociation of the carcinogen from various cell lines.

Chapter 8: In this chapter, nanohybrids of Rose Bengal, a notable cancer drug with ZnO nanoparticles were synthesized and characterized. DCFH oxidation demonstrates enhanced ROS generation in RB-ZnO compared to free RB. Antimicrobial and cytotoxicity assays using various cell lines confirm the *in vitro* toxicity results.

References:

- [1] A.T. Bell, The Impact of Nanoscience on Heterogeneous Catalysis, *Science*, 299 (2003) 1688-1691.
- [2] Y. Dai, Y. Wang, B. Liu, Y. Yang, Metallic Nanocatalysis: An Accelerating Seamless Integration with Nanotechnology, *Small*, 11 (2015) 268-289.
- [3] Nanoscience and Nanotechnologies: Opportunities and Uncertainties, Royal Society, 2004.
- [4] C. Ostiguy, G. Lapointe, L. Ménard, Y. Cloutier, M. Trottier, M. Boutin, M. Antoun, C. Normand, Nanoparticles Actual Knowledge about Occupational Health and Safety Risks and Prevention Measures, (2006).
- [5] M.R. Hoffmann, S.T. Martin, W. Choi, D.W. Bahnemann, Environmental Applications of Semiconductor Photocatalysis, *Chem. Rev.*, 95 (1995) 69-96.
- [6] D. Ravelli, D. Dondi, M. Fagnoni, A. Albini, Photocatalysis. A Multi-faceted Concept for Green Chemistry, *Chem. Soc. Rev.*, 38 (2009) 1999-2011.
- [7] M. Mansoob, Metal oxides as photocatalysts, *J. Saudi Chem. Soc.*, 19 (2015) 462–464.
- [8] S. Sarkar, A. Makhal, T. Bora, K. Lakhsman, A. Singha, J. Dutta, S.K. Pal, Hematoporphyrin–ZnO Nanohybrids: Twin Applications in Efficient Visible-Light Photocatalysis and Dye-Sensitized Solar Cells, *ACS Appl. Mater. Interfaces*, 4 (2012) 7027-7035.
- [9] L.A. Lane, X. Qian, A.M. Smith, S. Nie, Physical Chemistry of Nanomedicine: Understanding the Complex Behaviors of Nanoparticles in Vivo, *Annu. Rev. Phys. Chem.*, 66 (2015) 521-547.
- [10] E.C. Cho, J. Xie, P.A. Wurm, Y. Xia, Understanding the Role of Surface Charges in Cellular Adsorption versus Internalization by Selectively Removing Gold Nanoparticles on the Cell Surface with a I₂/KI Etchant, *Nano Lett.*, 9 (2009) 1080-1084.
- [11] W.H. De Jong, P.J.A. Borm, Drug delivery and Nanoparticles: Applications and Hazards, *Int. J. Nanomedicine*, 3 (2008) 133-149.
- [12] R.A. Petros, J.M. DeSimone, Strategies in the Design of Nanoparticles for Therapeutic Applications, *Nat. Rev. Drug Discov.*, 9 (2010) 615-627.
- [13] V.P. Torchilin, Recent Approaches to Intracellular Delivery of Drugs and DNA and Organelle Targeting, *Annu. Rev. Biomed. Eng.*, 8 (2006) 343-375.

- [14] J.B. Hall, M.A. Dobrovolskaia, A.K. Patri, S.E. McNeil, Characterization of Nanoparticles for Therapeutics, *Nanomedicine*, 2 (2007) 789-803.
- [15] T.S. Hauck, S. Giri, Y. Gao, W.C. Chan, Nanotechnology Diagnostics for Infectious Diseases Prevalent in Developing Countries, *Adv. Drug Deliv. Rev.*, 62 (2010) 438-448.
- [16] M.E. Davis, Z. Chen, D.M. Shin, Nanoparticle Therapeutics: An Emerging Treatment Modality for Cancer, *Nat. Rev. Drug Discov.*, 7 (2008) 771-782.
- [17] V.F. Smolen, Bioavailability and Pharmacokinetic Analysis of Drug Responding Systems, *Annu. Rev. Pharmacol. Toxicol.*, 18 (1978) 495-522.
- [18] J.W. Rasmussen, E. Martinez, P. Louka, D.G. Wingett, Zinc Oxide Nanoparticles for Selective Destruction of Tumor Cells and Potential for Drug Delivery Applications, *Expert Opin. Drug Deliv.*, 7 (2010) 1063-1077.
- [19] J.S. Walsh, G.T. Miwa, Bioactivation of Drugs: Risk and Drug Design, *Annu. Rev. Pharmacol.*, 51 (2011) 145-167.
- [20] P. Fasinu, V. Pillay, V.M. Ndesendo, L.C. du Toit, Y.E. Choonara, Diverse Approaches for the Enhancement of Oral Drug Bioavailability, *Biopharm Drug Dispos.*, 32 (2011) 185-209.
- [21] A. Kumari, S.K. Yadav, S.C. Yadav, Biodegradable Polymeric Nanoparticles Based Drug Delivery Systems, *Coll. Surf. B*, 75 (2010) 1-18.
- [22] S. Chaudhuri, S. Sardar, D. Bagchi, S.S. Singha, P. Lemmens, S.K. Pal, Sensitization of an Endogenous Photosensitizer: Electronic Spectroscopy of Riboflavin in the Proximity of Semiconductor, Insulator, and Metal Nanoparticles, *J. Phys. Chem. A*, 119 (2015) 4162-4169.
- [23] S. Chaudhuri, S. Batabyal, N. Polley, S.K. Pal, Vitamin B₂ in Nanoscopic Environments under Visible Light: Photosensitized Antioxidant or Phototoxic Drug?, *J. Phys. Chem. A*, 118 (2014) 3934-3943.
- [24] S. Sardar, S. Chaudhuri, P. Kar, S. Sarkar, P. Lemmens, S.K. Pal, Direct Observation of Key Photoinduced Dynamics in a Potential Nano-Delivery Vehicle of Cancer Drugs., *Phys. Chem. Chem. Phys.*, 17 (2015) 166-177.
- [25] B. Mishra, B.B. Patel, S. Tiwari, Colloidal Nanocarriers: A Review on Formulation Technology, Types and Applications Toward Targeted Drug Delivery., *Nanomedicine*, 6 (2010) 9-24.

- [26] L. Zhang, F.X. Gu, J.M. Chan, A.Z. Wang, R.S. Langer, O.C. Farokhzad, Nanoparticles in Medicine: Therapeutic Applications and Developments, *Clin. Pharmacol. Ther.*, 83 (2008) 761-769.
- [27] W.H. De Jong, P.J. Borm, Drug Delivery and Nanoparticles: Applications and Hazards, *Int. J. Nanomedicine*, 3 (2008) 133-149.
- [28] D.R. Cardoso, S.H. Libardi, L.H. Skibsted, Riboflavin as a Photosensitizer. Effects on Human Health and Food Quality, *Food Funct.*, 3 (2012) 487-502.
- [29] R. Huang, H.J. Kim, D.B. Min, Photosensitizing Effect of Riboflavin, Lumiflavin, and Lumichrome on the Generation of Volatiles in Soy Milk, *J. Agric. Food. Chem.*, 54 (2006) 2359-2364.
- [30] G.V. Ferrari, M.P. Montaña, F.C.D. Dimarco, N.B.P.a. Debattista, N.A.G. Walter A. Massad b, A Comparative Photochemical Study on the Behavior of 3,30-dihydroxyflavone and its Complex with La(III) as Generators and Quenchers of Reactive Oxygen Species, *J. Photochem. Photobiol. B: Biology*, 124 (2013) 42-49.
- [31] M.M. Wolf, C. Schumann, R. Gross, T. Domratcheva, R. Diller, Ultrafast Infrared Spectroscopy of Riboflavin: Dynamics, Electronic Structure, and Vibrational Mode Analysis, *J. Phys. Chem. B*, 112 (2008) 13424-13432.
- [32] A. Saha, A.K. Mukherjee, Spectroscopic and Thermodynamic Study of Charge Transfer Interaction of Doxycycline Hydrochloride with Riboflavin in Aqueous Ethanol Media of Varying Compositions, *J. Phys. Chem. B*, 108 (2004) 18988-18992.
- [33] S.L.J. Tan, R.D. Webster, Electrochemically Induced Chemically Reversible Proton-Coupled Electron Transfer Reactions of Riboflavin (Vitamin B₂), *J. Am. Chem. Soc.*, 134 (2012) 5954-5964.
- [34] G. McNeill, X. Jia, L.J. Whalley, H.C. Fox, J. Corley, A.J. Gow, C.E. Brett, J.M. Starr, I.J. Deary, Antioxidant and B Vitamin Intake in Relation to Cognitive Function in Later Life in the Lothian Birth Cohort 1936, *Eur. J. Clin. Nutr.*, 65 (2011) 619-626.
- [35] H. Ciliberto, M. Ciliberto, A. Briend, P. Ashorn, D. Bier, M. Manary, Antioxidant Supplementation for the Prevention of Kwashiorkor in Malawian Children: Randomised, Double Blind, Placebo Controlled Trial, *BMJ*, 330 (2005) 1109.
- [36] R.R. Williams, V.H. Cheldelin, Destruction of Riboflavin by Light, *Science*, 96 (1942) 22-23.
- [37] A.W. Galston, R.S. Baker, Inactivation of Enzymes by Visible Light in the Presence of Riboflavin, *Science*, 109 (1949) 485-486.

- [38] N.J. Turro, M. Grätzel, A.M. Braun, Photophysical and Photochemical Processes in Micellar Systems, *Angew. Chem. Intern. Ed.*, 19 (1980) 675-696.
- [39] B. Halliwell, Antioxidants in Human Health and Disease, *Annu. Rev. Nutr.*, 16 (1996) 33-50.
- [40] S. Peng, S. Sun, Synthesis and Characterization of Monodisperse Hollow Fe₃O₄ Nanoparticles, *Angew. Chem. Int. Ed.*, 46 (2007) 4155-4158.
- [41] N. Goswami, S. Chaudhuri, A. Giri, P. Lemmens, S.K. Pal, Surface Engineering for Controlled Nanocatalysis: Key Dynamical Events from Ultrafast Electronic Spectroscopy, *J. Phys. Chem. C*, 118 (2014) 23434-23442.
- [42] C.P. Selby, A. Sancar, Molecular Mechanisms of DNA Repair Inhibition by Caffeine, *Proc. Natl. Acad. Sci. U.S.A.*, 87 (1990) 3522-3525.
- [43] R.W. Larsen, R. Jasuja, R.K. Hetzler, P.T. Muraoka, V.G. Andrada, D.M. Jameson, Spectroscopic and Molecular Modeling Studies of Caffeine Complexes with DNA Intercalators, *Biophys. J.*, 70 (1996) 443-452.
- [44] D.B. Davies, D.A. Veselkov, L.N. Djimant, A.N. Veselkov, Heteroassociation of Caffeine and Aromatic Drugs and their Competitive Binding with a DNA Oligomer., *Eur. Biophys. J.*, 30 (2001) 354-366.
- [45] J.R. Mercer, K. Gray, N. Figg, S. Kumar, M.R. Bennett, The Methyl Xanthine Caffeine Inhibits DNA Damage Signaling and Reactive Species and Reduces Atherosclerosis in ApoE^{-/-} Mice, *Arterioscler. Thromb. Vasc. Biol.*, 32 (2012) 2461-2467.
- [46] S. Banerjee, S. Chaudhuri, A.K. Maity, P. Saha, S.K. Pal, Role of Caffeine in DNA Recognition of a Potential Food-Carcinogen Benzo[a]pyrene and UVA Induced DNA Damage, *J. Mol. Recogn.*, 27 (2014) 510-520.
- [47] D. Bechet, P. Couleaud, C. Frochot, M.L. Viriot, F. Guillemin, M. Barberi-Heyob, Nanoparticles as Vehicles for Delivery of Photodynamic Therapy Agents, *Trends Biotechnol.*, 26 (2008) 612-621.
- [48] P.P. Fu, Q. Xia, H.-M. Hwang, P.C. Ray, H. Yu, Mechanisms of Nanotoxicity: Generation of Reactive Oxygen Species, *J. Food Drug Anal.*, 22 (2014) 64-75.
- [49] H.-M. Xiong, ZnO Nanoparticles Applied to Bioimaging and Drug Delivery, *Adv. Mat.*, 25 (2013) 5329-5335.
- [50] E. Panzarini, V. Inguscio, L. Dini, Timing the Multiple Cell Death Pathways Initiated by Rose Bengal Acetate Photodynamic Therapy, *Cell Death Dis.*, 2 (2011) e169.

- [51] S.S. Mohideen, Y. Yamasaki, Y. Omata, L. Tsuda, Y. Yoshiike, Nontoxic Singlet Oxygen Generator as a Therapeutic Candidate for Treating Tauopathies, *Sci. Rep.*, 5 (2015).
- [52] L. Dini, V. Inguscio, B. Tenuzzo, E. Panzarini, Rose Bengal Acetate Photodynamic Therapy-Induced Autophagy, *Cancer Biol. Ther.*, 10 (2010) 1048-1055.
- [53] S. Chaudhuri, S. Sardar, D. Bagchi, S. Dutta, S. Debnath, P. Saha, P. Lemmens, S.K. Pal, Photoinduced Dynamics and Toxicity of a Cancer Drug in Proximity of Inorganic Nanoparticles under Visible Light, *Chem. Phys. Chem.*, 17 (2016) 270-277.

Chapter 2

An Overview of Steady-State, Dynamical, Theoretical Tools and Systems

In order to investigate the ultrafast processes involved in the studies on chemically and biologically relevant aqueous/non-aqueous environments, different steady-state and dynamical tools have been employed. These include, Förster resonance energy transfer (FRET), P(r) distribution from FRET, Nanosurface energy transfer (NSET) and photoinduced electron transfer (PET). In this chapter, we have included a brief discussion about the above mentioned tools. Overviews of the various systems and the fluorescent probes used in the studies have also been provided.

2.1. Steady-State and Dynamical Tools:

2.1.1. Förster Resonance Energy Transfer (FRET): FRET is an electrodynamic phenomenon involving the non-radiative transfer of the excited state energy from the donor dipole (D) to an acceptor dipole (A) in the ground state (Figure 2.1.a). FRET has got wide applications in all fluorescence applications including medical diagnostics, DNA analysis and optical imaging. Since FRET can measure the size of a protein molecule or the thickness of a membrane, it is also known as “spectroscopic ruler” [1]. FRET is very often used to measure the distance between two sites on a macromolecule. Basically,

FRET is of two types: (a) Homo-molecular FRET and (b) Hetero-molecular FRET. In the former case the same fluorophore acts both as energy donor and acceptor, while in the latter case two different molecules act as donor and acceptor.

Each donor-acceptor (D-A) pair participating in FRET is characterized by a distance known as Förster distance (R_0) i.e., the D-A separation at which energy transfer is 50% efficient. The R_0 value ranges from 20 to 60 Å. The rate of resonance energy transfer (k_T) from donor to an acceptor is given by [2],

$$k_T = \frac{1}{\tau_D} \left(\frac{R_0}{r} \right)^6 \quad (2-1)$$

where τ_D is the lifetime of the donor in the absence of acceptor and r is the donor to acceptor (D-A) distance. The rate of transfer of donor energy depends upon the extent of overlap of the emission spectrum of the donor with the absorption spectrum of the acceptor ($J(\lambda)$), the quantum yield of the donor (Q_D), the relative orientation of the donor and acceptor transition dipoles (κ^2) and the distance between the donor and acceptor molecules (r) (Figure 2.1.b). In order to estimate FRET efficiency of the donor and hence to determine distances between donor-acceptor pairs, the methodology described below is followed [2]. R_0 is given by,

$$R_0 = 0.211 [\kappa^2 n^{-4} Q_D J(\lambda)]^{1/6} \text{ (in Å)} \quad (2-2)$$

where n is the refractive index of the medium, Q_D is the quantum yield of the donor and $J(\lambda)$ is the overlap integral. κ^2 is defined as,

$$\kappa^2 = (\cos \theta_T - 3 \cos \theta_D \cos \theta_A)^2 = (\sin \theta_D \sin \theta_A \cos \phi - 2 \cos \theta_D \cos \theta_A)^2 \quad (2-3)$$

where θ_T is the angle between the emission transition dipole of the donor and the absorption transition dipole of the acceptor, θ_D and θ_A are the angles between these dipoles

and the vector joining the donor and acceptor and ϕ is angle between the planes of the

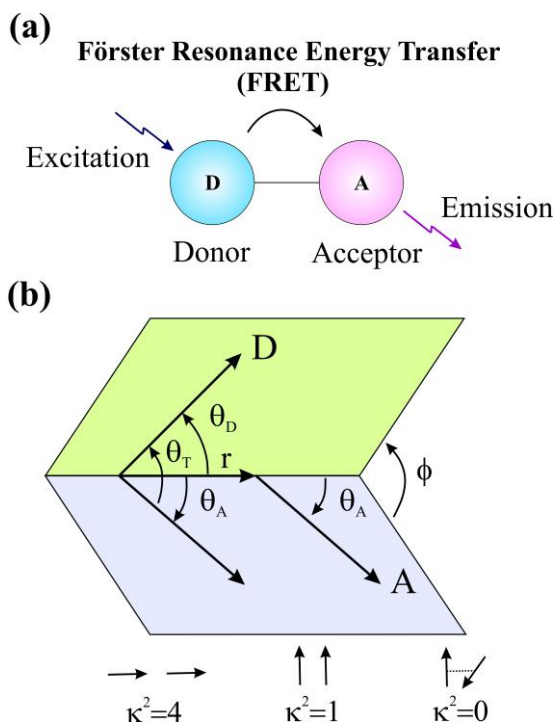


Figure 2.1. (a) Schematic illustration of the Förster resonance energy transfer (FRET) process. (b) Dependence of the orientation factor κ^2 on the directions of the emission and absorption dipoles of the donor and acceptor, respectively.

donor and acceptor (Figure 2.1.b). κ^2 value can vary from 0 to 4. For collinear and parallel transition dipoles, $\kappa^2=4$; for parallel dipoles, $\kappa^2=1$; and for perpendicularly oriented dipoles, $\kappa^2=0$. For donor and acceptors that randomize by rotational diffusion prior to energy transfer, the magnitude of κ^2 is assumed to be $2/3$. However, in systems where there is a definite site of attachment of the donor and acceptor molecules, to get physically relevant results, the value of κ^2 has to be estimated from the angle between the donor emission and acceptor absorption dipoles [3]. $J(\lambda)$, the overlap integral, which expresses the degree of spectral overlap between the donor emission and the acceptor absorption, is given by,

$$J(\lambda) = \frac{\int_0^{\infty} F_D(\lambda) \varepsilon_A(\lambda) \lambda^4 d\lambda}{\int_0^{\infty} F_D(\lambda) d\lambda} \quad (2-4)$$

where $F_D(\lambda)$ is the fluorescence intensity of the donor in the wavelength range of λ to $\lambda+d\lambda$ and is dimensionless. $\varepsilon_A(\lambda)$ is the extinction coefficient (in $M^{-1}cm^{-1}$) of the acceptor at λ . If λ is in nm, then $J(\lambda)$ is in units of $M^{-1}cm^{-1}nm^4$.

Once the value of R_0 is known, the efficiency of energy transfer can be calculated. The efficiency of energy transfer (E) is the fraction of photons absorbed by the donor which are transferred to the acceptor and is defined as,

$$E = \frac{k_T(r)}{\tau_D^{-1} + k_T(r)} \quad (2-5)$$

or

$$E = \frac{R_0^6}{r^6 + R_0^6} \quad (2-6)$$

The transfer efficiency is measured using the relative fluorescence intensity of the donor, in absence (F_D) and presence (F_{DA}) of the acceptor as,

$$E = 1 - \frac{F_{DA}}{F_D} \quad (2-7a)$$

For D-A systems decaying with multiexponential lifetimes, E is calculated from the amplitude weighted lifetimes $\langle \tau \rangle = \sum_i \alpha_i \tau_i$ of the donor in absence (τ_D) and presence (τ_{DA})

of the acceptor as,

$$E = 1 - \frac{\tau_{DA}}{\tau_D} \quad (2-7b)$$

The D-A distances can be measured using equations (2-6), (2-7a) and (2-7b). The distances measured using equations (2-7a) and (2-7b) are revealed as R^S (steady-state measurement) and R^{TR} (time-resolved measurement), respectively. In one of the studies from our group [4], we have shown that the energy transfer efficiency E , calculated from steady-state experiment (equation 2-7a) might be due to re-absorption of donor emission, but not due to dipole-dipole interaction (FRET).

2.1.2. Nanosurface Energy Transfer (NSET): The D–A separations can also be calculated using another prevailing technique, NSET [5, 6], in which the energy transfer efficiency depends on the inverse of the fourth power of the D–A separation [7]. The NSET technique is based on the model of Persson and Lang [6], which is concerned with the momentum and energy conservation in the dipole-induced formation of electron–hole pairs. Here the rate of energy transfer is calculated by performing a Fermi golden rule calculation for an excited-state material depopulating with the simultaneous scattering of an electron in the nearby metal to above the Fermi level. The Persson model states that the damping rate to a surface of a noble metal may be calculated by,

$$k_{NSET} = 0.3 \times \left(\frac{\mu^2 \omega}{\hbar \omega_F k_F d^4} \right) \quad (2.8)$$

which can be expressed in more measurable parameters through the use of the Einstein A_{21} coefficient [8],

$$A_{21} = \frac{\omega^3}{3\epsilon_0 \hbar \pi c^3} |\mu|^2 \quad (2.9)$$

To give the following rate of energy transfer in accordance with Coulomb's law ($1/4\pi\epsilon_0$):

$$k_{NSET} = 0.225 \frac{c^3 \Phi_D}{\omega^2 \omega_F k_F d^4 \tau_D} \quad (2.10)$$

where, c is the speed of light, Φ_D is the quantum yield of the donor, ω is the angular frequency for the donor, ω_F is the angular frequency for acceptor, d is the D–A separation, μ is the dipole moment, τ_D is the average lifetime of the donor, and k_F is the Fermi wave-vector [9, 10]. In our studies, we used k_{NSET} as,

$$k_{NSET} = \frac{1}{\tau_{donor-acceptor}} - \frac{1}{\tau_{donor}} \quad (2.11)$$

where, $\tau_{donor-acceptor}$ is the average lifetime of the D–A system [11].

2.1.3. Data Analysis of Time-Resolved Fluorescence Transients: Curve fitting of the time-resolved fluorescence transients were carried out using a nonlinear least square fitting

procedure to a function $(X(t) = \int_0^t E(t')R(t-t')dt')$ comprised of convolution of the IRF ($E(t)$)

with a sum of exponentials $(R(t) = A + \sum_{i=1}^N B_i e^{-t/\tau_i})$ with pre-exponential factors (B_i),

characteristic lifetimes (τ_i) and a background (A). Relative concentration in a

multiexponential decay is expressed as, $c_n = \frac{B_n}{\sum_{i=1}^N B_i} \times 100$. The average lifetime (amplitude-

weighted) of a multiexponential decay [2] is expressed as,

$$\tau_{av} = \sum_{i=1}^N c_i \tau_i \quad (2.12)$$

2.1.3.1. Distance Distribution in Donor-Acceptor Systems: Distance distribution between donor and acceptor can be estimated according to the procedure described in the

literature [2, 12]. The observed fluorescence transients of the donor in absence of acceptor in a micelle can be fitted using a nonlinear least-squares fitting procedure (software SCIENTIST) to the following function,

$$I_D(t) = \int_0^t E(t')P(t'-t)dt' \quad (2-13)$$

which comprises the convolution of the instrument response function (IRF) ($E(t)$) with exponential ($P(t) = \sum_i \alpha_{Di} \exp(-t/\tau_{Di})$). The convolution of the distance distribution function $P(r)$ in the fluorescence transients of donor in presence of acceptor in the system under studies (micelle) is estimated using the same software (SCIENTIST) in the following way.

The intensity decay of donor-acceptor pair, spaced at a distance 'r', is given by

$$I_{DA}(r,t) = \sum_i \alpha_{Di} \exp \left[-\frac{t}{\tau_{Di}} - \frac{t}{\tau_{Di}} \left(\frac{R_0}{r} \right)^6 \right] \quad (2-14)$$

and the intensity decay of the sample considering $P(r)$ is given by,

$$I_{DA}(t) = \int_{r=0}^{\infty} P(r)I_{DA}(r,t)dr \quad (2-15)$$

Where $P(r)$ consist of the following terms:

$$P(r) = \frac{1}{\sigma\sqrt{2\pi}} \exp \left[-\frac{1}{2} \left(\frac{\bar{r} - r}{\sigma} \right)^2 \right] \quad (2-16)$$

In this equation, \bar{r} is the mean of the Gaussian with a standard deviation of σ . Usually distance distributions are described by the full width at half maxima. This half width is given by $hw = 2.354\sigma$.

2.1.4. Photoinduced Electron Transfer: There are several mechanisms for quenching of a fluorophore such as intersystem crossing or the heavy atom effect, electron exchange or Dexter interactions, photoinduced electron transfer (PET), and FRET. In PET, a complex is formed between the electron donor (D_p) and the electron acceptor (A_p). The subscript P is used to identify the quenching as due to a PET mechanism. This charge transfer complex can return to the ground state without emission of a photon, but in some cases, exciplex emission is observed. Finally, the extra electron on the acceptor is returned to the electron donor. The direction of electron transfer in the excited state is determined by the oxidation and reduction potential of the ground and excited states. Upon excitation the electron donor transfers an electron to the acceptor with a rate k_p , forming the charge transfer complex $[D_p^+ A_p^-]^*$ (Figure. 2.2). This complex may emit as an exciplex ($h\nu_E$) or be quenched and return to the ground state. The important part of this process is the decrease in total energy of the charge transfer complex. The energy decreases because the ability to

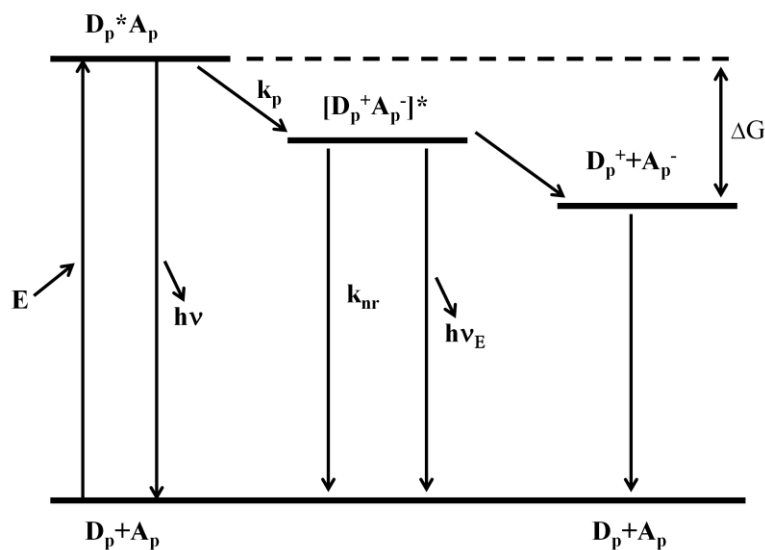


Figure 2.2. Energy diagram for photoinduced electron transfer (PET). The excited molecule is assumed to be the electron donor. ν and ν_E are emission from the fluorophore and exciplex, respectively.

donate or accept electrons changes when a fluorophore is in the excited state. Excitation provides the energy to drive charge separation. D_P and A_P do not form a complex when both are in the ground state because this is energetically unfavorable. The energy released by electron transfer can also change if the ions become solvated and/or separated in a solvent with a high dielectric constant.

2.2. Systems:

2.2.1. Organized Assemblies (Biomimetics): Amphiphilic molecules like surfactant, aggregates to form macromolecular assemblies like micelles and reverse micelles, which very often resemble the structural properties of biomolecules. In the following section, we will discuss about these entities.

2.2.1.1. Micelles: Micelles are spherical or nearly spherical aggregates of amphiphilic surfactant molecules (shown in Figure 2.3) formed in aqueous solution above a concentration known as critical micellar concentration (CMC). Micelles are formed above a critical temperature called “Kraft point” which is different for different surfactants. Micellar aggregates have diameter varying within 10 nm and the aggregation number, i.e., the number of surfactant molecules per micelle, ranges from 20 to 200. Israelachvili et al. [13] have proposed that surfactant molecular packing considerations are determinant in the formation of large surfactant aggregates. In particular, it is considered that the surfactant packing parameter θ ($\theta=v/\sigma l$, where v is the surfactant molecular volume, σ is the area per polar head, and l is the length of hydrophobic part) gives a good idea of the shape of aggregates which will form spontaneously [13]. It is considered that normal or direct rod-like micelles are formed when $2<\theta<3$ [14]. Micelles can be both neutral (triton X-100) and

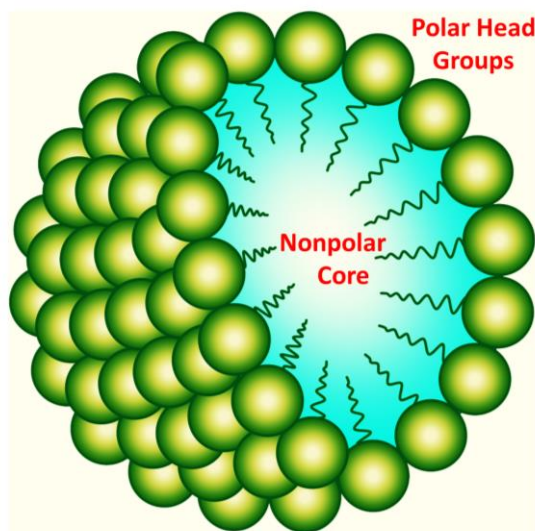


Figure 2.3. Schematic representation of the structure of a micelle.

ionic (sodium dodecyl sulfate, SDS (anionic) and hexadecyltrimethylammonium bromide, CTAB (cationic)). The structure of a typical micelle is schematically shown in Figure 2.3. The core of a micelle is essentially “dry” and consists of the hydrocarbon chains with the polar and charged head groups projecting outward toward the bulk water. The stern layer, surrounding the core, comprises of the ionic or polar head groups, bound counter ions and water molecules. Between the stern layer and the bulk water there is a diffused Guoy-Chapman (GC) layer, which contains the free counter ions and water molecules. In non-ionic polyoxyethylated surfactants e.g. triton X-100 (TX-100), the hydrocarbon core is surrounded by a palisade layer, which consists of the polyoxyethylene groups hydrogen-bonded to water molecules [15]. Small angle X-ray and neutron scattering have provided detailed information on the structure of the CTAB micelles [16, 17]. According to these studies, CMC and aggregation number of CTAB micelle are 0.8 mM and 52 respectively and the thickness of the stern layer is 6-9 Å [16-19]. The overall radius of CTAB micelle is about 50 Å. For TX-100 micelle, the CMC, thickness of the palisade layer and overall

radius of the hydrophobic core are reported to be 0.1 mM, 51 Å and 25-27 Å, respectively and that of SDS micelles are 8.6 mM [20], 33 Å [21] and 5 Å, respectively [22].

2.2.1.2. Reverse Micelle (RM): Reverse micelle or water-in-oil microemulsions (Figure 2.4) are nanopools of polar solvent protected by a monolayer of surfactant molecules at the periphery with polar headgroups pointing inward into the polar solvent and the hydrocarbon tails directed toward the nonpolar organic solvents [23, 24]. RMs with water nanopools resemble the water pockets found in various bioaggregates such as proteins, membranes and mitochondria. Thus, these systems are very often considered as templates for the synthesis of nanoparticles and as excellent biomimetic for exploration of biological membranes and biologically confined water molecules [25, 26]. Aqueous RMs are generally characterized by the degree of hydration (w_0), which is the ratio of molar concentration of water to that of surfactant, where the radius of the water pool (r in Å) is empirically defined as, $r = 2 \times w_0$ [27]. Shapes and sizes of the surfactant aggregates depend strongly on the type and concentration of the surfactant and on the nature of counter ion [28] and external solvent. In principle, reverse micelles can be formed in the presence and in the absence of solubilized water. However, it has generally been proposed that if the medium is completely water-free, there is not a well-defined CMC (critical micelle concentration) and the aggregates formed are very small and polydisperse, indicating minimum cooperativity in the surfactant association. This has been particularly established for surfactant sodium bis(2-ethylhexyl) sulfosuccinate (AOT) in several organic solvents [29]. RMs with w_0 values less than 20 are stable and monodisperse over a wide range of temperatures. The AOT-alkane-water system is interesting as the solution is homogeneous and optically transparent over a wide range of temperature, pressure and pH.

The AOT RM can compartmentalize a large amount of water in its central core, and the nanoscale aggregation process is fairly well-characterized with respect to size and shape at various water contents. The CMC of AOT in hydrocarbon solvent is about 0.1 mM [30]. In liquid alkanes, AOT RMs ($w_0 = 0$) are completely associated and each micelle contains 23 monomers. The structures of these RMs are slightly asymmetric and are of round cylindrical nature. Spherical RMs are generally formed by surfactants with high values of the packing parameter, $\theta > 3$. AOT RMs can dissolve large amounts of water, being able to reach w_0 values as large as 40-60, depending on the surrounding nonpolar organic medium and temperature [31]. At low w_0 values, the systems are usually referred to as reverse micelle, whereas the term water-in-oil microemulsion is frequently used for higher w_0 values. Fluorescence spectroscopy has been extensively used to study the AOT RM system. Fluorescent probes have been used to determine the viscosity, binding site, rigidity and proximity within the water pool. These studies have shown that water inside the RM is generally of two types: i) interfacial (bound) and ii) core (free) water. One of the studies [32] has shown the existence of third type of water (trapped) molecules present between the polar headgroups of the individual surfactant molecules. Thus, the interior of RMs is extremely heterogeneous. Dielectric relaxation studies [33] indicate the presence of 7 ns component for bound water in RM, very similar to those of water molecules in the close vicinity of biological macromolecules (biological water). In contrast to AOT which does not require any cosurfactant to form reverse micelles, cationic surfactants do not form RMs in the absence of cosurfactants [34]. Several nonionic or neutral surfactants. (for example, Brij 30) have been reported to form RMs in pure and mixed hydrocarbon solvents [35].

Reverse micelles also have been extensively employed as media to synthesize different metal and semiconductor nanoparticles.

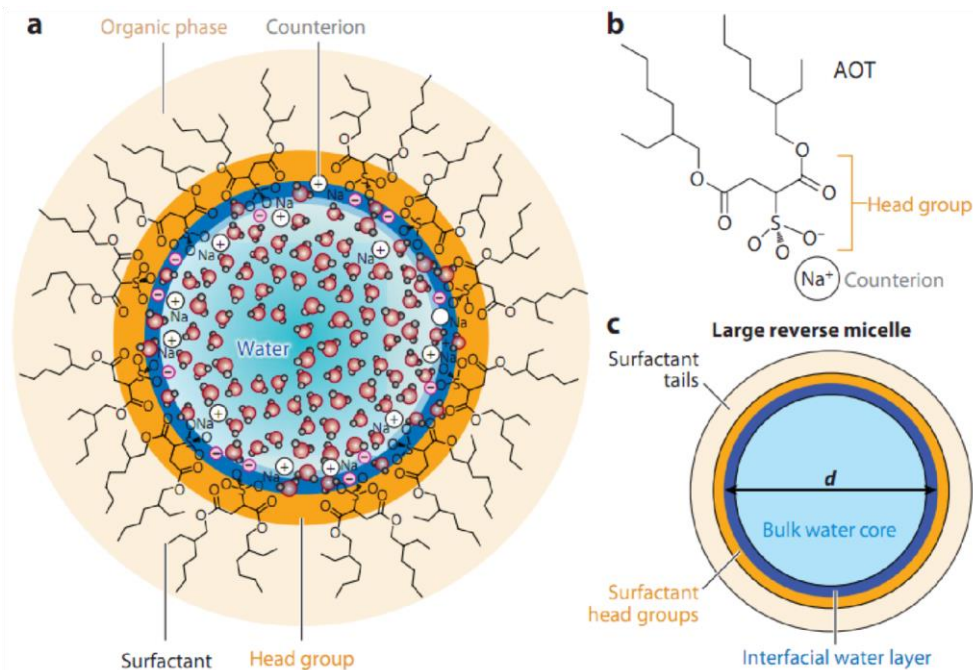


Figure 2.4. (a) Schematic depiction of a potential structure of a reverse micelle. Water molecules reside in the interior, sometimes interacting with headgroups and counterions. Surfactant tails reside in contact with the continuous, nonpolar, organic supporting phase. (b) Chemical structure of AOT (sodium bis(2-ethylhexyl) sulfosuccinate). (c) Schematic of a large reverse micelle showing important features of the structure.

2.2.2. Deoxyribonucleic Acids (DNAs): Nucleic acids form the central molecules in transmission, expression and conservation of genetic information. DNA serves as carrier of genetic information [36]. The classic example of how biological function follows from biomolecular structure comes from the elucidation of double helical structure of DNA by Watson and Crick [37]. DNAs are polynucleotides with each nucleotide comprising of deoxyribose sugar, purine and pyrimidine bases and phosphate groups. The main bases whose intermolecular hydrogen bonding holds the DNA strands together are adenine, guanine, thymine and cytosine. There are generally three forms of DNA: the A, B and Z-

form. Native DNA, however, exists in B-form. Native DNA is about a metre long and comprises of hundreds of base pairs. The distance between two base pairs in B-DNA is 3.4 Å [38]. In about 4 M NaCl, B-form is converted into Z-form. DNA structures consist of major and minor grooves and intercalation spaces through which DNA interacts with ligands. There are two modes of interaction of DNA with ligands: (i) intercalation, where the planar polycyclic heteroaromatic ligands occupy the space in between the base pairs of DNA and interact through π - π interaction (Figure 2.5) [39], and (ii) groove binding where the ligands bind in the major and minor grooves of DNA [40]. The water molecules at the surface of DNA are critical to the structure and to the recognition by other molecules, proteins and drugs [41].

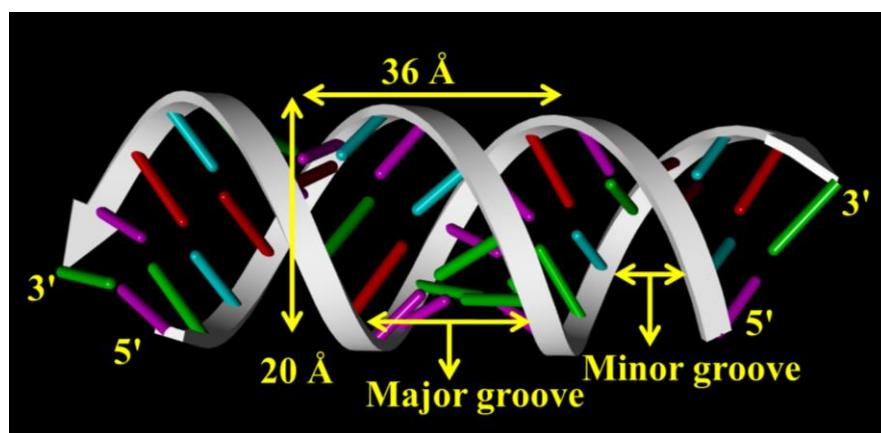


Figure 2.5. Schematic representation of deoxyribonucleic acids (DNAs).

2.2.3. Molecular Probes: In this section we will discuss about the different probe molecules that have been used in the course of study.

2.2.3.1. Riboflavin (Rf): Rf (Figure 2.6.A) is well known as vitamin B₂. It is the central component of the cofactors FAD and FMN, and is therefore required by all flavo-proteins. As such, vitamin B₂ is required for a wide variety of cellular processes. It plays a key role

in energy metabolism, and for the metabolism of fats, carbohydrates and proteins. Milk, cheese, leafy green vegetables, liver, kidneys, legumes, tomatoes, yeast and mushrooms are good source of Rf, but exposure to light destroys Rf. Rf is very important for the preservation of food in right light condition [42]. The photochemical reactions of Rf are well understood [43]. It has already been demonstrated that the intramolecular ET process is responsible for the photoreduction of the chromophore [44, 45]. It has been proposed that two photoproducts, Lumichrome and Lumiflavin are generated via an intermediate compound deuteroflavin during the photodetioration of the Rf chromophore in presence of oxygen [45]. The role of proton transfer from the ribityl chain to the side nitrogen moiety for the generation of the photoproduct is also identified. In a recent study, it has been established that Rf is a potential photosensitizer and the activated triplet state in the molecule is concluded to be responsible for the photosensitization [46, 47]. It is to be noted that the photoproducts of Rf are also very hazardous for the biological activity as they degrade important amino acids including the tryptophan and tyrosine. Rf has two distinct absorption bands at 445 nm and 375 nm with extinction coefficient of $12200 \text{ M}^{-1}\text{cm}^{-1}$ at 450 nm [48, 49]. The emission peak of Rf in buffer is 520 nm [50].

2.2.3.2. Methylene Blue (MB): MB is a heterocyclic aromatic chemical compound with molecular formula: $\text{C}_{16}\text{H}_{18}\text{ClN}_3\text{S}$. It has many uses in a range of different fields. At room-temperature it appears as a solid and is odourless and a dark green powder, which yields a blue solution when dissolved in water. They are widely used as model water contaminant [51]. Its structure is given in Figure 2.6.B. When dissolved in water, the UV-visible spectrum of MB showed three absorption maxima. The first band was observed at 246 nm

and then 291 nm and more intensely 663 nm. The absorption maxima wavelength of MB ($\lambda_{\text{max}} = 663 \text{ nm}$) was used for the analysis during decolorization of MB dye.

2.2.3.3. Bilirubin (BR): BR (Figure 2.6.C), the yellow-orange breakdown product of normal heme catabolism in mammalian systems, introduces great biological and diagnostic values [52]. Both antioxidant and toxic properties have been attributed to BR [53], which is normally conjugated with glucuronic acid and then excreted in the bile. However, when its conjugation with glucuronic acid is inhibited, as in neonatal jaundice and in hereditary forms of congenital jaundice, excess BR bind and deposit to various tissues, giving rise to severe hyperbilirubinemia and neurotoxicity. Phototherapy, the most effective treatment for jaundice to date, decreases the BR levels in the blood by changing the *ZZ*-BR isomer into water-soluble *ZE*-BR [54-56]. Because this reaction is readily reversible, equilibrium is established between native BR and the *ZE* isomer when BR is photoirradiated in a closed system. The second fastest reaction that occurs when BR is exposed to light is the production of lumirubin, a structural isomer of BR.

2.2.3.4. Benzo[*a*]pyrene (BP): It is a potent environmental carcinogen which can bind to DNA, extremely hydrophobic and belongs to the class of polycyclic aromatic hydrocarbons (PAHs) [57]. Its structure is given in Figure 2.6.D. Being a pyrene derivative it is characterized by a high quantum yield near unity in micellar solutions [58] along with multiple vibronic bands in its emission spectrum [57].

2.2.3.5. Rose Bengal (RB): (4,5,6,7-tetrachloro-2',4',5',7'-tetraiodo-fluorescein disodium or RB) is an illustrious type II photosensitizer. Its structure (Figure 2.6.E) consists of several chlorines and iodines on the xanthene rings, exhibits facile photocatalytic

conversion of triplet oxygen ($^3\text{O}_2$) to singlet oxygen ($^1\text{O}_2$) [59-61]. This property is

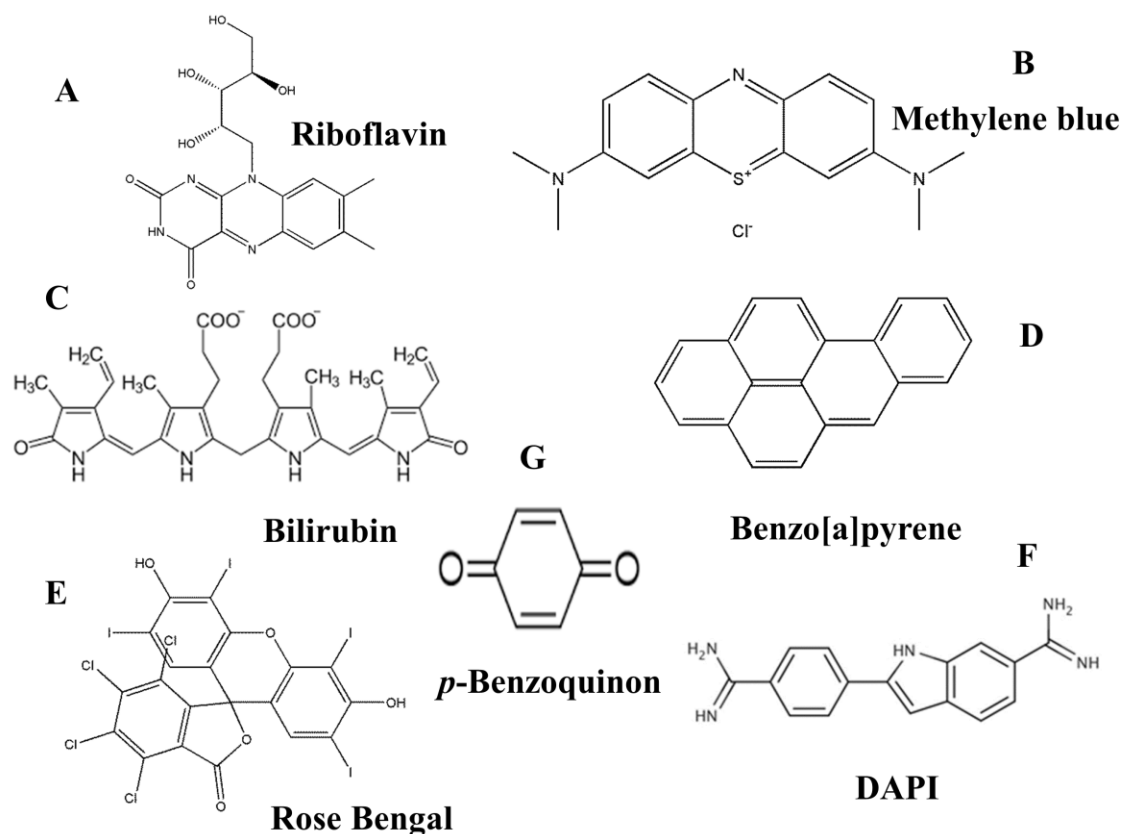


Figure 2.6. Schematic representation of the fluorescent probes used in the course of study.

achieved upon irradiation with green light, [62] since it has an extremely large cross-section in the green ($\text{EM} = 99,800 \text{ M}^{-1}\text{cm}^{-1}$ at 549 nm in water) that is only minimally affected by local environment. As a photosensitizer, RB can be used to eradicate microorganisms such as viruses [63, 64], Gram-positive bacterial species [65] and protozoa [66]. It can also induce photodynamic effects *in vitro* on red blood cells [67], cardiomyocytes [68], retinal pigment epithelial cells [69], *ex vivo* in nerve axon [70], corneal endothelium [71], heart [72] and pancreatic acini [73]. Due to its anionic nature,

RB is inhibited from crossing cell membranes and entering cells in the absence of a carrier at low concentrations [74]. Therefore, in order to favour its intracellular accumulation, several RB hydrophobic derivatives (e.g., acetate or phosphate) have been developed [75]. Addition of acetate groups to the xanthene ring converts the molecule RB into a fluorogenic substrate derivative, RBAc makes it more hydrophobic and thus improving the molecule's permeability in the cells. ROS production by RB is achieved upon irradiation by visible green light, whose wavelength ranges between 530 and 560 nm. The minimally penetrating nature of such green light makes RB particularly effective in many cutaneous lesions and dermatological diseases [76].

2.2.3.6. 4',6-Diamidino-2-phenylindole (DAPI): The dye DAPI is another commercially available fluorescent cytological stain for DNA. Its structure is given in Figure 2.6.F. Studies on the DAPI-DNA complexes show that the probe exhibits a wide variety of interactions of different strength and specificity with DNA [77].

2.2.3.7. *p*-Benzoquinone (BQ): BQ (Figure 2.6.G) is a well-known probe for electron accepting and shuttling for any electron rich material/compound, which readily accepts electron and adapted to the resonance species hydroquinone. Large doses could induce local irritation, colonic convulsions, decreased blood pressure and death due to paralysis of the medullary centres.

References:

- [1] L. Stryer, Fluorescence Energy Transfer as a Spectroscopic Ruler, *Ann. Rev. Biochem.*, 47 (1978) 819-846.
- [2] J.R. Lakowicz, *Principles of Fluorescence Spectroscopy*, Kluwer Academic/Plenum, New York, 1999.
- [3] D. Banerjee, S.K. Pal, Simultaneous Binding of Minor Groove Binder and Intercalator to Dodecamer DNA: Importance of Relative Orientation of Donor and Acceptor in FRET, *J. Phys. Chem. B*, 111 (2007) 5047-5052.
- [4] P. Majumder, R. Sarkar, A.K. Shaw, A. Chakraborty, S.K. Pal, Ultrafast Dynamics in a Nanocage of Enzymes: Solvation and Fluorescence Resonance Energy Transfer in Reverse Micelles, *J. Colloid Interface Sci.*, 290 (2005) 462-474.
- [5] M. Montalti, N. Zaccheroni, L. Prodi, N. O'Reilly, S.L. James, Enhanced Sensitized NIR Luminescence from Gold Nanoparticles via Energy Transfer from Surface-Bound Fluorophores, *J. Am. Chem. Soc.*, 129 (2007) 2418-2419.
- [6] B.N.J. Persson, N.D. Lang, Electron-Hole Pair Quenching of Excited States Near a Metal, *Phys. Rev. B*, 26 (1982) 5409-5415.
- [7] J. Gersten, A. Nitzan, Spectroscopic Properties of Molecules Interacting with Small Dielectric Particles, *J. Chem. Phys.*, 75 (1981) 1139-1152.
- [8] D. Craig, T. Thirunamachandran, *Molecular Quantum Electrodynamics*, Academic Press, London, 1984.
- [9] T.L. Jennings, M.P. Singh, G.F. Strouse, Fluorescent Lifetime Quenching near $d = 1.5$ nm Gold Nanoparticles: Probing NSET Validity, *J. Am. Chem. Soc.*, 128 (2006) 5462-5467.
- [10] M.A.H. Muhammed, A.K. Shaw, S.K. Pal, T. Pradeep, Quantum Clusters of Gold Exhibiting FRET, *J. Phys. Chem. C*, 112 (2008) 14324-14330.

- [11] A. Makhal, S. Sarkar, S.K. Pal, H. Yan, D. Wulferding, F. Cetin, P. Lemmens, Ultrafast Excited State Deactivation of Doped Porous Anodic Alumina Membranes, *Nanotechnology*, 23 (2012) 305705.
- [12] S. Batabyal, T. Mondol, S.K. Pal, Picosecond-Resolved Solvent Reorganization and Energy Transfer in Biological and Model Cavities, *Biochimie*, 95 (2013) 1127-1135.
- [13] J.N. Israelachvili, D.J. Mitchell, B.W. Ninham, Theory of Self-Assembly of Hydrocarbon Amphiphiles into Micelles and Bilayers, *J. Chem. Soc. Faraday Trans.*, 272 (1976) 1525-1568.
- [14] D.J. Mitchell, B.W. Ninham, Micelles, Vesicles and Microemulsions, *J. Chem. Soc. Faraday Trans.*, 77 (1981) 601-629.
- [15] H.H. Paradies, Shape and Size of a Nonionic Surfactant Micelle. Triton X-100 in Aqueous Solution, *J. Phys. Chem.*, 84 (1980) 599-607.
- [16] S.S. Berr, Solvent Isotope Effects on Alkyltrimethylammonium Bromide Micelles as a Function of Alkyl chain Length, *J. Phys. Chem.*, 91 (1987) 4760-4765.
- [17] S.S. Berr, E. Caponetti, J.S. Johnson, J.R.R.M. Jones, L.J. Magid, Small-Angle Neutron Scattering from Hexadecyltrimethylammonium Bromide Micelles in Aqueous Solutions, *J. Phys. Chem.*, 90 (1986) 5766-5770.
- [18] X.G. Lei, G.H. Zhao, Y.C. Liu, N.J. Turro, Influence of Binding Strength of Added Electrolytes on the Properties of Micelles and of Micellized Radical Pairs, *Langmuir*, 8 (1992) 475-480.
- [19] H.L. Tavernier, F. Laine, M.D. Fayer, Photoinduced Intermolecular Electron Transfer in Micelles: Dielectric and Structural Properties of Micelle Headgroup Regions, *J. Phys. Chem. A*, 105 (2001) 8944-8957.
- [20] N.J. Turro, X.G. Lei, K.P. Ananthapadmanabhan, M. Aronson, Spectroscopic Probe Analysis of Protein-Surfactant Interactions: The BSA/SDS System, *Langmuir*, 11 (1995) 2525-2533.
- [21] P.A. Hassan, S.R. Raghavan, E.W. Kaler, Microstructural Changes in SDS Micelles Induced by Hydrotropic Salt, *Langmuir*, 18 (2002) 2543-2548.

- [22] A.K. Shaw, S.K. Pal, Activity of Subtilisin Carlsberg in Macromolecular Crowding, *J. Photochem. Photobiol. B*, 86 (2007) 199-206.
- [23] T.K. De, A. Maitra, Solution Behaviour of Aerosol OT in Non-polar Solvents, *Adv. Colloid Interface Sci.*, 59 (1995) 95-193.
- [24] P.L. Luisi, M. Giomini, M.P. Pileni, B.H. Robinson, Reverse Micelles as Hosts for Proteins and Small Molecules, *Biochim. Biophys. Acta Rev. Biomembr.*, 947 (1988) 209-246.
- [25] K. Bhattacharyya, Solvation Dynamics and Proton Transfer in Supramolecular Assemblies, *Acc. Chem. Res.*, 36 (2003) 95-101.
- [26] B. Cohen, D. Huppert, K.M. Solntsev, Y. Tsfadia, E. Nachliel, M. Gutman, Excited State Proton Transfer in Reverse Micelles, *J. Am. Chem. Soc.*, 124 (2002) 7539–7547.
- [27] M.P. Pileni, Water in Oil Collidal Droplets Used as Microreactors, *Adv. Colloid Interface Sci.*, 46 (1993) 139-163.
- [28] F. Caboi, G. Capuzzi, P. Baglioni, M. Monduzzi, Microstructure of Ca–AOT/Water/Decane w/o Microemulsions, *J. Phys. Chem. B*, 101 (1997) 10205-10212.
- [29] M. Zulauf, H.F. Eicke, Inverted Micelles and Microemulsions in the Ternary System Water/Aerosol-OT/Isooctane as Studied by Photon Correlation Spectroscopy, *J. Phys. Chem.*, 83 (1979) 480-486.
- [30] Y.C. Jean, H.J. Ache, Determination of Critical Micelle Concentrations in Micellar and Reversed Micellar Systems by Positron Annihilation Techniques, *J. Am. Chem. Soc.*, 100 (1978) 984-985.
- [31] C. Petit, P. Lixon, M.P. Pileni, Structural Study of Divalent Metal bis(2-ethylhexyl) Sulfosuccinate Aggregates, *Langmuir*, 7 (1991) 2620–2625.
- [32] T.K. Jain, M. Varshney, A. Maitra, Structural Studies of Aerosol OT Reverse Micellar Aggregates by FT-IR Spectroscopy, *J. Phys. Chem.*, 93 (1989) 7409-7416.
- [33] M.A. Middleton, R.S. Schechter, K.P. Johnston, Dielectric Properties of Anionic and Nonionic Surfactant Microemulsions, *Langmuir*, 6 (1990) 920–928.

- [34] J. Lang, N. Lalem, R. Zana, Quaternary Water in Oil Microemulsions. 1. Effect of Alcohol Chain Length and Concentration on Droplet Size and Exchange of Material between Droplets, *J. Phys. Chem.*, 95 (1991) 9533-9541.
- [35] S. Rakshit, N. Goswami, S.K. Pal, Slow Solvent Relaxation Dynamics of Nanometer Sized Reverse Micellar Systems through Tryptophan Metabolite, Kynurenine, *Photochem. Photobiol.*, 88 (2012) 38-45.
- [36] O. Avery, C. Macleod, M. McCarty, Studies on the Chemical Nature of the Substances Inducing Transformation of the Substances Inducing Transformation of Pneumococcal Types, *J. Expt. Med.*, 7 (1944) 137-158.
- [37] J.D. Watson, F.H.C. Crick, Molecular Structure of Nucleic Acids, *Nature*, 171 (1953) 737-738.
- [38] D.L. Nelson, M.M. Cox, *Lehninger Principles of Biochemistry*, Worth, New York, 2000.
- [39] L.S. Lerman, The Structure of DNA-Acridine Complex, *Proc. Natl. Acad. Sci. U.S.A.*, 49 (1963) 94-102.
- [40] P.B. Dervan, Molecular Recognition of DNA by Small Molecules, *Bioorg. Med. Chem.*, 9 (2001) 2215-2235.
- [41] S.K. Pal, A.H. Zewail, Dynamics of Water in Biological Recognition, *Chem. Rev.*, 104 (2004) 2099-2123.
- [42] O.W. Parks, C. Allen, Photodegradation of Riboflavin to Lumichrome in Milk Exposed to Sunlight, *J. Dairy Sci.*, 60 (1977) 1038-1041.
- [43] W.J. Nickerson, G. Strauss, The Photochemical Cleavage of Water by Riboflavin, *J. Am. Chem. Soc.*, 82 (1960) 5007-5008.
- [44] W.M. Moore, J.T. Spence, F.A. Raymond, S.D. Colson, Photochemistry of Riboflavin. I. The Hydrogen Transfer Process in the Anaerobic Photobleaching of Flavins, *J. Am. Chem. Soc.*, 85 (1963) 3367-3372.
- [45] B. Holmström, G. Oster, Riboflavin as an Electron Donor in Photochemical Reactions, *J. Am. Chem. Soc.*, 83 (1961) 1867-1871.

- [46] M. Halwer, The Photochemistry of Riboflavin and Related Compounds, *J. Am. Chem. Soc.*, 73 (1951) 4870-4874.
- [47] E. Silva, Biological Implications of Aerobically Obtained Riboflavin-Sensitized Photoproducts of Tryptophan, *J. Photochem. Photobiol.*, B, 14 (1992) 142-144.
- [48] M.G. Duyvis, R. Hilhorst, C. Laane, D.J. Evans, D.J.M. Schmedding, Role of Riboflavin in Beer Flavor Instability: Determination of Levels of Riboflavin and Its Origin in Beer by Fluorometric Apoprotein Titration, *J. Agric. Food Chem.*, 50 (2002) 1548-1552.
- [49] R. Saha, S. Rakshit, P.K. Verma, R.K. Mitra, S.K. Pal, Protein-cofactor binding and ultrafast electron transfer in riboflavin binding protein under the spatial confinement of nanoscopic reverse micelles, *J. Mol. Recognit.*, 26 (2013) 59-66.
- [50] S. Rakshit, R. Saha, P.K. Verma, R.K. Mitra, S.K. Pal, Ultrafast Electron Transfer in Riboflavin Binding Protein in Macromolecular Crowding of Nano-Sized Micelle, *Biochimie*, 94 (2012) 2673-2680.
- [51] N. Xu, Z. Shi, Y. Fan, J. Dong, J. Shi, M.Z.C. Hu, Effects of Particle Size of TiO₂ on Photocatalytic Degradation of Methylene Blue in Aqueous Suspensions, *Ind. Eng. Chem. Res.*, 38 (1999) 373-379.
- [52] J.D. Ostrow, Bile Pigments and Jaundice: Molecular, Metabolic and Medical Aspects, Marcel Dekker, New York, 1986.
- [53] R. Stocker, A.N. Glazer, B.N. Ames, Antioxidant Activity of Albumin-Bound Bilirubin, *Proc. Natl. Acad. Sci. U.S.A.*, 84 (1987) 5918-5922.
- [54] D.A. Lightner, A.F. McDonagh, Molecular Mechanisms of Phototherapy for Neonatal Jaundice, *Acc. Chem. Res.*, 17 (1984) 417-424.
- [55] A.A. Lamola, W.E. Blumberg, R. McClead, A. Fanaroff, Photoisomerized Bilirubin in Blood from Infants Receiving Phototherapy, *Proc. Natl. Acad. Sci. U.S.A.*, 78 (1981) 1882-1886.
- [56] S.E. Braslavsky, A.R. Holzwarth, K. Schaffner, Solution Conformations, Photophysics, and Photochemistry of Bile Pigments; Bilirubin and Biliverdin, Dimethyl Esters and Related Linear Tetrapyrroles, *Angew. Chem. Int. Ed.*, 22 (1983) 656-674.

- [57] S.C. Beck, D.T. Cramb, Condensed Phase Dispersive Interactions of Benzo[a]pyrene with Various Solvents and with DNA: A Twist on Solvatochromism, *J. Phys. Chem. B*, 104 (2000) 2767-2774.
- [58] S. Banerjee, N. Goswami, S.K. Pal, A Potential Carcinogenic Pyrene Derivative under Forster Resonance Energy Transfer to Various Energy Acceptors in Nanoscopic Environments, *Chem. Phys. Chem.*, 14 (2013) 3581-3593.
- [59] D. Neckers, Rose bengal, *J. Photochem. Photobiol. A*, 47 (1989) 1-29.
- [60] J. Paczkowski, J. Lamberts, B. Paczkowska, D. Neckers, Photophysical Properties of Rose Bengal and Its Derivatives (XII), *J. Free. Radic. Biol. Med.*, 1 (1985) 341-351.
- [61] I.E. Kochevar, C.R. Lambert, M.C. Lynch, A.C. Tedesco, Comparison of Photosensitized Plasma Membrane Damage Caused by Singlet Oxygen and Free Radicals, *Biochim. Biophys. Acta*, 1280 (1996) 223-230.
- [62] P.C. Lee, M.A. Rodgers, Laser Flash Photokinetic Studies of Rose Bengal Sensitized Photodynamic Interactions of Nucleotides and DNA, *Photochem. Photobiol*, 45 (1987) 79-86.
- [63] J. Lenard, A. Rabson, R. Vanderoef, Photodynamic Inactivation of Infectivity of Human Immunodeficiency Virus and Other Enveloped Viruses Using Hypericin and Rose Bengal: Inhibition of Fusion and Syncytia Formation, *Proc. Natl. Acad. Sci. U.S.A.*, 90 (1993) 158-162.
- [64] J. Chodosh, M. Banks, W. Stroop, Rose Bengal Inhibits Herpes Simplex Virus Replication in Vero and Human Corneal Epithelial Cells in Vitro, *Invest Ophthalmol. Vis. Sci.*, 33 (1992) 2520-2527.
- [65] T. Dahl, W.R. Midden, D. Neckers, Comparison of Photodynamic Action by Rose Bengal in Gram-Positive and Gram-Negative Bacteria, *Photochem. Photobiol.*, 48 (1988) 607-612.
- [66] R. Masone, R. Docamp, The Photodynamic Action of Rose Bengal on Trypanosoma Cruzi, *Acta tropica*, 41 (1984) 99-108.

- [67] D.P. Valenzeno, J.P. Pooler, Cell Membrane Photomodification: Relative Effectiveness of Halogenated Fluoresceins for Photohemolysis, *Photochem. Photobiol.*, 35 (1982) 343-350.
- [68] L. Ver Donck, J. Van Reempts, G. Vandeplassche, M. Borgers, A New Method to Study Activated Oxygen Species Induced Damage in Cardiomyocytes and Protection by Ca^{2+} Antagonists, *J.Mol. Cell Cardiol.*, 20 (1988) 811-823.
- [69] I.A. Menon, P.K. Basu, S.D. Persad, S. Rosatone, J.D. Wiltshire, A Study on the Sequence of Phototoxic Effects of Rose Bengal Using Retinal Pigment Epithelial Cells in Vitro, *Exp. Eye Res.*, 49 (1989) 67-73.
- [70] J. Pooler, D.P. Valenzeno, Kinetic Factors Governing Sensitized Photooxidation of Excitable Cell Membranes, *Photochem. Photobiol.*, 28 (1978) 219-226.
- [71] D. Hull, E. Strickland, K. Green, Photodynamically Induced Alteration of Cornea Endothelial Cell Function, *Invest. Ophthalmol. Vis. Sci.*, 18 (1979) 1226-1231.
- [72] D. Hearse, Y. Kusama, M. Bernier, Rapid Electrophysiological Changes Leading to Arrhythmias in The Aerobic Rat Heart. Photosensitization Studies with Rose Bengal-Derived Reactive Oxygen Intermediates, *Circ. Res.*, 65 (1989) 146-153.
- [73] E. Matthews, Z. Cui, Photodynamic Action of Rose Bengal on Isolated Rat Pancreatic Acini: Stimulation of Amylase Release, *FEBS Lett.*, 256 (1989) 29-32.
- [74] A.C. Croce, E. Wyroba, G. Bottiroli, Distribution and Retention of Rose Bengal and Disulphonated Aluminium Phthalocyanine: A Comparative Study in Unicellular Eukaryote, *J. Photochem. Photobiol. B*, 16 (1992) 318-330.
- [75] D.K. Luttrull, O. Valdes-Aguilera, S.M. Linden, J. Paczkowski, D. Neckers, Rose Bengal Aggregation in Rationally Synthesized Dimeric Systems, *Photochem. Photobiol.*, 47 (1988) 551-557.
- [76] E. Panzarini, V. Inguscio, L. Dini, Overview of Cell Death Mechanisms Induced by Rose Bengal Acetate-Photodynamic Therapy, *Int. J. Photoenergy*, 2011 (2011) 713726.

[77] W.D. Wilson, F.A. Tanious, H.K. Barton, R.L. Jones, K. Fox, R.L. Wydra, L. Streckowski, DNA Sequence Dependent Binding Modes of 4',6-Diamidino-2-phenylindole (DAPI), *Biochemistry*, 29 (1990) 8452-8461.

Chapter 3

Instrumentation and Sample Preparation

In this chapter the details of instrumental setup and sample preparation techniques used in our studies have been described.

3.1. Instrumental Setups:

3.1.1. Steady-State UV-Vis Absorption and Emission Measurement: Steady-state UV-Vis absorption and emission spectra of the probe molecules were measured with Shimadzu UV-2450 spectrophotometer and Jobin Yvon Fluoromax-3 fluorimeter, respectively. Schematic ray diagrams of these two instruments are shown in Figures 3.1 and 3.2.

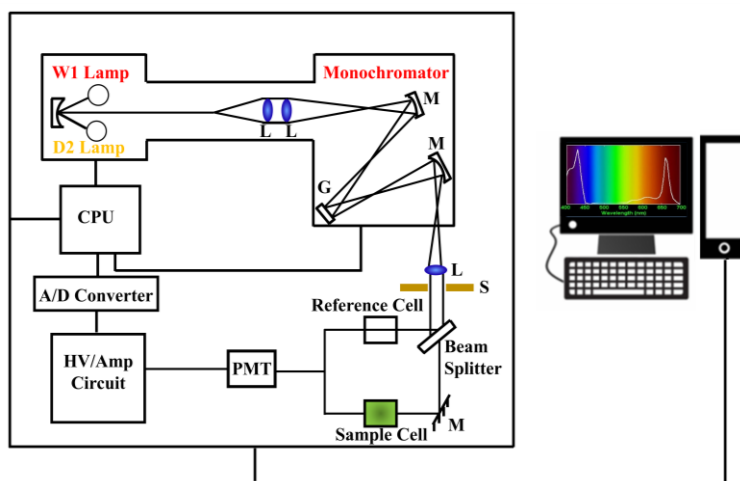


Figure 3.1. Schematic ray diagram of an absorption spectrophotometer. Tungsten halogen (W1) and Deuterium lamps (D2) are used as light sources in the visible and UV regions, respectively. M, G, L, S, PMT designate mirror, grating, lens, shutter and photomultiplier tube, respectively. CPU, A/D converter and HV/Amp indicate central processing unit, analog to digital converter and High-voltage/Amplifier circuit, respectively.

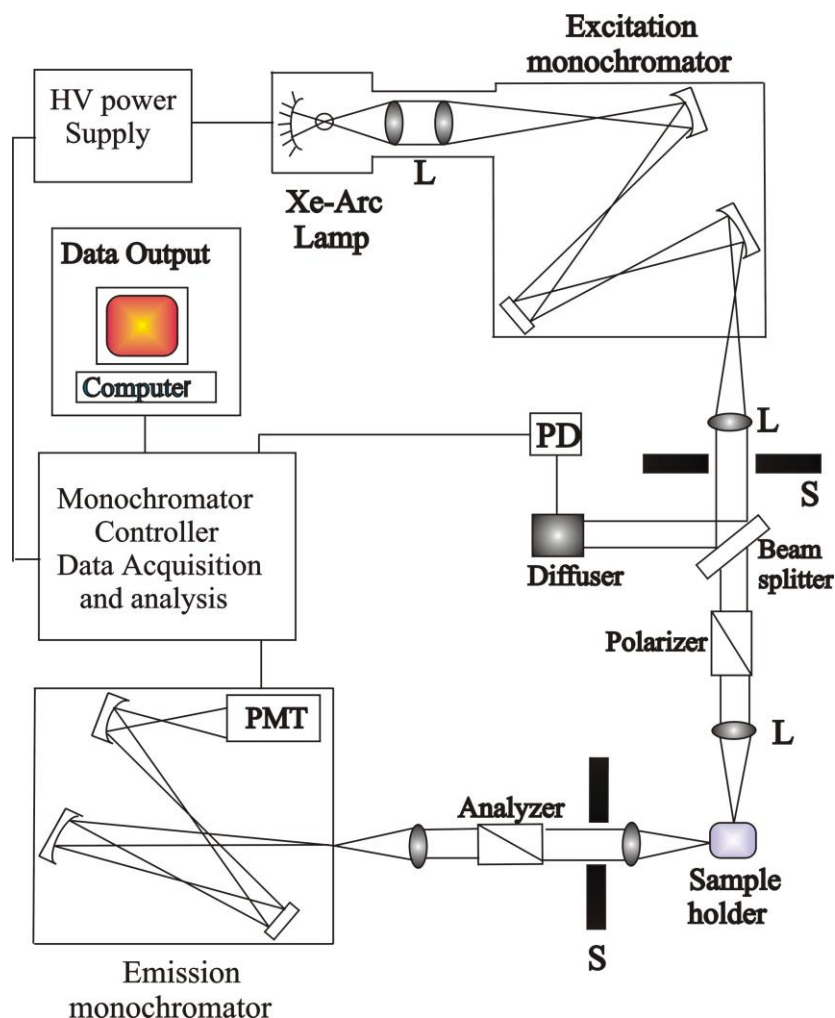


Figure 3.2. Schematic ray diagram of an emission spectrofluorimeter. *M, G, L, S, PMT and PD* represent mirror, grating, lens, shutter, photomultiplier tube and reference photodiode, respectively.

3.1.2. Time-Correlated Single Photon Counting (TCSPC) Technique: All the picosecond-resolved fluorescence transients were recorded using TCSPC technique. The schematic block diagram of a TCSPC system is shown in Figure 3.3. TCSPC setup from Edinburgh instruments, U.K., was used during fluorescence decay acquisitions. The instrument response functions (IRFs) of the laser sources at different excitation wavelengths varied between 60 ps to 80 ps. The fluorescence from the sample was detected by a photomultiplier after dispersion through a grating monochromator [1]. For all transients, the polarizer in the emission side was adjusted to be at 54.7° (magic angle) with

respect to the polarization axis of excitation beam. For 290-300 nm laser excitation, we have used a femtosecond-coupled TCSPC setup in which the sample was excited by the

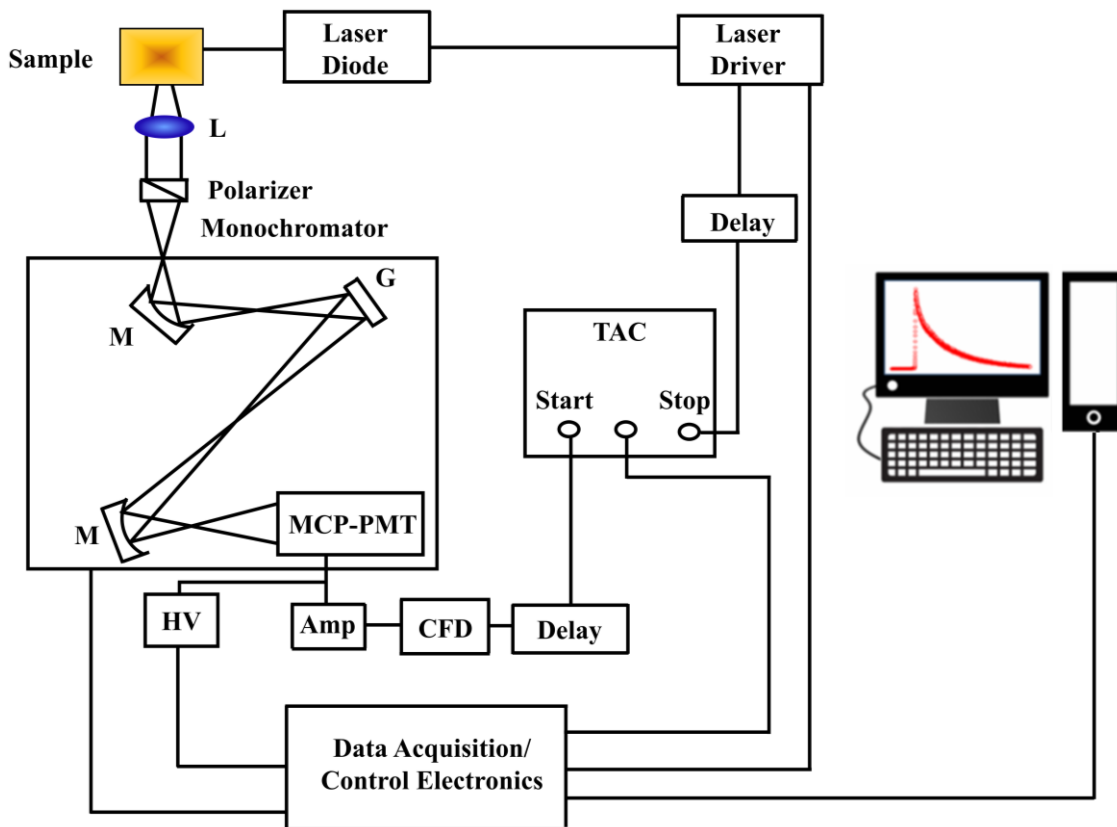


Figure 3.3. Schematic ray diagram of a time correlated single photon counting (TCSPC) spectrophotometer. A signal from microchannel plate photomultiplier tube (MCP-PMT) is amplified (Amp) and connected to start channel of time to amplitude converter (TAC) via constant fraction discriminator (CFD) and delay. The stop channel of the TAC is connected to the laser driver via a delay line. L, M, G and HV represent lens, mirror, grating and high voltage source, respectively.

third harmonic laser beam (290-300 nm) of the 870-900 nm (0.5 nJ per pulse) using a mode-locked Ti-sapphire laser with an 80 MHz repetition rate (Tsunami, Spectra-Physics), pumped by a 10 W Millennia (Spectra-Physics) followed by a pulse-peaker (rate 8 MHz) and a third harmonic generator (model 3980, Spectra-Physics). The third harmonic beam was used for excitation of the sample inside the TCSPC instrument (IRF = 70 ps) and the second harmonic beam was collected for the start pulse.

3.1.3. Transmission Electron Microscopy (TEM): A JEOL JEM-2100 high-resolution TEM (HRTEM) (Figure 3.4) equipped with an energy dispersive X-ray (EDAX) spectrometer was used to characterize the microscopic structures of samples and to analyze their elemental composition. The sizes of the nanoparticles were determined from the TEM images obtained at 200 kV. Samples for TEM were prepared by placing a drop of the colloidal solution on a carbon-coated copper grid and allowing the film to evaporate overnight at room-temperature.

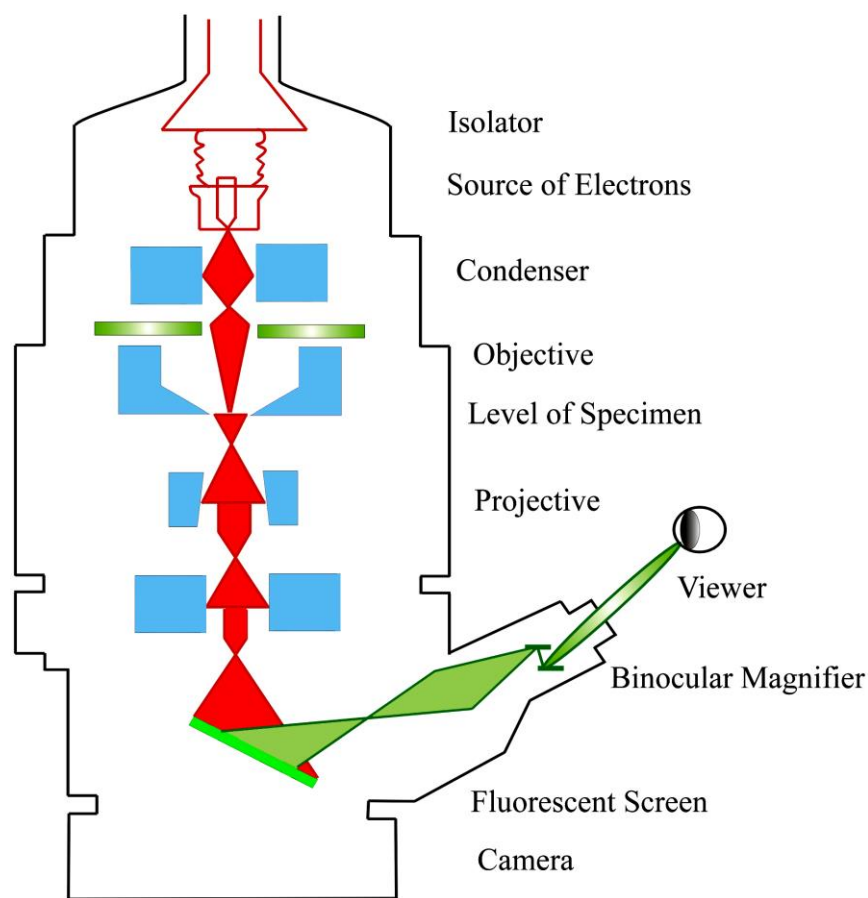


Figure 3.4. Schematic diagram of a typical transmission electron microscope (TEM). After the transmission of electron beam through a specimen, the magnified image is formed either in the fluorescent screen or can be detected by a CCD camera.

3.1.4. Fourier Transform Infrared (FTIR) Measurement: FTIR spectroscopy is a technique that can provide very useful information about functional groups in a sample. An infrared spectrum represents the fingerprint of a sample with absorption peaks which corresponds to the frequencies of vibrations between the bonds of the atoms making up the material. Because each different material is a unique combination of atoms, no two compounds produce the exact same infrared spectrum. Therefore, infrared spectroscopy can result in a positive identification (qualitative analysis) of all different kinds of material. In addition, the size of the peaks in the spectrum is a direct indication of the amount of material present. The two-beam Michelson interferometer is the heart of FTIR

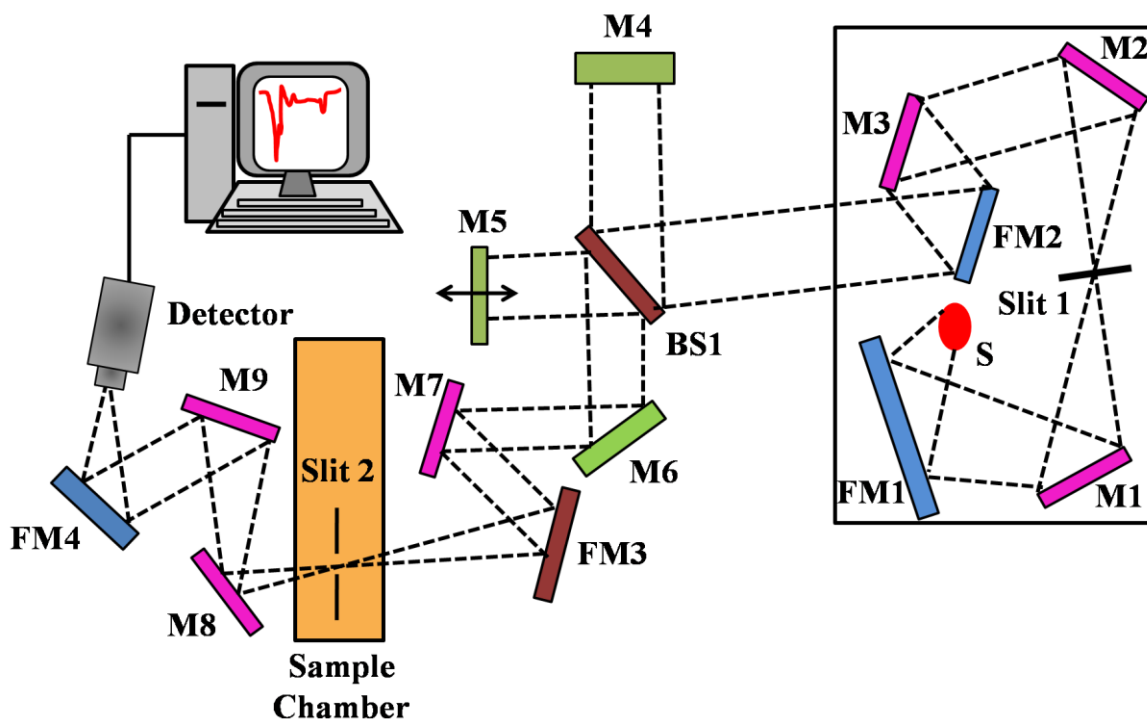


Figure 3.5. Schematic of Fourier Transform Infrared (FTIR) spectrometer. It is basically a Michelson interferometer in which one of the two fully-reflecting mirrors is movable, allowing a variable delay (in the travel-time of the light) to be included in one of the beams. M, FM and BS1 represent the mirror, focussing mirror and beam splitter, respectively. M5 is a moving mirror.

spectrometer. It consists of a fixed mirror (M4), a moving mirror (M5) and a beam-splitter (BS1), as illustrated in Figure 3.5. The beam-splitter is a laminate material that reflects and

transmits light equally. The collimated IR beam from the source is partially transmitted to the moving mirror and partially reflected to the fixed mirror by the beam-splitter. The two IR beams are then reflected back to the beam-splitter by the mirrors. The detector then sees the transmitted beam from the fixed mirror and reflected beam from the moving mirror, simultaneously. The two combined beams interfere constructively or destructively depending on the wavelength of the light (or frequency in wavenumbers) and the optical path difference introduced by the moving mirror. The resulting signal is called an interferogram which has the unique property that every data point (a function of the moving mirror position) which makes up the signal, has information about every infrared frequency which comes from the source. Because the analyst requires a frequency spectrum (a plot of the intensity at each individual frequency) in order to make identification, the measured interferogram signal cannot be interpreted directly. A means of “decoding” the individual frequencies is required. This can be accomplished *via* a well-known mathematical technique called the Fourier transformation. This transformation is performed by the computer which then presents the user with the desired spectral information for analysis. FTIR measurements were performed on a JASCO FTIR-6300 spectrometer (transmission mode). Each spectrum consists of 100 scans ($1500\text{--}4000\text{ cm}^{-1}$) acquired at 0.5 cm^{-1} resolution.

3.1.5. Laser Raman Spectroscopy: Raman spectroscopy is a useful technique for the identification of a wide range of substances solids, liquids, and gases. It is a straightforward, non-destructive technique requiring no sample preparation. Raman spectroscopy involves illuminating a sample with monochromatic light and using a spectrometer to examine light scattered by the sample.

At the molecular level photons can interact with matter by absorption or scattering processes. Scattering may occur either elastically, or inelastically. The elastic process is termed Rayleigh scattering, while the inelastic process is termed Raman scattering. The electric field component of the scattering photon perturbs the electron cloud of the molecule and may be regarded as exciting the system to a 'virtual' state. Raman scattering occurs when the system exchanges energy with the photon, and the system subsequently decays to vibrational energy levels above or below that of the initial state. The frequency shift corresponding to the energy difference between the incident and scattered photon is termed as the Raman shift. Depending on whether the system has lost or gained vibrational energy, the Raman shift occurs either as an up or down-shift of the scattered photon frequency relative to that of the incident photon. The down-shifted and up-shifted components are called, respectively, the Stokes and anti-Stokes lines. A plot of detected number of photons versus Raman shift from the incident laser energy gives a Raman spectrum. Different materials have different vibrational modes, and therefore characteristic Raman spectra. This makes Raman spectroscopy a useful technique for material identification. There is one important distinction to make between the Raman spectra of gases and liquids, and those taken from solids in particular, crystals. For gases and liquids it is meaningful to speak about the vibrational energy levels of the individual molecules which make up the material. Crystals do not behave as if composed of molecules with specific vibrational energy levels, instead the crystal lattice undergoes vibration. These macroscopic vibrational modes are called phonons.

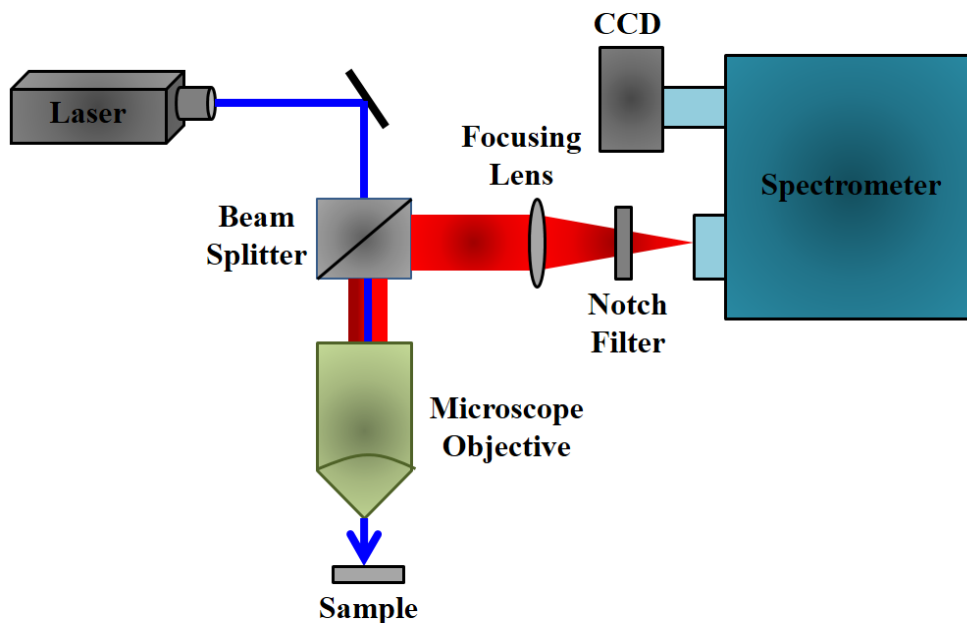


Figure 3.6. Schematic diagram of a Raman spectrometer is shown.

In our Raman spectrometers (LabRAM HR, Jobin Yvon), lasers are used as a photon source due to their highly monochromatic nature, and high beam fluxes (Figure 3.6). This is necessary as the Raman effect is weak, typically the Stokes lines are $\sim 10^5$ times weaker than the Rayleigh scattered component. In the visible spectral range, Raman spectrometers use notch filters to cut out the signal from a very narrow range centred on the frequency corresponding to the laser radiation. Most Raman spectrometers for material characterization use a microscope to focus the laser beam to a small spot ($< 1-100 \mu\text{m}$ diameter). Light from the sample passes back through the microscope optics into the spectrometer. Raman shifted radiation is detected with a charge-coupled device (CCD) detector, and a computer is used for data acquisition and curve fitting. These factors have helped Raman spectroscopy to become a very sensitive and accurate technique. In our experiments, Raman scattering measurements were performed in a back scattering geometry using a micro-Raman setup consisting of a spectrometer (model LabRAM HR,

JobinYvon) and a Peltier-cooled CCD detector. An air cooled argon ion laser with a wavelength of 488 nm was used as the excitation light source. Raman spectra of all samples have been recorded at room temperature in the frequency range of 50–4000 cm^{-1} .

3.1.6. Thermogravimetric-Differential Thermal Analyzer (TG-DTA) Setup: The thermogravimetric (TG) analysis was carried out using Diamond thermogravimetric (TG)-differential thermal analyzer (DTA) from Perkin Elmer. The TG determines the weight change of a sample whereas the DTA measures the change in temperature between a sample and the reference as a function of temperature and/or time. The schematic of the TG-DTA setup is shown in Figure 3.7. When a weight change occurs on the sample side, the beam holding the platinum pans is displaced. This movement is detected optically and the driving coil current is changed to return the displacement to zero. The detected driving coil current change is proportional to the sample weight change and the output is the TG signal. The DTA detects the temperature difference between the sample holder and the reference holder using the electromotive force of thermocouples, which are attached to the holders. This difference is measured as the DTA signal.

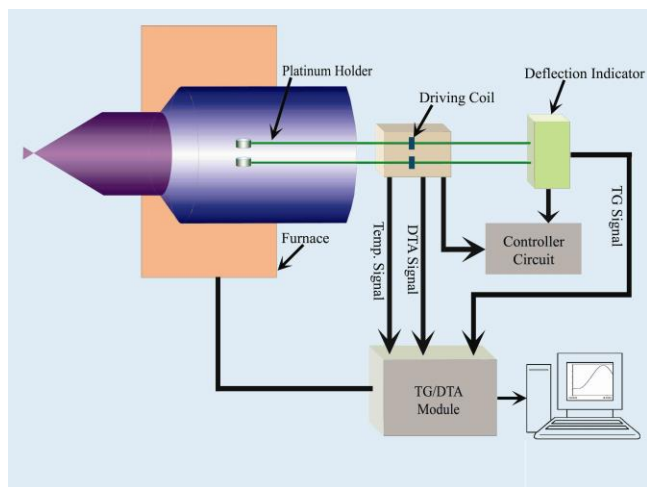


Figure 3.7. The schematic representation of TG-DTA setup.

3.1.8. Viscosity Measurement: The viscosity of the mixtures were measured by an automated micro viscometer (AVMn) from Anton Paar (Austria). The viscosity of the sample are measured by Höppler falling ball principle. The basic concept is to measure the elapsed time required for the ball to fall under gravity through a sample-filled tube inclined at an angle. The tube is mounted on a pivot bearing which quickly allows rotation of the tube by 180 degrees, thereby allowing a repeat test to run immediately. Several measurements are taken and the average time is converted into a final viscosity value in centipoise (cP).

The dynamic viscosity in Höppler falling ball method is calculated by the following equation:

$$\eta = t(\rho_1 - \rho_2)K * F \quad (3-1)$$

where: η is the dynamic viscosity [mPa.s]; t is the travelling time of the ball [s]; ρ_1 is the density of the ball [g cm^{-3}]; ρ_2 density of the sample [g cm^{-3}]; K ball constant [$\text{mPa}\cdot\text{cm}^3 \text{g}^{-1}$]; F working angle constant.

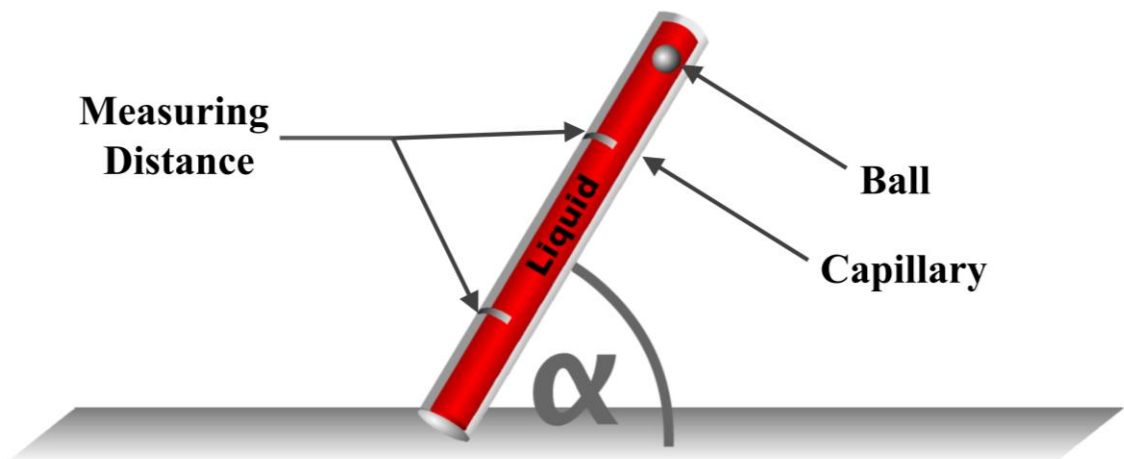


Figure 3.8. Schematic representation of the automated micro viscometer.

3.1.9. Refractive Indices Measurement: Refractive indices of the solutions were measured by using a Rudolph J357 automatic refractometer. The instrument measures the refractive indices using sodium D-line of wavelength 589.3 nm with accuracies ± 0.00004 . The measurement of the refractive index of the sample is based on the determination of the critical angle of total reflection. A light source, usually a long-life LED, is focused onto a prism surface via a lens system. Due to the focusing of light to a spot at the prism surface, a wide range of different angles is covered. As the measured sample is in direct contact

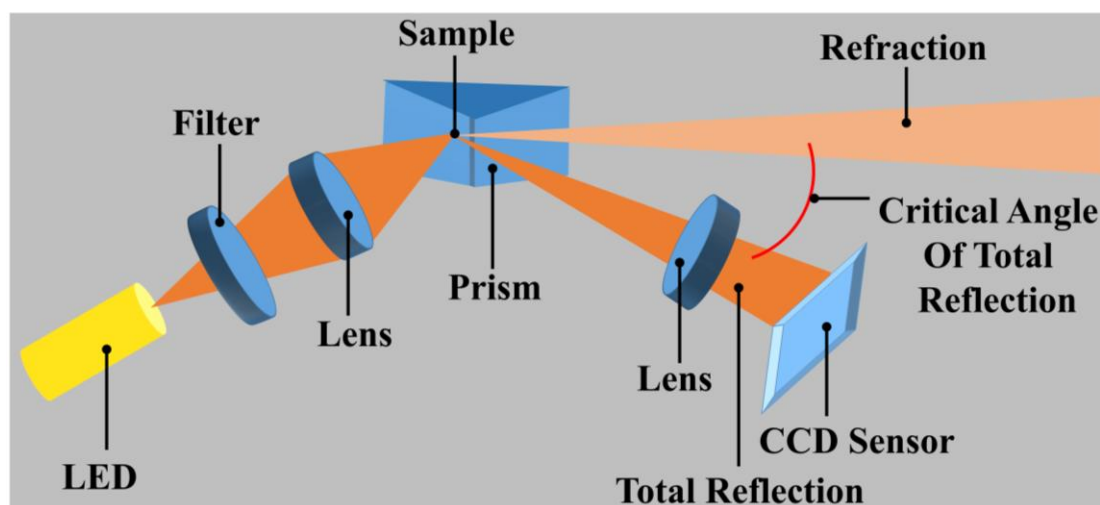


Figure 3.9. Schematic representation of the refractometer.

with the measuring prism. Depending on its refractive index, the incoming light below the critical angle of total reflection is partly transmitted into the sample, whereas for higher angles of incidence the light is totally reflected. This dependence of the reflected light intensity from the incident angle is measured with a high-resolution sensor array. From the video signal taken with the CCD sensor the refractive index of the sample can be calculated.

3.2. Sample Preparation: In this section the different sample preparation methods have been discussed.

3.2.1. Chemicals Used: The chemicals, spectroscopic probes, and biomolecules were procured from the following sources. Analytical-grade chemicals were used for synthesis without further purification. All the aqueous solutions were prepared using double distilled water. Millipore water was used throughout the experiments. The chemicals phosphate buffer (disodium hydrogen phosphate, monosodium hydrogen phosphate), sodium tartrate, sodium hydroxide, potassium bromide, bilirubin, magnesium chloride, riboflavin (Rf), 2,2-diphenyl-1-picrylhydrazyl (DPPH), caffeine, rose bengal (RB), 4',6-diamidino-2-phenylindole (DAPI), benzo[α]pyrene, zinc acetate dehydrate [$\text{Zn}(\text{CH}_3\text{COO})_2 \cdot 2\text{H}_2\text{O}$], 30 nm ZnO NPs, TiO_2 NPs, Al_2O_3 NPs, riboflavin, gold (III) chloride, sodium citrate, caffeine, benz[*o*]pyrene and CT-DNA were obtained from Sigma-Aldrich. Oleylamine/oleylacid capped ~23 nm Fe_3O_4 NPs were purchased from Ocean NanoTech, LLC (Springdale, USA). Methylene blue was purchased from Carlo Erba. Hexadecyltrimethylammonium bromide (CTAB) (Fluka), isooctane (Spectrochem) Sodium bis(2ethylhexyl) sulfosuccinate (AOT) and sodium dodecyl sulfate (SDS) were obtained from Fluka. Dimethyl sulphoxide (DMSO), Hydrochloric acid ethanol, acetonitrile and sodium azide was purchased from Merck. All the chemicals and the proteins were of highest purity available and used without further purification.

3.2.2. Preparation of Micellar Solution: The micellar solutions were prepared by dissolving surfactant salts in buffer of required pH. Micellar solutions of the probe were prepared by adding known concentrated aqueous probe solution to micellar solution of desired concentration with simultaneous stirring of the mixture for an hour [2].

3.2.3. Preparation of Reverse Micellar Solution: Reverse micellar solutions of specific degree of hydration ($w_0 = [\text{H}_2\text{O}]/[\text{Surfactant}]$) were prepared by addition of calculated

volume of aqueous solution of the probe in known volume of 100 mM AOT solution in isooctane [3, 4]. In order to ensure that each reverse micelle contains not more than one probe molecule, the overall probe concentration was kept less than that of micellar concentration.

3.2.4. Synthesis of 5 nm ZnO NPs: In order to synthesize colloidal solution of ZnO nanoparticles (NPs), zinc acetate dihydrate, $\text{Zn}(\text{CH}_3\text{COO})_2 \cdot 2\text{H}_2\text{O}$ (Merck), was used as starting material. 40 mL of 2 mM zinc acetate solution was prepared in ethanol (Merck). Then 20 mL of 4 mM NaOH solution in ethanol was added to it under constant stirring. The reaction beaker was then kept in a preheated water bath at 60 °C for 2 h to hydrolyse, after which a transparent ZnO NP colloid was obtained [5].

3.2.5. Synthesis of Riboflavin Nanohybrids with ZnO NPs, TiO₂ NPs and Al₂O₃ NPs: 20 μM Rf solution was prepared in alcohol. 0.5mg/ml of solid 30 nm ZnO, TiO₂ and Al₂O₃ were added to prepared Rf solution and were stirred constantly for 12h. The sensitization of ZnO NPs, TiO₂ NPs and Al₂O₃ NPs with Rf dye was performed at room temperature in the dark. After the sensitization process, the solution was centrifuged for a while and the clear supernatant solution of unattached dyes was decanted. Then the nanohybrids were washed with alcohol 3-4 times. Then the samples were dried in a water bath. The Rf concentration in the nanohybrids was 3 μM [6].

3.2.6. Synthesis of Riboflavin-Gold Nanohybrids: 10 mL 80 μM Rf solution was prepared in water. 100 mM stock solution of AuCl₃ was prepared. 50 μl of Au (III) chloride solution was mixed with 10 mL of the stock riboflavin solution. The mixture was

kept under UV-light ($\lambda_{\max}=365$ nm) for 15 minutes till the characteristic surface plasmon resonance band was observed at 540 nm [7]. Here, a different technique is used to remove free riboflavin from AuNPs. Since it is difficult to retrieve Rf-AuNPs after centrifugation, the excess dye was driven out by dialysis prior to the experiments. The Rf and AuNPs concentrations in the nano hybrids were 40 μ M and 0.1nM, respectively.

3.2.7. Synthesis of Citrate-Capped Gold Nanoparticles: 0.5 M stock solution of sodium citrate and 100 mM stock solution of AuCl₃ were prepared in water. 20 μ L of stock sodium citrate was added to 4 mL of 0.5mM of AuCl₃ solution while boiling it. The solution turned reddish in colour. The formation of gold NPs was confirmed by surface plasmon resonance band at 540 nm [8].

3.2.8. Synthesis of Rose Bengal Nano hybrids with ZnO NPs: RB solution of 0.5 mM was prepared in acetonitrile. To the prepared RB solution, 1mg/ml of solid 30 nm ZnO NPs were added and constantly stirred for 12h. ZnO NP sensitization with RB dye was performed at room temperature in the dark. The solution was centrifuged for some time and the clear supernatant solution of free dyes was decanted after the sensitization process. The samples were finally dried in a water bath after washing 3-4 times with acetonitrile.

3.2.9. Preparation of DNA Fragment: For the preparation of DNA fragments, a 1300-bp sequence of Origin Recognition Complex (ORC1) DNA from *Leishmania donovani* was amplified from pGAT2ORC1 plasmid by PCR (Eppendorf, Germany) using primers LdORC1R1+ (5'GCAC TGA ATT CAA ATG AAG CGG AGC CGG CGA GC 3') and LdORC1Not1.1- (5' GCT TCT GCG GCC GCC AAG TGC AGC GCT GCC CCG T 3'). The PCR product was purified using PCR clean up kit (Axygen, USA).

3.2.10. Preparation of Dye-DNA Complex: BP-DNA complexes were prepared as per the methodology reported previously [9] by Geacintov et al. In the fluorescence experiments of BP and CT-DNA, concentration of BP was 1 μ M while that of CT-DNA was 1 mM. For steady state and time resolved studies the [dye]:[DNA] ratio was kept low to ensure complete complexation of the probe [10].

3.2.11. Preparation of Dichlorofluorescein and ROS Measurements: DCFH was prepared from DCFH-DA (dichlorofluorescein diacetate obtained from Calbiochem). 0.5 mL of 1.0 mM DCFH-DA in methanol was mixed with 2.0 mL of 0.01 N NaOH at room temperature for 30 min. The mixture was then neutralized with 10 mL of 25 mM NaH_2PO_4 , pH 7.4. All the measurements were performed in a total volume of 2.0 mL water that contained 10 μ L of DCFH solution, RB (3 μ M), ZnO (200 μ M) and RB-ZnO (individual concentrations of RB and ZnO in the nanohybrid in DMSO are 3 μ M and 200 μ M, respectively) [11].

3.2.12. Cells and Cell Culture Conditions: Squamous epithelial cells were collected from the inner lining of the human mouth. WI-38 (fibroblast), MCF-7 (breast cancer) and HeLa cells were grown in Dulbecco's modified Eagle's medium (DMEM) supplemented with 10% fetal bovine serum and penicillin-streptomycin (0.5 U/ml of penicillin and 0.5 μ g/ml streptomycin) in 35 mm dishes at 37°C in an atmosphere of air with 5% CO_2 and constant humidity [12].

3.2.13. Bacterial Strain and Culture Conditions: The antibacterial assay was performed using *E. coli* XL1-Blue cells. The cells were cultured at 37 °C in a liquid LB (Luria-Bertani) medium. When the optical density reached around 0.6, the culture was serially

diluted ten thousand times with LB medium and treated with drugs containing RB (3 μM), ZnO (200 μM) and RB-ZnO (individual concentrations of RB and ZnO in the nanohybrid in DMSO are 3 μM and 200 μM respectively). The RB concentration is calculated from the absorption maxima around 540 nm as ZnO lack absorbance above 380 nm. The samples were then kept under the green light (λ_{max} of 520 nm, ~14600 LUX) for four hours. The photodynamic effect was studied by plating the treated samples in LB agar plates and incubated them overnight at 37°C. After overnight incubation, the colonies were counted.

3.2.14. Fungal Strain and Culture Conditions: The antifungal assay was studied using *C. albicans*. The cells were cultured at 30 °C in a liquid Yeast Extract Peptone Dextrose (YEPD) broth. When the optical density reached around 0.6, the inoculum was serially diluted ten thousand times with YEPD medium and treated with RB (3 μM), ZnO (200 μM) and RB-ZnO (individual concentrations of RB and ZnO in the nanohybrid in DMSO were 3 μM and 200 μM respectively). The samples were then given the green light (λ_{max} of 520 nm, ~14600 LUX) exposure for four hours. To study the effect of light, the inoculum was plated and incubated for 24 hours. Finally, the colonies were counted after the incubation.

3.2.15. 3-(4,5-dimethylthiazol-2-yl)-2,5-diphenyltetrazolium bromide (MTT) Assay: A colorimetric method for the estimation of cell densities using MTT proved to be more accurate and timesaving than conventional hemocytometer counting [13]. It is one of the *in vitro* cytotoxicity assays which is based on mitochondrial dehydrogenase activity of the cells [14]. 1.9×10^5 cells HeLa were seeded and cultured in 10% FBS-supplemented DMEM. 165 μl cells from the stock culture were seeded in 96-well plate for the photodynamic treatment. Cells were incubated with RB (3 μM), ZnO (200 μM) and RB-

ZnO (individual concentration of RB and ZnO in the nanohybrid in DMSO were 3 μ M and 200 μ M, respectively) for an hour and were given green light exposure (λ_{max} : 520 nm, ~ 14600 LUX) for four hours. After overnight incubation, MTT assay was performed with fresh medium. 5 mg/ml MTT stock was prepared in sterile PBS. 15 μ l of the MTT stock solution was added to the cells and incubated for four hours. 150 μ l DMSO was added to solubilize the formazan before taking the absorbance at 570 nm.

3.2.16. Fluorescence Microscopy Studies: Micrographs of HeLa cells were taken using Zeiss AxioObserver Z1 Fluorescence Microscope which was attached with an Apotome apparatus. The cells were washed twice with PBS and fixed with 4% paraformaldehyde (Sigma) according to the standard protocol [15]. Finally, they were stained with Fluoroshield Mounting Medium with DAPI (ABCAM) before capturing the images at 40X magnification.

3.2.17. Quantum Yield (Q_D) Calculation: Q_D of the dye in any medium was calculated according to the following equation,

$$Q = Q_R \left(\frac{I}{I_R} \right) \left(\frac{OD_R}{OD} \right) \left(\frac{n^2}{n_R^2} \right) \quad (3-2)$$

where Q and Q_R are the values of quantum yield of the dye in the respected medium and the reference . I and I_R are the integrated fluorescence intensities of the dye and reference respectively. OD and OD_R are the optical densities of the dye and reference at the corresponding excitation wavelength, and n and n_R are the refractive indices of dye and reference solutions respectively. Refractive indices of the solutions were measured by using Rudolph J357 automatic refractometer.

References:

- [1] D.V. O'Conner, D. Philips, Time-Correlated Single Photon Counting, Academic Press, London, 1984.
- [2] S. Rakshit, R. Saha, P.K. Verma, R.K. Mitra, S.K. Pal, Ultrafast Electron Transfer in Riboflavin Binding Protein in Macromolecular Crowding of Nano-Sized Micelle, *Biochimie*, 94 (2012) 2673-2680.
- [3] S. Rakshit, R. Saha, S.K. Pal, Modulation of Environmental Dynamics at the Active Site and Activity of an Enzyme under Nanoscopic Confinement: Subtilisin Carlsberg in Anionic AOT Reverse Micelle, *J. Phys. Chem. B*, (2013) 11565-11574.
- [4] S. Rakshit, N. Goswami, S.K. Pal, Slow Solvent Relaxation Dynamics of Nanometer Sized Reverse Micellar Systems through Tryptophan Metabolite, Kynurenine, *Photochem. Photobiol.*, 88 (2012) 38-45.
- [5] S. Sardar, S. Chaudhuri, P. Kar, S. Sarkar, P. Lemmens, S.K. Pal, Direct Observation of Key Photoinduced Dynamics in a Potential Nano-Delivery Vehicle of Cancer Drugs, *Phys. Chem. Chem. Phys.*, 17 (2015) 166-177.
- [6] S. Chaudhuri, S. Sardar, D. Bagchi, S.S. Singha, P. Lemmens, S.K. Pal, Sensitization of an Endogenous Photosensitizer: Electronic Spectroscopy of Riboflavin in the Proximity of Semiconductor, Insulator, and Metal Nanoparticles, *J. Phys. Chem. A*, 119 (2015) 4162-4169.
- [7] Y. Shang, C. Min, J. Hu, T. Wang, H. Liu, Y. Hu, Synthesis of Gold Nanoparticles by Reduction of HAuCl_4 under UV Irradiation, *Solid State Sci.*, 15 (2013) 17-23.
- [8] J.J. Storhoff, R. Elghanian, R.C. Mucic, C.A. Mirkin, R.L. Letsinger, One-Pot Colorimetric Differentiation of Polynucleotides with Single Base Imperfections Using Gold Nanoparticle Probes, *J. Am. Chem. Soc.*, 120 (1998) 1959-1964.
- [9] N.E. Geacintov, T. Prusik, J.M. Khosrofian, Properties of Benzopyrene-DNA Complexes Investigated by Fluorescence and Triplet Flash Photolysis Techniques, *J. Am. Chem. Soc.*, 98 (1976) 6444-6452.
- [10] S. Banerjee, D. Bhowmik, P.K. Verma, R.K. Mitra, A. Sidhhanta, G. Basu, S.K. Pal, Ultrafast Spectroscopic Study on Caffeine Mediated Dissociation of Mutagenic Ethidium from Synthetic DNA and Various Cell Nuclei, *J. Phys. Chem. B*, 115 (2011) 14776-14783.

- [11] S. Chaudhuri, S. Sardar, D. Bagchi, S. Dutta, S. Debnath, P. Saha, P. Lemmens, S.K. Pal, Photoinduced Dynamics and Toxicity of a Cancer Drug in Proximity of Inorganic Nanoparticles under Visible Light, *Chem. Phys. Chem.*, 17 (2016) 270-277.
- [12] S. Banerjee, S. Chaudhuri, A.K. Maity, P. Saha, S.K. Pal, Role of Caffeine in DNA Recognition of a Potential Food-Carcinogen Benzo[a]pyrene and UVA Induced DNA Damage, *J. Mol. Recogn.*, 27 (2014) 510-520.
- [13] F.M. Freimoser, C.A. Jakob, M. Aebi, U. Tuor, The MTT [3-(4,5-Dimethylthiazol-2-yl)-2,5-Diphenyltetrazolium Bromide] Assay is a Fast and Reliable Method for Colorimetric Determination of Fungal Cell Densities, *Appl. Environ. Microbiol.*, 65 (1999) 3727-3729.
- [14] M. Ishiyama, H. Tominaga, M. Shiga, K. Sasamoto, Y. Ohkura, K. Ueno, A Combined Assay of Cell Viability and in Vitro Cytotoxicity with a Highly Water-Soluble Tetrazolium Salt, Neutral Red and Crystal Violet, *Biol. Pharm. Bull.*, 19 (1996) 1518-1520.
- [15] E. Harlow, D. Lane, Fixing Attached Cells in Paraformaldehyde, *Cold Spring Harb Protoc*, 2006 (2006) pdb.prot4294.

Chapter 4

Photo-Sensitization of Medicinally Important Drugs

4.1. Introduction:

A vital micronutrient, riboflavin (vitamin B₂) is an essential vitamin found in milk, cheese, vegetables, yeast, mushrooms, eggs and meat products [1, 2]. It is a crucial precursor of the coenzymes flavin mononucleotide (FMN) and flavin adenine dinucleotide (FAD) [3-6]. These coenzymes with dehydrogenase and oxidase activities play a key role in electron transport chain for cellular metabolism in human beings [7, 8]. Although, use of the vitamin as antioxidant drug is conventional in medicine [9, 10], the activity of the vitamin under visible light has a long history of scientific reports [11, 12]. It is well known that upon photoexcitation, the isoalloxazine ring system undergoes intramolecular photo-reduction in which the ribityl side chain donates electron in the absence of an external reductant [13]. A few photoproducts are formed due to oxidation of the side chain. It is converted to lumichrome upon photolysis in neutral aqueous solutions, and into lumiflavin in alkaline conditions [1, 14-16]. The vitamin under visible light can also generate reactive oxygen species (ROS) such as superoxide anions and singlet oxygen [17, 18]. Upon photoexcitation, the vitamin ($^1\text{Rf}^*$) is converted to excited triplet riboflavin ($^3\text{Rf}^*$), through intersystem crossing which is reduced by abstraction of electrons or hydrogen ion to form riboflavin radical [19]. The riboflavin radical eventually reacts with atmospheric triplet oxygen to form superoxide anion and singlet oxygen [8, 20].

The density of oxygen, the concentration of the vitamin riboflavin and the presence of other oxidizable reactants or quenchers determines the distribution of the reactive oxygen species (ROS) formed in a particular system [18, 21, 22]. The excited state relaxation of the vitamin in protein environments is found to be ultrafast (femtosecond-picosecond) in nature and due to the electron transfer from the vitamin to the proximal amino acids in the protein [23, 24]. Antioxidant activity of the vitamin is generally estimated by monitoring free radical scavenging of a stable free radical 2,2-diphenyl-1-picrylhydrazyl (DPPH; violet colour), in absence of visible light [25]. It is well established that the vitamin supplement in the diet can enhance the scavenging kinetics in cellular medium [26]. The vitamin is found to donate a proton/electron to the radical DPPH eventually reducing the radical to DPPH₂ form, revealing decolourization (from violet to yellow) of the medium [27, 28]. Although antioxidant property of the vitamin is estimated using DPPH as model oxidizing agent in absence of light [29], very little is known about the photosensitized antioxidant activity of riboflavin [30], which is the focus of the present study. In a recent report, antimicrobial activity of riboflavin under visible light irradiation is illustrated [31].

Here we have studied the antioxidant activity of vitamin B₂ under visible light irradiation (blue light, $\lambda_{\text{max}} = 450 \text{ nm}$) in a variety of nanoscopic physiologically important environments. We have compared the experimental observation of the antioxidant activity with that in dark in ethanol water (1:1) solution. Our observation of photo-antioxidant activity of the vitamin in a number of micelles with different charges (anionic, cationic and neutral) reveals the importance of the location of the oxidizing agent for the efficacy of antioxidant activity of the vitamin in the physiologically relevant environments. For instance, the cationic hexadecyltrimethylammonium bromide (CTAB) micelle is capable of mimicking histone protein [32], the neutral (polar) TritonX-

100 (TX-100) resembles a protein cavity [33] and the anionic sodium dodecyl sulphate (SDS) micelle can be a good substitute of the negatively charged DNA surface [34, 35]. On the other hand, our studies of the photo-antioxidant property in AOT reverse micelle (RMs) with various degrees of hydration (different hydrodynamic diameters of the water pool) clearly show the importance of the proximity of the oxidizing agent with respect to the excited vitamin. Reverse micelles (RMs) are nanopools of polar solvent surrounded by a monolayer of surfactant molecules at the periphery with polar head groups pointing inward toward the polar solvent and the hydrocarbon tails are directed toward the nonpolar organic solvents [36]. Reverse micelles with water nanopools resemble the water pockets found in various bio-aggregates such as proteins, membranes and mitochondria [37]. Thus, these systems are very often considered as excellent biomimetics for exploration of biological membranes and biologically confined water molecules [38]. While the antioxidant property of the vitamin is followed by observing decolourization kinetics of DPPH in the environments, in order to quantitatively estimate the distance between the oxidizing agent (DPPH) and the excited vitamin prior to the antioxidant activity, we have employed picosecond resolved Förster Resonance Energy Transfer (FRET) in the nanoscopic environments of micelles and RMs with various degrees of hydration. We have also analyzed the probability distribution of the RF-DPPH distances in the nanoenvironments. Overall, our studies unravel a mechanistic pathway for the photoinduced antioxidant property of the important vitamin in a number of physiologically important nanoenvironments.

4.2. Results and Discussion:

4.2.1. Vitamin B₂ in Nanoscopic Environments under Visible Light: Photosensitized Antioxidant or Phototoxic Drug? [39]:

The molecular structures of riboflavin (Rf; vitamin B₂) and model free-radical (DPPH) are shown in the upper panel of Figure 4.1. Riboflavin (nitrogen circled red) transfers electrons to appropriate hydrogen acceptors in photochemical reactions [13] whereas the nitrogen centered (circled blue) free radical accepts electron or hydrogen radical to form stable diamagnetic molecule in the antioxidant mechanism [40, 41]. The absorption and emission spectra of Rf in ethanol water (1:1) solution are shown in the lower panel of Figure 4.1.

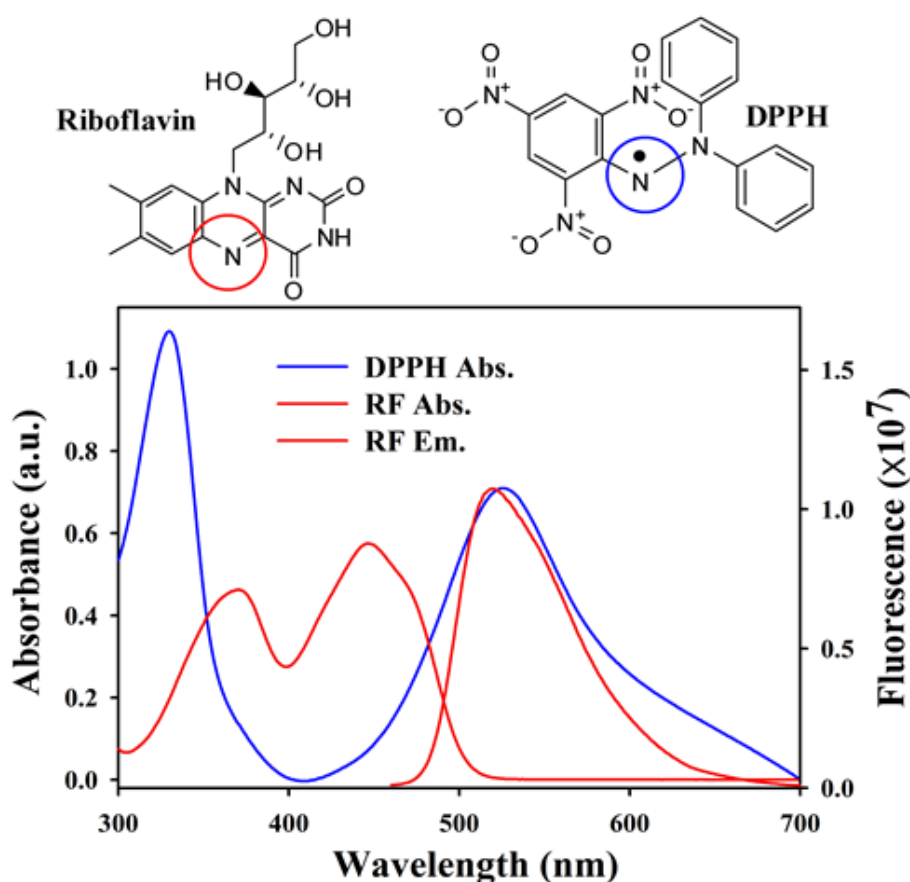


Figure 4.1. Upper panel. Circled Nitrogen in red denotes the electron donor of riboflavin which transfer its electrons to appropriate hydrogen acceptors in photochemical reactions and circled nitrogen in blue depicts the nitrogen centered free radical (see text). **Lower panel.** Absorption and Emission spectra of Riboflavin ($\lambda_{ex} = 450 \text{ nm}$, $\lambda_{em} = 520 \text{ nm}$) and DPPH (absorption peak at 520 nm).

The absorption spectrum of DPPH in the Figure 4.1 clearly reveals a significant spectral overlap with the emission spectrum of RF. The large spectral overlap is also indicative of the possibility of “excited state energy transfer” from RF to the free radical

DPPH prior to the radical scavenging and there is a change in the relative fluorescence intensity.

Figure 4.2 shows the kinetics of free radical scavenging activity of RF in ethanol water (1:1) solution in the dark compared to that in presence of blue light ($\lambda_{em}=450$ nm). The free radical scavenging kinetics of RF in absence and presence of blue light have been fitted with single exponential decay functions and the time constants are found to be 2051 sec to 66 sec respectively. A significant enhancement in the rate of radical scavenging of the vitamin in presence of blue light is clearly evident from the Figure 4.2. It is also evident from the Figure 4.2 that there is a significant retardation of the scavenging activity in presence of sodium azide (NaN_3), a potential ROS quencher.

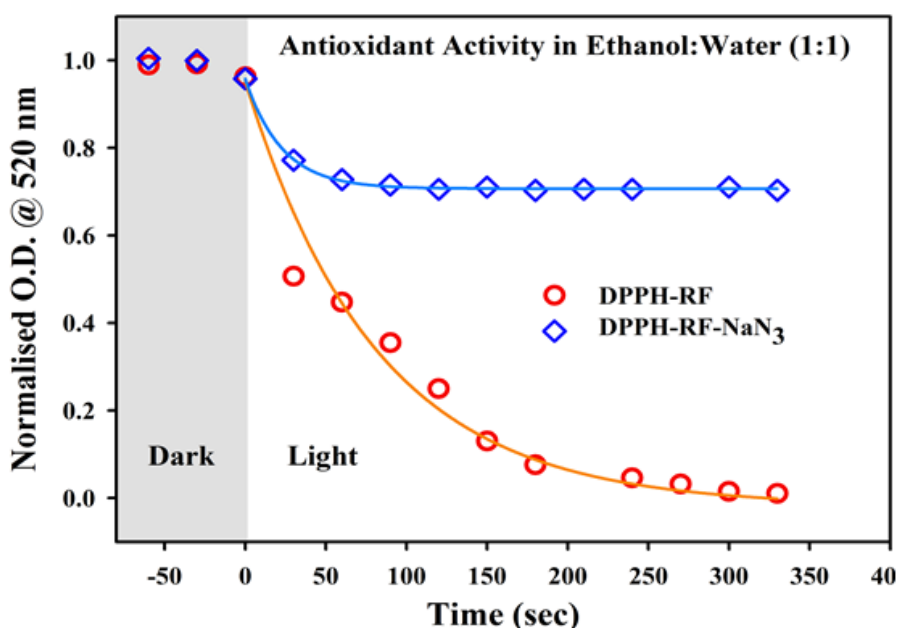


Figure 4.2. depicts the absorption kinetics (degradation monitored at 520 nm) of Riboflavin-DPPH in presence and absence of sodium azide (50 mM) in ethanol water (1:1) solution. Blue light irradiation is given from the point “0” at X-axis.

Earlier reports state that the proximal radical scavenging activity of most antioxidants occur by donating H-atoms, either by H-atom transfer (HAT) or stepwise electron transfer–proton-transfer (ET–PT) or sequential proton-loss–electron-transfer

(SPLET) [42-45]. Our observation on reduction of photo-antioxidant activity of the vitamin Rf in presence of ROS quencher NaN_3 clearly reveals the formation of ROS from the excited Rf following the mechanism detailed in the earlier literature [8]. In the absence of sodium azide, ROS generated from excited vitamin quenches DPPH proximally as well as through distance resulting in enhanced yield of scavenging (~100% in our time window). By addition of NaN_3 , only proximal DPPH can access riboflavin for radical scavenging which initially causes higher rate (time constant of 23 sec) of degradation, but low yield (about 30% scavenging in our time window). The structural integrity of the vitamin in presence of NaN_3 has been confirmed through absorption and emission spectra of Rf (data not shown). Our observation indicates that scavenging of the DPPH free radical in the solution is essentially governed by the generation of ROS from the excited vitamin and thus proximity between Rf and DPPH in solution has minimal effect on the photoinduced antioxidant property of the vitamin. In earlier studies [40, 46] the redox reaction mechanism of DPPH with ROS has been elaborated. While several reaction product in the redox processes involving DPPH converts oxygen anion (O_2^-) into oxidants (OH^\cdot , HOO^\cdot), formation of minor amount of reaction products have been found by using TLC techniques [46].

Figure 4.3.a shows antioxidant activity of the vitamin in aqueous micellar solutions, namely SDS (anionic), CTAB (cationic) and TX-100 (neutral) in dark and light conditions. While a significant enhancement of the activity upon irradiation is evident, the rate of antioxidant activity in presence of light is observed to depend on the nature of charges in the head groups of the micelles. Rf shows almost similar affinity to all the micelles under investigation discarding role of specific Rf localization in the different antioxidant activity. Our studies indicate that Rf essentially stay outside the micelles in the bulk solution. Our experiments were performed with equal

concentrations of RF and DPPH in micelles with various charges on the head groups. From the Figure 4.3.a, it is clear that the scavenging activities in the micelles follow the sequence of SDS >TX-100 > CTAB. The degradation time (in sec) of DPPH in SDS, TX-100 and CTAB were found to be 54.5, 275 and 300 respectively after fitting with first order decay function. The highest activity in the SDS micelle with anionic head group among other varieties can be rationalized in the following way. The free radical DPPH which has a large hydrophobic moiety is expected to lead the localization of the radical in the hydrophobic core of the micelles independent of the nature of the charges at the head group. DPPH is found to be sparingly soluble in bulk water. However, it has been reported earlier that the free radical in the DPPH is cationic in nature [44, 47] and is expected to reside near the interface of the anionic SDS micelles offering more accessibility to the excited RF in the bulk solution. In a recent study, enhanced DPPH radical scavenging activity of Rutin in anionic SDS micelle compared to other micellar charged varieties (CTAB, TX-100 etc) has been reported. Convenient localization of Rutin in the micellar interface in SDS and DPPH in the hydrophobic core are concluded to be reason for the enhanced activity.

Figure 4.3.b shows the antioxidant activity of RF in RMs with various degrees of hydrations. It has to be noted that RF, being polar would reside in the water pool of the RMs [24], whereas the hydrophobic DPPH is expected to reside in the bulk isooctane. However, the cationic charge in the free radical [47] is expected to compel the radical DPPH at the anionic interface of the AOT-RMs. A clear decrease in the antioxidant activity with the increase in the degree of hydration (from $w_0=5$ to $w_0=20$) is evident from the Figure 4.3.b. It is also noted that the decay time (in sec) of DPPH in AOT-RMs with $w_0=5$, $w_0=10$ and $w_0=20$ were found to be 50, 70 and 79 respectively

after fitting with first order decay function. The observation shows the importance of

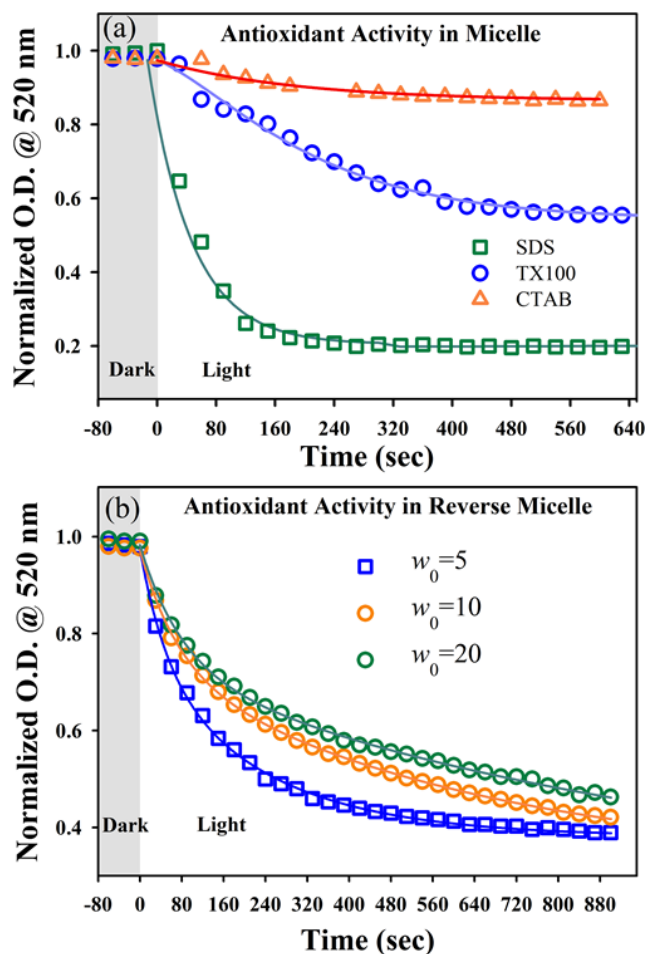


Figure 4.3. (a) depicts the absorption kinetics of DPPH (degradation monitored at 520 nm) in three micellar systems of SDS, TX-100 and CTAB and (b) shows the absorption kinetics of DPPH (degradation monitored at 520 nm) in AOT-reverse micelles with $w_0=5$, $w_0=10$ and $w_0=20$, in the presence of blue light (450 nm) and in dark, Blue light irradiation is given from the point “0” at X-axis.

the proximity of model oxidizing agent DPPH with the excited RF, which also reveals less importance of ROS in the reaction pathway that may lead distal effect [48]. The negligible role of ROS in the photoinduced antioxidant activity of the vitamin in the nanoenvironments including SDS micelles is also clear from Figure 4.4.a, where very minimum effect of NaN_3 (ROS quencher) in the antioxidant kinetics is observed (40 sec degradation time after fitting with first order decay function). In this context, it is worth mentioning that generation of ROS from the photoexcited RF should be

indiscriminative and it is expected to oxidize the RF itself leading to photodegradation of the vitamin.

In order to investigate the photodegradation of the RF in various environments, emission of the vitamin at 520 nm (DPPH has no emission) is found to be good marker rather than the absorption at 450 nm (peak absorption of the vitamin B₂) as the interference of the absorption due to DPPH (absorption peak at 520 nm) is unavoidable at the detection wavelength. It has to be noted that the photodegradation of the parent Rf may result some luminescent photoproducts including lumichrome or lumiflavin and may interfere with the emission of Rf. However, the fluorescence quantum yields of the major photoproducts; lumichrome (0.008 in water), lumiflavin (0.14 in water), are significantly lower than that of the parent Rf (0.3 in water). Thus photodegradation of the parent molecule (Rf) would always reduce the fluorescence intensity. Although, final intensity of emission may be convoluted with the photo-products, the kinetics of fluorescence quenching is expected to reflect the rate of photo-conversion of Rf to other products, in other word photodegradation. The photodegradation of Rf in ethanol water (1:1) solution shows first order kinetics (Figure 4.4.b) and the rate of deterioration decreases (from 281 sec to 6000 sec) in presence of NaN₃ revealing the role of ROS in the self-degradation of the vitamin. Figures 4.4.c and 4.4.d show kinetics of Rf emission in SDS micelles in presence and absence of DPPH respectively. As shown in Figure 4.4.c, the emission kinetics of Rf in SDS micelles in presence of DPPH show a rise of time constant 63 sec followed by a decay of time constant of 144 sec. Existence of multiple excited state events is clear from the kinetics pattern. The rise component of the emission is consistent with the DPPH scavenging (Figure 4.4.a) time constant of 40 sec and thus can be assigned as the loss of energy transfer from Rf to DPPH in the micelle leading to temporal absorption quenching at 520 nm. The decay time constant

(Figure 4.4.c) of 144 sec is similar to the self-degradation time constant of 163 sec as shown in Figure 4.4.d. The Figure 4.4.d shows monotonous (single exponential with time constant of 163 sec) decrease of Rf emission in absence of DPPH in the micellar solution under blue light irradiation.

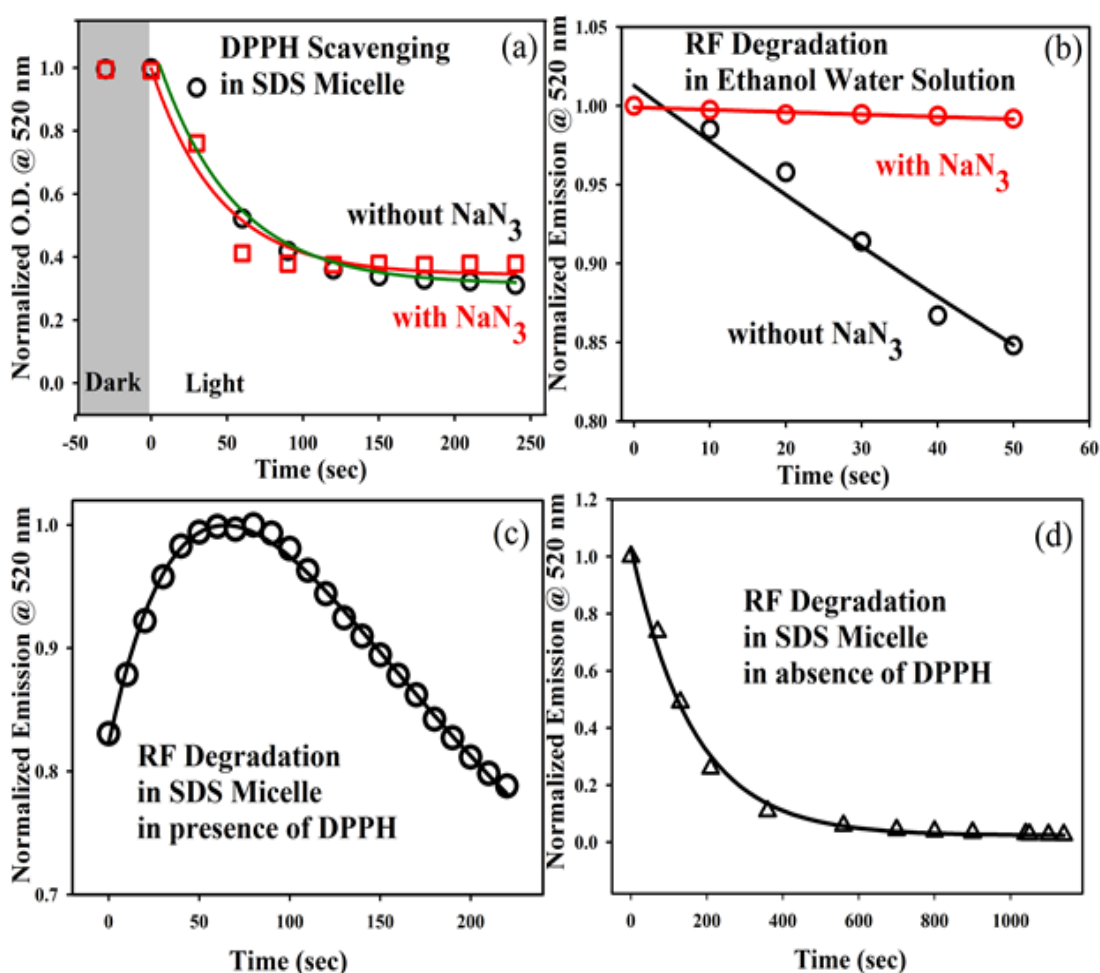


Figure 4.4. (a) depicts the absorption kinetics of riboflavin-DPPH in SDS micelles with and without 50 mM sodium azide, in presence of blue light and in dark; blue light irradiation is given from the point “0” at X-axis. (b) shows the emission spectra of riboflavin with and without 50mM sodium azide in ethanol water (1:1) solution Figures (c) and (d) show emission spectra of riboflavin in SDS micelles in presence and absence of DPPH respectively.

From our above observations on the photoinduced antioxidant properties of the vitamin RF in nanoscopic environments, the importance of the proximity of the model oxidizing agent DPPH with the excited Rf is clearly revealed. Whereas proximity of the vitamin with the oxidizing agent (DPPH) in the nanoscopic environments of micelles and reverse micelles are found to be important, a quantitative estimation of the

proximity leading to various degrees of photo-oxidation in the nanoenvironments is

Table 4.1. Picosecond-resolved fluorescence data fitting of Riboflavin with DPPH in micelles.

System	τ_1 (ns)	τ_2 (ns)	τ_3 (ns)	τ_{avg} (ns)
SDS micelle				
RF		0.11 (20%)	4.61 (80%)	3.7
RF-DPPH	0.03 (40%)	0.50 (14%)	4.54 (46%)	2.2
TX-100 micelle				
RF		0.22 (20%)	4.43 (80%)	3.6
RF-DPPH	0.10 (26%)	1.23 (10%)	4.59 (65%)	3.1
CTAB micelle				
RF		0.45 (40%)	2.38 (60%)	1.6
RF-DPPH	0.10 (18%)	0.50 (38.7%)	2.70 (43.3%)	1.4

(Numbers in parenthesis denote the relative weightage in percentage with ± 5 error).

Table 4 2. Förster Resonance Energy transfer (FRET) parameters of Riboflavin-DPPH with measured FRET efficiencies (E_{FRET}).

System	Q_Y	J (λ)	R_0	E_{FRET}	r (\AA)
Micelles					
SDS	0.250	7.91×10^{14}	35.49	41.0	37.70
TX-100	0.235	7.89×10^{14}	35.10	12.5	48.54
CTAB	0.220	7.97×10^{14}	34.70	14.0	46.90
AOT Reverse micelles					
$w_0=5$	0.230	6.23×10^{14}	22.91	74.4	19.20
$w_0=10$	0.260	7.02×10^{14}	35.02	53.7	34.20
$w_0=20$	0.270	7.14×10^{14}	35.34	48.7	35.65

Table 4 3. Picosecond-resolved fluorescence data fitting of Riboflavin with DPPH in reverse micelles.

System	τ_1 (ns)	τ_2 (ns)	τ_3 (ns)	τ_{avg} (ns)
AOT Reverse micelles ($w_0=5$)				
RF		1.34 (25%)	4.80 (75%)	3.9
RF-DPPH	0.05 (63%)	0.63 (14%)	4.15 (23%)	1.0
AOT Reverse micelles ($w_0=10$)				
RF		1.11 (20%)	4.84 (80%)	4.1
RF-DPPH	0.05 (48%)	0.86 (11%)	4.38 (41%)	1.9
AOT Reverse micelles ($w_0=20$)				
RF		0.62 (20%)	4.69 (80%)	3.9
RF-DPPH	0.07 (48%)	1.00 (16%)	5.00 (36%)	2.0

(Numbers in parenthesis denote the relative weightage in percentage with ± 5 error).

essential. In this regard, we have employed picosecond resolved FRET experiments, where the vitamin and the model oxidizing agent DPPH are considered to be energy donor and acceptor respectively for the spectral overlap of the donor emission with the absorption spectrum of the acceptor as shown in Figure 4.1.b. Figures 4.5.a-c show picosecond resolved emission transients of RF in various micelles in absence (donor) and presence of DPPH (donor-acceptor).

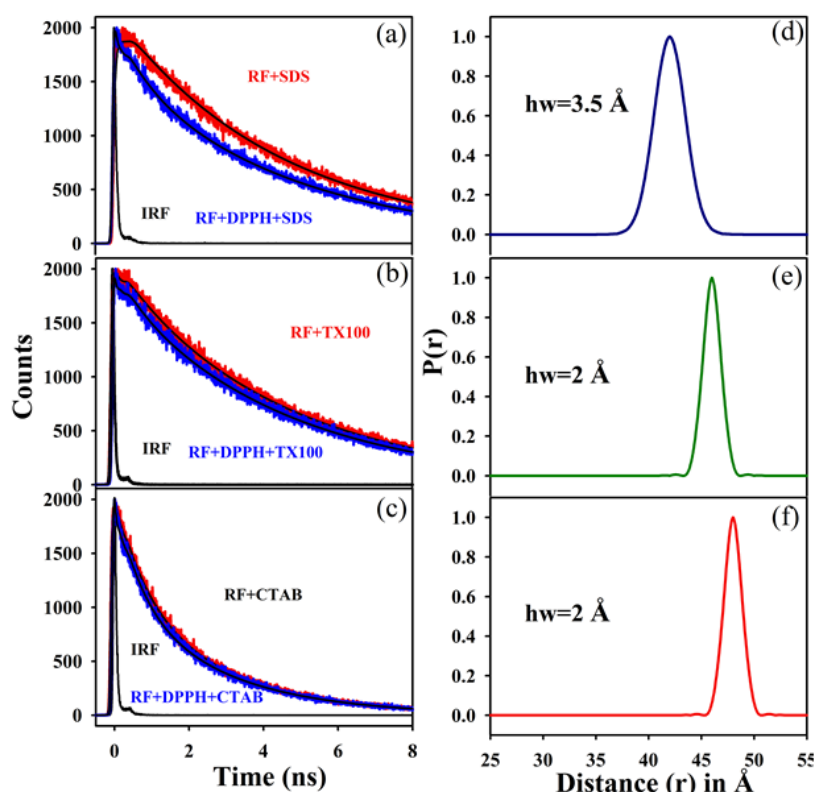


Figure 4.5. (a) to (c) depict the fluorescence lifetime quenching of riboflavin in SDS, TX-100 and CTAB micelles respectively considering the distance distribution between donor (riboflavin) and acceptor (DPPH) (d) to (f) show the corresponding probability of distance distribution ($P(r)$) with respect to mean donor-acceptor distance.

The details of the numerical fitting of the fluorescence transients are tabulated in Table 4.1. The probability distribution of the donor-acceptor distances in the micelles is shown in Figures 4.5.d-f. The parameters related to FRET and the estimated donor-acceptor distances are shown in Table 4.2. From the Figure 4.5 and Table 4.2, it is evident that the SDS micelle allows more proximity of the vitamin with the oxidizing

agent DPPH than other varieties of the micelles prior to the photo-oxidation. The observation is consistent with the fact that in the SDS micelle RF shows highest rate of photo-oxidation kinetics (Figure 4.3.a) compared to other micelles. It is also evident from the Table 4.2 and Figure 4.3.a that the donor-acceptor distances in the micelles essentially dictate efficacy of the photo-oxidation kinetics rates. The calculated half width (hw), revealing heterogeneity or fluctuation in the observed distance between the donor and the acceptor is shown in the Figures 4.5.d-f. It is worth mentioning here that DPPH is completely insoluble in water and can only reside in the hydrophobic core of the micelles, however, cationic charge in the free radical site [47] is expected to bring DPPH in closer proximity of the micellar surface. In the same argument in the CTAB micelle with cationic surface, the free radical DPPH is expected to reside away from the surface leading to higher donor acceptor distance and lowest photo-oxidation kinetics rate (Figure 4.3.a). In the TX-100 micelle with polar head groups, the photo-oxidation kinetics rate (Figure 4.3.a) and donor-acceptor distance is in between other two micelles (SDS and CTAB).

The experimental control of RF-DPPH distance can be achieved from the studies on the donor acceptor pair in reverse micellar system, where hydrodynamic radius of the nano-pool of water is shown to be manipulated in nanometre precision [49]. Considering the case of AOT reverse micelle with anionic head group, the DPPH is expected to reside at the interface between polar (water) and nonpolar (isooctane) phases because of the cationic charge [47]. As observed in the case of micellar system the vitamin RF is expected to have negligible affinity to the interface and prefer to reside in the central water pool. Thus, increase of hydrodynamic radius of the water pool with the addition of more water in the surfactant solution, the RF-DPPH distance can be controlled precisely. As shown in Figure 4.6, RF-DPPH distances gradually

increase with the increase in the hydration number (w_0) of the AOT reverse micelle. Figures 4.6.a-c show picosecond resolved emission transients of RF in RMs with various degrees of hydration in absence (donor) and presence of DPPH (donor-acceptor). The details of the numerical fitting of the fluorescence transients are tabulated in Table 4.3. The probability distribution of the donor-acceptor distances in the micelles are shown in Figures 4.6.d-f.

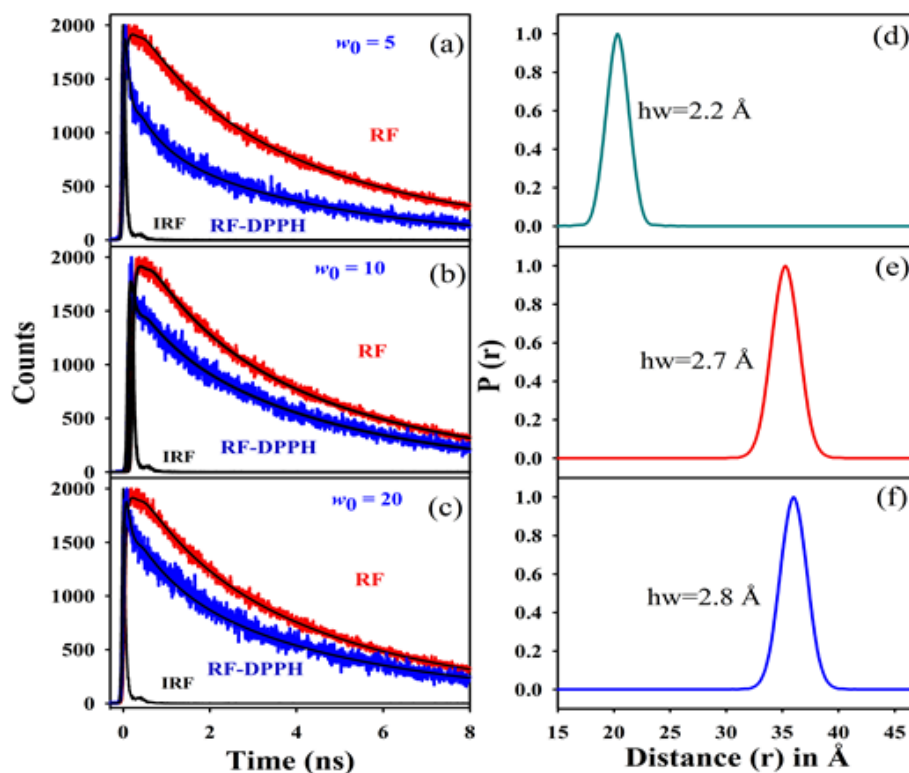
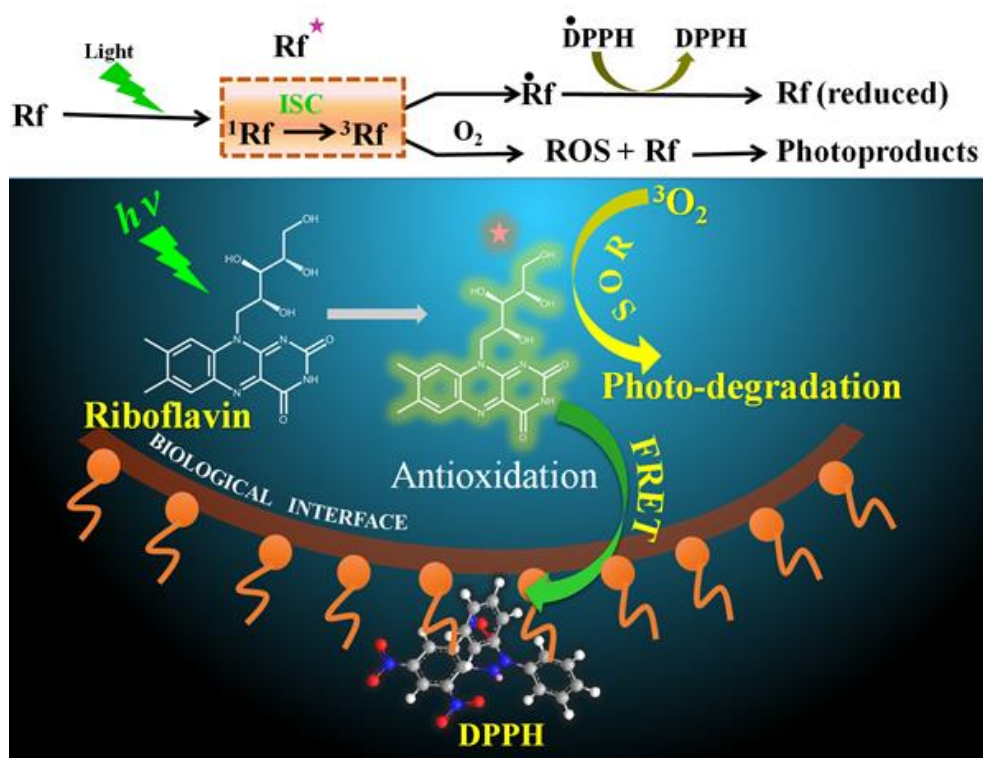


Figure 4.6. (a) to (c) depict the fluorescence lifetime quenching of riboflavin in $w_0=5$, $w_0=10$ and $w_0=20$ micelles respectively considering the distance distribution between donor (riboflavin) and acceptor (DPPH). (d) and (f) show the corresponding probability of distance distribution ($P(r)$) with respect to mean donor-acceptor distance.

The parameters related to FRET and the estimated donor-acceptor distances are shown in Table 4.2. From the Figure 4.6 and Table 4.2, it is evident that proximity of the vitamin with the oxidizing agent DPPH increases with w_0 values prior to the photo-oxidation. The observation is consistent with the fact that in the RM with $w_0=5$, RF shows highest rate of photo-oxidation kinetics in Figure 4.3.b compared to that in $w_0=10$ and 20. It is also evident from the Table 4.2 and Figure 4.3.b that the donor-

acceptor distances in the reverse micelles essentially dictate efficacy of the rates of photo-oxidation kinetics. This observation is consistent with the case in micellar solutions. The calculated half width (hw), revealing heterogeneity or fluctuation [50] in the observed distances between the donor and the acceptor are shown in the Figures 4.5.d-f. Although a direct correlation of such fluctuations in the photo-oxidation turnover is not clear from the present study, the hw values in the case of micelles and RMs show opposite trends with respect to the donor-acceptor distances. From our studies in the nanoscopic systems, a unified molecular picture of the photo-toxicity and photosensitized antioxidant properties of the vitamin is distinct and given in Scheme 4.1.



Scheme 4.1. Upper panel. The mechanistic pathway illustrates the excited singlet riboflavin which is converted to triplet riboflavin after absorbing energy from light. Excited triplet riboflavin transfers electron in the presence of an oxidizing agent (DPPH) or interact with triplet oxygen to form photoproducts by ROS generation. Excited singlet and triplet states of riboflavin is depicted by “*” symbol in the scheme. **Lower panel.** Radical-scavenging of Vitamin B₂ (Riboflavin) in the nanoscopic systems by proximity with the oxidizing agent DPPH. The mechanism of ROS generation leading to the self-destruction employing dissolved oxygen is also shown [8, 21, 51].

4.3. Conclusion:

The effect of visible light on vitamin B₂ present in food has a long record of empirical evidence. In these studies, we have deduced that the antioxidant activity of photosensitized riboflavin in ethanol water (1:1) solution and in various nanoscopic systems. The photoinduced antioxidant activity of the vitamin is significantly efficient than in dark condition. We have suggested a new mechanistic pathway where the excited vitamin quenches the free radical DPPH without being facilitated by the reactive oxygen species prior to electron transfer, which is pictorially represented in Scheme 1. Moreover, our experiments reveal that the radical-scavenging mechanism is strikingly different in solvents from that in confined environments. Our studies also confirm that picosecond resolved Förster Resonance Energy transfer (FRET) in the biomimetic nanoscopic environments catches proximity of an oxidizing agent (DPPH) with the excited vitamin (riboflavin) just prior to the photosensitized antioxidant activity. In summary, vitamin B₂ under visible light irradiation may play a dual role of “photosensitized antioxidant” and “phototoxic drug” depending upon proximity of an oxidizing species. Photo-induced electron transfer from the vitamin to the oxidizing agent in proximity is the key for the antioxidant effect. On the other hand, the excited vitamin undergoes intersystem crossing and eventually employs dissolved oxygen to generate reactive oxygen species (ROS) resulting in phototoxicity/self-degradation. As the generation of ROS and the photosensitized antioxidant activity of the vitamin has a general appeal in the cellular milieu, our studies on the physiologically relevant nanoscopic environments would find the importance in the design of new strategy in phototherapy of several diseases.

References:

- [1] R. Huang, H.J. Kim, D.B. Min, Photosensitizing Effect of Riboflavin, Lumiflavin, and Lumichrome on the Generation of Volatiles in Soy Milk, *J. Agric. Food Chem.*, 54 (2006) 2359-2364.
- [2] G.V. Ferrari, M.P. Montaña, F.C.D. Dimarco, N.B.P.a. Debattista, N.A.G. Walter A. Massad b, A Comparative Photochemical Study on the Behavior of 3,30-dihydroxyflavone and its Complex with La(III) as Generators and Quenchers of Reactive Oxygen Species, *J. Photochem. Photobiol. B: Biology*, 124 (2013) 42–49.
- [3] B.T. van Maldegem, M. Duran, R.J. Wanders, H.R. Waterham, F.A. Wijburg, Flavin Adenine Dinucleotide Status and the Effects of High-Dose Riboflavin Treatment in Short-Chain Acyl-CoA Dehydrogenase Deficiency, *Pediatr. Res.*, 67 (2010) 304-308.
- [4] M.M. Wolf, C. Schumann, R. Gross, T. Domratcheva, R. Diller, Ultrafast Infrared Spectroscopy of Riboflavin: Dynamics, Electronic Structure, and Vibrational Mode Analysis, *J. Phys. Chem. B*, 112 (2008) 13424-13432.
- [5] A. Saha, A.K. Mukherjee, Spectroscopic and Thermodynamic Study of Charge Transfer Interaction of Doxycycline Hydrochloride with Riboflavin in Aqueous Ethanol Media of Varying Compositions, *J. Phys. Chem. B*, 108 (2004) 18988-18992.
- [6] S.L.J. Tan, R.D. Webster, Electrochemically Induced Chemically Reversible Proton-Coupled Electron Transfer Reactions of Riboflavin (Vitamin B₂), *J. Am. Chem. Soc.*, 134 (2012) 5954-5964.
- [7] C. Lu, Z. Han, G. Liu, X. Cai, Y. Chen, S. Yao, Photophysical and Photochemical Processes of Riboflavin (Vitamin B₂) by Means Of the Transient Absorption Spectra in Aqueous Solution, *Sc. China Ser. B-Chem.*, 44 (2001) 39-48.
- [8] R. Huang, E. Choe, D.B. Min, Kinetics for Singlet Oxygen Formation by Riboflavin Photosensitization and the Reaction between Riboflavin and Singlet Oxygen, *J. Food Sci. C*, 69 (2004) C726-C732.
- [9] G. McNeill, X. Jia, L.J. Whalley, H.C. Fox, J. Corley, A.J. Gow, C.E. Brett, J.M. Starr, I.J. Deary, Antioxidant and B Vitamin Intake in Relation to Cognitive Function in Later Life in the Lothian Birth Cohort 1936, *Eur. J. Clin. Nutr.*, 65 (2011) 619-626.
- [10] H. Ciliberto, M. Ciliberto, A. Briend, P. Ashorn, D. Bier, M. Manary, Antioxidant Supplementation for the Prevention of Kwashiorkor in Malawian Children: Randomised, Double Blind, Placebo Controlled Trial, *BMJ*, 330 (2005) 1109.

- [11] R.R. Williams, V.H. Cheldelin, Destruction of Riboflavin by Light, *Science*, 96 (1942) 22-23.
- [12] A.W. Galston, R.S. Baker, Inactivation of Enzymes by Visible Light in the Presence of Riboflavin, *Science*, 109 (1949) 485-486.
- [13] W.L. Cairns, D.E. Metzler, Photochemical Degradation of Flavins. VI. A New Photoproduct and Its Use in Studying the Photolytic Mechanism, *J. Am. Chem. Soc.*, 93 (1971) 2772-2777.
- [14] P. Droessler, W. Holzera, A. Penzkofer, P. Hegemann, pH Dependence of the Absorption and Emission Behaviour of Riboflavin in Aqueous Solution, *Chem. Phys.*, 282 (2002) 429-439.
- [15] E.C. Smith, D.E. Metzler, The Photochemical Degradation of Riboflavin, *J. Am. Chem. Soc.*, 85 (1963) 3285-3288.
- [16] E. Sikorska, I.V. Khmelinskii, W. Prukała, S.L. Williams, M. Patel, D.R. Worrall, J.L. Bourdelande, J. Koput, M. Sikorski, Spectroscopy and Photophysics of Lumiflavins and Lumichromes, *J. Phys. Chem. A*, 108 (2004) 1501-1508.
- [17] E. Haggi, N. Blasich, L. Gutiérrez, G. Vázquez, S. Criado, S. Miskoski, G. Ferrari, M. Paulina Montaña, N.A. García, On the Generation And Quenching of Reactive-Oxygen-Species by Aqueous Vitamin B₂ and Serotonin under Visible-Light Irradiation, *J. Photochem. Photobiol. B*, 113 (2012) 22-28.
- [18] A. Mahns, I. Melchheier, C.V. Suschek, H. Sies, L.O. Klotz, Irradiation of Cells with Ultraviolet-A (320-400 Nm) in the Presence of Cell Culture Medium Elicits Biological Effects Due to Extracellular Generation of Hydrogen Peroxide, *Free. Rad. Res.*, 37 (2003) 391-397.
- [19] C.-Y. Lu, W.-F. Wang, W.-Z. Lin, Z.-H. Han, S.-D. Yao, N.-Y. Lin, Generation and Photosensitization Properties of the Oxidized Radical of Riboflavin: a Laser Flash Photolysis Study, *J. Photochem. Photobiol. B*, 52 (1999) 111-116.
- [20] A. de La Rochette, I. Birlouez-Aragon, E. Silva, P. Morliere, Advanced Glycation Endproducts as UVA Photosensitizers of Tryptophan and Ascorbic Acid: Consequences for the Lens, *Biochim. Biophys. Acta*, 11 (2003) 235-241.
- [21] D.B. Min, J.M. Boff, Chemistry and Reaction of Singlet Oxygen in Foods, *Compr. Rev. Food Sci.*, 1 (2002) 58-72.
- [22] M.V.R. Kumari, T. Yoneda, M. Hiramatsu, Scavenging Activity of B-Catechin on Reactive Oxygen Species Generated by Photosensitization of Riboflavin, *Biochem. Mol. Biol. Int.*, 38 (1996) 1163-1170.

- [23] D. Zhong, A.H. Zewail, Femtosecond Dynamics of Flavoproteins: Charge Separation and Recombination in Riboflavine (Vitamin B₂)-Binding Protein and in Glucose Oxidase Enzyme, *Proc. Natl. Acad. Sci. U.S.A.*, 98 (2001) 11867–11872.
- [24] R. Saha, S. Rakshit, P.K. Verma, R.K. Mitra, S.K. Pal, Protein-Cofactor Binding and Ultrafast Electron Transfer in Riboflavin Binding Protein under the Spatial Confinement of Nanoscopic Reverse Micelles, *J. Mol. Recogn.*, 26 (2013) 59-66.
- [25] S. Kedare, R.P. Singh, Genesis and Development of DPPH Method of Antioxidant Assay, *J. Food Sci. Technol.*, 48 (2011) 412-422.
- [26] E. Beutler, Glutathione Reductase: Stimulation in Normal Subjects by Riboflavin Supplementation, *Science*, 165 (1969) 613-615.
- [27] I. Mohammad, I. Zafar, H. Javid, H. Hidayat, A. Manzoor, E. Asma, I.C. Muhammad, Chemical Constituents and Antioxidant Activity of Geranium Wallichianum, *Rec. Nat. Prod.*, 3 (2009) 193-197.
- [28] O.A. Chat, M.H. Najjar, A.A. Dar, Evaluation of Reduction Kinetics of 2,2-Diphenyl-1-Picrylhydrazyl Radical by Flavonoid Glycoside Rutin in Mixed Solvent Based Micellar Media, *Colloids Surf., A*, 436 (2013) 343-353.
- [29] W.A. Mulla, V.R. Salunkhe, S.B. Kuchekar, M.N. Qureshi, Free Radical Scavenging Activity of Leaves of *Alocasia indica* (Linn), *Indian J. Pharm. Sci.*, 71 (2009) 303-307.
- [30] D.R. Cardoso, S.H. Libardia, L.H. Skibsted, Riboflavin as a Photosensitizer. Effects on Human Health and Food Quality, *Food Func.*, 3 (2012) 487-502.
- [31] J.Y. Liang, J.M. Yuann, C.W. Cheng, H.L. Jian, C.C. Lin, L.Y. Chen, Blue Light Induced Free Radicals from Riboflavin on *E. Coli* DNA Damage, *J. Photochem. Photobiol. B*, 119 (2013) 60-64.
- [32] D. Zhong, S.K. Pal, A.H. Zewail, Femtosecond Studies of Protein–DNA Binding and Dynamics: Histone I, *Chem. Phys. Chem.*, 2 (2001) 219–227.
- [33] S.K. Pal, J. Peon, A.H. Zewail, Biological Water at the Protein Surface: Dynamical Solvation Probed Directly with Femtosecond Resolution, *Proc. Natl. Acad. Sci. U.S.A.*, 99 (2002) 1763-1768.
- [34] R.K. Mitra, S.S. Sinha, S.K. Pal, Interactions of Nile Blue with Micelles, Reverse Micelles and a Genomic DNA, *J. Fluoresc.*, 18 (2008) 423–432.
- [35] D. Banerjee, S.K. Pal, Ultrafast Charge Transfer and Solvation of DNA Minor Groove Binder: Hoechst 33258 in Restricted Environments, *Chem. Phys. Lett.*, 432 (2006) 257–262.

- [36] Q. Li, T. Li, J. Wu, Comparative Study on the Structure of Reverse Micelles. 2. FT-IR, ¹H NMR, and Electrical Conductance of H₂O/AOT/NaDEHP/n-Heptane Systems, *J. Phys. Chem. B*, 104 (2000) 9011-9016.
- [37] A.K. Shaw, S.K. Pal, Fluorescence Relaxation Dynamics of Acridine Orange in Nanosized Micellar Systems and DNA, *J. Phys. Chem. B*, 111 (2007) 4189-4199.
- [38] K. Bhattacharyya, B. Bagchi, Slow Dynamics of Constrained Water in Complex Geometries, *J. Phys. Chem. A*, 104 (2000) 10603-10613.
- [39] S. Chaudhuri, S. Batabyal, N. Polley, S.K. Pal, Vitamin B₂ in Nanoscopic Environments under Visible Light: Photosensitized Antioxidant or Phototoxic Drug?, *J. Phys. Chem. A*, 118 (2014) 3934-3943.
- [40] P. Ionita, Is DPPH Stable Free Radical a Good Scavenger for Oxygen Active Species, *Chem. Pap.*, 59 (2005) 11-16.
- [41] M. Patel Rajesh, J. Patel Natvar, In Vitro Antioxidant Activity of Coumarin Compounds by DPPH, Super Oxide and Nitric Oxide Free Radical Scavenging Methods, *J. Adv. Pharm. Edu. Res.*, 1 (2011) 52-68.
- [42] D.R. Weinberg, C.J. Gagliardi, J.F. Hull, C.F. Murphy, C.A. Kent, B.C. Westlake, A. Paul, D.H. Ess, D.G. McCafferty, T.J. Meyer, Proton-Coupled Electron Transfer, *Chem. Rev.*, 112 (2012) 4016-4093.
- [43] H.Y. Zhang, H.F. Ji, How Vitamin E Scavenges DPPH Radicals in Polar Protic Media, *New J. Chem.*, 30 (2006) 503-504.
- [44] M.C. Foti, C. Daquino, C. Geraci, Electron-Transfer Reaction of Cinnamic Acids and Their Methyl Esters with the DPPH(*) Radical in Alcoholic Solutions, *J. Org. Chem.*, 69 (2004) 2309-2314.
- [45] G. Li, K.D. Glusac, Light-Triggered Proton and Electron Transfer in Flavin Cofactors, *J. Phys. Chem. A*, 112 (2008) 4573-4583.
- [46] E. Hristeac, M. Caproiu, G. Pencu, M. Hillebrand, T. Constantinescu, A. Balaban, Reaction of 2,2-Diphenyl-1-picrylhydrazyl with HO•, O₂•⁻, HO⁻, and HOO⁻ Radicals and Anions, *Int. J. Mol. Sci.*, 7 (2006) 130-143.
- [47] A. Malik, A. Kushnoor, V. Saini, S. Singhal, S. Kumar, Y.C. Yadav, In Vitro Antioxidant Properties of Scopoletin, *J. Chem. Pharm. Res.*, 3 (2011) 659-665.
- [48] S. Fujisawa, T. Atsumi, M. Ishihara, Y. Kadoma, Cytotoxicity, ROS-generation Activity and Radical-Scavenging Activity of Curcumin and Related Compounds, *Anticancer Res.*, 24 (2004) 563-569.

- [49] N. Nandi, K. Bhattacharyya, B. Bagchi, Dielectric Relaxation and Solvation Dynamics of Water in Complex Chemical and Biological Systems, *Chem. Rev.*, 100 (2000) 2013-2046.
- [50] S. Nag, B. Sarkar, M. Chandrakesan, R. Abhyanakar, D. Bhowmik, M. Kombrabail, S. Dandekar, E. Lerner, E. Haas, S. Maiti, A Folding Transition Underlies the Emergence of Membrane Affinity in Amyloid-beta, *Phys. Chem. Chem. Phys.*, 15 (2013) 19129-19133.
- [51] A. de La Rochette, E. Silva, I. Birlouez-Aragon, M. Mancini, A.M. Edwards, P. Morliere, Riboflavin Photodegradation and Photosensitizing Effects are Highly Dependent on Oxygen and Ascorbate Concentrations, *Photochem. Photobiol.*, 72 (2000) 815-820.

Chapter 5

Sensitization of Medicinally Important Drugs with Inorganic Nanoparticles

5.1. Introduction:

Riboflavin (Rf) or vitamin B₂ is an essential micronutrient and substantially present in dietary products such as vegetables, mushrooms, yeast, milk, cheese, eggs and meat [1-3]. Although remarkable medicinal use of the vitamin as food supplement followed immediately after the Noble-winning (in chemistry, 1938) structural determination of the micronutrient, alternative use of the vitamin as a potential photodynamic therapy (PDT) agent is also evident in early [4] as well as in contemporary [5] literature. Upon light irradiation of a specific wavelength, a photosensitizer absorbs photon and elevated from ground state to an excited singlet state which in due course decays to the triplet excited state via intersystem crossing (ISC). Then the triplet excited state energy is transferred to molecular oxygen at ground state to produce singlet oxygen which is a central intermediate for cytotoxic action in PDT. It is well established that Rf upon visible light irradiation generates reactive oxygen species (ROS) such as singlet oxygen and superoxide anion [6, 7]. Riboflavin photosensitization has been used as a therapy for the treatment of keratosis, where the vitamin is an endogenous photosensitizer [8, 9].

In the past two decades, nanoparticle (NP)-based therapeutic products have flourished for the enhancement of drug action [10-13]. Nanomaterials are attributed

with distinguished physicochemical properties, such as very small size, greater surface area to mass ratio, and high reactivity, which is different from that of bulk materials of similar composition [11]. Nanomaterials as drug carriers can overcome some of the constraints such as low solubility and diffusivity, shortened blood circulation half-life, high immunogenicity and low bioavailability found in conventional therapeutic and diagnostic agents [11, 14]. Due to a higher surface area to volume ratio, nanocarriers show upgraded pharmacokinetics and biodistribution of therapeutic agents and reduce toxicity by their accumulation at the target site [15]. The solubility of hydrophobic drugs increases by the formation of nanoconjugates and render them convenient for parenteral administration. Moreover, the stability of various therapeutic agents such as peptides and oligonucleotides increases which can be utilised to conduct the drug to central nervous system due to their limited size and greater barrier permeability [15, 16]. However, reports on sensitization of drugs by NPs through their electronic coupling are sparse in the literature. On the other hand, formation of nanohybrid of a drug with an inorganic nanoparticle is the key for the modulation of drug activity in the nanohybrid. In one of our earlier reports, we have explored the photoinduced ultrafast dynamics in a well-known cancer drug, protoporphyrin IX (PP) sensitized with ZnO NPs (PP-ZnO). We successfully showed that the PP-ZnO nanohybrid exhibits enhanced activity in PDT compared to that of only PP. Zinc oxide NPs act as drug delivery vehicle and also facilitate the charge separation which eventually enhances the drug activity [17].

In the present study, we have synthesized nanohybrids of vitamin B₂ with various inorganic NPs such as zinc oxide (ZnO), titanium oxide (TiO₂), aluminium oxide (Al₂O₃) and gold NPs of approximately 30 nm sizes. We confirmed the sizes of the NPs using high resolution transmission electron microscopy (HRTEM). Raman

spectroscopic studies provide an insight on the nature of the attachment of riboflavin to the surfaces of the semiconductor (TiO_2 and ZnO), the insulator (Al_2O_3) NPs and metal (gold NPs). In order to measure the photo-antioxidant activity of the nanohybrids, we have performed the well-known 2, 2-diphenyl-1-picrylhydrazyl (DPPH) assay under blue light irradiation ($\lambda_{\text{max}} = 450 \text{ nm}$). Time-resolved fluorescence studies on the nanohybrids were carried out to understand the electron transfer from photoexcited Rf to ZnO or TiO_2 which eventually intensifies the ROS activity in the Rf-semiconductor nanostructures. The phenomenon of nano surface energy transfer (NSET) is predominant in the nanohybrids of riboflavin with gold. Our studies unravel a mechanistic pathway of drug sensitization with various inorganic NPs to determine the photoinduced antioxidant property of this important vitamin.

5.2. Results and Discussion:

5.2.1. Sensitization of an Endogenous Photosensitizer: Electronic Spectroscopy of Riboflavin in the Proximity of Semiconductor, Insulator and Metal Nanoparticles [18]:

Figure 5.1.a shows a high-resolution transmission electron microscopic (HR-TEM) image of ZnO NP. Lattice fringes of ZnO NP is found to be $\sim 0.26 \text{ nm}$ which corresponds to the distance between two (002) planes [17]. The average particle size is found to be $\sim 28.5 \pm 0.4 \text{ nm}$ from experimental TEM data. Figure 5.1.b and 5.1.c show lattice fringes of TiO_2 and Al_2O_3 with interplanar distances 0.36 nm between two (101) planes and 0.42 nm between two (110) planes, [19, 20] respectively. The average particle size is estimated to be $\sim 24.4 \text{ nm}$ for TiO_2 and $\sim 41 \text{ nm}$ for Al_2O_3 . From the HRTEM images, TiO_2 NPs seem to be faceted with different crystal planes. However,

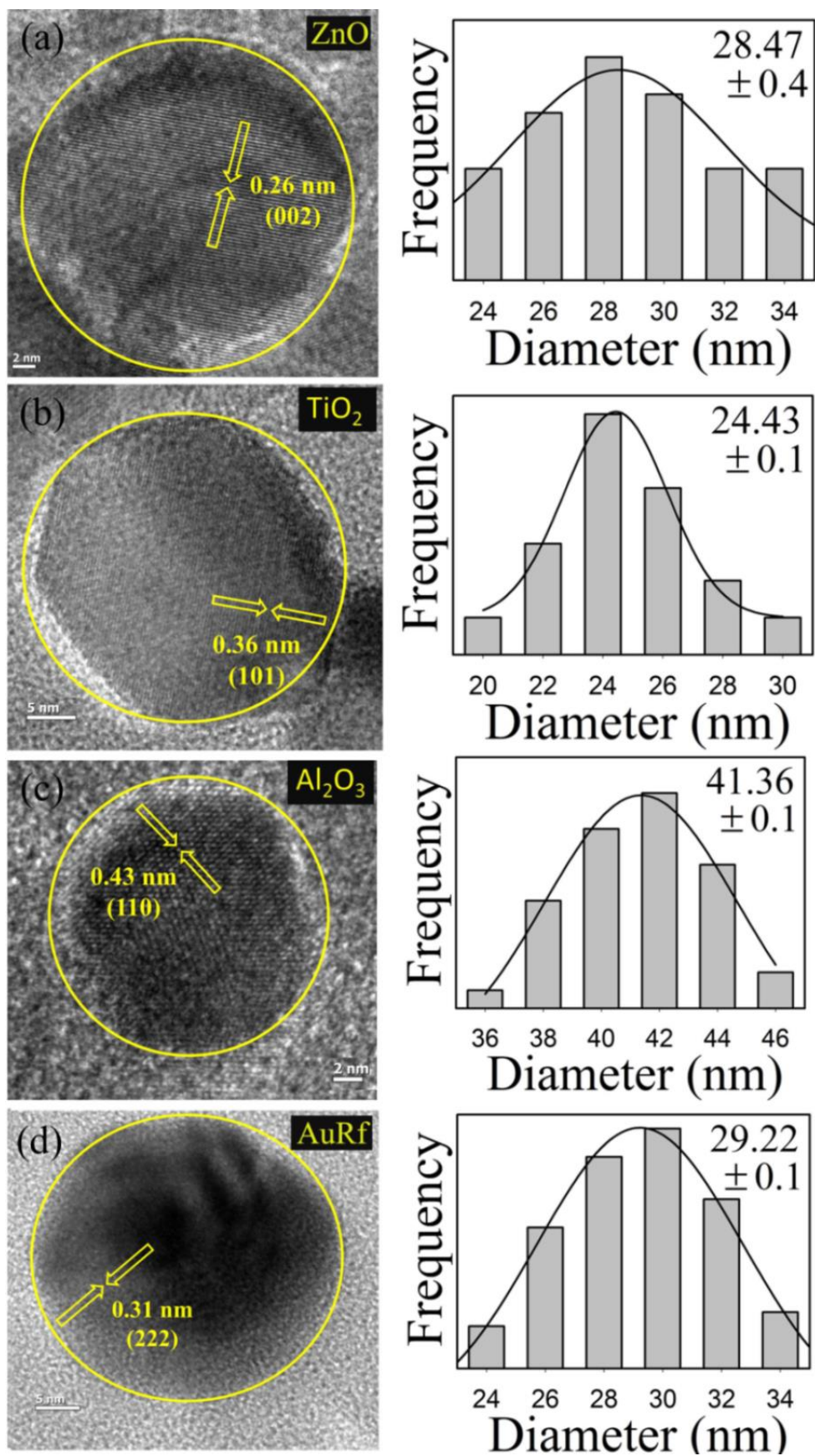


Figure 5.1. (a-d) HRTEM images of various nanoparticles. The right panel shows the corresponding particle size distribution of the NPs.

careful investigation on the inter-fringe distances, for a number of NPs reveals a distance of 0.36 nm which is consistent with (101) plane of TiO₂ crystal. Thus, surface roughness of the TiO₂ NPs is concluded to be responsible for the faceted appearance of the NPs. The lattice fringes of Rf-AuNP distinctly show an interplanar distance of ~0.31 nm, [21] corresponding to the interspace between two (222) planes. The average particle size for Rf-AuNP is found to be ~29 nm.

UV-Visible spectroscopy is a useful technique to understand the complexation between Rf and the NPs [22]. The absorption maxima of Rf is at 360 nm and 445 nm in water and ethanol, respectively. The absorption, emission and excitation spectra of Rf with its nanohybrids are shown in Figure 5.2.a, 5.2.b and 5.2.c, respectively, in water for gold nanohybrids and in ethanol for the rest. The Rf absorption in the presence of different NPs are shown in Figure 5.2.a. The change in absorbance peak at 445 nm is due to complex formation when Rf attaches to surfaces of ZnO, TiO₂ and Al₂O₃ NPs. This kind of observation is well documented in the literature [17, 19]. No distinct peak of Rf is observed in these nanohybrids due to the very low riboflavin concentration and large scattering of the nanoparticles. However, the presence of riboflavin is evident in emission and excitation spectrum of Figure 5.2.b and Figure 5.2.c, respectively. The concentration of riboflavin is estimated by differential spectra method (data not shown). However, a surface plasmon band (SPB) exists in Rf-AuNP due to the contribution of AuNPs. The SPB exists as a result of collective oscillations of the electron at the NP surface (6s electrons for AuNPs) which is correlated with the electromagnetic field of the incoming light [23]. From the normalised steady-state emission data of Rf with its various nanohybrids (Rf-ZnO, Rf-TiO₂ and Rf-Al₂O₃ in ethanol and Rf-AuNPs in water), no change in peak position is observed. Figure 5.2.c shows the corresponding excitation spectra.

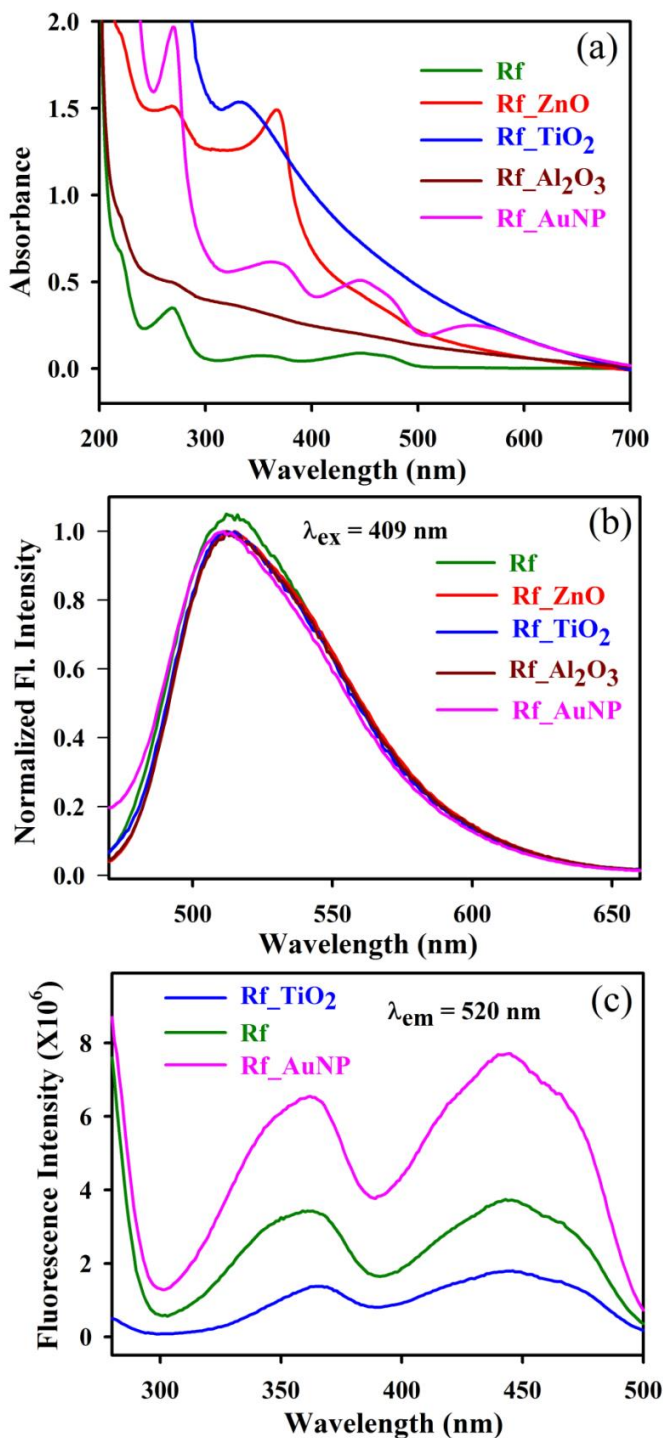


Figure 5.2. (a) Absorption, (b) emission and (c) excitation spectra of Rf in ethanol and Rf-nanocomposites (Rf-ZnO, Rf-TiO₂ and Rf-Al₂O₃ in ethanol and Rf-AuNP in water).

The Raman spectra of Rf-nanohybrids with ZnO, TiO₂ and Al₂O₃ NPs show similar vibrational modes as that of the corresponding NPs (as shown in Figure 5.3.b) which proves the good retention of crystal structure of the NPs after the complex formation. The invariance of the peak positions of Rf-nanohybrids suggests that the

complexation is mainly due to physisorption [22]. However, when Rf is attached to gold NP the characteristic Rf peak is shifted from 1346 cm^{-1} to 1358 cm^{-1} and also broadened (Figure 5.3.a). Moreover, the peak at 1563 cm^{-1} for AuNPs is moved to 1540 cm^{-1} in presence of Rf molecules. This suggests a covalent bond formation between Rf and AuNP [24].

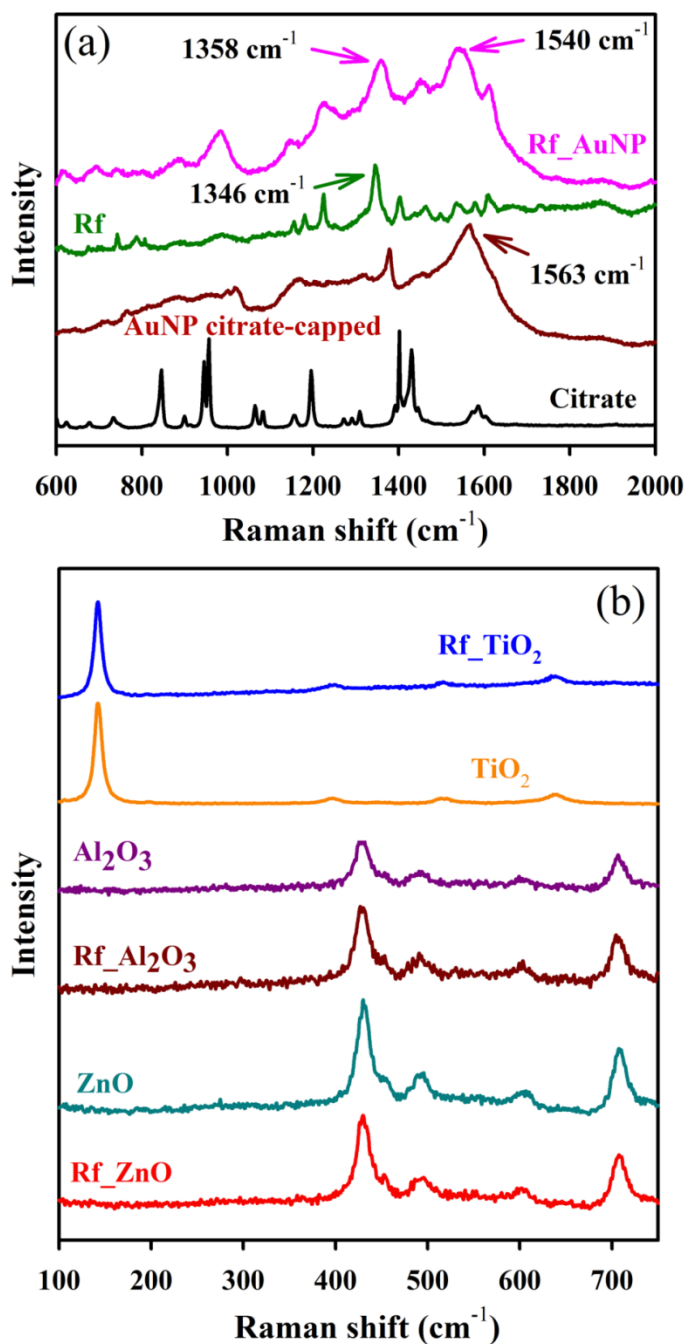


Figure 5.3. Raman spectra of (a) Rf and Rf-AuNPs in solid phase and (b) different nanoparticles and their nanohybrids with Rf in solid phase.

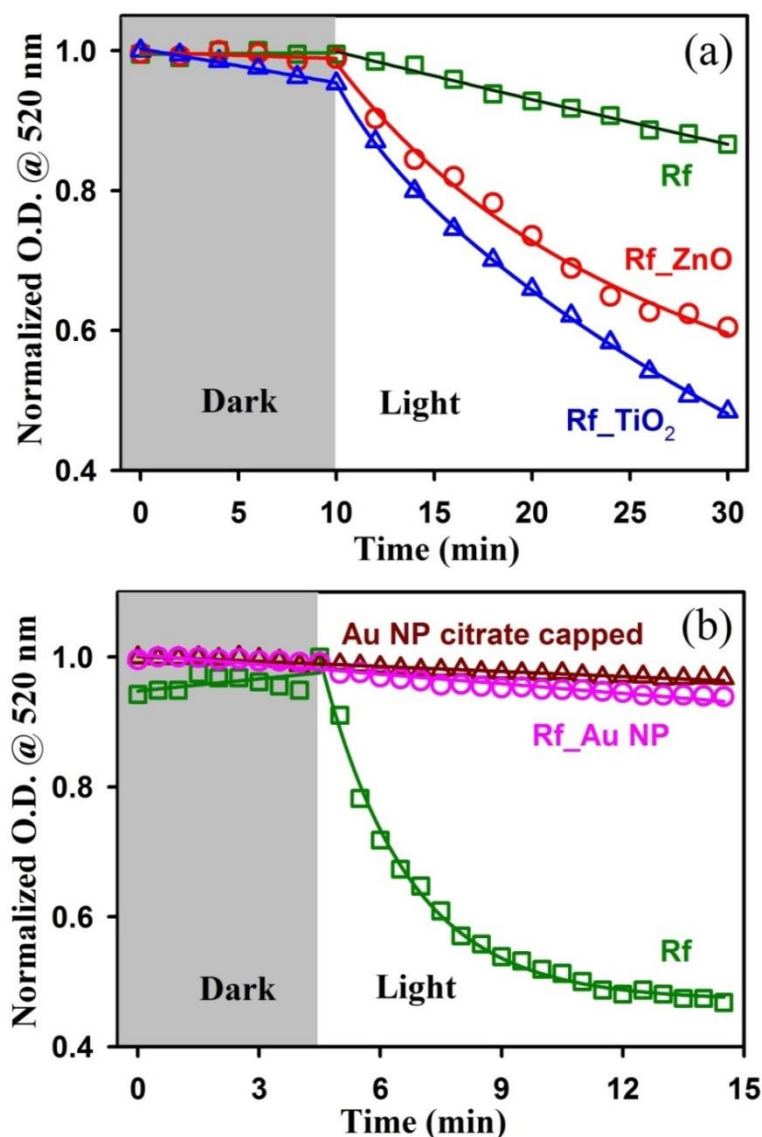


Figure 5.4. The absorption kinetics (at 520 nm) of DPPH in presence of (a) Rf-ZnO, Rf-TiO₂ in ethanol (b) Rf-AuNPs in ethanol:water mixture (1:1) under blue light irradiation.

Figure 5.4.a demonstrates antioxidant activity of the Rf nanohybrids with colloidal ZnO and TiO₂ NPs in alcohol without and with light exposure, respectively. Antioxidant activities of the nanohybrids as well as that of the vitamin are usually monitored by the decolourization kinetics of a stable free radical 2, 2-diphenyl-1-picrylhydrazyl (DPPH). The vitamin or nanohybrids donate a proton/electron to the violet-coloured radical DPPH which reduces the radical to DPPH₂ form which is yellow in colour [25]. The free radical quenching kinetics of Rf, Rf-ZnO and Rf-TiO₂ under blue light irradiation have been fitted with biexponential decay functions. The time

constants are calculated to be 140 min, 50 min and 26 min, respectively. The increase in the rate of radical scavenging activity of the vitamin attached to semiconductor NPs under blue light is clearly evident from Figure 5.4.a. Moreover, there is no change in the activity of Rf-Al₂O₃ nanohybrids (data not shown here) compared to Rf in ethanol solution. Hence, the rate of photo-induced antioxidant activity in the presence of light is highly dependent on the nature of the nanoparticles. Figure 5.4.b illustrates that the antioxidant activity of the Rf-AuNP nanohybrids is mostly suppressed compared to that of the solution of Rf only. The antioxidant activities of Rf, Rf-ZnO, Rf-TiO₂, and Rf-Al₂O₃ as shown in Figure 5.4.a were performed in ethanol whereas antioxidant activities which are given in Figure 5.4.b were carried out in ethanol-water (1:1) mixture as Rf-AuNPs were synthesized in aqueous phase and the free radical DPPH is soluble in ethanol. It has to be noted that Rf concentration is ten times more in Rf-AuNP than that in Rf-ZnO, Rf-TiO₂, Rf-Al₂O₃. Thus, the control Rf in Figure 5.4.b shows more enhanced activity than the control Rf in Figure 5.4.a.

In order to explain the above observations based on the DPPH assay of the Rf-nanohybrids, picosecond resolved fluorescence spectroscopy were performed. The fluorescence decay profiles for free Rf, Rf-ZnO and Rf-TiO₂ were obtained upon excitation at 409 nm in ethanol and monitored at 520 nm as shown in Figure 5.5.a. The time constants of the fluorescence transients at 520 nm for the singlet excited-state of Rf in ethanol solution showed single exponential decay, with a lifetime of 3.4 ns. The quenching of the life-time transients is observed in Rf-ZnO and Rf-TiO₂ and no change in life-time is observed in Rf-Al₂O₃. The observation is consistent with the fact that the excited vitamin transfers electrons to the semiconductor NPs [26-28]. The lifetime components of the transients are tabulated in Table 5.1. In order to confirm the electron

migration from Rf, the well-known electron acceptor benzoquinone (BQ) is bound to

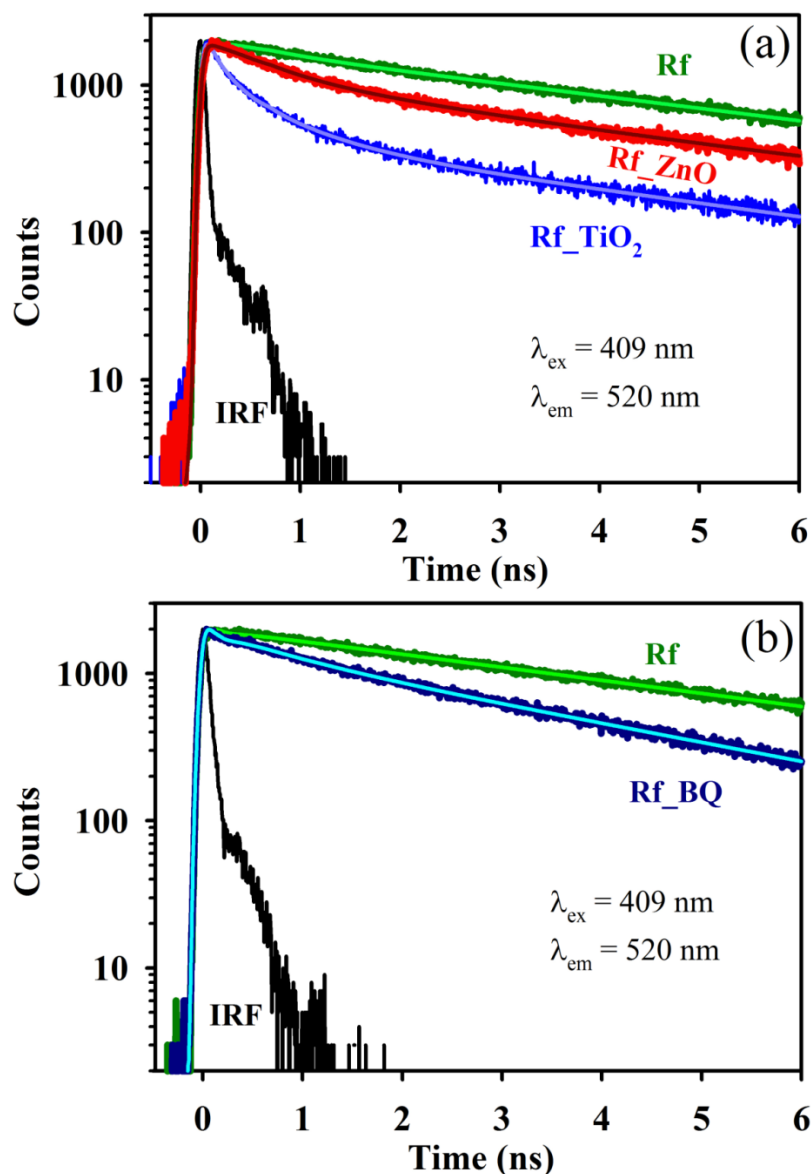


Figure 5.5. The picosecond-resolved fluorescence transients of Rf (excitation at 409 nm) in absence and presence of (a) ZnO, TiO₂ (b) BQ in ethanol.

Rf and the possible excited-state interactions in Rf-BQ composite is investigated with maximum BQ concentration of 10 μM (Figure 5.5.b). The electron transfer timescales from Rf to BQ are found to be similar to that of Rf-ZnO and Rf-TiO₂ (Table 5.1). This corroborates with the photo-induced antioxidant activity data (Figure 5.4.a). The enhancement in the photo-induced antioxidant activity in Rf-ZnO and Rf-TiO₂ nano hybrids is due to efficient electron-hole charge separation created by illumination with light in semiconductors with wide-band gap ($\sim 3.0\text{-}3.2 \text{ eV}$). On the other hand, the

photoinduced antioxidant activity of Rf-AuNPs is diminished (Figure 5.4.b). This suggests that the vitamin is de-excited by transferring its non-radiative energy to the gold nanoparticles.

Table 5.1. Dynamics of picosecond-resolved fluorescence transients of Rf and Rf nanohybrids^a.

Sample	Excitation wavelength (nm)	Detection wavelength (nm)	τ_1 (ns)	τ_2 (ns)	τ_3 (ns)	τ_{avg} (ns)
Rf in ethanol	409	520	0.11 (32%)	4.89 (68%)	-	3.40
Rf-ZnO nanohybrid	409	520	0.44 (47%)	2.19 (23%)	6.41 (7.2%)	2.63
Rf-TiO ₂ nanohybrid	409	520	0.15 (65%)	0.65 (21%)	4.72 (14%)	0.89
Rf-BQ	409	520	0.05 (3%)	0.72 (27%)	3.34 (70%)	2.56
Rf in water	409	520	4.76 (100%)			4.75
Rf-AuNP in water	409	520	0.40 (48%)	4.65 (52%)		2.49

^aNumbers in the parenthesis indicate relative weightages.

Figure 5.6.a illustrates a large spectral overlap of Rf emission and surface plasmon absorbance of Au NP which indicates a fair possibility of energy transfer from Rf to AuNP. The fluorescence intensity of the Rf is quenched and also the peak is shifted by 12 nm when it is attached to AuNPs in aqueous medium as shown in Figure 5.6.a, inset. However, due to the change in the polarity of the solvent, riboflavin emission is shifted from 515 nm in ethanol (Figure 5.2.b) to 522 nm in water. The fluorescence decay time of the Rf in water without AuNP is given by a single exponential with the average life-time value of 4.76 ns. However, there is a quenching of decay time in Rf-AuNP and the time scales are fitted by biexponential decay. The details of the fitting parameters of the fluorescence lifetime are given in Table 5.1. The emission transient of Rf in water is fitted with single exponential decay of timescale

4.76 ns. While the lifetime Rf-AuNPs in water is quenched and fitted bi-exponentially with one faster component of 0.4 ns (48%) due to the energy transfer from Rf to AuNPs and a longer component of 4.65 ns (52%) consistent with the decay of Rf only.

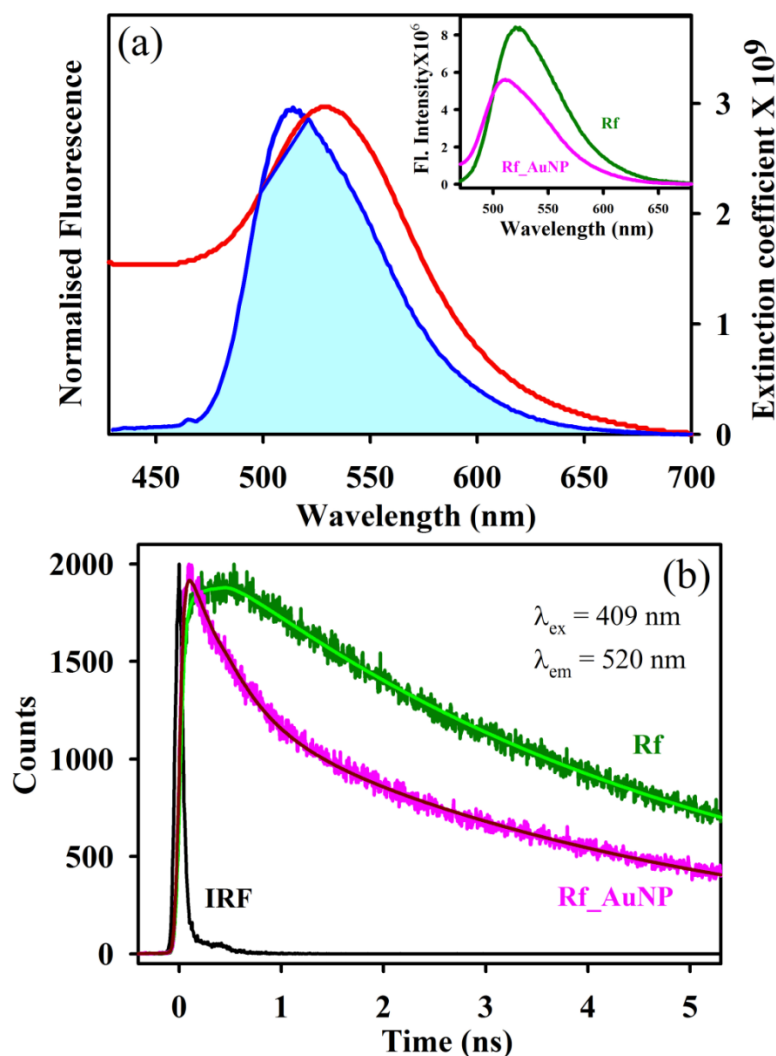


Figure 5.6. (a) Spectral overlap of donor Rf (dark green) and acceptor AuNPs (pink). Inset shows the steady-state emission quenching of Rf after complexation with AuNP. (b) The picosecond-resolved fluorescence transients of Rf and Rf-AuNPs (excitation at 409 nm). All the spectra were taken in aqueous medium.

The model of Förster's Resonance Energy-Transfer (FRET) is employed for the determination of the donor-acceptor distance using equation 2.7. The energy transfer efficiency and the overlap integral $[J(\lambda)]$ are calculated to be 53.7% from equation 2.1 and $1.36 \times 10^{20} \text{ M}^{-1} \text{ cm}^{-1} \text{ nm}^4$ from equation 2.4, respectively. The Förster radius (r_0) is found to be 34 nm. From equation 2.6, the calculated donor-acceptor separation (r) is

28 nm. As the estimated distance between the donor-acceptor exceeds 100\AA , the phenomenon of AuNPs based surface energy transfer (SET) process is a convenient spectroscopic ruler for long-distance measurement, which follows $1/d^4$ distance dependence. NP-induced lifetime modification serves as a ruler to unravel the distance range well beyond 10 nm [29]. This kind of long distance SET from fluorescent dyes to Au NPs is well documented in the literature. In order to approve the NSET formulism, the distance between donor Rf and acceptor AuNP is determined to be 16.71 nm ($d_0 = 17.36$ nm) from equations 2.10 and 2.11, respectively. Herein, we propose nano-surface energy transfer (NSET) from the donor Rf to the acceptor AuNPs as the calculated donor-acceptor distance is in consonance with the size of the gold NPs (radius 15 nm). Hence, it is worth emphasizing that the energy transfers from Rf to AuNP results in the reduced antioxidant activity of the Rf-AuNP nanohybrids as shown in Figure 5.4.b.

5.3. Conclusion:

We have conducted an in-depth investigation of the crucial photoinduced dynamics in riboflavin upon complexation with various inorganic nanoparticles (NPs) such as zinc oxide (ZnO), titanium oxide (TiO_2), aluminium oxide (Al_2O_3) and gold NPs of approximately 30 nm sizes. Raman spectroscopic studies reveal that riboflavin is adsorbed on the surface of the semiconductor (TiO_2 and ZnO) and the insulator (Al_2O_3) NPs whereas a covalent attachment is observed with metal (gold). 2, 2-diphenyl-1-picrylhydrazyl (DPPH) assay under visible light irradiation was conducted to prove that semiconductors with a wide band gap show a more enhanced photoinduced antioxidant activity than insulators. Furthermore, the antioxidant activity is decreased in the gold nanohybrids as the electron is not shuttled to the model oxidant (DPPH). Time-resolved fluorescence studies on Rf-ZnO and Rf- TiO_2 nanohybrids unravel the efficient electron transfer from photoexcited Rf to ZnO and TiO_2 . To confirm the energy transfer of the

riboflavin to AuNPs, we have employed picosecond-resolved fluorescence studies and found that nano surface energy transfer (NSET) is predominant over Förster's resonance energy-transfer (FRET). NSET from Rf to Au NPs occur due to strong spectral overlap of Rf emission and surface plasmon absorption of the gold NP which is responsible for low antioxidant activity. The result of the study of photoinduced dynamics in the Rf-nanohybrids could be incorporated in designing more effective photodynamic therapeutic agents.

References:

- [1] E. Barton-Wright, T. Moran, H. Sarson, Riboflavin and Vitamin B₁ In Nineteenth Century Buns and Ale, *Nature*, 152 (1943) 273.
- [2] R. Huang, H.J. Kim, D.B. Min, Photosensitizing Effect of Riboflavin, Lumiflavin, and Lumichrome on the Generation of Volatiles in Soy Milk, *J. Agric. Food. Chem.*, 54 (2006) 2359-2364.
- [3] S. Chaudhuri, S. Batabyal, N. Polley, S.K. Pal, Vitamin B₂ in Nanoscopic Environments under Visible Light: Photosensitized Antioxidant or Phototoxic Drug?, *J. Phys. Chem. A*, 118 (2014) 3934-3943.
- [4] A. Tsugita, Y. Okada, K. Uehara, Photosensitized Inactivation of Ribonucleic Acids in the Presence of Riboflavin, *Biochim. Biophys. Acta*, 103 (1965) 360-363.
- [5] G.M. Bernal, M.J. LaRiviere, N. Mansour, P. Pytel, K.E. Cahill, D.J. Voce, S. Kang, R. Spretz, U. Welp, S.E. Noriega, Convection-Enhanced Delivery and In Vivo Imaging of Polymeric Nanoparticles for the Treatment of Malignant Glioma, *Nanomed. Nanotechnol. Biol. Med.*, 10 (2014) 149-157.
- [6] R. Huang, E. Choe, D.B. Min, Kinetics for Singlet Oxygen Formation by Riboflavin Photosensitization and the Reaction between Riboflavin and Singlet Oxygen, *J. Food Sci. C*, 69 (2004) C726-C732.
- [7] A. de La Rochette, E. Silva, I. Birlouez-Aragon, M. Mancini, A.M. Edwards, P. Morliere, Riboflavin Photodegradation and Photosensitizing Effects are Highly Dependent on Oxygen and Ascorbate Concentrations, *Photochem. Photobiol.*, 72 (2000) 815-820.
- [8] G. Wollensak, E. Spoerl, T. Seiler, Riboflavin/Ultraviolet-A-Induced Collagen Crosslinking for the Treatment of Keratoconus, *Am. J. Ophthalmol.*, 135 (2003) 620-627.
- [9] R.T. Kashiwabuchi, Y. Khan, F.R.d.S. Carvalho, F. Hirai, M.S. Campos, P.J. McDonnell, Antimicrobial Susceptibility of Photodynamic Therapy (UVA/Riboflavin) against *Staphylococcus aureus*, *Arq. Bras. Oftalmol.*, 75 (2012) 423-426.
- [10] R.A. Petros, J.M. DeSimone, Strategies in the Design of Nanoparticles for Therapeutic Applications, *Nat. Rev. Drug Discov.*, 9 (2010) 615-627.
- [11] L. Zhang, F.X. Gu, J.M. Chan, A.Z. Wang, R.S. Langer, O.C. Farokhzad, Strategies in the Design of Nanoparticles for Therapeutic Applications, *Clin. Pharmacol. Ther.*, 83 (2008) 761-769.

- [12] D. Bechet, P. Couleaud, C. Frochot, M.L. Viriot, F. Guillemin, M. Barberi-Heyob, Nanoparticles as Vehicles for Delivery of Photodynamic Therapy Agents, *Trends Biotechnol.*, 26 (2008) 612-621.
- [13] C.J. Cheng, G.T. Tietjen, J.K. Saucier-Sawyer, W.M. Saltzman, A Holistic Approach to Targeting Disease with Polymeric Nanoparticles, *Nat. Rev. Drug Discov.*, 14 (2015) 239-247.
- [14] M.E. Davis, Z. Chen, D.M. Shin, Nanoparticle Therapeutics: An Emerging Treatment Modality for Cancer, *Nat. Rev. Drug Discov.*, 7 (2008) 771-782.
- [15] B. Mishra, B.B. Patel, S. Tiwari, Colloidal Nanocarriers: A Review on Formulation Technology, Types and Applications Toward Targeted Drug Delivery., *Nanomedicine*, 6 (2010) 9-24.
- [16] H.-M. Xiong, ZnO Nanoparticles Applied to Bioimaging and Drug Delivery, *Adv. Mat.*, 25 (2013) 5329-5335.
- [17] S. Sardar, S. Chaudhuri, P. Kar, S. Sarkar, P. Lemmens, S.K. Pal, Direct Observation of Key Photoinduced Dynamics in a Potential Nano-Delivery Vehicle of Cancer Drugs., *Phys. Chem. Chem. Phys.*, 17 (2015) 166-177.
- [18] S. Chaudhuri, S. Sardar, D. Bagchi, S.S. Singha, P. Lemmens, S.K. Pal, Sensitization of an Endogenous Photosensitizer: Electronic Spectroscopy of Riboflavin in the Proximity of Semiconductor, Insulator, and Metal Nanoparticles, *J. Phys. Chem. A*, 119 (2015) 4162-4169.
- [19] S. Sardar, S. Sarkar, M.T.Z. Myint, S. Al-Harhi, J. Dutta, S.K. Pal, Role of Central Metal Ions in Hematoporphyrin-Functionalized Titania in Solar Energy Conversion Dynamics, *Phys. Chem. Chem. Phys.*, 15 (2013) 18562-18570.
- [20] A. Reller, D.L. Cocke, High Resolution Transmission Electron Microscopic (HRTEM) Determination of the Preferentially Exposed Faces on γ -Al₂O₃ and η -Al₂O₃, *Catal. Lett.*, 2 (1989) 91-95.
- [21] X. Liu, M. Atwater, J. Wang, Q. Huo, Extinction Coefficient of Gold Nanoparticles with Different Sizes and Different Capping Ligands, *Colloids Surf. B*, 58 (2007) 3-7.
- [22] E. Vaishnavi, R. Renganathan, Photochemical Events during Photosensitization of Colloidal ZnO Nanoparticles by Riboflavin, *Bull. Mater. Sci.*, 35 (2012) 1173-1179.
- [23] M.-C. Daniel, D. Astruc, Gold Nanoparticles: Assembly, Supramolecular Chemistry, Quantum-Size-Related Properties, and Applications toward Biology, Catalysis, and Nanotechnology, *Chem. Rev.*, 104 (2004) 293-346.

- [24] J. De Gelder, K. De Gussem, P. Vandenaabeele, L. Moens, Reference Database of Raman Spectra of Biological Molecules, *J. Raman Spectrosc.*, 38 (2007) 1133-1147.
- [25] O.A. Chat, M.H. Najar, A.A. Dar, Evaluation of Reduction Kinetics of 2,2-Diphenyl-1-Picrylhydrazyl Radical by Flavonoid Glycoside Rutin in Mixed Solvent Based Micellar Media, *Colloids Surf., A*, 436 (2013) 343-353.
- [26] V.B. Arce, J. Scotto, P.E. Allegretti, M.A. Melo, C. Airoidi, M.L. Salum, R. Erra-Balsells, R. Pis Diez, D.O. Mártire, Combined Experimental and Computational Investigation of the Fluorescence Quenching of Riboflavin by Cinnamic Alcohol Chemisorbed on Silica Nanoparticles, *J. Phys. Chem. C*, 118 (2014) 15348-15355.
- [27] J.P. Escalada, V.B. Arce, G.V. Porcal, M.A. Biasutti, S. Criado, N.A. García, D.O. Mártire, The Effect of Dichlorophen Binding to Silica Nanoparticles on Its Photosensitized Degradation in Water, *Water Res.*, 50 (2014) 229-236.
- [28] J.P. Escalada, V.B. Arce, L. Carlos, G.V. Porcal, M.A. Biasutti, S. Criado, N.A. Garcia, D.O. Martire, Photodegradation Routes of the Herbicide Bromoxynil in Solution and Sorbed on Silica Nanoparticles, *Env. Sci. Process. Impact*, 16 (2014) 858-865.
- [29] M.A.H. Muhammed, A.K. Shaw, S.K. Pal, T. Pradeep, Quantum Clusters of Gold Exhibiting FRET, *J. Phys. Chem. C*, 112 (2008) 14324-14330.

Chapter 6

Surface Modification of Nanoparticles Using Medicinally Important Ligands

6.1. Introduction:

Magnetite (Fe_3O_4) is a mixed-valence (Fe^{2+} - Fe^{3+}) metal oxide, which has been extensively explored in many fields such as magnetic resonance contrast agents, magnetic drug targeting, energy storage, catalysis etc. [1-6]. It has a cubic inverse spinel structure with electron can hop between Fe^{2+} and Fe^{3+} ions at room temperature. This allows the formation of efficient catalyst surfaces [7, 8]. It is a well-established fact that, novel chemical and physical properties originate if the particle sizes reduced to the nanometer regime. Therefore, synthetic techniques for the preparations of magnetite nanoparticles have been continuously further developed and are topics of ongoing research. Numerous methods have been described to synthesize magnetite nanoparticle such as sol-gel synthesis, hydrothermal, sonochemical, co-precipitation, hydrolysis and thermolysis of precursors etc. [7, 9-16]. Magnetite has also been engineered into a wide range of nanostructures, including uniform nanocrystals, wires, cubes, hollow nanostructures as well as many others [7, 17-19].

For biological and environmental applications, it is essential to have the particles in an aqueous medium. This can be obtained with proper surface coating and functionalization using organic ligands. However, the synthesis of well-dispersed Fe_3O_4 NPs without aggregation in aqueous medium showed very limited success. This is because they suffer from limited stability and uniformity due to their high reactivity

under ambient conditions as well as large magnetization [20]. In contrast, non-aqueous methods offer a better control over nanoparticles size and shape; therefore, well-dispersed magnetic Fe_3O_4 nanoparticles have been made often in organic solutions [16, 21]. Although non-aqueous methods can provide highly mono-disperse NPs in scalable amounts, they all have drawbacks with respect to their biological application perspective. Organic surfactant molecules present in the solution for stabilizing the NPs are insoluble in water due to their long hydrophobic chain.

To overcome this problem, only a few ligand exchange methods have been reported that can be used to transfer the particles from organic phases to aqueous solutions [22-24]. For example, Wang et al. have reported a general method to transfer the oleic acid stabilized NPs into the aqueous phase by using α -cyclodextrin, where size and the morphology of the nanoparticles remain unaltered after the phase transfer [24]. The properties of the NPs depend on the size as well as functional ligands. It is also important to mention that for mixed valence oxide NPs, while the application in the field of magnetics, catalysis and biology has been widely studied, their optical properties remain largely unexplored. Previously, our group has explored the emergence of novel optical properties as a result of functionalization in case of $\text{La}_{0.67}\text{Sr}_{0.33}\text{MnO}_3$ (LSMO NP) and Mn_3O_4 NPs [25, 26]. However, till now, there is no such report for the generation of novel optical properties with suitable ligands in case of Fe_3O_4 NPs. Moreover, in recent times, significant efforts have also been made to study the catalytic/photocatalytic performances of mixed valence NPs [26, 27].

The size of the NPs greatly influences their catalytic behavior. Generally, NP with lower size has higher surface energy and therefore shows higher catalytic activity. Additionally, improved optical properties often lead to better catalytic performance. For example, Mn_3O_4 NPs of ~ 5 nm size shows enhanced catalytic degradation of

organic dyes. It has been proven that the oxidation state of Mn ion has significant role on the catalytic behavior of Mn_3O_4 NPs. Akin to the variable oxidation state of Mn in Mn_3O_4 NPs, Fe_3O_4 NPs also contain Fe ion with variable oxidation state. Thus, small sized functionalized Fe_3O_4 NPs with novel optical properties may provide better catalytic performance compared to larger NPs. Therefore, the development of new strategies to pull out the monodisperse Fe_3O_4 NPs from the organic to the aqueous phase and a following ‘core etching’ to improve the NPs optical properties for better catalytic performance is of great interest and the motive of our study.

Herein, we report a top-down approach to fabricate Fe_3O_4 NPs that is based on a surface modification method followed by a ligand exchange strategy. We have used sodium tartrate as ligand for surface modification of the NPs. It is more environmentally benign, highly soluble in water, and consists of two –OH and two –COOH groups which allows a complexation with the surface of Fe_3O_4 NPs, therefore leading to a better controlled fabrication process. In our study, we have used ~23 nm Fe_3O_4 NPs protected by oleylamine/oleylacid, which has been proved to be an effective capping agent in non-aqueous medium, and carried out a surface modification that results to a reduction of particle diameter from ~23 nm to ~5 nm due to core etching. The surface modified tartrate capped Fe_3O_4 NPs (T- Fe_3O_4) have been characterized by various spectroscopic and microscopic techniques. We have observed multiple absorption bands in the UV-Vis region, that are assigned to ligand-to metal charge transfer transitions (LMCT, associated with tartrate- $\text{Fe}^{2+/3+}$ interactions). The surface modified ~5 nm T- Fe_3O_4 NPs show better photocatalytic activity towards a model cationic organic dye (methylene blue, MB) compared to other existing reports. Most importantly, we demonstrate a recycling of the catalyst for many periods, without any significant loss in catalytic activity and selectivity. Control studies with radical

scavenger rule out the possibility of radical pathways like reactive oxygen species (ROS) generation. We propose that the MB degradation kinetics follow a Langmuir-Hinshelwood mechanism, with the surface electron transfer evidenced by our ultrafast spectroscopy data.

We have also explored the potential use of the nanoparticle in the treatment of hyperbilirubinemia, a physiological state of high bilirubin level [27]. Bilirubin (BR) is the yellow breakdown product that is formed during the process of heme degradation. An increased BR level in the blood leads to jaundice. Among many conventional treatments, 'phototherapy' is the most common method for reducing high BR level. In spite of inexpensive and easy to use; there is still some reluctance in the use of phototherapy for fear of unknown immediate and/or long term side effects. As an alternative, researchers have developed various nanocatalysts such as TiO_2 , ZnO , and Mn_3O_4 to treat jaundice [26, 28, 29]. However, photocatalytic degradation of BR cannot be controlled with the existing state-of-the-art photocatalysts, in particular when the particle morphology remains unaltered. To overcome this problem, we have introduced other functionalized NPs, i.e., T- Fe_3O_4 NPs for the degradation of BR under UV light. Through ultrafast spectroscopy, we have demonstrated that UV light induces efficient energy transfer from the T- Fe_3O_4 NPs to the BR leading to efficient BR degradation. In order make the degradation effective and tunable in presence of light, we have attached Mn ions on the surface of the T- Fe_3O_4 NPs. To the best of our knowledge, this is the first report towards efficient, tunable catalyst through surface functionalization. Like, Mn_3O_4 NPs, we have observed that the degradation rate is faster even in absence of light while Mn ions are attached on the surface of T- Fe_3O_4 NPs. In presence of light, Mn ions reduce the catalytic efficiency. Picosecond resolved fluorescence study reveals that the UV light induces the transfer of excited state

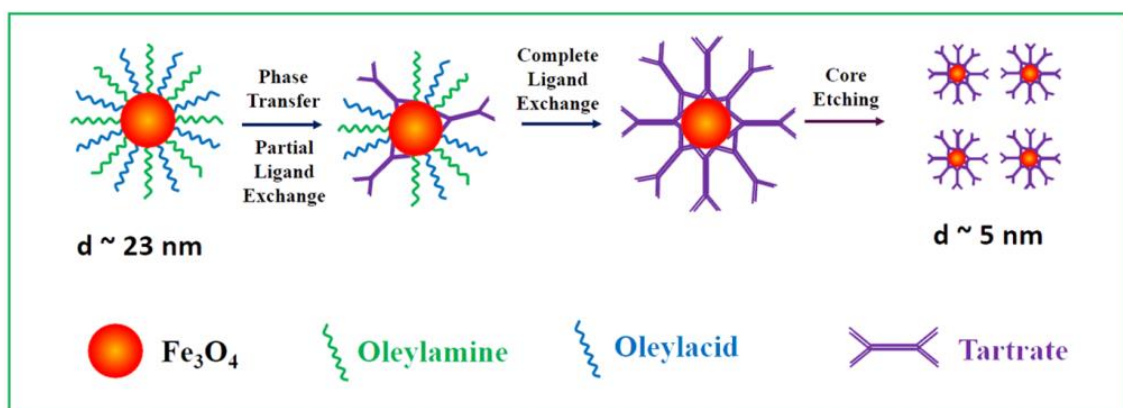
electrons of the T-Fe₃O₄ NPs to the surface attached Mn³⁺ and thus the required transformation for the bilirubin degradation i.e., Mn³⁺ to Mn⁴⁺, gets hindered which results in unusual catalytic activity.

6.2. Results and Discussion:

6.2.1. Surface Engineering for Controlled Nanocatalysis: Key Dynamical Events from Ultrafast Electronic Spectroscopy [30]:

6.2.1.1. TEM and HRTEM Studies: Figure 6.1.a demonstrates the TEM image of colloidal Fe₃O₄ NPs used for surface modification studies. It is found that the particles are spherical in shape with a narrow size distribution and the average diameter is observed to be ~23 nm (Figure 6.1.b). The high resolution image shown in Figure 6.1.c confirms the crystallinity of the NPs. The interplanar distance between the fringes is about 0.243 nm which corresponds to the distance between (222) planes of the Fe₃O₄ cubic crystal lattice. The highly crystalline nature is further confirmed by selected-area electron diffraction (SAED) analysis (Figure 6.1.d). After successful phase transfer, extensive TEM studies have been carried out in order to characterize the water soluble tartrate capped Fe₃O₄ (T-Fe₃O₄) NPs in detail. Figure 6.1.e depicts the HRTEM image of the particles after being fabricated by tartrate ligand. From the micrograph, it is evident that nearly mono-disperse ~23 nm Fe₃O₄ NPs have been transformed into spherical NPs with a relatively uniform size distribution having average diameter ~5 nm. The size distribution of the T-Fe₃O₄ NPs is shown in Figure 6.1.f. The SAED pattern (Figure 6.1.g) and the HRTEM image showing lattice fringes (Figure 6.1.h & i), indicate that the fabricated particles are highly crystalline in nature. Although, the lattice fringes observed in T-Fe₃O₄ NPs, which is ~0.309 nm (Figure 6.1.j), is different from the parent Fe₃O₄ particles indicating that T-Fe₃O₄ NPs are lying on a different

plane after fabrication. A plausible mechanism that phase transfer of ~ 23 nm Fe_3O_4 NPs and their fabrication with tartrate ligand is shown in a schematic diagram (Scheme 6.1).



Scheme 6.1. Schematic representation showing stepwise transformation and fabrication of ~ 23 nm Fe_3O_4 NPs by tartrate ligand.

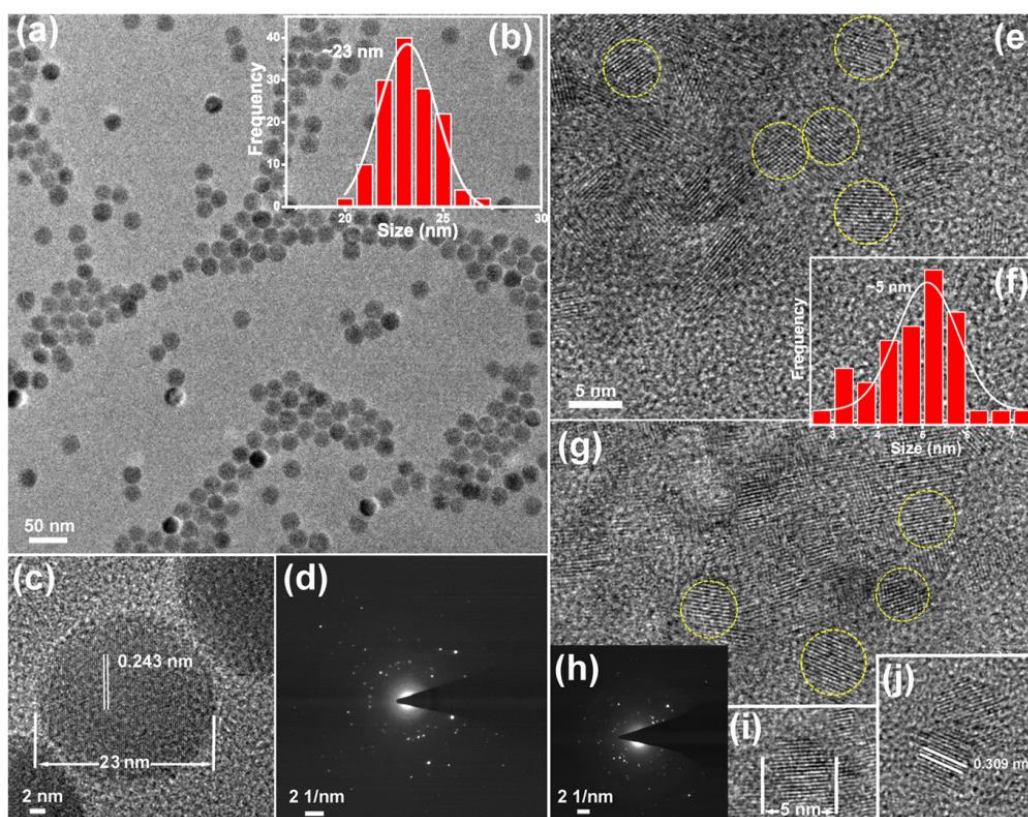


Figure 6.1. (a) TEM image of ~ 23 nm Fe_3O_4 NPs before fabrication. (b) Size distribution curve. (c) HRTEM image of single Fe_3O_4 particle showing the (222) plane. (d) SAED patterns of the Fe_3O_4 NPs before fabrication. (e) & (g) HRTEM images of the Fe_3O_4 NPs after fabrication with tartrate ligand. (f) Size distribution curve showing the average diameter of the NPs is ~ 5 nm. (h) SAED patterns of the Fe_3O_4 NPs after fabrication. (i) HRTEM image of single ~ 5 nm Fe_3O_4 particle. (j) (220) plane of T- Fe_3O_4 NPs.

6.2.1.2. UV-Visible, Luminescence and FTIR Studies: It is well-known that surface electronic structure of NPs may change due to functionalization of the NPs with organic ligands [26]. Before fabrication with tartrate ligand, we have checked the optical absorption spectrum of Fe_3O_4 NPs in chloroform. As shown in Figure 6.2.a (black curve), it has no such distinct absorption signature in the UV-Vis region. However, aqueous solution of T- Fe_3O_4 NPs shows a well-defined absorption spectrum with characteristic peaks in the UV region (Figure 6.2.a).

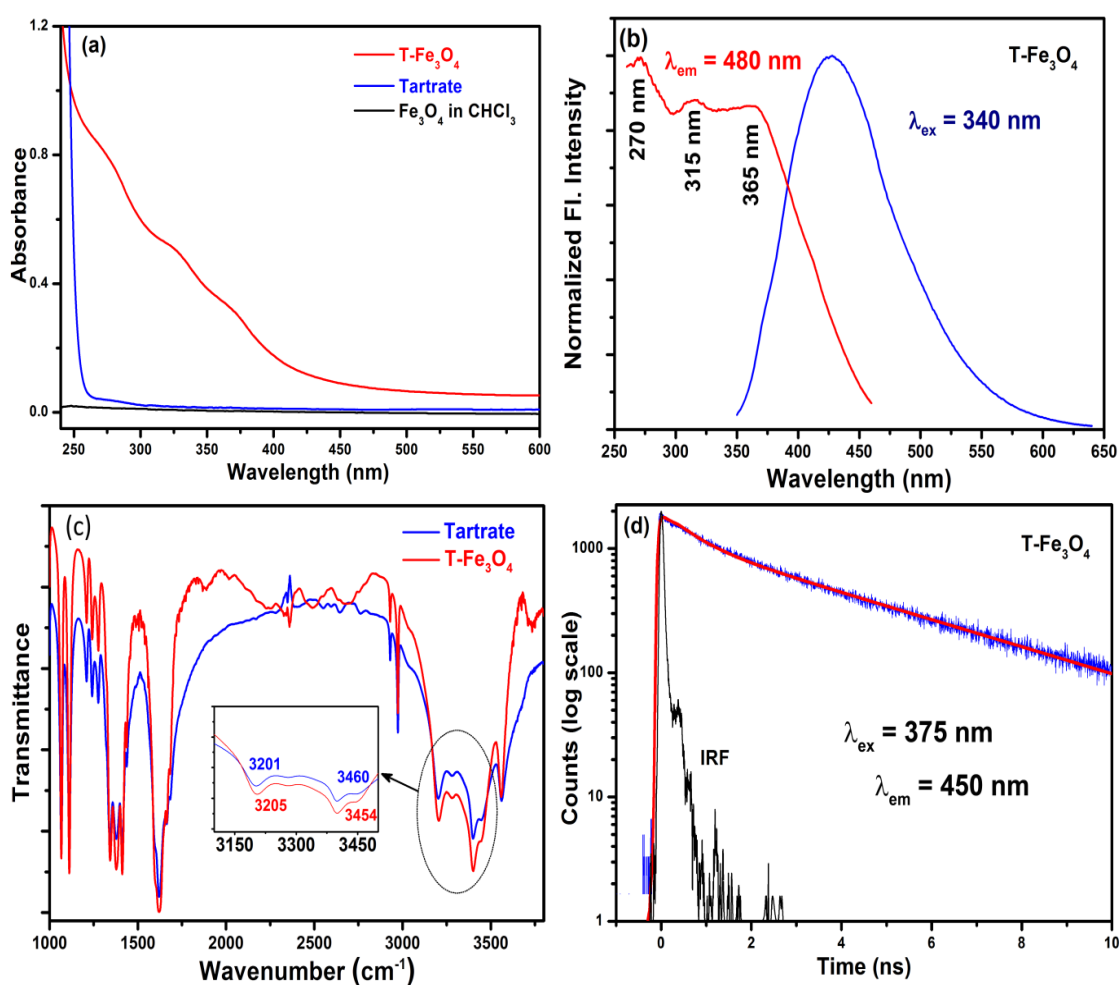


Figure 6.2. (a) UV-Vis absorption spectra of ~ 23 nm Fe_3O_4 NPs in chloroform (black), tartrate (blue) and T- Fe_3O_4 NPs (red) in aqueous medium. (b) Excitation and emission spectra of T- Fe_3O_4 NPs. (c) FTIR spectra of tartrate (blue) and T- Fe_3O_4 NPs (red). The -OH region of the spectra has been shown in the inset. (d) Picosecond resolved fluorescence transient of aqueous T- Fe_3O_4 solution.

Since, tartrate has no such characteristic feature in the UV-Vis region, we anticipate that the high energy bands originate due to the ligand to metal charge transfer transition (LMCT). Apparently, tartrate, having two α -hydroxy carboxylate groups is considered to be strong field ligand and would preferably coordinate with $\text{Fe}^{2+}/\text{Fe}^{3+}$ metal ions centre on the NPs surface. Therefore, it is expected that both $\text{Fe}^{2+}/\text{Fe}^{3+}$ will be in low spin state due to the presence of strong ligand field. Since, it is more difficult to reduce Fe^{2+} compared to Fe^{3+} , the LMCT bands involving Fe^{2+} ion are expected to arise in the high energy region and therefore the bands at 272, 320 and 368 nm are attributed to LMCT to Fe^{2+} (${}^1\text{A}_{1g} \rightarrow {}^1\text{E}_g$), LMCT to Fe^{3+} (${}^2\text{T}_{2g} \rightarrow {}^2\text{E}_g$) and LMCT to Fe^{2+} (${}^1\text{A}_{1g} \rightarrow {}^1\text{T}_{2g}$) in a low-spin octahedral environment [31, 32]. Interestingly, after high pH and temperature (at pH~12 and 70°C for 6 hrs) treatment, T- Fe_3O_4 NPs show blue luminescence ($\lambda_{\text{em}} = 440$ nm) upon excitation with 340 nm wavelength. Figure 6.2.b depicts the excitation and emission spectra of T- Fe_3O_4 NPs in aqueous medium. The consistency of the luminescence excitation spectrum with that of the UV-Vis absorption indicates the emission may originate predominantly from the LMCT excited states. Moreover, for 340 nm excitation, the integrated luminescence quantum yield for T- Fe_3O_4 NPs is 0.0056, using Hoechst 33258 as the reference. Previously, Govindaiah et al. have reported luminescent Fe_3O_4 NPs protected with 5-Amino-1,10-phenanthroline ligand, however, the origin of luminescence was due to the functionalizing ligand [33].

Picosecond resolved luminescence lifetime experiments have also been performed in order to check the excited state dynamics of the T- Fe_3O_4 NPs. In order to get the direct evidence of ligand functionalization onto the surface of NPs. FTIR spectra (Figure 6.2.c) of both tartrate and T- Fe_3O_4 NPs exhibit a broad peak from 3400 to 3600 cm^{-1} , which originate due to the stretching vibration of the hydroxyl groups of tartrate ligand.

Pure tartrate has peaks at 3201 and 3460 cm^{-1} , which become shifted to 3205 and 3454 cm^{-1} upon functionalization with Fe_3O_4 NPs, clearly confirm the binding of ligands with NPs surface. It is well-known that Fe_3O_4 has a characteristic Fe-O vibration band at around 580 cm^{-1} [34]. However, in our case we do not observe such a band probably because of the high concentration of tartrate ligand. Figure 6.2.d reveals the decay transients of the T- Fe_3O_4 NPs upon excitation with 375 nm laser. Lifetime values are obtained by the multi-exponential fitting of the luminescence at 440 nm. Time components are 580 ps (45%) and 3.95 ns (55%). The short average lifetime (2.45 ns) is in agreement with spin allowed transition and consistent with the previous values on the luminescence lifetime originated from LMCT [35].

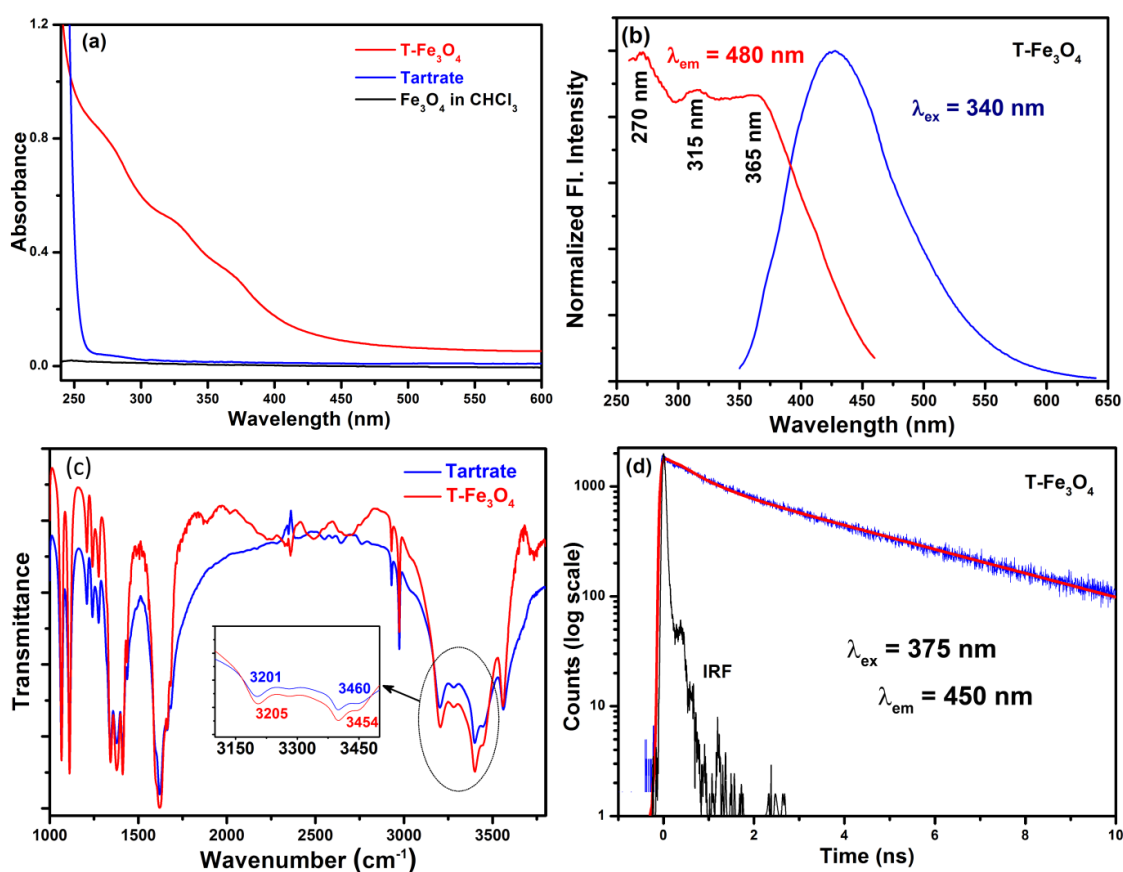


Figure 6.2. (a) UV-Vis absorption spectra of ~ 23 nm Fe_3O_4 NPs in chloroform (black), tartrate (blue) and T- Fe_3O_4 NPs (red) in aqueous medium. (b) Excitation and emission spectra of T- Fe_3O_4 NPs. (c) FTIR spectra of tartrate (blue) and T- Fe_3O_4 NPs (red). The OH region of the spectra has been shown in the inset. (d) Picosecond resolved fluorescence transient of aqueous T- Fe_3O_4 solution.

6.2.1.3. Photocatalysis:

6.2.1.3.1. Photodegradation of Methylene Blue: After examining the optical and structural characteristics of T-Fe₃O₄ NPs, to take full advantage of their photoluminescence properties, we have performed detailed photocatalytic measurements under UV light. We have selected methylene blue (MB) as a model probe for photocatalytic experiment. It is a potent cationic dye used in the textile industry, with maximum absorption of light around 660 nm. As a control study,

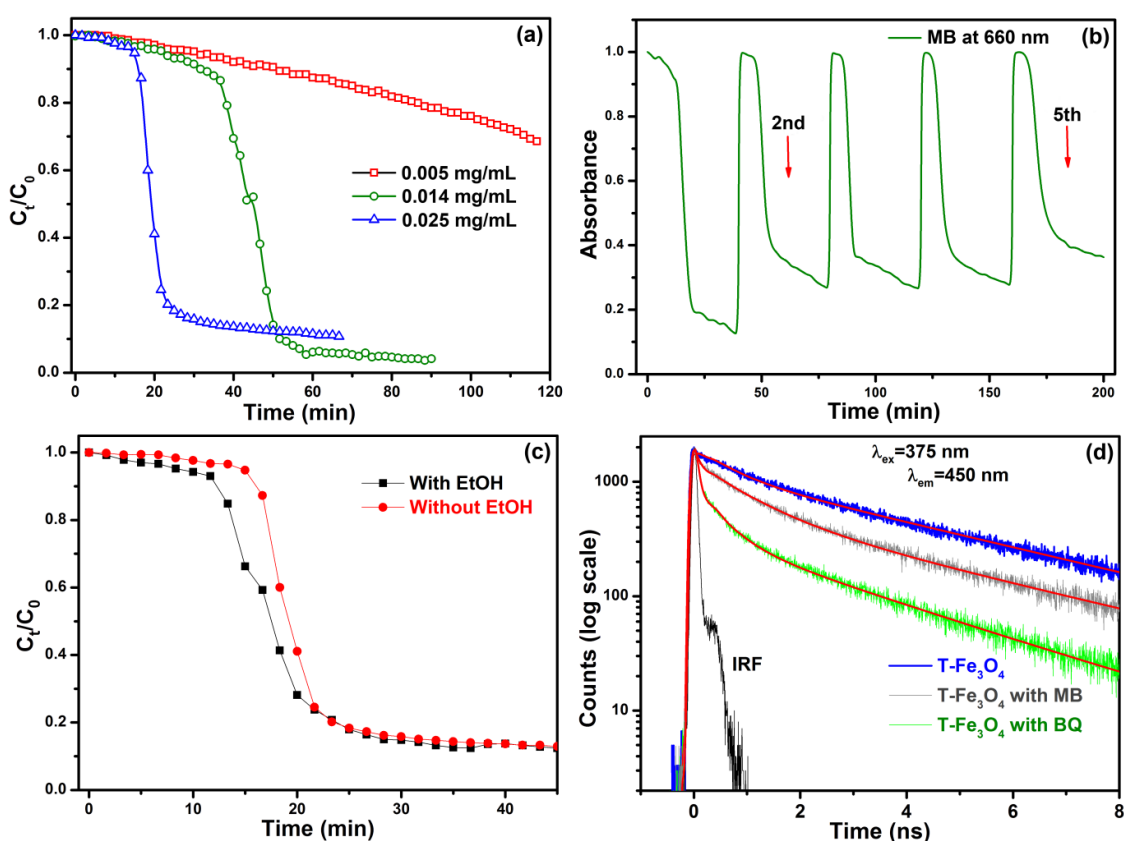
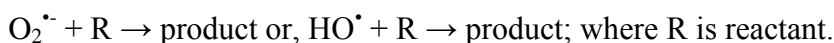
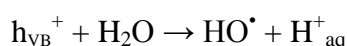
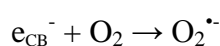
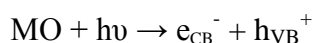


Figure 6.3. (a) Photocatalytic degradation of fixed concentrated methylene blue solution with various amount of T-Fe₃O₄ NPs. (b) Cycling curve of photocatalytic degradation of methylene blue in presence of fixed concentration (0.025 mg/mL) of Fe₃O₄ NPs. (c) Photocatalytic degradation of methylene blue by T-Fe₃O₄ NPs in presence and absence of ethanol. Concentration of T-Fe₃O₄ NPs = 0.025 mg/mL. (d) Picosecond resolved fluorescence decay transients of T-Fe₃O₄ NPs in the absence and presence of methylene blue and benzoquinone.

we have tested the photocatalytic properties of tartrate and as-prepared T-Fe₃O₄ NPs under UV light. However, the peak intensity at 660 nm remains almost unchanged even after 120 min in both cases. Later on, we have examined the photocatalytic behavior of

luminescent T-Fe₃O₄ NPs under similar experimental condition and observed unprecedented photocatalytic behavior. As the rate of a catalytic reaction depends on factors like concentration, and surface area of the catalyst, therefore, we have studied catalyst concentration dependent kinetics. From the Figure 6.3.a, it has been found that the rate of the reaction increases with increase of the catalyst concentration. It is obvious for a surface catalysis reaction because increase in catalyst concentration means more surface area available for effective catalysis. It can also be seen that degradation of MB followed an “induction period” and subsequent “acceleration period”. Note that, earlier reports on Fe₃O₄ NPs suggest that MB undergoes degradation process instantaneously after the exposure of UV light. However, induction time has been reported for TiO₂ mediated photocatalysis [36]. We propose that during induction period, build-up of reaction intermediates occurs and the surface of the NPs becomes saturated with the MB molecules. As revealed from Figure 6.3.a, the induction time becomes shorter with increase of NPs concentration in a fixed concentrated aqueous MB solution of pH 5. Furthermore, to confirm the stability of the high photocatalytic performance of the T-Fe₃O₄ NPs, recycling experiments have been conducted. We have carried out five consecutive cycles (Figure 6.3.b) that show that the rate of the photocatalytic degradation remains almost constant indicating the high stability of the catalyst even under long time UV exposure. This observation indicates that the catalytic properties of the T-Fe₃O₄ NPs become rejuvenated after each cycle. This finding is especially important for its industrial application. Figure 6.3.b depicts that in the first cycle, the excellent photocatalytic activity (90% MB degradation) is obtained in the presence of very small amount of T-Fe₃O₄ NPs (0.025 mg/mL) and the degradation become 65% after fifth cycle. The results demonstrate that these T-Fe₃O₄ NPs can indeed serve as highly effective and convenient recyclable photocatalyst.

Often the question for the mechanism involved in photocatalysis. It is well-known that different photocatalytic pathways have been established for the degradation of organic dyes [37, 38]. Here, we first consider the approach which is based on the generation of reactive oxygen species (ROS). Presence of strong UV light excites electron from the valence band (VB) to the conduction band (CB) of the metal oxide (MO), leaving a positively charged hole in the VB. The electron in the CB and the hole in the VB then reacts with O₂ and H₂O on the MO surface, therefore generates reactive oxygen species (ROS) such as O₂^{•-} and HO[•]. The mechanistic pathway is shown below [39]:



The generation of ROS and subsequent radical chain reactions result to the degradation of organic dye. As the fabricated T-Fe₃O₄ NPs exhibit absorption bands in the UV-Vis region, presence of strong UV light may generate ROS. So, the mechanism as explained above is highly possible here. If so, then the rate of photocatalytic degradation is expected to be slow down in presence of ethanol, which is a well-known radical scavenger. However, as shown in Figure 6.3.c, the catalytic rate of MB degradation remains almost same in presence and absence of ethanol, which rules out the role of ROS generation in the photocatalytic process. However, the kinetic behavior of MB degradation can be described by Langmuir–Hinshelwood (LH) model [40, 41]. The generalized LH model can be expressed as:

$$R = \frac{dC_0}{dt} = k_s S C_0 = \frac{k_s S k_0 C_0}{1 + k_0 C_0}$$

Where, 'R' is the rate of the reaction. ' k_s ' is the rate constant of the reaction. ' C_0 ' is the initial concentration of the MB in water. ' k_o ' is the adsorption constant for MB molecules. 'S' is the surface area of the T-Fe₃O₄ NPs. Since, MB has very high adsorption, so the rate is proportional to the surface area (S) of the NPs present in the system. The rate constant values are found to be increasing with the increase in concentration of T-Fe₃O₄ NPs suggesting zero-order dependence of the reaction rate on surface area.

As discussed above, the surface interaction between MB and T-Fe₃O₄ NPs is confirmed and the enhanced photocatalytic activity could be explained by the following mechanism: it is well-known that electron transfer is associated with the MB degradation [42]. As T-Fe₃O₄ NPs have good photoluminescence properties upon excitation with UV light, photo-induced electron transfer (PET) may possibly account to the degradation process. In order to unravel that, we have performed picosecond resolved fluorescence studies (Figure 6.3.d), which directs significant quenching of the decay transient of T-Fe₃O₄ NPs upon complexation with MB molecules. As a control study, we have considered the complexation of the T-Fe₃O₄ NPs with an organic molecule, benzoquinone (BQ), which is well-known as an electron acceptor and efficiently accepts excited electrons from the Nanosurface [43]. In presence of BQ, a very sharp decay (monitored at 450 nm) is observed, which is associated with the PET process (Figure 6.3.d). It can be seen from Table 6.1 that the T-Fe₃O₄ NPs in presence of MB exhibit an ultrafast time component of 75 ps with a majority (57%) which is akin to the component, i.e., 45 ps (83%) in the presence of BQ, at the same excitation of 375 nm. The result implies the favorable PET process from the T-Fe₃O₄ NPs to the MB molecules at the surface of the NPs.

6.2.1.3.2. Controlled Photodegradation of Bilirubin: Following the photocatalytic degradation of MB, we have examined the potential of modified T-Fe₃O₄ NPs towards the degradation of bilirubin (BR).

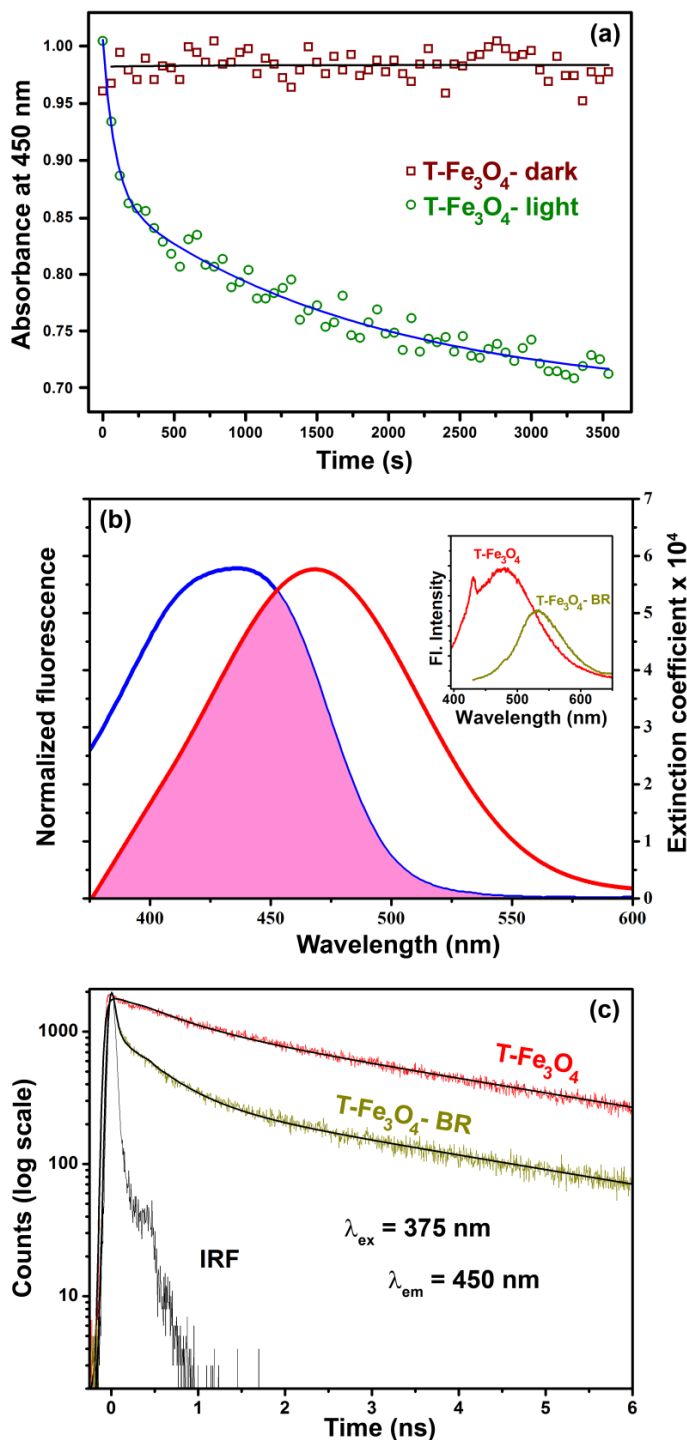


Figure 6.4. (a) Absorption kinetics of bilirubin (degradation monitored at 450 nm) under UV light as well as in dark in absence and presence of T-Fe₃O₄ (b) Spectral overlap of T-Fe₃O₄ emission and bilirubin absorption. (c) Fluorescence lifetime quenching of T-Fe₃O₄ in water in absence and presence of bilirubin.

The characteristic absorbance band of BR at 450 nm has been chosen for monitoring the kinetic study using UV-Vis spectroscopy. Figure 6.4.a shows the relative concentration (C_t/C_0) of BR with respect to the UV irradiation time. In the absence of UV light, we observe almost minimal degradation which depicts the different behaviour of Fe^{2+}/Fe^{3+} system compared to Mn^{3+}/Mn^{4+} system in Mn_3O_4 NPs which can efficiently degrade BR in dark condition. However, T- Fe_3O_4 NPs can effectively degrade BR (30%) in the presence of UV light. As the optical absorption spectrum of BR overlaps with the emission of T- Fe_3O_4 NPs (Figure 6.4.b), we propose FRET from T- Fe_3O_4 NPs (donor) to BR (acceptor), is responsible for the observed degradation. Picosecond-resolved fluorescence spectroscopy is a useful technique that provides information about the excited-state dynamics. The decay transients of T- Fe_3O_4 NPs in aqueous medium in absence (donor) and presence of BR (donor-acceptor) have been shown in Figure 6.4.c. The decay transient of the donor has been fitted with two components, with an average lifetime of 2.45 ns. The fluorescence decay trace of the donor-acceptor could be fitted with a fast component, apparently corresponding to some non-radiative channel, along with two other components. The details of the numerical fitting of the fluorescence transients are tabulated in Table 6.1. From the fitting result, we have estimated the Förster distance to be 19.44 Å. The short donor-acceptor distance indicates that BR molecules are in close proximity of the surface of the NPs. It has to be noted that FRET based efficient BR degradation by ZnO NPs was reported previously [28].

However, in the present study, the degradation efficiency is lower compared to other reports. Therefore, in order to enhance the degradation rate, we have incorporated Mn ions on the NPs surface. After the addition of $MnCl_2$, the T- Fe_3O_4 NPs solution has been heated at high temperature for six hours at pH 12. It is noteworthy to mention that

at high pH, all the Mn^{2+} will be converted to Mn^{3+} . The attachment has been confirmed

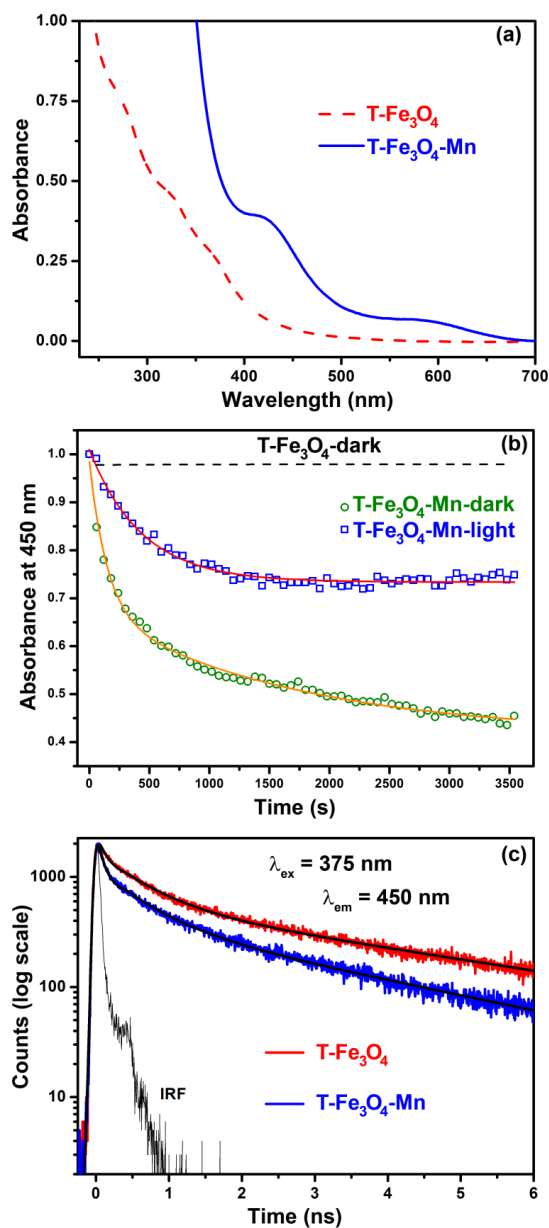


Figure 6.5. (a) UV-Vis absorption spectra of $\text{T-Fe}_3\text{O}_4$ NPs in absence (red) and presence (blue) of manganese ion in aqueous medium. (b) Absorption kinetics of bilirubin (degradation monitored at 450 nm) under UV light as well as in dark in the absence and presence of $\text{T-Fe}_3\text{O}_4$ -Mn (c) Picosecond resolved fluorescence transients of aqueous $\text{T-Fe}_3\text{O}_4$ solution in absence and presence of manganese ion.

by the absorption spectroscopy (Figure 6.5.a). The observed peaks around 430 nm and 565 nm exist due to the d-d transition of Mn^{3+} ion on the NPs surface. After attachment, we have tested the Mn^{3+} attached $\text{T-Fe}_3\text{O}_4$ NPs for the degradation of bilirubin. The degradation kinetics with Mn^{3+} attached $\text{T-Fe}_3\text{O}_4$ NPs in absence and

presence of light has been shown in Figure 6.5.b. It can be seen that BR degradation is much faster in absence of light. However, the rate is similar to T-Fe₃O₄ NPs in presence of light. It is well known that Mn₃O₄ NPs can catalytically degrade BR in absence of light. It has been proposed that upon addition of bilirubin, Mn³⁺ ions in the surface will be converted to Mn⁴⁺ state which generates few reactive oxygen species (ROS) that ultimately degrade bilirubin. In case of Mn³⁺ attached T-Fe₃O₄ NPs, we propose the similar mechanism for the BR degradation in the absence of light. In presence of light, Mn³⁺ has negligible effect which indicates that UV light blocks the Mn³⁺ to Mn⁴⁺ conversion. Thus, the only possibility is the excited state electron transfer from T-Fe₃O₄ NPs to Mn³⁺ ions. Here, we observed the electron transfer in the excited state. Picosecond resolved fluorescence transients of T-Fe₃O₄ NPs in aqueous medium in absence and presence of Mn³⁺ ions have been shown in Figure 6.5.c. An electron from T-Fe₃O₄ NPs is transferred to of Mn³⁺ which results in a faster component in the fluorescence lifetime. The details of the numerical fitting of the fluorescence transients are tabulated in Table 6.1. There are few studies which report that Fe₃O₄ NPs block electron transfer in an electrochemical process [44, 45]. The results described in this study indicate that excited state electron of T-Fe₃O₄ NPs prevents the conversion of Mn³⁺ to Mn⁴⁺ which are attached on its surface leading to slower catalytic rate.

Table 6.1. Lifetime values T-Fe₃O₄ NPs in the absence and presence of BQ, MB, Mn ions and BR^a.

System	τ_1	τ_2	τ_3	τ_{av}
T-Fe ₃ O ₄	-	580 ps (45%)	3.95 ns (55%)	2.45 ns
T-Fe ₃ O ₄ + BQ	45 ps (83%)	395 ps (10%)	2.60 ns (07%)	235 ps
T-Fe ₃ O ₄ + MB	75 ps (57%)	930 ps (27%)	3.95 ns (16%)	950 ps
T-Fe ₃ O ₄ + Mn ions	75 ps (64%)	707 ps (24%)	3.06 ns (12%)	0.60 ns
T-Fe ₃ O ₄ + BR	25 ps (38%)	470 ps (43%)	3.92 ns (19%)	0.98 ns

^a(Numbers in parentheses indicate relative percentage. $\lambda_{em} = 450$ nm, $\lambda_{ex} = 375$ nm. Standard error ~ 5%).

6.3. Conclusion:

We have successfully demonstrated a facile top-down approach to fabricate a commercially available ferrofluid using tartrate ligand. Oleic amine/oleyl acid capped ~23 nm Fe_3O_4 NPs have been efficiently phase transferred into aqueous phase from chloroform. The controlled tartrate etching process in aqueous solution converts the particle diameter from 23 nm to ~ 5 nm. LMCT optical bands in the electronic spectra enable the elucidation of the quantum origins of excellent blue luminescence. When evaluated for their possible use in photocatalysis, the fabricated T- Fe_3O_4 NPs exhibit a significantly improved performance compared to the reports in existing literature. The rejuvenating catalytic properties of T- Fe_3O_4 NPs have been illustrated, which reveals the particle as a recyclable and a highly efficient photocatalyst. The results indicate that ROS generation pathway is not the case here, rather it follows Langmuir-Hinshelwood model. The catalytic degradation rate for the bilirubin has been accelerated in absence of UV light when the surface of the T- Fe_3O_4 NPs has been modified with Mn ions. However, in the presence of UV light, the degradation is slower due to the blockage of Mn^{3+} to Mn^{4+} transformation through the excited state electron transfer from T- Fe_3O_4 NPs to the Mn^{3+} ion. This result has importance in direct therapeutic applications against hyperbilirubinemia. We believe that the method described in this study, might be extended to other magnetic transition metal oxide nanoparticles which will effectively lead to the development of multifunctional nanomaterials having excellent optical, magnetic and catalytic properties.

References:

- [1] Y.-w. Jun, Y.-M. Huh, J.-s. Choi, J.-H. Lee, H.-T. Song, Sungjun, Sungjun, S. Yoon, K.-S. Kim, J.-S. Shin, e. al., Nanoscale Size Effect of Magnetic Nanocrystals and Their Utilization for Cancer Diagnosis via Magnetic Resonance Imaging, *J. Am. Chem. Soc.*, 127 (2005) 5732-5733.
- [2] S.-W. Cao, Y.-J. Zhu, M.-Y. Ma, L. Li, L. Zhang, Hierarchically Nanostructured Magnetic Hollow Spheres of Fe_3O_4 and $\gamma\text{-Fe}_2\text{O}_3$: Preparation and Potential Application in Drug Delivery, *J. Phys. Chem. C*, 112 (2008) 1851-1856.
- [3] O. Veiseh, J.W. Gunn, M. Zhang, Design and Fabrication of Magnetic Nanoparticles for Targeted Drug Delivery and Imaging, *Adv. Drug Deliv. Rev.*, 62 (2010) 284-304.
- [4] B. Li, H. Cao, J. Shao, M. Qu, J.H. Warner, Superparamagnetic Fe_3O_4 Nanocrystals@graphene Composites for Energy Storage Devices, *J. Mater. Chem.*, 21 (2011) 5069-5075.
- [5] T. Zeng, W.-W. Chen, C.M. Cirtiu, A. Moores, G. Song, C.-J. Li, Fe_3O_4 Nanoparticles: A Robust and Magnetically Recoverable Catalyst for Three-Component Coupling of Aldehyde, Alkyne and Amine, *Green Chem.*, 12 (2010) 570-573.
- [6] C.W. Lim, I.S. Lee, Magnetically Recyclable Nanocatalyst Systems for the Organic Reactions, *Nano Today*, 5 (2010) 412-434.
- [7] S.H. Sun, H. Zeng, Size-Controlled Synthesis of Magnetite Nanoparticles, *J. Am. Chem. Soc.*, 124 (2002) 8204-8205.
- [8] S. Soeya, J. Hayakawa, H. Takahashi, K. Ito, C. Yamamoto, A. Kida, H. Asano, M. Matsui, Development of Half-Metallic Ultrathin Fe_3O_4 Films for Spin-Transport Devices, *Appl. Phys. Lett.*, 80 (2002) 823-825.
- [9] O.M. Lemine, K. Omri, B. Zhang, L. El Mir, M. Sajieddine, A. Alyamani, M. Bououdina, Sol-Gel Synthesis of 8 nm Magnetite (Fe_3O_4) Nanoparticles and Their Magnetic Properties, *Superlatt. Microstruct.*, 52 (2012) 793-799.
- [10] T.J. Daou, G. Pourroy, S. Bégin-Colin, J.M. Grenèche, C. Ulhaq-Bouillet, P. Legaré, P. Bernhardt, C. Leuvrey, G. Rogez, Hydrothermal Synthesis of Monodisperse Magnetite Nanoparticles, *Chem. Mater.*, 18 (2006) 4399-4404.
- [11] K.V.P.M. Shafi, A. Ulman, X. Yan, N.-L. Yang, C. Estournès, H. White, M. Rafailovich, Sonochemical Synthesis of Functionalized Amorphous Iron Oxide Nanoparticles, *Langmuir*, 17 (2001) 5093-5097.

- [12] T. Fried, G. Shemer, G. Markovich, Ordered Two-Dimensional Arrays of Ferrite Nanoparticles, *Adv. Mater.*, 13 (2001) 1158-1161.
- [13] H. Iida, K. Takayanagi, T. Nakanishi, T. Osaka, Synthesis of Fe₃O₄ Nanoparticles with Various Sizes and Magnetic Properties by Controlled Hydrolysis, *J. Colloid Interface Sci.*, 314 (2007) 274-280.
- [14] W.W. Yu, J.C. Falkner, C.T. Yavuz, V.L. Colvin, Synthesis of Monodisperse Iron Oxide Nanocrystals by Thermal Decomposition of Iron Carboxylate Salts, *Chem. Commun.*, (2004) 2306-2307.
- [15] T. Hyeon, S.S. Lee, J. Park, Y. Chung, H.B. Na, Synthesis of Highly Crystalline and Monodisperse Maghemite Nanocrystallites without a Size-Selection Process, *J. Am. Chem. Soc.*, 123 (2001) 12798-12801.
- [16] S. Laurent, D. Forge, M. Port, A. Roch, C. Robic, L. Vander Elst, R.N. Muller, Magnetic Iron Oxide Nanoparticles: Synthesis, Stabilization, Vectorization, Physicochemical Characterizations, and Biological Applications, *Chem. Rev.*, 108 (2008) 2064-2110.
- [17] H.T. Yang, T. Ogawa, D. Hasegawa, M. Takahashi, Synthesis and Magnetic Properties of Monodisperse Magnetite Nanocubes, *J. Appl. Phys.*, 103 (2008).
- [18] G. Gao, X. Liu, R. Shi, K. Zhou, Y. Shi, R. Ma, E. Takayama-Muromachi, G. Qiu, Shape-Controlled Synthesis and Magnetic Properties of Monodisperse Fe₃O₄ Nanocubes, *Cryst. Growth Des.*, 10 (2010) 2888-2894.
- [19] S. Peng, S. Sun, Synthesis and Characterization of Monodisperse Hollow Fe₃O₄ Nanoparticles, *Angew. Chem. Int. Ed.*, 46 (2007) 4155-4158.
- [20] W. Wu, Q.G. He, C.Z. Jiang, Magnetic Iron Oxide Nanoparticles: Synthesis and Surface Functionalization Strategies, *Nanoscale Res. Lett.*, 3 (2008) 397-415.
- [21] S. Si, C. Li, X. Wang, D. Yu, Q. Peng, Y. Li, Magnetic Monodisperse Fe₃O₄ Nanoparticles, *Cryst. Growth Des.*, 5 (2005) 391-393.
- [22] W.Y. William, C. Emmanuel, M.S. Christie, D. Rebekah, L.C. Vicki, Aqueous Dispersion of Monodisperse Magnetic Iron Oxide Nanocrystals Through Phase Transfer, *Nanotechnology*, 17 (2006) 4483-4487.
- [23] T. Zhang, J. Ge, Y. Hu, Y. Yin, A General Approach for Transferring Hydrophobic Nanocrystals into Water, *Nano Lett.*, 7 (2007) 3203-3207.
- [24] Y. Wang, J.F. Wong, X. Teng, X.Z. Lin, H. Yang, "Pulling" Nanoparticles into Water: Phase Transfer of Oleic Acid Stabilized Monodisperse Nanoparticles into Aqueous Solutions of α -Cyclodextrin, *Nano Lett.*, 3 (2003) 1555-1559.

- [25] A. Giri, N. Goswami, M.S. Bootharaju, P.L. Xavier, R. John, N.T.K. Thanh, T. Pradeep, B. Ghosh, A.K. Raychaudhuri, S.K. Pal, Emergence of Multicolor Photoluminescence in $\text{La}_{0.67}\text{Sr}_{0.33}\text{MnO}_3$ Nanoparticles, *J. Phys. Chem. C*, 116 (2012) 25623-25629.
- [26] A. Giri, N. Goswami, M. Pal, M.T. Zar Myint, S. Al-Harhi, A. Singha, B. Ghosh, J. Dutta, S.K. Pal, Rational Surface Modification of Mn_3O_4 Nanoparticles to Induce Multiple Photoluminescence and Room Temperature Ferromagnetism, *J. Mater. Chem. C*, 1 (2013) 1885-1895.
- [27] A. Giri, N. Goswami, C. Sasmal, N. Polley, D. Majumdar, S. Sarkar, S.N. Bandyopadhyay, A. Singha, S.K. Pal, Unprecedented Catalytic Activity of Mn_3O_4 Nanoparticles: Potential Lead of a Sustainable Therapeutic Agent for Hyperbilirubinemia, *RSC Adv.*, 4 (2014) 5075-5079.
- [28] T. Bora, K.K. Lakshman, S. Sarkar, A. Makhal, S. Sardar, S.K. Pal, J. Dutta, Modulation of Defect-Mediated Energy Transfer from ZnO Nanoparticles for the Photocatalytic Degradation of Bilirubin, *Beilstein J. Nanotechnol.*, 4 (2013) 714-725.
- [29] J.B. Hall, M.A. Dobrovolskaia, A.K. Patri, S.E. McNeil, Characterization of Nanoparticles for Therapeutics, *Nanomedicine*, 2 (2007) 789-803.
- [30] N. Goswami, S. Chaudhuri, A. Giri, P. Lemmens, S.K. Pal, Surface Engineering for Controlled Nanocatalysis: Key Dynamical Events from Ultrafast Electronic Spectroscopy, *J. Phys. Chem. C*, 118 (2014) 23434-23442.
- [31] D. Templeton, Molecular and Cellular Iron Transport, in, Taylor and Francis, 2002, 848.
- [32] D.M. Sherman, Electronic Spectra of Fe^{3+} Oxides and Oxide Hydroxides in the Near IR to Near UV, *Am. Mineral.*, 70 (1985) 1262-1269.
- [33] P. Govindaiah, T.J. Park, Y.J. Jung, S.J. Lee, D.Y. Ryu, J.H. Kim, I.W. Cheong, Luminescent Iron Oxide Nanoparticles Prepared by One-Pot Aphen-Functionalization, *Macromol. Res.*, 18 (2010) 1109-1114.
- [34] K. Yang, H. Peng, Y. Wen, N. Li, Re-Examination of Characteristic FTIR Spectrum of Secondary Layer in Bilayer Oleic Acid-Coated Fe_3O_4 Nanoparticles, *Appl. Surf. Sci.*, 256 (2010) 3093-3097.
- [35] A. Vogler, H. Kunkely, Luminescence from Hexacyanoruthenate(III), *Inorg. Chim. Acta.*, 53 (1981) L215-L216.

- [36] J. Virkutyte, B. Baruwati, R.S. Varma, Visible Light Induced Photobleaching of Methylene Blue over Melamine-Doped TiO₂ Nanocatalyst, *Nanoscale*, 2 (2010) 1109-1111.
- [37] K. Rajeshwar, M.E. Osugi, W. Chanmanee, C.R. Chenthamarakshan, M.V.B. Zaroni, P. Kajitvichyanukul, R. Krishnan-Ayer, Heterogeneous Photocatalytic Treatment of Organic Dyes in Air and Aqueous Media, *J. Photochem. Photobiol. C: Photochem. Rev.*, 9 (2008) 171-192.
- [38] R.V. Solomon, I.S. Lydia, J.P. Merlin, P. Venuvanalingam, Enhanced Photocatalytic Degradation of Azo Dyes Using Nano Fe₃O₄, *J. Iran Chem. Soc.*, 9 (2012) 101-109.
- [39] S. Sarkar, A. Makhal, T. Bora, K. Lakhsman, A. Singha, J. Dutta, S.K. Pal, Hematoporphyrin-ZnO Nanohybrids: Twin Applications in Efficient Visible-Light Photocatalysis and Dye-Sensitized Solar Cells, *ACS Appl. Mater. Interfaces*, 4 (2012) 7027-7035.
- [40] N. Goswami, R. Saha, S.K. Pal, Protein-Assisted Synthesis Route of Metal Nanoparticles: Exploration of Key Chemistry of the Biomolecule, *J. Nanopart. Res.*, 13 (2011) 5485-5495.
- [41] S. Sarkar, A. Makhal, S. Baruah, M.A. Mahmood, J. Dutta, S.K. Pal, Nanoparticle-Sensitized Photodegradation of Bilirubin and Potential Therapeutic Application, *J. Phys. Chem. C*, 116 (2012) 9608-9615.
- [42] S.-K. Lee, A. Mills, Novel Photochemistry of Leuco-Methylene Blue, *Chem. Commun.*, (2003) 2366-2367.
- [43] N. Goswami, A. Giri, S. Kar, M.S. Bootharaju, R. John, P.L. Xavier, T. Pradeep, S.K. Pal, Protein-Directed Synthesis of NIR-Emitting, Tunable HgS Quantum Dots and their Applications in Metal-Ion Sensing, *Small*, 8 (2012) 3175-3184.
- [44] E. Katz, I. Willner, Magneto-controlled Quantized Electron Transfer to Surface-confined Redox Units and Metal Nanoparticles, *Sensors*, 6 (2006) 420-427.
- [45] Y. Lili, W. Hui, W. Beina, W. Ziyi, C. Hongmei, F. Congying, J. Nengqin, Magnetic Fe₃O₄-Reduced Graphene Oxide Nanocomposites-Based Electrochemical Biosensing, *Nano-Micro Lett.*, 6 (2014) 258-267.

Chapter 7

Mechanism of Photo-Sensitized Carcinogenic Cell Damage by a Food Carcinogen and Protective Role of a Medicinally Important Molecule

7.1. Introduction:

Electron transfer (ET) reactions are notable for their significance in chemistry, biophysics, radiation biology and cancer biochemistry [1-4]. A new concept of reductive DNA damage induced by ultrafast ET reactions of prehydrated electrons, a novel species of electrons produced by radiolysis of water under ionizing radiation, has emerged in some of the recent works [5, 6]. Such studies report that the effectiveness of prehydrated electrons induced reductive DNA damage is about two fold compared to that of oxidative DNA damage by hydroxyl radical. Some radiations lead to cellular damage by both direct and indirect interactions with the cell components. For example, UVB (280-320 nm) radiation is directly absorbed by DNA which results in the formation of cyclobutane pyrimidine dimers (CPDs) and photoproducts [7] and are responsible for the tumorigenic effects [8]. UVA (320-400 nm) radiation, which is present more abundantly in sunlight compared to UVB, can induce various forms of DNA damage in the presence of endogenous or exogenous photosensitizers. It has recently been demonstrated that UVA can induce CPDs by direct absorption of DNA [9, 10]. Some of the earlier studies have reported that coexposure of UVA radiation and

benzo[a]pyrene (BP), can induce DNA damages like single-strand breaks (SSBs) and double-strand breaks (DSBs) in both *in vivo* and *in vitro* experimental conditions [11, 12]. BP is a potential carcinogenic polycyclic aromatic hydrocarbon (PAH) [13] to which people are frequently exposed through fuel and tobacco combustion along with grilled and smoked food products [3, 14]. Though BP is not carcinogenic per se and needs to be activated into a diol-epoxide derivative, which covalently binds to DNA (at N2 and N7 of guanine and N3 of adenine), the possibility of direct intercalation of unmodified BP to DNA cannot be ruled out [15]. As one of our recent works highlight UVA radiation induced ultrafast ET from BP to DNA [3], the DNA damages resulting from the coexposure to BP and UVA radiation can be partially attributed to reductive DNA damage though other carcinogenic pathways involving reactive oxygen species (ROS) causing oxidative DNA damages can also be involved. In our previous study [3] it has been proposed that ET pathway from BP to DNA can be targeted to prevent BP mediated DNA damage/carcinogenesis which is one of the main motives of this present work.

In order to target the UVA radiation induced ET pathway from BP to DNA, one of the most widely consumed xanthine alkaloid [16, 17], 1,3,7-trimethylxanthine commonly known as caffeine has been considered in the present study. Caffeine is known to inactivate essentially two proteins (ataxia-telangiectasia-mutated (ATM) and ATM-and Rad3-related (ATR)), primarily responsible for the genome stability [18]. A number of earlier studies show that the alkaloid has some significant effect on the DNA recognition of intercalating drugs through “interceptor” and “protector” properties of caffeine [19-21]. The specific molecular interaction of caffeine with different DNA intercalating agents like doxorubicin, ethidium (Et), acridine orange (AO), novantrone etc. underlying in the “interceptor” action of caffeine results in the inhibition of

cytostatic/cytotoxic effects of such intercalating drugs [19, 21, 22]. The “protector” activity of caffeine arises due to the competition between caffeine and other drug molecules for the same binding sites on DNA [20, 21]. Some of our previous works emphasize the role of caffeine as an interceptor molecule which helps to dissociate Et from biomimetic systems [23], synthetic DNA and various cell nuclei [24]. In another recent study, we have reported that caffeine can host some hydrophobic molecules like 4-(dicyanomethylene) 2-methyl-6-(p-dimethylaminostyryl) 4H-pyran (DCM), coumarin500 (C500) and 2-(p-toluidino) naphthalene-6-sulfonate (TNS) by encapsulating them into its dimeric structure [25]. Such encapsulating property of caffeine due to its dimeric structure plays a key role in the solubilization of extremely hydrophobic BP molecules in the aqueous solvent [26, 27]. However, whether such solubilizing activity of caffeine can release BP from the DNA bound state, eventually preventing the ET from BP to DNA under UVA radiation along with the effect of caffeine on such BP and UVA radiation induced reductive DNA damage are some of the areas that have never been explored and are the motives of this present work.

In this study, we have used steady-state emission and UV absorption spectroscopy to monitor the interaction of caffeine with BP molecules and molecular modeling studies to explore the energy-optimized geometry of the caffeine-BP complex. Steady-state and picosecond-resolved fluorescence spectroscopy have been used to monitor the effect of caffeine on ET reaction from BP to DNA under UVA radiation, using a laser source of 375 nm. Agarose gel electrophoresis (AGE) has been performed to monitor the DNA damage in terms of DNA double strand breaks (DSBs) by BP under UVA radiation in absence and presence of caffeine. Calf thymus (CT) DNA has been used for spectroscopic studies whereas polymerase chain reaction (PCR) amplified DNA fragments of ~1300 bp have been used to monitor DNA damage

through AGE. Time-gated fluorescence microscopy has been used to investigate the caffeine mediated release of BP from various cell lines including squamous epithelial cells collected from the inner lining of the human mouth, WI-38 (fibroblast), MCF-7 (breast cancer) and HeLa (cervical cancer) cells in *ex vivo* conditions.

7.2. Results and Discussion:

7.2.1. Ultrafast Spectroscopic Study on Caffeine Mediated Dissociation of Mutagenic Ethidium from Synthetic DNA and Various Cell Nuclei [24]:

7.2.1.1. Caffeine-BP Complexation in Aqueous Medium: Structural

Characterization: Figure 7.1.a shows the molecular structures of caffeine and benzo[a]pyrene (BP) whose associations are reflected in the subsequent Figures 7.1.b and 7.1.c. Figure 7.1.b shows the relative fluorescence intensity of BP dissolved maximally in aqueous caffeine solutions with varied caffeine concentration (ranging from 0 to 100 mM). Presence of three well characterized emission peaks of BP at 410, 430 and 455 nm as shown in Figure 7.1.b with no signature of broad emission feature that peaks around 490 nm characteristic for BP aggregates [3, 15] suggest that BP in caffeine solutions are present primarily as monomers. As evident from the Figure 7.1.b, the fluorescence intensity of BP increases with enhancement of caffeine content in the aqueous solutions which is in close agreement with the previously reported studies [26] emphasizing the role of caffeine in solubilizing BP. The caffeine mediated solubilization of BP in aqueous medium has been further studied by UV-visible absorption spectra of the solutions upon diluting them 11 times with caffeine solutions of equivalent concentrations as shown in Figure 7.1.b upper inset. The purpose of diluting the BP content in the caffeine solution is to keep the optical density (O.D.) values of BP much below 1 to avoid significant light scattering for the proper

calculation of BP concentration from its molar extinction coefficient as per the Lambert Beer law [28]. The multiple peaks in the absorption spectra of BP in caffeine solutions at 330, 349, 368 and 388 nm, as shown in Figure 7.1.b upper inset are assigned to the individual electronic transitions of BP as reported earlier [29]. The enhancement in the O.D. values of BP with the increase in caffeine concentration clearly indicates that the number of BP molecules in aqueous medium is directly proportional to the number of caffeine molecules in it. Figure 7.1.b lower inset shows the solubility of BP in aqueous caffeine solution as a function of caffeine concentration, monitored from the absorption spectra of BP using molar extinction coefficient that has been calculated from its

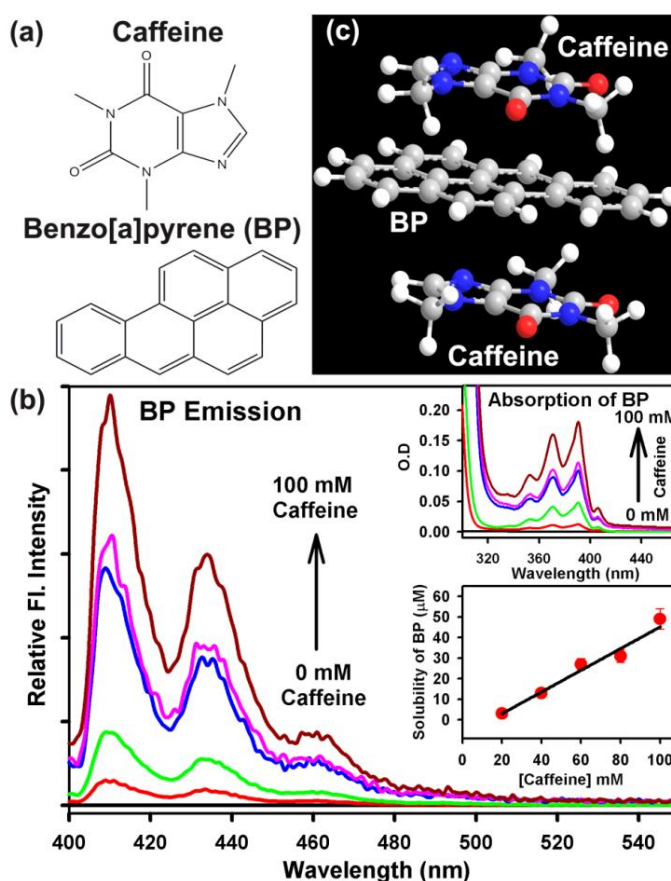


Figure 7.1. (a) Molecular structure of caffeine and benzo[a]pyrene (BP). (b) The fluorescence spectra of BP solubilized in aqueous caffeine solution with caffeine concentration varying from 0 to 100 mM, the upper inset shows the UV-visible absorption spectra of the same while the lower inset shows the solubility of BP at different caffeine concentrations as obtained from absorption measurements. (c) The energy minimized structure of caffeine-BP complex obtained from the molecular modeling studies.

known concentrations in similar medium. While calculating the concentration of BP in the caffeine solutions the dilution factor has been considered. The plot of BP solubility vs caffeine concentration, calculated from the O.D. values of BP as shown in Figure 7.1.b lower inset, holds well to the one reported previously from the fluorescence intensities of the same [26].

Caffeine mediated solubilization of extremely hydrophobic BP molecules in aqueous medium can be explained in terms of complexation between the two as previously observed for 4-(dicyanomethylene)-2-methyl-6-(p-dimethylaminostyryl) 4H-pyran (DCM) molecules [25], where it has been reported that caffeine can host some hydrophobic molecules in aqueous medium due to its dimeric nature.

Table 7.1. Parameters from molecular modeling of caffeine-BP complex.

Complex	Total energy* (E) (kcal/mole)	Complex Energy# (kcal/mole)	ΔE^\ddagger (kcal/mole)
Caffeine-Caffeine	52.62	42.34	-10.28
Caffeine-BP	0.92	-10.5	-11.42
Caffeine-BP- Caffeine	27.23	3.73	-23.5

*Mathematical sum of energy (E) for each molecule in the complex.

#Total energy calculated for various configurations of the molecular complexes.

‡Difference between mathematical sum of energies of individual molecules and calculated energies of each complex.

In this regard, we performed some molecular modeling calculations to find a mechanistic model of confinement of BP molecules within the caffeine dimer as shown in Figure 7.1.c. As shown in Table 7.1, our molecular modeling studies reveal a stable stacked dimer of caffeine molecules with stabilization energy of ~10 kcal/mole which is consistent with previous reports [25, 30]. The molecular modeling studies suggest that at lower caffeine concentration 1:1 caffeine-BP heterodimer is stable with stabilization energy comparable to that of caffeine dimer while at higher caffeine concentration a ternary complex of two caffeine molecules with one BP molecule is much more stable

with higher stabilization energy as shown in Table 7.1 and Figure 7.1.c. The structure of caffeine-BP complex as derived from our molecular modeling studies (Figure 7.1.c) is consistent with the stacking sandwich type model (caffeine-BP-caffeine) proposed previously from NMR experiments [27].

7.2.1.2. Effect of Caffeine on Electron Transfer (ET) Reaction from BP to DNA

under UVA Radiation: Upon monitoring the interaction between caffeine and BP in aqueous medium, the effect of caffeine on DNA bound BP has been monitored through steady-state and picosecond-resolved fluorescence spectroscopy. Figure 7.2.a shows that the emission intensity of DNA bound BP upon exciting with UVA radiation, enhances with the increase in caffeine concentration from 0 to 10 mM. As our previous study [3] suggests that electron transfer (ET) reaction takes place from BP to DNA under UVA radiation, the enhancement in emission intensity of the DNA bound BP in presence of caffeine indicates the possibility of caffeine mediated inhibition of such non-radiative ET pathway. For further confirmation of the role of caffeine in inhibiting the mentioned ET reaction, fluorescence lifetimes of BP in presence of DNA under UVA radiation, at different caffeine concentrations have been monitored at 410 nm as shown in Figure 7.2.b and the decay parameters are presented in Table 7.2. The purpose of monitoring the fluorescence transients at 410 nm lies under the fact that the contribution of BP aggregates is minimum or negligible at 410 nm and therefore the fluorescence originates essentially from the BP monomers [3]. The fluorescence lifetime of DNA bound BP molecules under UVA radiation in absence of caffeine as shown in Figure 7.2.b and Table 7.2, is consistent with the one reported in our previous study [3]. Figure 7.2.b and Table 7.2 show that the contribution of electron transfer components (70 and 900 ps) [3] in the fluorescence lifetime of BP gradually decrease with the increase in caffeine concentration along with the manifestation of a longer

lifetime component of 30 ns which is similar to the lifetime of BP upon complexation.

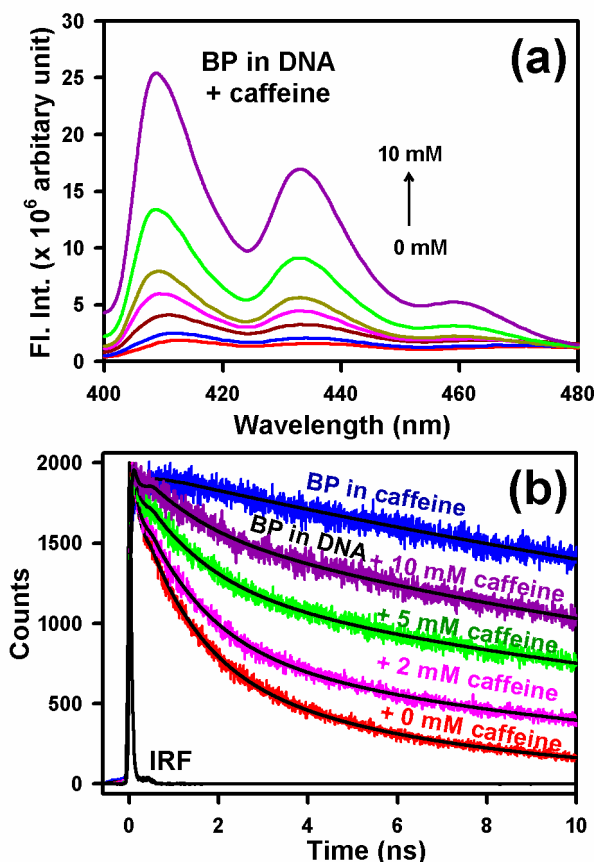


Figure 7.2. (a) The enhancement in the fluorescence intensity and (b) lifetime of BP in CT-DNA with the increase in caffeine concentration from 0 to 10 mM along with the fluorescence transient of BP in caffeine solution. Fluorescence transients have been monitored (λ_{em}) at 410 nm. Excitation wavelength (λ_{ex}) = 375 nm).

The values of the mentioned time components have been fixed in the fitting of the fluorescence transients to monitor the variation in the relative contribution of the components with increase in caffeine concentration. Gradual increase of 30 ns component of DNA-BP system in presence of increasing concentration of caffeine clearly reveals detachment of BP from DNA to the caffeine moiety in aqueous solution. The observation is consistent with the fact that the ET processes of BP in the DNA moiety is severely blocked when BP is detached from DNA upon complexation with caffeine. By measuring the relative contribution of the longer lifetime component (30 ns), which is a signature of the total population of BP bound to caffeine upon releasing

from DNA, and knowing the total concentration of DNA bound BP ($[BP]$) and caffeine ($[Caffeine]$) in the solution, we have calculated the relative association constant (K) between caffeine and BP in aqueous DNA solution using the following equation [31],

$$K = \frac{[Caffeine - BP]}{([BP] - [Caffeine - BP]) \times ([Caffeine] - [Caffeine - BP])} \quad (1)$$

where $[Caffeine-BP]$, $([BP]-[Caffeine-BP])$, $([Caffeine]-[Caffeine-BP])$ represent concentration of Caffeine-BP complex, BP bound to DNA and free Caffeine in the solution respectively. The relative association constant of BP with caffeine is calculated to be $\sim 100 \text{ M}^{-1}$ which is comparable with the association constant between caffeine and a well-known DNA intercalating dye ethidium (Et) [19, 24]. It has to be noted that molecular recognition of Et/BP depends on the length of the host DNA [31]. DNA recognition of Et/BP upon DNA fragmentation requires further investigation and is the motive of our future work.

Table 7.2. The lifetime components of BP in CT-DNA at different caffeine concentrations.

[caffeine] mM	τ_1 (ns)	τ_2 (ns)	τ_3 (ns)	τ_4 (ns)	$\langle \tau_{avg} \rangle$ (ns)
0	0.07 (32%)	0.90 (37%)	5.61 (31%)		2.10
0.5	0.07 (33%)	0.90 (31%)	4.34 (30%)	30.00 (6%)	3.29
1	0.07 (32%)	0.90 (30%)	4.37 (30%)	30.00 (8%)	4.02
2	0.07 (32%)	0.90 (24%)	3.72 (27%)	30.00 (17%)	6.30
3	0.07 (25%)	0.90 (32%)	5.61 (23%)	30.00 (20%)	7.69
5	0.07 (24%)	0.90 (22%)	5.61 (20%)	30.00 (34%)	11.49
10	0.07 (23%)	0.90 (12%)	5.61 (15%)	30.00 (50%)	15.98
BP in caffeine solution	-	-	-	30.00 (100%)	30.00

Lifetime components monitored at 410 nm (λ_{em}). τ represents the time constant in ns and the figures in the parenthesis represent relative contribution of the component. $\langle \tau_{avg} \rangle$ represents average lifetime in ns. Error $\pm 10\%$. The values of τ_1 , τ_2 and τ_4 have been kept fixed.

7.2.1.3. Role of Caffeine in the Prevention of BP and UVA Induced DNA Damage:

The caffeine mediated release of BP from DNA, consequently inhibiting the UVA radiation induced ET from BP to DNA as observed from our fluorescence spectroscopic studies, motivated us to find the efficacy of caffeine in the prevention of BP and UVA radiation induced DNA damage. In this regard, 1300 bp DNA fragments were coexposed to BP and UVA in absence (-) and presence (+) of caffeine and the formation of double-strand breaks (DSBs) in the DNA was monitored by agarose gel electrophoresis as shown in the upper panel of Figure 7.3. As evident from the Figure 7.3, coexposure of the DNA fragments to BP and UVA (lane G) results in the formation of a smear around 250 bp as shown by the dotted arrow and the result is in close agreement with earlier studies [12]. Given the composition of the loading it is unlikely that the buffer could denature the DNA under study. In addition, the intactness of the ds DNA marker under the same loading buffer also rules out the possibility of DNA denaturation. Thus, the fragments obtained in lane G can be considered as DSBs and not SSBs. However, in presence of caffeine (lane H), the linear DNA fragments produce their corresponding band (shown by bold arrow in Figure 7.3) at around 1300 bp in accordance with the DNA marker and no smaller fragments of DNA due to DSBs are observed which emphasizes the efficacy of caffeine in preventing the DSBs in DNA. One of the possible mechanisms imparting caffeine such preventive role against DNA damage can be the inhibition of ET from BP to DNA. Here it has to be noted that the absence of sharp DNA bands in lanes G and H upon coexposure to BP and UVA even in presence of caffeine, is due to the fact that intercalation of BP into the DNA prevents ethidium (Et) in the agarose gel to get into the DNA to produce the sharp bands of DNA bound Et under UV-transilluminator. Therefore the weak bands are due to the DNA bound BP which also fluoresces blue-green under the transilluminator.

Such inference has been drawn upon repetition of the above experiment with visualization under transilluminator both before and after staining with Et which produced blue-green emission of BP from the DNA bands in lanes G and H. For better understanding of the obtained results, we have employed steady state spectroscopy to monitor the binding affinity of Et towards DNA upon exposure to UVA radiation both in absence and presence of BP and found that the binding affinity of Et to DNA decreases upon coexposure of BP and UVA. Such BP and UVA induced reduction in the binding of Et to DNA may be rationalized in terms of significant perturbation of DNA structure including the formation of cyclobutane pyrimidine dimers (CPDs), 8-oxoguanine and single/double strand breaks which invite further investigation. In presence of caffeine, BP does not get completely released from DNA but the effective concentration of BP in the DNA decreases which is enough to prevent the DSBs. As a control set of experiments, DNA fragments have been exposed only to BP without UVA dose (lane C) which result in no DSBs holding well to the fact that DSBs form under the coexposure of BP and UVA [12]. Sharp DNA bands produced by DNA intercalated Et in the gel upon exposing the DNA fragments to BP without UVA dose (lane C) signify the weaker association of BP with DNA which gets released from the DNA during electrophoresis. Excess BP and caffeine-BP complex which are not bound to DNA remain in the loading wells of the agarose gel (lanes C, D, G and H) and do not migrate during electrophoresis as they carry no charge. As BP and Et have comparable spectral overlaps of their absorption coefficients with the transilluminator emission at 312 nm, both the dyes have similar absorption of photons from the said source. On the other hand, the fluorescence quantum yield of BP is around unity [32] while that of DNA bound Et [33] is ~0.15 which is the reason behind the extensive fluorescence of BP under the transilluminator. However, BP undergoes through nonradiative electron

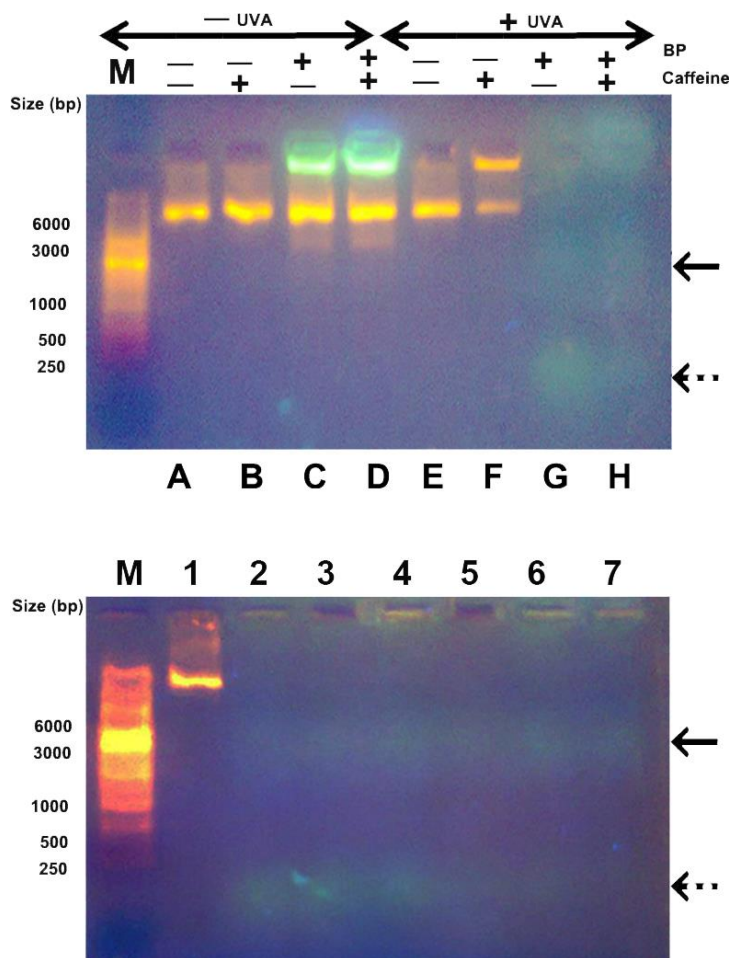


Figure 7.3. Upper Panel. DNA fragments of 1300-bp were exposed to (3×10^{-4} M) BP with UVA radiation (~ 400 J/cm²) (lanes G and H) in absence (lane G) and presence of caffeine (lane H), loaded onto a 0.8% Agarose gel and electrophoresed. DNA fragments without caffeine (lane E) and with caffeine (lane F) in presence of UVA radiation were also loaded and electrophoresed. Similar experiments without UVA radiation were commenced (lanes A, B, C and D) as control. The absence and presence are represented with the symbols (-) and (+) respectively for UVA radiation, BP and caffeine. M represents the lane loaded with DNA marker of varying sizes (in base pairs). The fragmented DNA resulting from double strand breaks (DSBs) (~ 200 -250 bps) is shown in dotted arrow while the bold arrow represents the 1300 bp DNA without any DSBs. The gel was stained with ethidium bromide and all the experiments had been repeated five times with similar results. **Lower Panel.** DNA fragments of 1300-bp exposed to (3×10^{-4} M) BP (lanes 2 to 7) with UVA radiation (~ 400 J/cm²) with varying caffeine concentration 0.0, 0.1, 0.5, 1.0, 5.0 and 10.0 mM respectively. Lane 1 contains similar DNA fragments exposed only to UVA radiation (~ 400 J/cm²) without BP and caffeine, as a control. M represents the lane loaded with DNA marker of varying sizes (in base pairs). The fragmented DNA resulting from double strand breaks (DSBs) (~ 200 -250 bps) is shown as dotted arrow. The gel was stained with ethidium bromide and all the experiments had been repeated three times with similar results.

transfer (ET) pathway upon associating with DNA. As a result, the emission intensity of excess BP and BP-caffeine complexes remaining in the wells is much higher compared to that of BP molecules associated with the DNA bands. Our control

experiments where DNA has been exposed only to caffeine in presence (lane F) and absence of UVA radiation (lane B) show that caffeine does not cause any significant change in the DNA which can be reflected through the gel electrophoresis. Furthermore, our control experiments suggest that only UVA radiation has some effect on the DNA fragments due to which a portion of DNA gets stuck into the loading well (lane E). Such retardation of DNA migration is known to arise from DNA-DNA cross-links [34]. Lower panel of Figure 7.3 shows DNA fragments of 1300-bp exposed to (3×10^{-4} M) BP (lanes 2 to 7) with UVA radiation (~ 400 J/cm²) with varying caffeine concentration 0.0, 0.1, 0.5, 1.0, 5.0 and 10.0 mM respectively. Lane 1 contains similar DNA fragments exposed only to UVA radiation (~ 400 J/cm²) without BP and caffeine, as a control. M represents the lane loaded with DNA marker of varying sizes (in base pairs). The fragmented DNA resulting from double strand breaks (DSBs) (~ 200 -250 bps) is shown as dotted arrow. The intensity of DSBs fragment as indicated by the dotted arrow gradually decreases with the increase in caffeine concentration.

To study the mechanism of such cross-link formation, the absorption spectra of DNA and the plastic material of 96-well plate in which the experiments were carried out, have been monitored as shown in the Figure 7.4.a and the emission intensity of the used UV source has also been checked within the same wavelength range as shown in Figure 7.4.b. As evident from Figure 7.4.b, along with the major emission peak at 365 nm, there are negligible or 100 times less intense contribution of the UV source at 313 and 334 nm. Some earlier works [9] suggest that low energy of UVA photons (322-390 nm) can be directly absorbed by DNA and are sufficient to produce cyclobutane pyrimidine dimers (CPDs) usually in the form of thymine-thymine cross-links, yet at a low level. The observed DNA-DNA cross-links can also occur indirectly through the

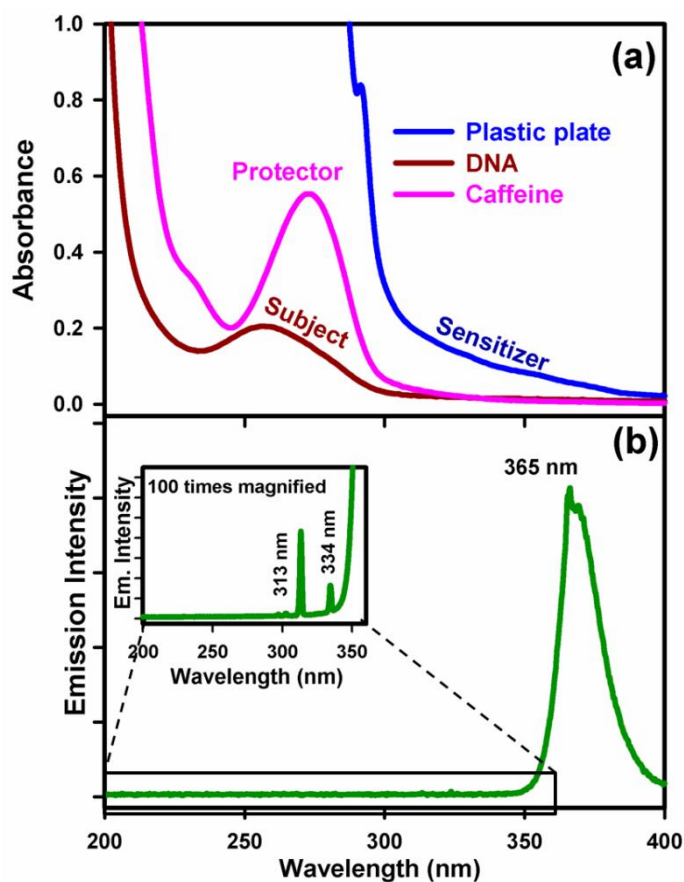


Figure 7.4. (a) UV absorption spectra of DNA (subject), caffeine (protector) and plastic material of the 96 well plate (sensitizer). (b) Emission intensity of the UV-source within the same wavelength range and inset shows the 100 times magnified image of a portion of the spectra marked by a rectangle.

formation of hydrogen peroxide (H_2O_2). One of the previous studies [35] find that UVA irradiation of DNA solution or phosphate buffer alone on plastic Petri dishes can result in the formation of H_2O_2 . The formation of H_2O_2 on plastic plates can be explained on the basis of the absorption spectrum of the plastic as shown in Figure 7.4.a (blue line) over the wavelength range of UVA radiation (320 – 399 nm). As plastic has significant absorbance in the UVA region, it can act as a sensitizer and expected to produce ROS like H_2O_2 that may result in oxidative damage of DNA [36] and DNA-DNA cross links [37]. Interestingly, such phenomenon of DNA-DNA cross-links is not observed in the agarose gel when the DNA fragments are exposed to UVA radiation in presence of caffeine (lane F of Figure 7.3). The relatively higher concentration of caffeine molecules in the experimental system compared to DNA

results in absorption of UVA radiation by caffeine to a greater extent (as shown in Figure 7.4.a, pink line) and acts as a protector preventing the formation of DNA-DNA cross-links by direct absorption of UVA photons by DNA. Another possible mechanism through which caffeine can prevent DNA-DNA cross-linking is through its free radical scavenging activity [38]. However, the significant amount of DNA which gets stuck to the loading well in the agarose gel as observed from lane E of upper panel of Figure 7.3 may not be solely due to the formation of intermolecular cross-links. In this regard, the possibility of the DNA being contaminated with the products extracted from the purification column can be ruled out, as we did not observe such attachment of DNA to the wells of other lanes in the agarose gel. The different types of DNA damages associated with such exposure of DNA to the UVA source can be preferably found out using a DNA plasmid assay employing DNA repair enzymes which is one of the motivations of our future works. Here it has to be noted that our experiment on the agarose gel is mostly the reproduction of the work reported by *Toyooka et al* on DNA DSBs due to coexposure of BP and UVA [12], except the study on the role of caffeine in the UVA and BP induced DNA fragmentation. We reproduced their results to highlight the caffeine-mediated prevention of such DNA fragmentation. Our sole aim is to establish the fact that the presence of caffeine inhibits DNA fragmentation which is apparent from lanes G and H in the Figure 7.3.

7.2.1.4. Caffeine Mediated Exclusion of BP from Various Cell Lines: Cellular Studies under *Ex Vivo* Condition: The *in vitro* experimental results emphasizing the role of caffeine in releasing BP from DNA upon forming caffeine-BP complex have been further verified in biological milieu using different animal cell lines. Figure 7.5.a shows the fluorescence micrographs of BP stained squamous epithelial cells (collected from the inner lining of human mouth) along with their corresponding bright field

images taken at 10 and 180 seconds following treatment with caffeine (+ caffeine) and with buffer without caffeine (- caffeine) as control. As evident from the fluorescence micrographs, BP stains both the nuclei and the cytoplasm unlike ethidium (Et) and DAPI which are known to stain specifically the nuclei of the cells [24]. The ability of BP to stain the whole cells can be attributed to its interactions with both DNAs and proteins as evident from one of our recent studies [3]. Our control experiments suggest that BP emission from the squamous epithelial cells undergoes significant photo-bleaching with time and the rate of photo-bleaching has been determined by plotting the relative fluorescence intensity of BP in the cell against time as shown in Figure 7.5.b and has been found out to be 74 seconds from its exponential fit. After addition of caffeine, there is significant BP emission outside the cells as evident from the fluorescence micrographs shown in Figure 7.5.a. Such BP emission from outside the cells just after the addition of caffeine is a clear signature of caffeine mediated exclusion of BP from the cells upon forming the caffeine-BP complex. Figure 7.5.c shows the time dependent emission intensity of BP outside the cells following the caffeine treatment. The first micrograph that can be taken next to the caffeine treatment is after 10 seconds which includes the time required for adjusting the focus. As evident from the Figure 7.5.c most of the BP gets released from the cells within the first 10 seconds at a very fast rate beyond the experimental resolution. After 10 seconds BP gets slowly released which is reflected in the slow enhancement of the emission intensity of BP outside the cells within 10 to 180 seconds. Figure 7.5.c inset shows the relative fluorescence intensity inside the cells with respect to that outside the cells against time (within 10 to 180 seconds) and the exponential decrease of such relative fluorescence intensity with time further signifies the temporal increase in emission intensity of BP outside the cells due to the release of BP molecules. Such exponential

decrease of the relative fluorescence intensity of BP can be fitted with a time constant of 127 seconds which signifies the time constant for slow release of BP from the cells after 10 seconds of caffeine treatment. As time dependent relative fluorescence intensity of BP has been monitored inside the cells with respect to that outside the same, the change in emission intensity due to some extent of photo-bleaching in presence of caffeine gets nullified. Here, it has to be noted that photo-bleaching of BP in presence of caffeine gets significantly reduced as caffeine-BP complexation prevents ET reaction between BP and biomolecules inside the cells. However, in the analysis shown in Figure 7.5.c inset, a significant component has been missed as most of the BP gets released from the cells within the first 10 seconds after the addition of caffeine which falls beyond our experimental time resolution. A caffeine dose dependent extraction of BP from the cell lines in 5 minutes incubation time is evident from Figure 7.5.d. An efficient extraction of BP at caffeine concentration of 140 mM is clearly evident from the inset of the Figure 7.5.d.

Upon monitoring the role of caffeine in releasing BP from squamous epithelial cells, such activity of caffeine has also been studied in fibroblast cells (WI-38). Figure 7.6.a shows the bright field and fluorescence micrographs of BP stained WI-38 cells taken at 10 and 70 seconds after the treatment with caffeine (+ caffeine) and with buffer without caffeine (– caffeine) as control. Similar to the observation in case of squamous epithelial cells, significant photo-bleaching of BP occurs in the control set of experiments within 10 to 70 seconds. The plot of relative fluorescence intensity of BP inside the WI-38 cells vs. time in absence of caffeine as shown in Figure 7.6.b, reveals a time constant of 32 seconds of such photo-bleaching from its exponential fit. Addition of caffeine leads to the release of BP resulting in BP emission from exterior of

the cells as evident from the fluorescence micrographs (Figure 7.6.a) and from the plot

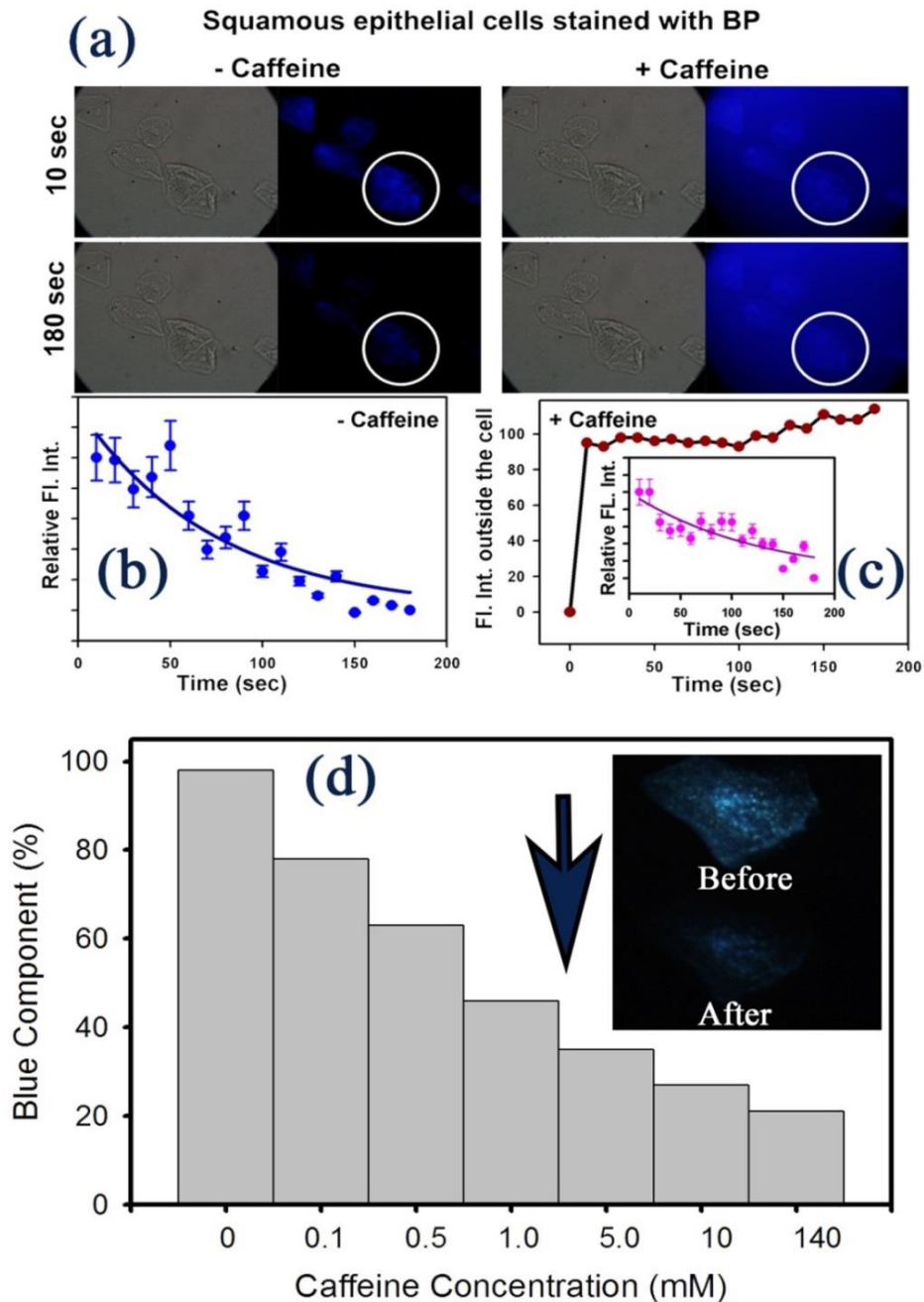


Figure 7.5. (a) Fluorescence micrographs of BP stained squamous epithelial cells taken at 10 and 180 seconds after the addition of caffeine (+ caffeine). Images in grayscale show the respective bright field micrographs. As a control set of experiments, micrographs were taken at similar timescales upon the addition of buffer without caffeine (– caffeine), white circles capture a particular cell in the fluorescence micrographs for better clarity of the viewer. The change in relative fluorescence intensity of BP inside the cells with time in absence (b) and presence (c inset) of caffeine where bold lines are the exponential fits of the experimental data points within 15% error. (c) The fluorescence intensity of BP outside the cells at different time intervals upon the addition of caffeine (+ caffeine) where bold line is the guide to the eye. (d) Caffeine dose dependent washing of BP from squamous epithelial cells in 5 minutes of incubation time. Inset of the figure shows the micrograph of a cell before and after washing with 140 mM caffeine solution. All the experiments are repeated three times.

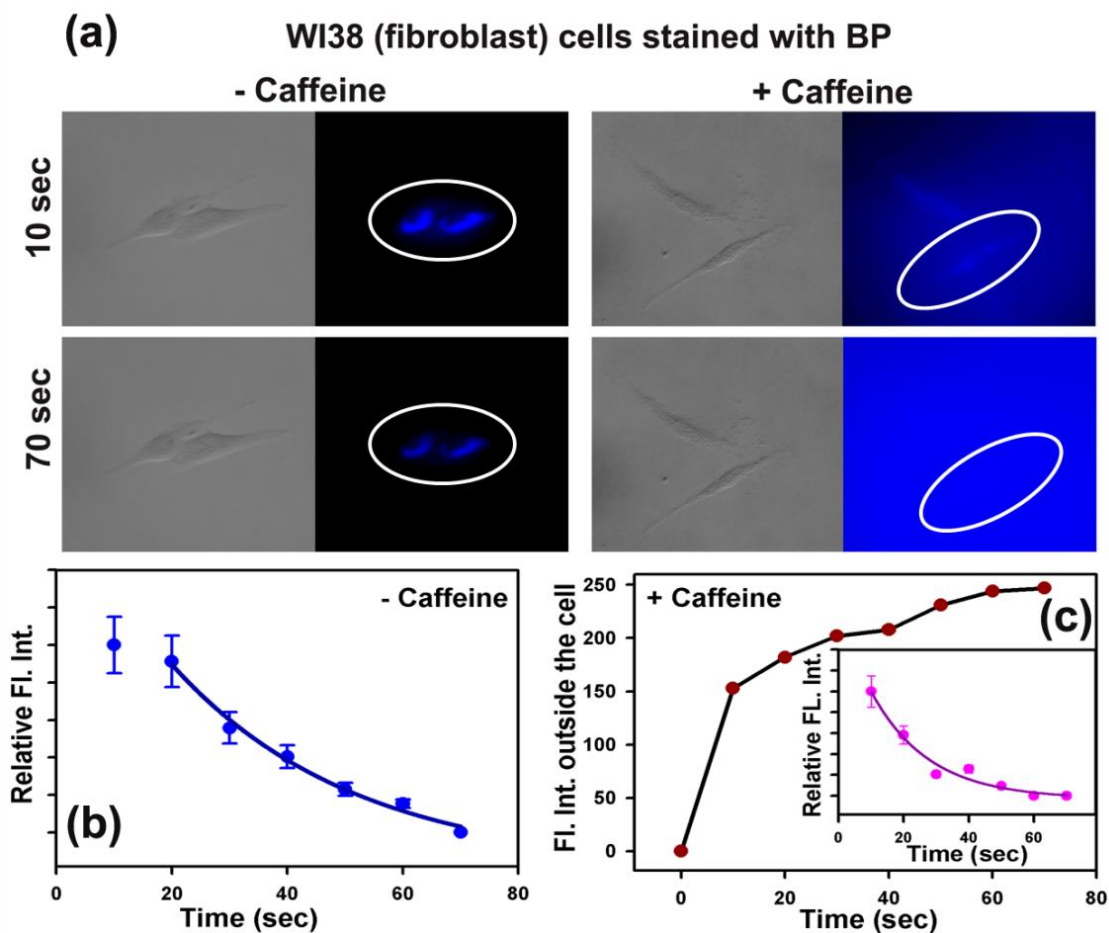


Figure 7.6. (a) Fluorescence micrographs of BP stained WI-38 (fibroblast) cells taken at 10 and 70 seconds after the addition of caffeine (+ caffeine). Images in grayscale show the respective bright field micrographs. As a control set of experiments, micrographs were taken at similar timescales upon the addition of buffer without caffeine (– caffeine), white circles capture cell(s) in the fluorescence micrographs for better clarity of the viewer. The change in relative fluorescence intensity of BP inside the cells with time in absence (b) and presence (c inset) of caffeine where bold lines are the exponential fits of the experimental data points within 15% error. (c) The fluorescence intensity of BP outside the cells at different time intervals upon the addition of caffeine (+ caffeine) where bold line is the guide to the eye. All the experiments are repeated three times.

of temporal emission intensity of BP outside the cells after the addition of caffeine as shown in Figure 7.6.c. It is evident from the Figure that a significant amount of BP gets released from the WI-38 cells within the first 10 seconds after the addition of caffeine. Figure 7.6.c inset shows the plot of relative emission intensity of BP inside the cell with respect to that outside the same vs. time following the caffeine treatment. The exponential fit of such plot reveals time constant of 18 seconds which signifies the

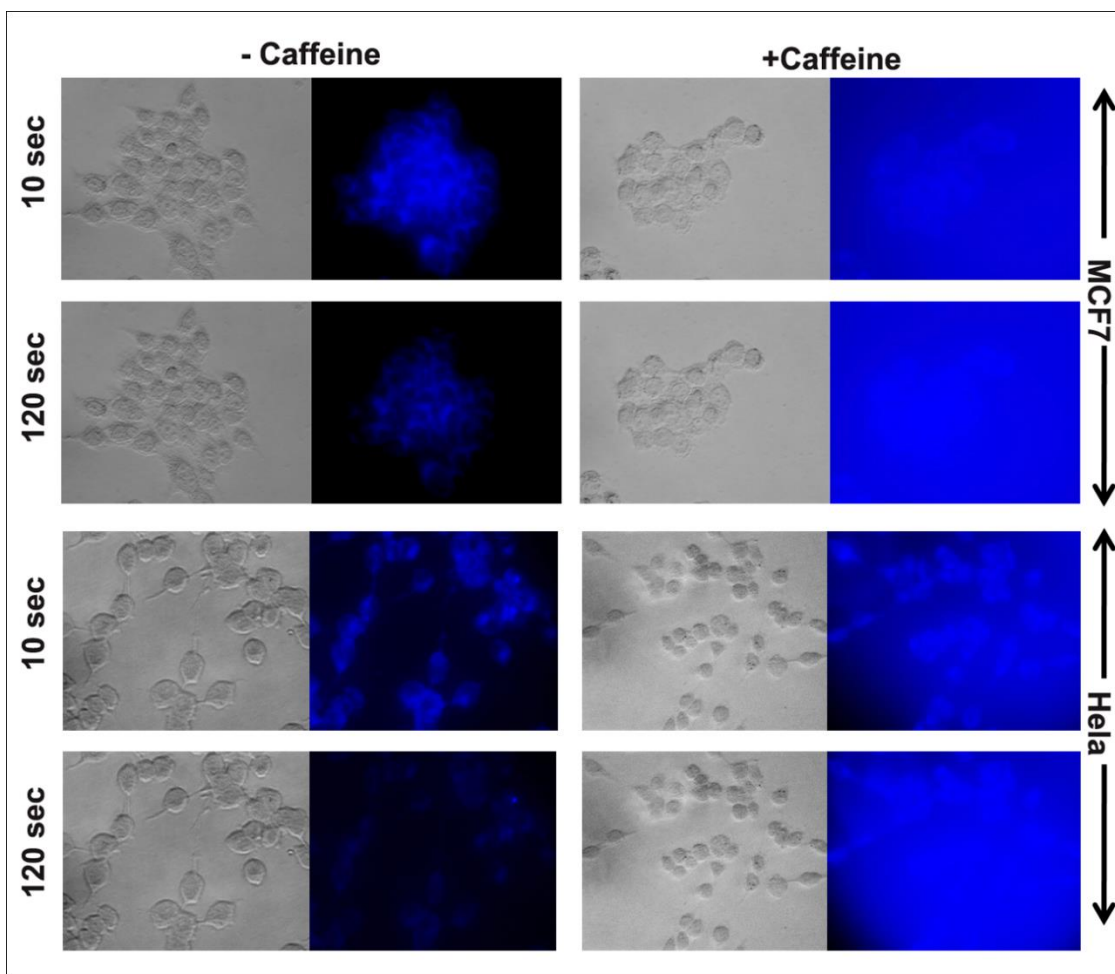


Figure 7.7. Fluorescence micrographs of BP stained MCF-7 (breast cancer) and HeLa (cervical cancer) cells taken at 10 and 120 seconds upon the addition of caffeine (+ caffeine) and buffer without caffeine (– caffeine). Images in grayscale show the respective bright field micrographs. All the experiments are repeated 3 times with similar results.

characteristic time of caffeine mediated BP release from the cells after 10 seconds of caffeine treatment. The caffeine mediated release of BP has not only been checked in normal cells but also in some cancerous cell lines like breast cancer (MCF-7) and cervical cancer (HeLa) cells, as shown in Figure 7.7. Both the bright field and fluorescence micrographs of BP stained MCF-7 and HeLa cells taken at 10 and 120 seconds upon the treatment with caffeine (+ caffeine) and with buffer without caffeine (– caffeine), are shown in Figure 7.7. The fluorescence micrographs of control studies (– caffeine) show significant photo-bleaching of BP similar to the observation with normal cells of squamous epithelium and WI-38. Upon treatment with caffeine, BP gets

released from both the cancerous cell lines of MCF-7 and HeLa which results in the enhancement of BP emission from the exterior of the corresponding cells as evident from Figure 7.7.

7.3. Conclusion:

Our present study emphasizes the role of caffeine on the biomolecular recognition of benzo[a]pyrene (BP) interrupting the electron transfer (ET) pathway from BP to DNA under UVA radiation. The steady-state emission and absorption spectroscopy results suggest that caffeine can host extremely hydrophobic BP molecules in aqueous medium by forming stacked sandwich type structures of caffeine-BP-caffeine complexes as revealed by the molecular modeling studies. The formation of caffeine-BP complexes further leads to the dissociation of BP from DNA and thus the ET from BP to DNA under UVA radiation gets inhibited in presence of caffeine as observed from our steady-state and picosecond resolved emission spectroscopy results. Such caffeine mediated prevention of ET from BP to DNA consequently protects the DNA from reductive DNA damage as monitored through our agarose gel electrophoresis. The cellular studies reveal the efficacy of caffeine in dissociating BP from both normal and cancerous cell lines. Our current study may find significance in the potential therapeutic use of caffeine for preventing DNA damage/DNA double strand breaks (DSBs) and eventually preventing cell death that arises due to such DNA damages.

References:

- [1] Q.B. Lu, Effects and Applications of Ultrashort-lived Prehydrated Electrons in Radiation Biology and Radiotherapy of Cancer, *Mutat. Res.*, 704 (2010) 190-199.
- [2] R.A. Marcus, Electron Transfer Reactions in Chemistry: Theory and Experiment (Nobel Lecture), *Angew. Chem. Int. Ed. Engl.*, 32 (1993) 1111-1121.
- [3] S. Banerjee, S. Sarkar, K. Lakshman, J. Dutta, S.K. Pal, UVA Radiation Induced Ultrafast Electron Transfer from a Food Carcinogen Benzo[a]pyrene to Organic Molecules, Biological Macromolecules and Inorganic Nano Structures, *J. Phys. Chem. B.*, 117 (2013) 3726–3737.
- [4] M. Fujitsuka, T. Majima, Hole and Excess Electron Transfer Dynamics in DNA, *Phys. Chem. Chem. Phys.*, 14 (2012) 11234-11244.
- [5] J. Nguyen, Y. Ma, T. Luo, R.G. Bristow, D.A. Jaffray, Q.B. Lu, Direct Observation of Ultrafast-Electron-Transfer Reactions Unravels High Effectiveness of Reductive DNA Damage, *Proc. Natl. Acad. Sci. U.S.A.*, 108 (2011) 11778-11783.
- [6] C.R. Wang, J. Nguyen, Q.B. Lu, Bond Breaks of Nucleotides by Dissociative Electron Transfer of Nonequilibrium Prehydrated Electrons: A New Molecular Mechanism for Reductive DNA Damage, *J. Am. Chem. Soc.*, 131 (2009) 11320-11322.
- [7] P.E. Nielsen, Chemical and Photochemical Probing of DNA Complexes, *J. Mol. Recognit.*, 3 (1990) 1-25.
- [8] F.R. de Gruijl, Photocarcinogenesis: UVA vs UVB, *Methods Enzymol.*, 319 (2000) 359-366.
- [9] P.M. Girard, S. Francesconi, M. Pozzebon, D. Graindorge, P. Rochette, R. Drouin, E. Sage, UVA-Induced Damage to DNA and Proteins: Direct versus Indirect Photochemical Processes, *Journal of Physics: Conference Series*, 261 (2011) 1-10.
- [10] E. Sage, P.M. Girard, S. Francesconi, Unravelling UVA-Induced Mutagenesis, *Photochem. Photobiol. Sci.*, 11 (2012) 74-80.
- [11] T. Toyooka, Y. Ibuki, M. Koike, N. Ohashi, S. Takahashi, R. Goto, Coexposure to Benzo[a]pyrene Plus UVA Induced DNA Double Strand Breaks: Visualization of Ku Assembly in the Nucleus Having DNA Lesions., *Biochem. Biophys. Res. Commun.*, 322 (2004) 631-636.
- [12] T. Toyooka, Y. Ibuki, F. Takabayashi, R. Goto, Coexposure to Benzo[a]pyrene and UVA Induces DNA Damage: First proof of Double-Strand Breaks in a Cell-Free System, *Environ. Mol. Mutagen.*, 47 (2006) 38-47.

- [13] R.S. Brown, O.H.J. Szolar, J.H.T. Luong, Cyclodextrin-aided Capillary Electrophoretic Separation and Laser-induced Fluorescence Detection of Polynuclear Aromatic Hydrocarbons (PAHs), *J. Mol. Recognit.*, 9 (1996) 515-523.
- [14] D.H. Phillips, Fifty Years of Benzo(a)pyrene, *Nature*, 303 (1983) 468-472.
- [15] S.C. Beck, D.T. Cramb, Condensed Phase Dispersive Interactions of Benzo[a]pyrene with Various Solvents and with DNA: A Twist on Solvatochromism, *J. Phys. Chem. B*, 104 (2000) 2767-2774.
- [16] B.B. Fredholm, K. Battig, J. Holmen, A. Nehlig, E.E. Zwartau, Actions of Caffeine in the Brain with Special Reference to Factors That Contribute to Its Widespread Use, *Pharmacol. Rev.*, 51 (1999) 83-133.
- [17] R.A. Marta, R. Wu, K.R. Eldridge, J.K. Martens, T.B. McMahon, Infrared Vibrational Spectra as a Structural Probe of Gaseous Ions Formed by Caffeine and Theophylline, *Phys. Chem. Chem. Phys.*, 12 (2010) 3431-3442.
- [18] D. Cortez, Caffeine Inhibits Checkpoint Responses without Inhibiting the Ataxia-Telangiectasia-Mutated (ATM) and ATM- and Rad3-Related (ATR) Protein Kinases, *J. Biol. Chem.*, 278 (2003) 37139-37145.
- [19] R.W. Larsen, R. Jasuja, R.K. Hetzler, P.T. Muraoka, V.G. Andrada, D.M. Jameson, Spectroscopic and Molecular Modeling Studies of Caffeine Complexes with DNA Intercalators, *Biophys. J.*, 70 (1996) 443-452.
- [20] D.B. Davies, D.A. Veselkov, L.N. Djimant, A.N. Veselkov, Heteroassociation of Caffeine and Aromatic Drugs and their Competitive Binding with a DNA Oligomer., *Eur. Biophys. J.*, 30 (2001) 354-366.
- [21] F. Traganos, B. Kaminska-Eddy, Z. Darzynkiewicz, Caffeine Reverses the Cytotoxic and Cell Kinetic Effects of Novantrone (mitoxantrone), *Cell Prolif.*, 24 (1991) 305-319.
- [22] M.B. Lyles, I.L. Cameron, H.R. Rawls, Structural Basis for the Binding Affinity of Xanthines with the DNA Intercalator Acridine Orange, *J. Med. Chem.*, 44 (2001) 4650-4660.
- [23] S. Banerjee, M. Tachiya, S.K. Pal, Caffeine-Mediated Detachment of Mutagenic Ethidium from Various Nanoscopic Micelles: An Ultrafast Förster Resonance Energy Transfer Study, *J. Phys. Chem. B*, 116 (2012) 7841-7848.
- [24] S. Banerjee, D. Bhowmik, P.K. Verma, R.K. Mitra, A. Sidhhanta, G. Basu, S.K. Pal, Ultrafast Spectroscopic Study on Caffeine Mediated Dissociation of Mutagenic

Ethidium from Synthetic DNA and Various Cell Nuclei, *J. Phys. Chem. B*, 115 (2011) 14776-14783.

[25] S. Banerjee, P.K. Verma, R.K. Mitra, G. Basu, S.K. Pal, Probing the interior of Self-assembled Caffeine Dimer at various Temperatures, *J. Fluoresc.*, 22 (2012) 753-769.

[26] E. Boyland, B. Green, The Interaction of Polycyclic Hydrocarbons and Purines, *Brit. J. Cancer*, 16 (1962) 347-360.

[27] Y. Nosaka, K. Akasaka, H. Hatano, Interaction of Benzo[*a*]pyrene and 6-Oxybenzo[*a*]pyrene with Caffeine. Structures of the Complexes as Studied by Nuclear Magnetic Resonance Chemical Shift and Relaxation, *J. Phys. Chem.*, 82 (1978) 2829-2833.

[28] A. Villringer, B. Chance, Non-Invasive Optical Spectroscopy and Imaging of Human Brain Function, *Trends Neurosci.*, 20 (1997) 435-442.

[29] J.S. Larsen, J. Waluk, S. Eriksson, E.W. Thulstrup, Electronic States of Benzo[*a*]pyrene. Linear and Magnetic Circular Dichroism, Polarized Fluorescence, and Quantum Chemical Calculations, *J. Am. Chem. Soc.*, 114 (1992) 1942-1949.

[30] L. Carlucci, A. Gavezzotti, Molecular Recognition and Crystal Energy Landscapes: An X-ray and Computational Study of Caffeine and Other Methylxanthines, *Chem. Eur. J.*, 11 (2005) 271 - 279.

[31] R. Sarkar, S.K. Pal, Ligand-DNA Interaction in a Nanocage of Reverse Micelle, *Biopolymers*, 83 (2006) 675-686.

[32] S. Banerjee, N. Goswami, S.K. Pal, A Potential Carcinogenic Pyrene Derivative under Forster Resonance Energy Transfer to Various Energy Acceptors in Nanoscopic Environments, *Chem. Phys. Chem.*, 14 (2013) 3581-3593.

[33] J.B. Le Pecq, Use of Ethidium Bromide for Separation and Determination of Nucleic Acids of Various Conformational Forms and Measurement of Their Associated Enzymes, *Methods. Biochem. Anal.*, 20 (2006) 41-86.

[34] Y. Lu, K. Morimoto, Is Habitual Alcohol Drinking Associated with Reduced Electrophoretic DNA Migration in Peripheral Blood Leukocytes from ALDH2-Deficient Male Japanese?, *Mutagenesis*, 24 (2009) 303-308.

[35] Z. Kuluncsics, D. Perdiz, E. Brulay, B. Muel', E. Sage, Wavelength Dependence of Ultraviolet-Induced DNA Damage Distribution: Involvement of Direct or Indirect Mechanisms and Possible Artefacts, *J. Photochem. Photobiol. B*, 49 (1999) 71-80.

- [36] J. Cadet, T. Douki, J.L. Ravanat, P.D. Mascio, Sensitized Formation of Oxidatively Generated Damage to Cellular DNA by UVA Radiation, *Photochem. Photobiol. Sci.*, 8 (2009) 903-911.
- [37] L.C. Colis, P. Raychaudhury, A.K. Basu, Mutational Specificity of γ -Radiation-Induced Guanine Thymine and Thymine Guanine Intrastrand Cross-Links in Mammalian Cells and Translesion Synthesis Past the Guanine Thymine Lesion by Human DNA Polymerase η , *Biochemistry*, 47 (2008) 8070-8079.
- [38] J. Rafael, L. Carmona, A. Galano, Is Caffeine a Good Scavenger of Oxygenated Free Radicals?, *J. Phys. Chem. B*, 115 (2011) 4538-4546.

Chapter 8

Nanoparticle-sensitization of Photodynamic Drugs for Cancer Therapy

8.1. Introduction:

In the last two decades, there has been a phenomenal progress in the field of targeted drug delivery by nanomaterials in order to increase solubility, prolong half-life and diminish the immunogenicity of the drug [1-4]. Semiconductor nanoparticles (NPs) with their distinct physicochemical properties have several biomedical applications in bioimaging and drug delivery. ZnO NPs unlike most semiconductor NPs are less toxic, low-cost with reasonable biocompatibility and hence are amenable to serve as a productive drug delivery vehicle [5, 6]. ZnO NPs are attributed with exclusive properties viz-their size is similar to that of biomolecules and their functionality is copious on large surface areas. The nanohybrids consist of drug-loaded ZnO NPs or ZnO hollow spheres incorporating drugs promote the intracellular delivery of the nanoparticles enabling the invasion of cancer cells through precise ligand–receptor recognition or by nonspecific binding forces such as hydrophobic or coulombic interactions [5]. As ZnO NPs possess a wide band gap of 3.3 eV, they can only be excited under UV-light of wavelength less than 380 nm. It is not judicious to use UV light for *in vivo* assays as it has high penetration depth and is detrimental to health. Fortuitously, ZnO NPs serve as competent drug delivery vehicles in photodynamic therapies (PDT) which are effective in obliterating dangerous drug-resistant pathogens

when standard antibiotic therapies fail and destroying somatic cells in cancer therapy [7]. PDT is a non-thermal and minimally invasive technique which involves the activation of a photosensitizing agent by light ranging from ultraviolet-A (UV-A) to near-infrared wavelengths [8]. A photosensitizer (PS) absorbs photons and elevated to singlet excited state prior to light exposure of a particular frequency [9]. The excited state of the photosensitizer either decays back to ground state or converts to the triplet state subjected to intersystem crossing. The excited triplet state then reacts with ambient oxygen and generates reactive oxygen species (ROS) which are cytotoxic and kill cells by reacting with intracellular components thereby destructing both cell walls as well as DNA [7, 10]. Generally, photosensitizers possess a high absorption coefficient in the spectral region of the excitation wavelength, pertinent energy in the triplet state so that effective energy transfer to ground state oxygen occurs and immense quantum yields of the triplet state. Moreover, they also exhibit long triplet state lifetimes as the efficiency of the photosensitizer is dependent on the photophysical properties of its lowest excited triplet state and its favourable photostability [11].

Rose Bengal (4,5,6,7-tetrachloro-2',4',5',7'- tetrakisiodofluoresceindisodium) or RB is a water-soluble, anionic, xanthene photosensitizer which generates singlet oxygen ($^1\text{O}_2$) from oxygen molecules (O_2) if irradiated with green light [12-15]. The presence of halogen atoms in RB molecule increases the ability of intersystem crossing to the triplet state that leads to the generation of singlet oxygen [16]. Therefore, RB is considered as a propitious sensitizer in PDT of tumours with minimum side effects [17-19]. Besides, it is commonly used in ophthalmology and has microbiocidal activity against bacteria, viruses, fungi and protozoa [20-22]. The small penetration depth of green light makes RB particularly useful in treatments of many cutaneous lesions and dermatological diseases [23]. There exist considerable literature that describe the use of

RB as a photodynamic sensitizer for cancer chemotherapy [24]. Constructive photosensitization predominantly depends on the physical and chemical characteristics of the PS, such as chemical purity, charge, solubility, distinct localization in tumour cells, sufficiently long residence time, minimum time interval between the drug administration and its accumulation in neoplastic cells. Moreover, the PS should be easily cleared from normal tissues, excitation at wavelength with favourable tissue penetration and absence of toxicity in the dark [25]. The intracellular localization and uptake of a photosensitizer in cells is vital to the photodynamic process as the photoinduced cellular damage occurs proximally with the oxidizing species formed by the excited molecules. The anionic nature and poor lipid solubility of RB obstruct its capability to cross biological membrane barriers which restricts its clinical application [26]. There are earlier reports where the RB's photodynamic efficiency is improved using delivery carriers such as liposomes, [26, 27] developing hydrophobic derivatives (e.g. phosphate or acetate) or tagging with organically modified Si NP [28-30]. In addition, there are studies which report the conjugation of RB with biocompatible polymer and even gold nanorods for potent photodynamic activity [31-34]. One of our previous articles reports the sensitization of an effective cancer drug, protoporphyrin IX (PP) with ZnO NPs. We subsequently explored the photoinduced ultrafast dynamics of the NP sensitized drug and proved that the nanohybrid displays improved activity in PDT in comparison to that of the free drug. Zinc oxide NPs serve as drug delivery vehicle and assist the charge separation which in due course enhances the drug activity [35]. Furthermore, in a complementary study, we sensitized vitamin B₂, a notable antioxidant, with various NPs and modulated the radical scavenging property [36].

Despite the importance of the topic and to the best of our knowledge, there is no literature till date which reports the sensitization of RB with ZnO NPs leading to an

increase of the photodynamic activity of the drug. Herein, in the present work, we synthesized nanohybrids of RB with Zinc oxide (ZnO NPs) of approximately 24 nm sizes. The sizes of the NPs and crystallinity were confirmed using high resolution transmission electron microscopy (HRTEM). Picosecond-resolved fluorescence experiments on the nanohybrids were performed to fathom out the efficient electron transfer from photoexcited RB to ZnO NPs which eventually upgrades the ROS activity in the RB-ZnO nanohybrids. Picosecond-resolved Förster resonance energy transfer (FRET) from ZnO NPs to RB has been used to understand the nanohybrid formation at the molecular level. The ROS formation has been monitored by the dichlorofluorescein (DCFH) oxidation. Enhanced ROS generation is observed in the presence of RB-ZnO nanohybrid compared to that of free RB upon green light illumination. The nanohybrid is used as a model photodynamic therapeutic agent in bacterial, fungal and HeLa cell lines.

8.2. Results and Discussion:

8.2.1. Photoinduced Dynamics and Toxicity of a Cancer Drug in Proximity of Inorganic Nanoparticles under Visible Light [37]:

Figure 8.1.a depicts a characteristic high-resolution transmission electron microscopic (HR-TEM) image of ZnO NPs. An interplanar distance of ~ 0.25 nm which corresponds to the spacing between two (002) planes, is analysed from the lattice fringe of ZnO NP. The average particle size is deduced from our experimental TEM data and found to be $\sim 23.9 \pm 0.5$ nm. The complexation of RB and ZnO NPs can be understood using UV-Vis spectroscopy as shown in Figure 8.1.b. The major absorption peak of RB appears at 560 nm with a shoulder at 540 nm in acetonitrile. The characteristic peaks of both RB

and ZnO are observed in the nanohybrids. There is a 5 nm peak shift in the absorbance

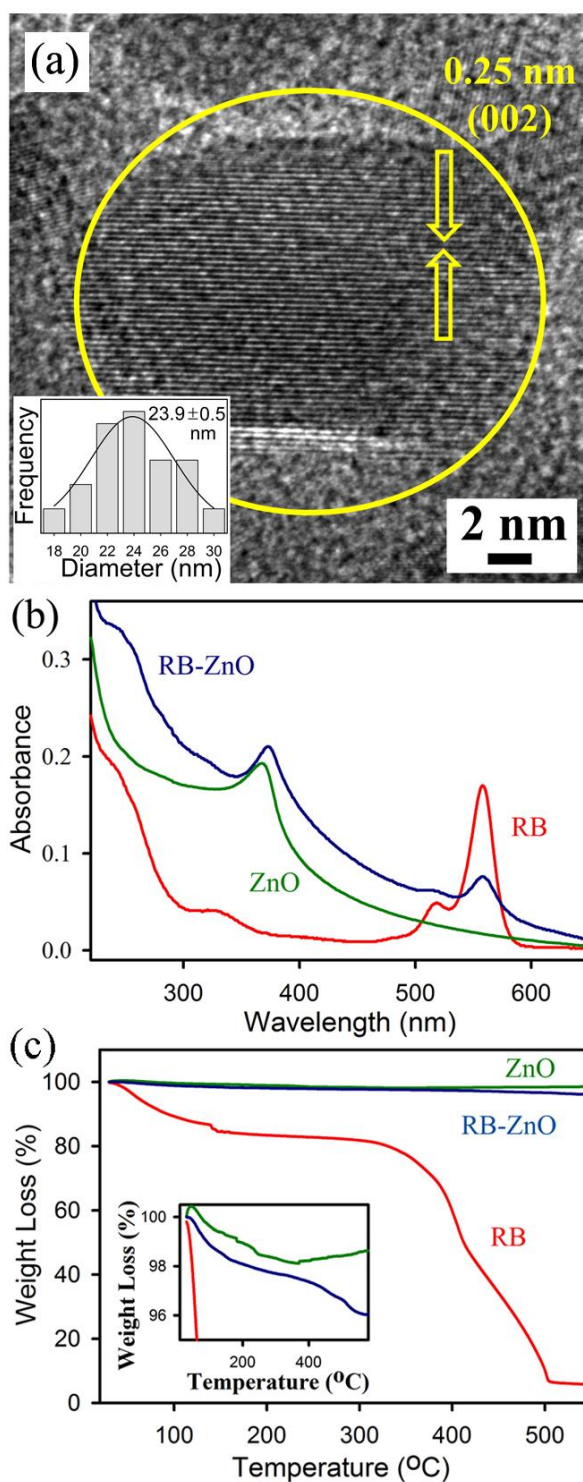


Figure 8.1. (a) HRTEM image of ZnO NPs. Inset shows the size distribution of ZnO NPs. (b) Absorption spectra of RB-ZnO (blue), RB (red) and ZnO (green). (c) Thermogravimetric analysis profile of RB-ZnO (blue), RB (red) and ZnO (green).

maxima of RB as well as ZnO in the RB-ZnO nanohybrid compared to free RB and ZnO NPs, respectively. This observation indicates that there is a perturbation in the

molecular structure of RB when bound to surfaces of ZnO NPs [38]. RB loading on ZnO NPs and the thermal stability of the nanohybrids have been studied by thermogravimetric analysis. Figure 8.1.c shows the thermogravimetric curves of RB, ZnO and RB-ZnO. An onset at about 330°C and a major decomposition at 400-500°C for RB are depicted in the TGA plot whereas pure ZnO NPs are very stable with negligible decomposition in air in the range of 30–600°C. The thermal decomposition of ~2.5% of the nanohybrids in between 400-500°C is attributed to the presence of RB molecules. Inset of Figure 8.1.c shows the magnified graph of RB-ZnO degradation. The number of RB molecules on one ZnO NP is calculated to be 643 which is consistent with the value calculated from the UV-visible absorption spectra. The absorption spectrum of RB-ZnO nanohybrids after baseline correction was exploited to quantify the number of RB molecules on ZnO surface of 30 nm. The RB concentration is calculated from the absorbance maxima at 560 nm as ZnO has no absorbance above 380 nm.

The emission spectra of RB and RB-ZnO are shown in acetonitrile in Figure 8.2.a and the corresponding excitation spectra are shown in the inset of Figure 8.2.a. The RB exhibits emission peak at 570 nm in acetonitrile upon excitation at 510 nm. The RB emission is significantly quenched when it is attached to the ZnO NPs. This observation indicates the efficient non-radiative photoinduced processes from RB to ZnO NPs. To further study the quenching, time-resolved fluorescence transients were carried out. The fluorescence decay profiles for free RB and RB-ZnO were obtained upon excitation at 510 nm in acetonitrile and monitored at 570 nm as shown in Figure 8.2.b. The time constants of the PL transients at 570 nm for the singlet excited-state of RB in acetonitrile solution showed single exponential decay, with a lifetime of 2.42 ns. The quenching of the life-time transients is observed in RB-ZnO with an average life-

time of 0.11 ns after the timescales are fitted by bi-exponential decay. The fitting parameter details of the fluorescence decays are displayed in Table 8.1. The average lifetime of the RB in the presence of ZnO NPs is faster owing to efficient electron transfer from excited RB to the conduction band of the ZnO NPs. RB-ZnO nano hybrid using ZnO NPs with approximate size ~ 24 nm which does not have intrinsic defect

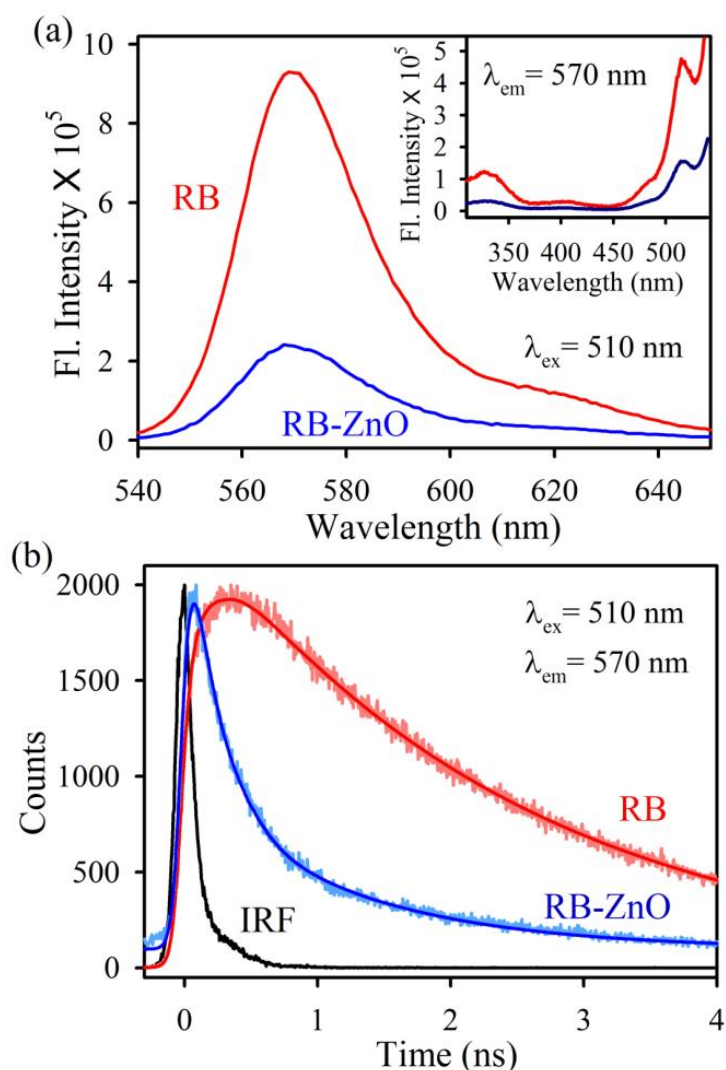


Figure 8.2. (a) Room temperature PL spectra of RB (red) and RB-ZnO (30 nm) (blue) upon excitation at 510 nm. Inset shows the excitation spectra of RB (red) and RB-ZnO (30 nm) (blue) at detection wavelength 570 nm. (b) Fluorescence decay profiles of RB (red) and RB-ZnO (30 nm) (blue) upon excitation at 510 nm and detection wavelength at 570 nm.

state emission has been used to study the interfacial dynamics. The 5 nm ZnO NPs which has an intrinsic defect state emission is used to investigate the molecular proximity between RB and ZnO NPs using Förster Resonance Energy Transfer (FRET)

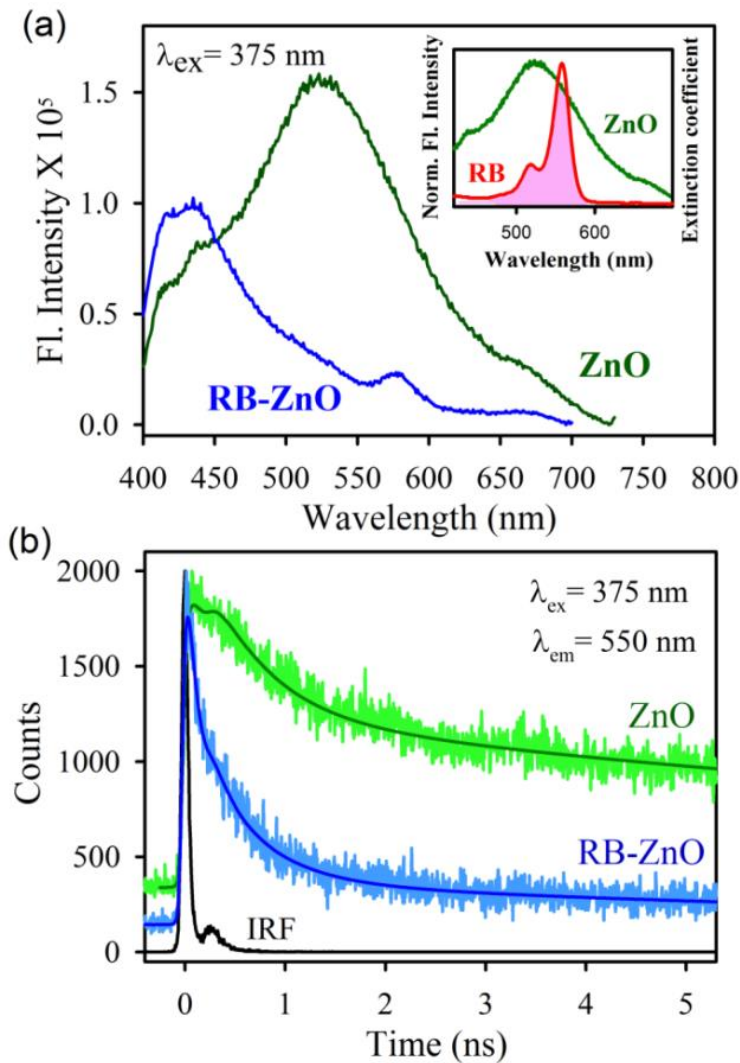


Figure 8.3. (a) Emission spectra of ZnO (5 nm) (green) and RB-ZnO (5 nm) (blue) upon excitation at 375 nm. Inset depicts the spectral overlap between ZnO (5 nm) emission and RB absorption spectra. (b) Fluorescence decay profiles of ZnO (5 nm) (green) and RB-ZnO (5 nm) (blue) upon excitation at 375 nm and detection wavelength at 550 nm.

technique. ZnO NPs have a particle size of 5 nm has a broad steady-state emission in the blue green region owing to defect centres located near the surface of NPs as shown in Figure 8.3.a.

The broad emission arises from two different vacancy centres, one as a result of doubly charged vacancy centres (V_o^{++}) located at 555 nm (P_2) and the other arises from singly charged vacancy centres (V_o^+) located at 500 nm (P_1) [39, 40]. There is a considerable decrease in the intensity of the defect state emission of ZnO NPs in the nanohybrid which occurs as a consequence of effective non-radiative photoinduced

processes from ZnO NPs to the RB. The spectral overlap between the donor ZnO NP emission and the RB absorption as shown in Figure 8.3.a inset, indicates the plausibility of convenient energy transfer from ZnO NPs to RB. In this regard, here we propose the phenomenon of Förster Resonance Energy Transfer (FRET) from the ZnO NPs (donor) to the RB (acceptor). FRET is a convenient tool to measure the donor-acceptor distance and so it is like a “spectroscopic ruler” [41]. The fluorescence decay transients of the 5 nm ZnO NPs (donor) in the presence and absence of the RB (acceptor) were measured at 550 nm (P₂, defect centre near the surface) after excitation at 375 nm (Figure 8.3.b).

Table 8.1. Picosecond-resolved fluorescence data fitting of RB and RB-ZnO Nanohybrids.

Sample	Excitation wavelength (nm)	Detection wavelength (nm)	τ_1 (ns)	τ_2 (ns)	τ_3 (ns)	τ_{avg} (ns)
RB	510	570	2.42 (100%)	-	-	2.42
RB-ZnO	510	570	0.04 (80%)	0.36 (20%)	-	0.11
ZnO (5nm)	375	550	0.60 (53%)	13.91 (47%)	-	6.85
RB-ZnO (5nm)	375	550	0.09 (63%)	0.52 (29%)	7.58 (8%)	0.81

^aNumbers in the parenthesis indicate relative weightages.

There is a prominent quenching in the excited state lifetime of ZnO NPs attached RB in comparison to bare ZnO NPs. The estimated distance between the donor ZnO NPs and the drug is found to be 1.5 nm. The calculated energy transfer is 88% and the overlap integral [$J(\lambda)$] is found out to be $2.98 \times 10^{15} \text{ M}^{-1} \text{ cm}^{-1} \text{ nm}^4$. Thus, the calculated FRET distance confirms the proximity of the RB drugs to the ZnO NPs. After the investigation of interfacial dynamics and molecular proximity, the rate of reactive oxygen species (ROS) production was evaluated by the conversion of

dichlorofluorescein (DCFH) to dichlorofluorecein (DCF) in the aqueous medium. The DCFH is a widely known marker which is used in ROS detection assays [42, 43]. The ROS generated in the medium oxidized non-fluorescent DCFH to fluorescent DCF. The fluorescence emission intensity of DCF was monitored with respect to time as shown in Figure 8.4.a. There is a maximum enhancement of fluorescence intensity under green light irradiation in RB-ZnO nanohybrids. The ROS production has increased to almost two fold in RB-ZnO compared to free RB. A control experiment was performed where ZnO NPs upon green light illumination shows negligible ROS generation as the NPs lack photon absorption in the green zone of optical spectrum. However, DCFH oxidation is inconclusive in determining the nature of generated ROS i.e. whether they are singlet oxygen or superoxide anions. On the other hand, Luminol oxidises to produce chemiluminescence in presence of superoxide [44]. It is seen in Figure 8.4.c that no chemiluminescence is obtained in the presence of RB-ZnO after green light irradiation for 15 minutes which rules out the possibility of superoxide generation by the nanohybrid. In order to elucidate the involvement of singlet oxygen, the DCFH oxidation assay was performed in the presence of sodium azide which is a well-known singlet oxygen quencher [45]. As shown in Figure 8.4.b, the rate of ROS generation is inhibited in presence of sodium azide. These observations indicate that the nature of ROS is predominantly singlet oxygen rather superoxide anions which is consistent with the report of mechanistic pathway of ROS upon photo irradiation of RB alone [11]. To investigate the role of dissolved oxygen in water, DCFH oxidation assay was performed after nitrogen purging for one hour. The decrease in DCFH oxidation indicates that the dissolved oxygen in the medium assists in the generation of singlet oxygen. Therefore, ZnO NPs when conjugated with RB drugs not only aid in efficient

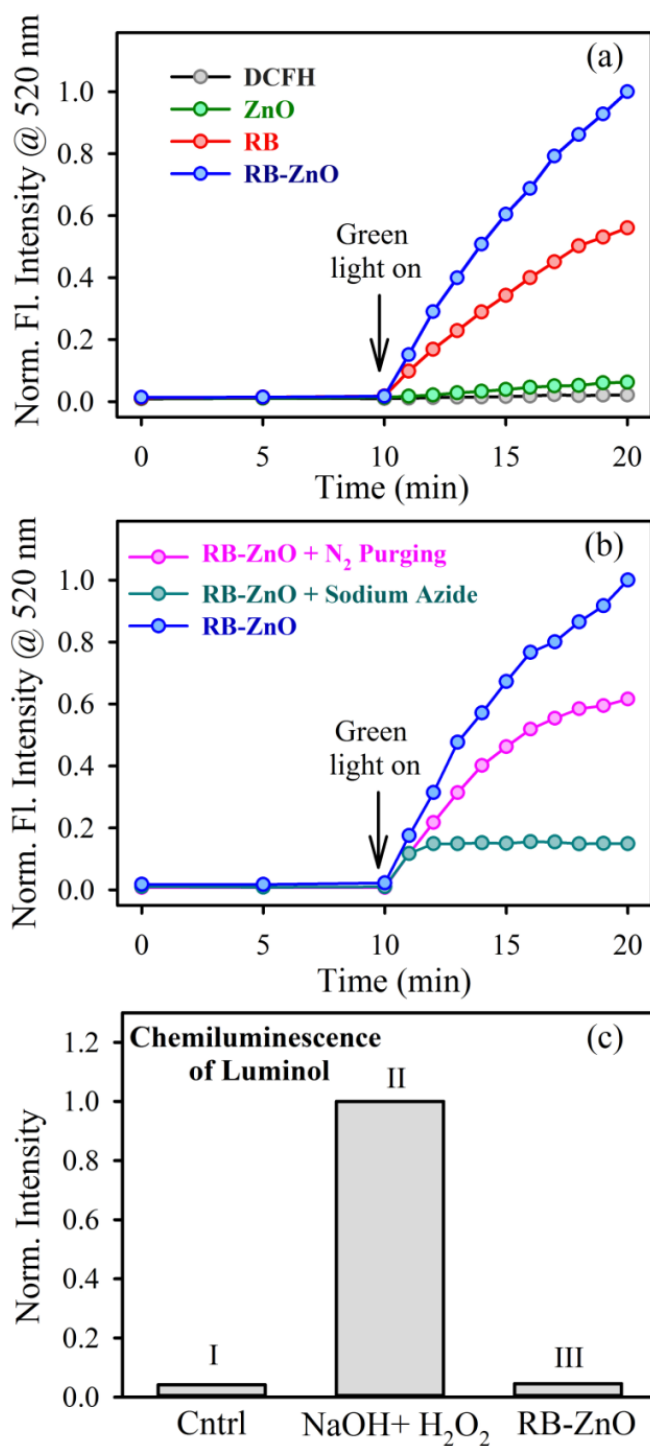
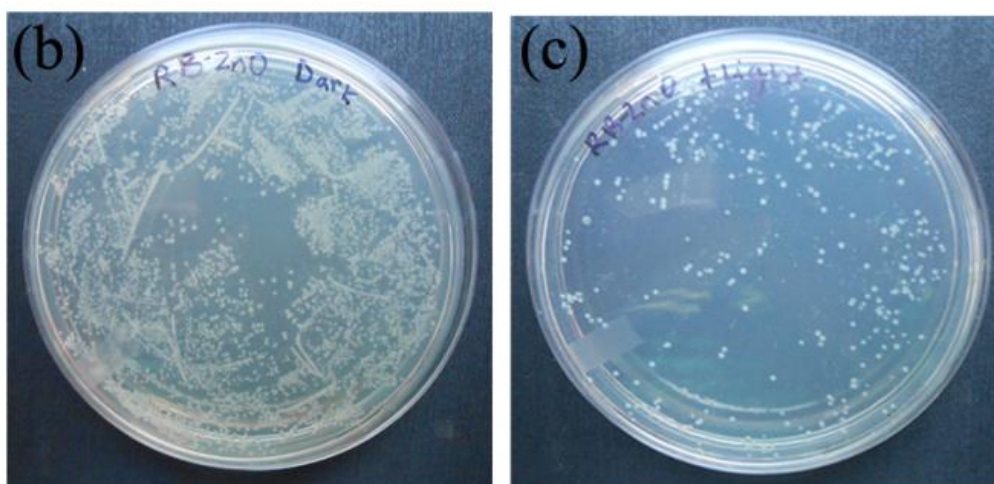
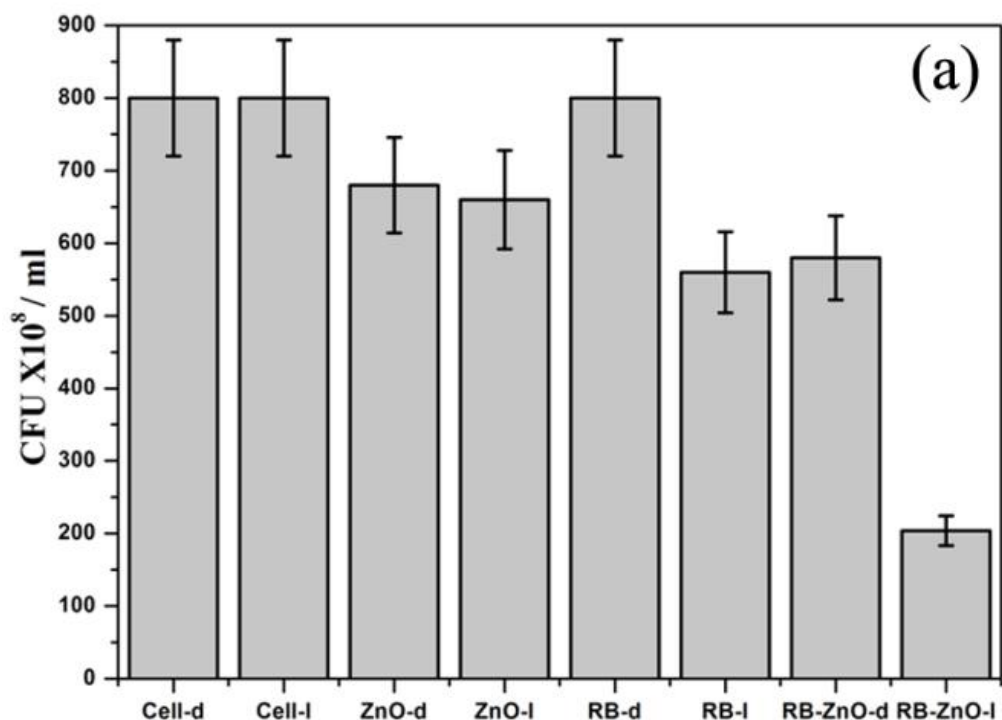


Figure 8.4. (a) DCFH oxidation with respect to time with addition of RB-ZnO (blue), RB (red), ZnO (green) and control DCFH (black) under dark followed by green light irradiation (b) DCFH oxidation with respect to time with RB-ZnO addition in an atmosphere of purged nitrogen (pink), sodium azide (green) and control (blue) under dark followed by green light irradiation (c) Luminol chemiluminescence prior to green light illumination for 15 minutes for (I) control, (II) NaOH + H₂O₂ and (III) RB-ZnO.

drug delivery vehicle but also augments ROS formation due to the enhanced charge separation of the excited drug in the proximity of the semiconductor NPs.

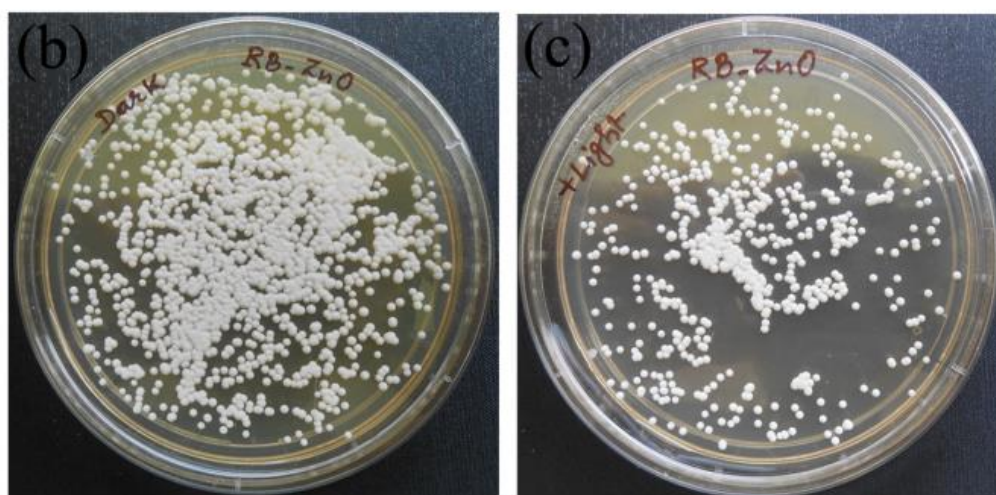
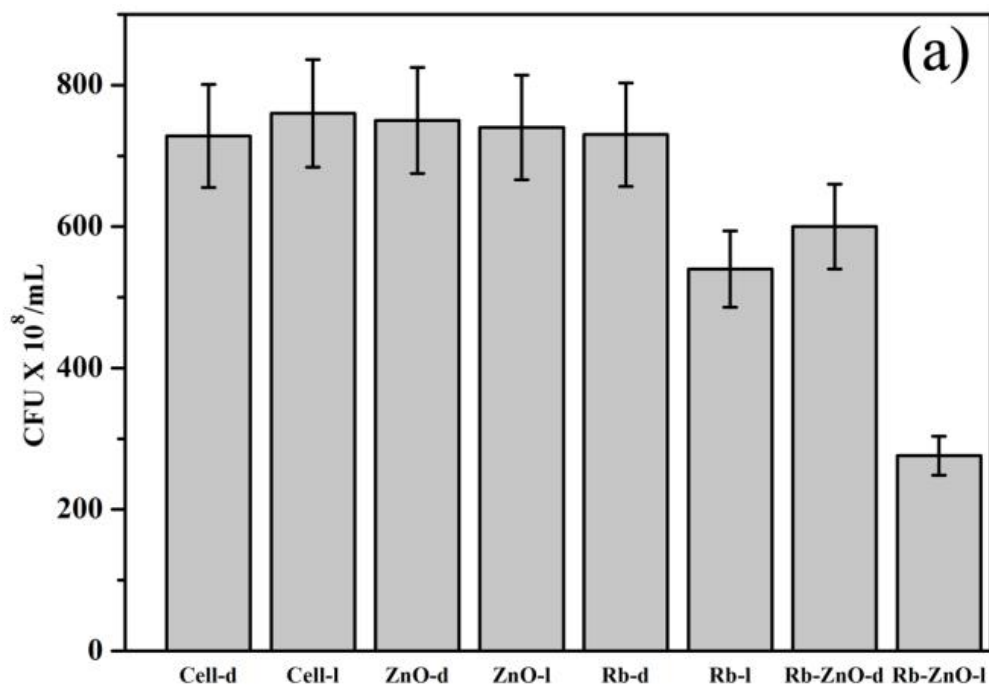
The in-depth characterization studies and analysis of photoinduced dynamics in RB-ZnO nanohybrid was followed by the use of the nanohybrid as an efficacious photodynamic therapeutic agent. In order to affirm the *in-vitro* results of ROS generation in the medium, the RB-ZnO nanohybrid has been employed to inhibit the growth of *Escherichia coli* (*E. coli*) and *Candida albicans* (*C. albicans*). Nanohybrids contain RB conjugated ZnO NPs of particle size of 24 nm instead of 5 nm due to lower *in vivo* toxicity [46]. The images of *E. coli* cultures treated with RB-ZnO nanohybrids with and without green light are shown in Figure 8.5.b and 8.5.c. The bacterial growth inhibition prior to photodynamic treatment is distinctly observed. The petri plate with RB-ZnO along with green light exposure contains a significantly less number of colonies. To rule out the toxicity solely arising from free drug and ZnO NPs, control plates with equimolar concentrations of drug and NPs were included in the experiment. In order to assess the viability, bacterial colonies were counted for control along with ones treated with RB drugs, ZnO NPs and RB-ZnO nanohybrids with and without green light exposure as shown in Figure 8.5.a. The colony forming unit (CFU) in control and ZnO treated samples are almost similar in the presence and absence of green light. This observation indicates that the concentration of ZnO NPs used in the assay shows minimal toxicity. 30% bacterial growth inhibition is observed in case of RB treated samples whereas maximum inhibition of 65% was deduced for RB-ZnO treated sample after photodynamic treatment. Similarly, the nanohybrid has a lethal effect on fungal cells under green light. Figure 8.6.b and 8.6.c shows pictures of *C. albicans* cultures incubated with RB-ZnO nanohybrids in the presence and absence of green light irradiation. There is 26% fungal inhibition in samples treated with RB prior to photodynamic treatment. The fungal inhibition has increased to 54% when RB-ZnO



- Green Light + Green Light
 RB-ZnO sensitized

Figure 8.5. (a) Antibacterial activity of RB-ZnO, RB and ZnO in the presence and absence of green light. Images of RB-ZnO treated *E. Coli* plates in the absence (b) and presence (c) of green light.

is used in the assay. The antimicrobial results vividly denote the active role of increased ROS formation in the presence of RB-ZnO nanohybrids compared to that of free RB. The *in vitro* cytotoxicity assays were conducted in HeLa cell line using MTT, which is



- Green Light + Green Light
 RB-ZnO Sensitized

Figure 8.6. (a) Antifungal activity of RB-ZnO, RB and ZnO in the presence and absence of green light. Images of RB-ZnO treated *C. albicans* plates in the absence (b) and presence (c) of green light.

a model marker of cell viability [47]. Bioreduction of MTT leads to formazan production [48] which was estimated at 570 nm. The cell cytotoxicity profile of RB along with the nanohybrid is illustrated in Figure 8.7.a. The cells were stained with DAPI before taking the microscopic images of control as well as RB-ZnO treated cells.

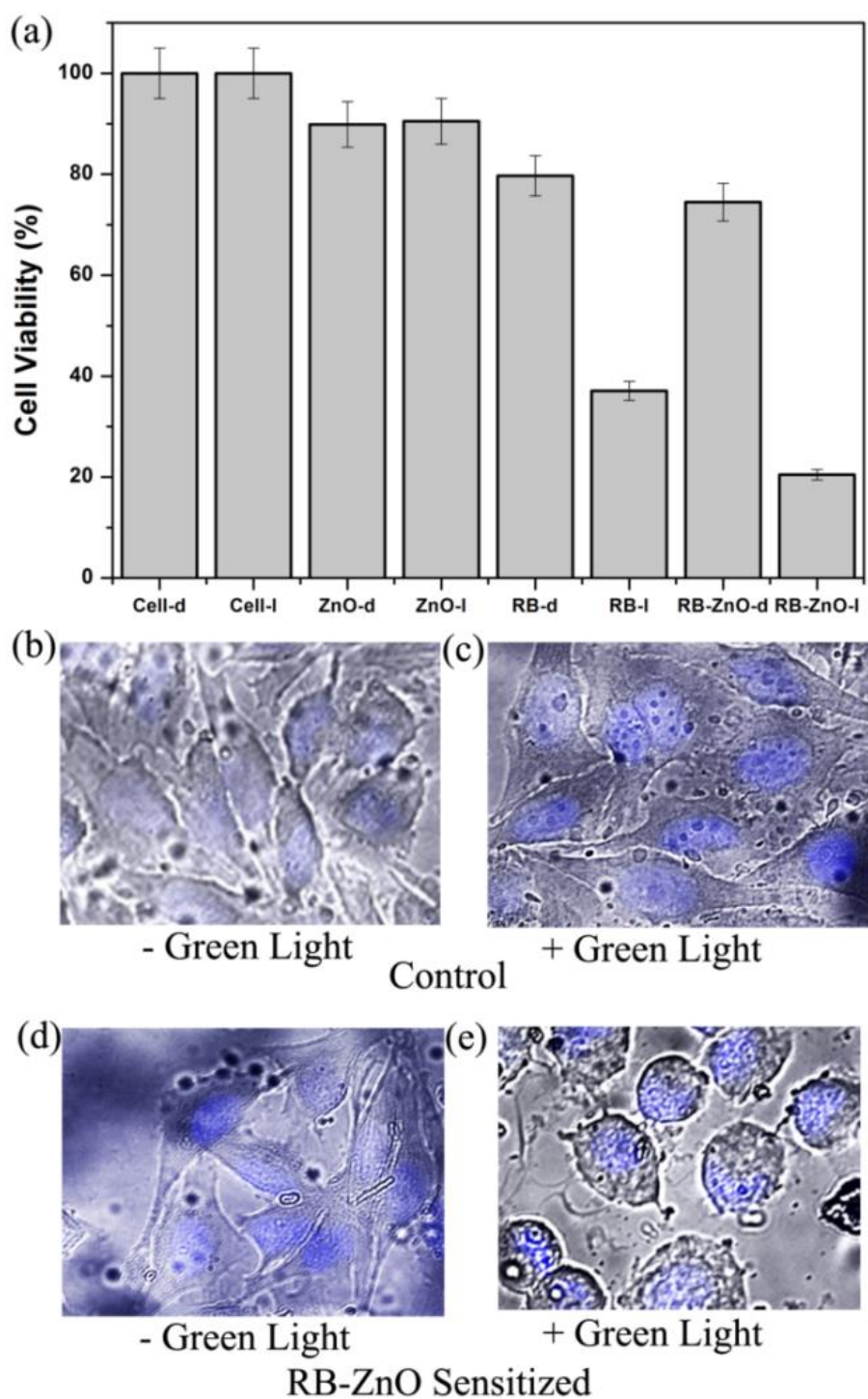


Figure 8.7. (a) *In vitro* cytotoxicity assay in HeLa cells with RB-ZnO, RB and ZnO using MTT as an indicator dye in presence and absence of green light. Images of control and RB-ZnO treated HeLa cells in the absence (b), (d) and the presence (c), (e) of green light.

DAPI specifically stains chromatin of nucleus and has a blue emission [49]. A distinct change in morphology with rounded nucleus is observed in case of RB-ZnO treated cells under green light irradiation (Figure 8.7.e) compared to that in dark (Figure 8.7.d)

whereas the morphology of the control cells remain intact (Figures 8.7.b and 8.7.c). After seeding 5000 cells/well in 96 well plate, the cells were subjected to drug treatment with RB, ZnO NPs and RB-ZnO followed by green light exposure for four hours. The cells were then incubated overnight at 37°C in an atmosphere of 5% CO₂ before the MTT assay was performed. The experiment was done in triplicate and the cell viability was determined by comparison with the control plate. It was observed that the cell viability in case of free RB was reduced to half and the value is less than one-third when the nanohybrid is used under green light irradiation. However, ZnO NPs show minimal cell cytotoxicity. The enhanced ROS generation as a result of charge separation of the drug in the proximity of semiconductor NPs is responsible for the augmentation of the drug activity. The present study will therefore be helpful in designing efficient photodynamic drugs.

8.3. Conclusion:

The application of rose bengal (RB) as a photodynamic therapeutic agent has a long record of pragmatic evidence. In the present study, we illustrated the vital photoinduced dynamics of RB upon complexation with semiconductor ZnO NPs. Here, we synthesized nanohybrids of RB with ZnO NPs of approximately 24 nm size and characterized them by high resolution transmission electron microscopy (HRTEM), UV-Vis absorption and steady-state fluorescence studies. Picosecond-resolved Förster resonance energy transfer (FRET) was employed to reveal the proximity of the drug and the semiconductor at the molecular level. It is inferred that the energy is transferred from the defect state emission of ZnO NPs to RB upon excitation with green light. Furthermore, picosecond-resolved fluorescence studies on RB-ZnO reveal an effective electron migration from photoexcited RB to ZnO NPs, resulting in elevation of the ROS activity in the nanohybrid. Dichlorofluorescein (DCFH-DCF) oxidation assay

proves that the ROS generation is found to be more than two fold magnitude greater in nano hybrid compared to that of free drug. Moreover, the photodynamic activity of the nano hybrid in bacterial, fungal and HeLa cell lines corroborates with the *in vitro* ROS detection assay. Hence, these studies could be incorporated in the development of safe, beneficial and low cost alternative photodynamic therapeutic agents to treat various diseases.

References:

- [1] J.B. Hall, M.A. Dobrovolskaia, A.K. Patri, S.E. McNeil, Characterization of Nanoparticles for Therapeutics, *Nanomedicine*, 2 (2007) 789-803.
- [2] J. Lenard, A. Rabson, R. Vanderoef, Photodynamic Inactivation of Infectivity of Human Immunodeficiency Virus and Other Enveloped Viruses Using Hypericin and Rose Bengal: Inhibition of Fusion and Syncytia Formation, *Proc. Natl. Acad. Sci. U.S.A.*, 90 (1993) 158-162.
- [3] T.S. Hauck, S. Giri, Y. Gao, W.C. Chan, Nanotechnology Diagnostics for Infectious Diseases Prevalent in Developing Countries, *Adv. Drug Deliv. Rev.*, 62 (2010) 438-448.
- [4] V.B. Arce, S.G. Bertolotti, F.J. Oliveira, C. Airoidi, A. Arques, L. Santos-Juanes, M.C. Gonzalez, C.J. Cobos, P.E. Allegretti, D.O. Mártire, Triplet state of 4-methoxybenzyl Alcohol Chemisorbed on Silica Nanoparticles, *Photochem. Photobiol. Sci.*, 11 (2012) 1032-1040.
- [5] H.-M. Xiong, ZnO Nanoparticles Applied to Bioimaging and Drug Delivery, *Adv. Mat.*, 25 (2013) 5329-5335.
- [6] J.W. Rasmussen, E. Martinez, P. Louka, D.G. Wingett, Zinc Oxide Nanoparticles for Selective Destruction of Tumor Cells and Potential for Drug Delivery Applications, *Expert Opin. Drug Deliv.*, 7 (2010) 1063-1077.
- [7] H. Kitching, A.J. Kenyon, I.P. Parkin, The Interaction of Gold and Silver Nanoparticles with a Range of Anionic and Cationic Dyes, *Phys. Chem. Chem. Phys.*, 16 (2014) 6050-6059.
- [8] J. Moan, Q. Peng, An Outline of the Hundred-Year History of PDT, *Anticancer Res.*, 23 (2003) 3591-3600.
- [9] B.Q. Spring, I. Rizvi, N. Xu, T. Hasan, The Role of Photodynamic Therapy in Overcoming Cancer Drug Resistance, *Photochem. Photobiol. Sci.*, 14 (2015) 1476-1491.
- [10] X. Ragàs, L.P. Cooper, J.H. White, S. Nonell, C. Flors, Quantification of Photosensitized Singlet Oxygen Production by a Fluorescent Protein, *Chem. Phys. Chem.*, 12 (2011) 161-165.
- [11] M.C. DeRosa, R.J. Crutchley, Photosensitized Singlet Oxygen and Its Applications, *Coordin. Chem. Rev.*, 233 (2002) 351-371.

- [12] S.D.-M. Islam, O. Ito, Solvent Effects on Rates of Photochemical Reactions of Rose Bengal Triplet State Studied by Nanosecond Laser Photolysis, *J. Photochem. Photobiol. A*, 123 (1999) 53-59.
- [13] S.H. Mousavi, J. Tavakkol-Afshari, A. Brook, I. Jafari-Anarkooli, Direct Toxicity of Rose Bengal in MCF-7 Cell Line: Role of Apoptosis, *Food Chem. Toxicol.*, 47 (2009) 855-859.
- [14] E. Panzarini, V. Inguscio, G.M. Fimia, L. Dini, Rose Bengal Acetate Photodynamic Therapy (RBAc-PDT) Induces Exposure and Release of Damage-Associated Molecular Patterns (DAMPs) in Human HeLa Cells, *PLoS ONE*, 9 (2014) e105778.
- [15] C.R. Lambert, I.E. Kochevar, Electron Transfer Quenching of the Rose Bengal Triplet State, *Photochem. Photobiol.*, 66 (1997) 15-25.
- [16] F.F. Sperandio, Y.Y. Huang, M.R. Hamblin, Antimicrobial Photodynamic Therapy to Kill Gram-Negative Bacteria, *Recent Pat Antiinfect Drug Discov.*, 8 (2013) 108-120.
- [17] E. Panzarini, V. Inguscio, L. Dini, Timing the Multiple Cell Death Pathways Initiated by Rose Bengal Acetate Photodynamic Therapy, *Cell Death Dis.*, 2 (2011) e169.
- [18] S.S. Mohideen, Y. Yamasaki, Y. Omata, L. Tsuda, Y. Yoshiike, Nontoxic Singlet Oxygen Generator as a Therapeutic Candidate for Treating Tauopathies, *Sci. Rep.*, 5 (2015).
- [19] L. Dini, V. Inguscio, B. Tenuzzo, E. Panzarini, Rose Bengal Acetate Photodynamic Therapy-Induced Autophagy, *Cancer Biol. Ther.*, 10 (2010) 1048-1055.
- [20] A.C.B.P. Costa, V.M.C. Rasteiro, C.A. Pereira, R.D. Rossoni, J.C. Junqueira, A.O.C. Jorge, The Effects of Rose Bengal and Erythrosine Mediated Photodynamic Therapy on *Candida albicans*, *Mycoses*, 55 (2012) 56-63.
- [21] C.O. Morton, M. Chau, C. Stack, In Vitro Combination Therapy Using Low Dose Clotrimazole and Photodynamic Therapy Leads to Enhanced Killing of the Dermatophyte *Trichophyton rubrum*, *BMC microbiology*, 14 (2014) 261.
- [22] A. Arboleda, D. Miller, F. Cabot, M. Taneja, M.C. Aguilar, K. Alawa, G. Amescua, S.H. Yoo, J.-M. Parel, Assessment of Rose Bengal versus Riboflavin Photodynamic Therapy for Inhibition of Fungal Keratitis Isolates, *Am. J. Ophthalmol.*, 158 (2014) 64-70. e62.

- [23] E. Panzarini, V. Inguscio, L. Dini, Overview of Cell Death Mechanisms Induced by Rose Bengal Acetate-Photodynamic Therapy, *Int. J. Photoenergy*, 2011 (2011) 713726.
- [24] M. Bolean, P. Paulino Tde, G. Thedei, Jr., P. Ciancaglini, Photodynamic Therapy with Rose Bengal Induces GroEL Expression in *Streptococcus mutans*, *Photomed. Laser. Surg.*, 28 (2010).
- [25] B.J. Park, K.-H. Choi, K.C. Nam, A. Ali, J.E. Min, H. Son, H.S. Uhm, H.-J. Kim, J.-S. Jung, E.H. Choi, Photodynamic Anticancer Activities of Multifunctional Cobalt Ferrite Nanoparticles in Various Cancer Cells, *J. Biomed. Nanotechnol.*, 11 (2015) 226-235.
- [26] C.-C. Chang, Y.-T. Yang, J.-C. Yang, H.-D. Wu, T. Tsai, Absorption and Emission Spectral Shifts of Rose Bengal Associated with DMPC Liposomes, *Dyes Pigments*, 79 (2008) 170-175.
- [27] M. Fadel, K. Kassab, Evaluation of the Photostability and Photodynamic Efficacy of Rose Bengal Loaded in Multivesicular Liposomes, *Trop. J. Pharm. Res.*, 10 (2011).
- [28] M. Bottone, C. Soldani, A. Fraschini, C. Alpini, A. Croce, G. Bottiroli, C. Pellicciari, Enzyme-Assisted Photosensitization with Rose Bengal Acetate Induces Structural and Functional Alteration of Mitochondria in HeLa cells, *Histochem. Cell Biol.*, 127 (2007) 263-271.
- [29] A. Uppal, B. Jain, P.K. Gupta, K. Das, Photodynamic Action of Rose Bengal Silica Nanoparticle Complex on Breast and Oral Cancer Cell Lines, *Photochem. Photobiol.*, 87 (2011) 1146-1151.
- [30] P.K. Gupta, K. Das, M. Sharma, Effect of Complexing with Silica Nanoparticles on the Phototoxicity of Some Photosensitisers, *Procedia. Engineering*, 92 (2014) 9-18.
- [31] A. Shrestha, M.R. Hamblin, A. Kishen, Characterization of a Conjugate between Rose Bengal and Chitosan for Targeted Antibiofilm and Tissue Stabilization Effects as a Potential Treatment of Infected Dentin, *Antimicrob. Agents Chemother.*, 56 (2012) 4876-4884.
- [32] M.J. Simpson, H. Poblete, M. Griffith, E.I. Alarcon, J.C. Scaiano, Impact of Dye-Protein Interaction and Silver Nanoparticles on Rose Bengal Photophysical Behavior and Protein Photocrosslinking, *Photochem. Photobiol.*, 89 (2013) 1433-1441.
- [33] A. Shrestha, M.R. Hamblin, A. Kishen, Photoactivated Rose Bengal Functionalized Chitosan Nanoparticles Produce Antibacterial/Biofilm Activity and Stabilize Dentin-Collagen, *Nanomedicine*, 10 (2014) 491-501.

- [34] B. Wang, J.H. Wang, Q. Liu, H. Huang, M. Chen, K. Li, C. Li, X.F. Yu, P.K. Chu, Rose-Bengal-Conjugated Gold Nanorods for in Vivo Photodynamic and Photothermal Oral Cancer Therapies, *Biomaterials*, 35 (2014) 1954-1966.
- [35] S. Sardar, S. Chaudhuri, P. Kar, S. Sarkar, P. Lemmens, S.K. Pal, Direct Observation of Key Photoinduced Dynamics in a Potential Nano-Delivery Vehicle of Cancer Drugs., *Phys. Chem. Chem. Phys.*, 17 (2015) 166-177.
- [36] S. Chaudhuri, S. Sardar, D. Bagchi, S.S. Singha, P. Lemmens, S.K. Pal, Sensitization of an Endogenous Photosensitizer: Electronic Spectroscopy of Riboflavin in the Proximity of Semiconductor, Insulator, and Metal Nanoparticles, *J. Phys. Chem. A*, 119 (2015) 4162-4169.
- [37] S. Chaudhuri, S. Sardar, D. Bagchi, S. Dutta, S. Debnath, P. Saha, P. Lemmens, S.K. Pal, Photoinduced Dynamics and Toxicity of a Cancer Drug in Proximity of Inorganic Nanoparticles under Visible Light, *Chem. Phys. Chem.*, 17 (2016) 270-277.
- [38] D. Xu, D.C. Neckers, Aggregation of Rose Bengal Molecules in Solution, *J. Photochem. Photobiol. A*, 40 (1987) 361-370.
- [39] A. van Dijken, E.A. Meulenlamp, D. Vanmaekelbergh, A. Meijerink, The Kinetics of the Radiative and Nonradiative Processes in Nanocrystalline ZnO Particles upon Photoexcitation, *J. Phys. Chem. B*, 104 (2000) 1715-1723.
- [40] K. Vanheusden, W.L. Warren, C.H. Seager, D.R. Tallant, J.A. Voigt, B.E. Gnade, Mechanisms Behind Green Photoluminescence in ZnO Phosphor Powders, *J. Appl. Phys.*, 79 (1996) 7983-7990.
- [41] C.J. Breshike, R.A. Riskowski, G.F. Strouse, Leaving Förster Resonance Energy Transfer Behind: Nanometal Surface Energy Transfer Predicts the Size-Enhanced Energy Coupling between a Metal Nanoparticle and an Emitting Dipole, *J. Phys. Chem. C*, 117 (2013) 23942-23949.
- [42] S.B. Koevary, Selective Toxicity of Rose Bengal to Ovarian Cancer Cells in Vitro, *Int. J. Physiol. Pathophysiol. Pharmacol.*, 4 (2012) 99-107.
- [43] C.P. LeBel, H. Ischiropoulos, S.C. Bondy, Evaluation of the Probe 2', 7'-dichlorofluorescein as an Indicator of Reactive Oxygen Species Formation and Oxidative Stress, *Chem. Res. Toxicol.*, 5 (1992) 227-231.
- [44] M.M. Tarpey, I. Fridovich, Methods of Detection of Vascular Reactive Species: Nitric Oxide, Superoxide, Hydrogen Peroxide, and Peroxynitrite, *Circ Res.*, 89 (2001) 224-236.

- [45] R. Huang, E. Choe, D.B. Min, Kinetics for Singlet Oxygen Formation by Riboflavin Photosensitization and the Reaction between Riboflavin and Singlet Oxygen, *J. Food Sci.*, 69 (2004) C726-C732.
- [46] S. Nair, A. Sasidharan, V.V. Divya Rani, D. Menon, S. Nair, K. Manzoor, S. Raina, Role of Size Scale of ZnO Nanoparticles and Microparticles on Toxicity Toward Bacteria and Osteoblast Cancer Cells, *J. Mater. Sci.: Mater. Med.*, 20 (2009) 235-241.
- [47] K. Chiba, K. Kawakami, K. Tohyama, Simultaneous Evaluation of Cell Viability by Neutral Red, MTT and Crystal Violet Staining Assays of the Same Cells, *Toxicol. In Vitro*, 12 (1998) 251-258.
- [48] M. Ishiyama, H. Tominaga, M. Shiga, K. Sasamoto, Y. Ohkura, K. Ueno, A Combined Assay of Cell Viability and in Vitro Cytotoxicity with a Highly Water-Soluble Tetrazolium Salt, Neutral Red and Crystal Violet, *Biol. Pharm. Bull.*, 19 (1996) 1518-1520.
- [49] K. Jin, X. Wang, L. Xie, X.O. Mao, W. Zhu, Y. Wang, J. Shen, Y. Mao, S. Banwait, D.A. Greenberg, Evidence for Stroke-Induced Neurogenesis in the Human Brain, *Proc. Natl. Acad. Sci. U.S.A.*, 103 (2006) 13198-13202.

List of Publications

(International Peer-Reviewed Journals)

1. **S. Chaudhuri**, S Sardar, D. Bagchi, S. Dutta, S. Debnath, P. Saha, P. Lemmens and S. K. Pal
“Photoinduced Dynamics and Toxicity of a Cancer Drug in Proximity of Inorganic Nanoparticles under Visible Light”, Chem. Phys. Chem. 17 (2016) 270.
2. **S. Chaudhuri**, S. Sardar, D. Bagchi, S. Singha, P. Lemmens and S. K. Pal
“Sensitization of an Endogenous Photosensitizer: Electronic Spectroscopy of Riboflavin in the Proximity of Semiconductor, Insulator and Metal Nanoparticles”, J. Phys. Chem. A 119 (2015) 4162.
3. **S. Chaudhuri**, S. Batabyal, N. Polley and S. K. Pal
“Vitamin B2 in Nanoscopic Environments under Visible Light: Photosensitized Antioxidant or Phototoxic Drug?”, J. Phys. Chem. A 118 (2014) 3934.
4. **S. Chaudhuri**, N. Goswami, A. Giri, P. Lemmens and S. K. Pal
“Surface Engineering for Controlled Nanocatalysis: Key Dynamical Events from Ultrafast Electronic Spectroscopy”, J. Phys. Chem. C 118 (2014) 23434.
5. S. Banerjee, **S. Chaudhuri**, A. K. Maity, P. Saha and S. K. Pal
“Role of Caffeine in DNA Recognition of a Potential Food-Carcinogen Benzo[a]pyrene and UVA Induced DNA damage”, J. Mol. Recog. 27 (2014) 510.
6. * D. Bagchi, **S. Chaudhuri**, S. Sardar, S. Choudhury, N. Polley, P. Lemmens and S. K. Pal
“Modulation of Stability and Functionality of a Phyto-antioxidant by Weakly Interacting Metal Ions: Curcumin in Aqueous Solution”, RSC Advances 5 (2015) 102516.

7. * S. Sardar, **S. Chaudhuri**, P. Kar, S. Sarkar, P. Lemmens and S. K. Pal
“Direct Observation of Key Photoinduced Dynamics in a Potential Nano-delivery Vehicle of Cancer Drugs”, *Phys. Chem. Chem. Phys.* 17 (2015) 166.

8. * S. Banerjee, **S. Chaudhuri** and S. K. Pal
“Ultrafast Spectroscopic Studies on the Interaction of a Potential Food Carcinogen with Biologically Relevant Macromolecules”, *International Review of Biophysical Chemistry (IREBIC)* 4 (2013) 161.

* Not included in the thesis.